

EXPLORATION OF HIGH EFFICIENCY PATHWAYS IN DUAL FUEL LOW
TEMPERATURE COMBUSTION ENGINES

by

PRABHAT RANJAN JHA

KALYAN K. SRINIVASAN, COMMITTEE CHAIR
SUNDAR R. KRISHNAN, COMMITTEE CO-CHAIR
JOSHUA A. BITTLE
MRUTHUNJAYA UDDI
SEMIH M. OLCMEN
LORENZO BARTOLUCCI

A DISSERTATION

Submitted in partial fulfillment of the requirements
for the degree of Doctor of Philosophy
in the Department of Mechanical Engineering
in the Graduate School of
The University of Alabama

TUSCALOOSA, ALABAMA

2021

Copyright Prabhat Ranjan Jha 2021
ALL RIGHTS RESERVED

ABSTRACT

It's crucial to use advanced combustion strategies to increase efficiency and decrease engine-out pollutants because of the compelling need to reduce the global carbon footprint. This dissertation proposes dual fuel low-temperature combustion as a viable strategy to decrease engine-out emissions and increase the thermal efficiency of future heavy-duty internal combustion (IC) engines. In dual fuel combustion, a low reactivity fuel (e.g. methane, propane) is ignited by a high reactivity fuel (diesel) in a compression-ignited engine. Generally, the energy fraction of low reactivity fuel is maintained at much higher levels than the energy fraction of the high reactivity fuel. For a properly calibrated engine, combustion occurs at lean and low-temperature conditions (LTC). This decreases the chances of the formation of soot and oxides of nitrogen within the engine. However, at low load conditions, this type of combustion results in high hydrocarbon and carbon monoxide emissions. The first part of this research experimentally examines the effect of methane (a natural gas surrogate) substitution on early injection dual fuel combustion at representative low loads of 3.3 and 5.0 bar BMEPs in a single-cylinder compression ignition engine (SCRE). Gaseous methane fumigated into the intake manifold at various methane energy fractions was ignited using a high-pressure diesel pilot injection at 310 CAD. Cyclic combustion variations at both loads were also analyzed to obtain further insights into the combustion process and identify opportunities to further improve fuel conversion efficiencies at low load operation. In the second part, the cyclic variations in dual fuel combustion of three different low reactivity fuels (methane, propane, and gasoline) ignited using

a high-pressure diesel pilot injection was examined and the challenges and opportunities in utilizing methane, propane, and gasoline in diesel ignited dual fuel combustion, as well as strategies for mitigating cyclic variations, were explored. Finally, in the third part a CFD model was created for diesel methane dual fuel LTC. The validated model was used to investigate the effect of methane on diesel autoignition and various spray targeting strategies were explored to mitigate high hydrocarbon and carbon monoxide emissions at low load conditions.

DEDICATION

I would like to dedicate my dissertation to my beloved grandparents, parents, and family for their love and countless support in my entire life.

LIST OF ABBREVIATIONS AND SYMBOLS

Abbreviations

AHRR	Apparent Heat Release Rate
BDC	Bottom Dead Center
BMEP	Brake Mean Effective Pressure
CAD	Crank Angle Degree
CFD	Computational Fluid Dynamics\
CA 5-90	Crank angle duration between locations of 5% and 90% cumulative heat release
CA5	Crank angle at which 5% of cumulative heat release occurs
CA50	Crank angle at which 50% of cumulative heat release occurs
CA90	Crank angle at which 90% of cumulative heat release occurs
CAPmax	Crank angle where pressure is maximum
CI	Compression Ignition
CO	Carbon Monoxide
CO ₂	Carbon Dioxide
COV	Coefficient Of Variation
COV IMEP	Coefficient of variation of IMEP
DAQ	Data Acquisition
DEF	Diesel energy fraction

EGR	Exhaust Gas Recirculation
EOC	End of Combustion
EOI	End of injection
EVC	Exhaust Valve closing
EVO	Exhaust Valve Opening
FCE	Fuel Conversion Efficiency
FID	Flame ionization detector
GCI	Gasoline Compression Ignition
HC	Unburned hydrocarbons
HCCI	Homogeneous Charge Compression Ignition
HDDE	Heavy Duty Diesel Engine
HTHR	High temperature heat release
ID	Ignition delay
IC	Internal Combustion
IFCE	indicated Fuel Conversion Efficiency
IMEP	Indicated Mean Effective Pressure
IVC	Intake Valve Closure
IVO	Intake Valve Opening
LHV	Lower Heating Value
LPG	Liquefied Petroleum Gas
LTC	Low Temperature Combustion
LTHR	Low temperature heat release
MEF	Methane energy fraction

MPA	Paramagnetic detector
MPRR	Maximum pressure rise rate
NDIR	Nondispersive infrared analyzer
NG	Natural Gas
NO _x	Oxides of Nitrogen
OHTHR	Onset of high temperature heat release
OLTHR	Onset of low temperature heat release
PES	Percentage energy substitute
PPC	Partially Premixed Combustion
QLHV	Mass-averaged lower heating value (kJ/kg)
RCCI	Reactivity Controlled Compression Ignition
rpm	revolution per minute
SADI	Stand Alone Direct Injector Driver
SCRE	Single Cylinder Research Engine
SD	Standard Deviation
SOC	Start of Combustion
SOI	Start of Injection
TDC	Top Dead Center

ACKNOWLEDGEMENTS

I would like to acknowledge my major advisors Dr. Kalyan K. Srinivasan and Dr. Sundar R. Krishnan and for their continued guidance, support and inspiration for the continued research work throughout my graduate studies. I would also like to thank them for helping run countless job on firepower cluster. I thoroughly appreciate their advice, patience and encouragement. Also, I would like to thank Dr. Semih M. Olcmen, Dr. Joshua A. Bittle, Dr. Mruthunjaya Uddi and Dr. Lorenzo Bartolucci for agreeing to serve on my Ph. D. committee. I am also grateful to my colleagues Dr. Hamidreza Mahabadipour, Kendyl Partridge, Abhinandan Narayanan and Dr. Deivanayagam Hariharan for their assistance in performing this work.

I would like to thank Alliance for Sustainable Energy, LLC, Managing and Operating Contractor for the National Renewable Energy Laboratory for the U.S. Department of Energy for supporting this work. I would also like to thank Convergent Science for providing us licenses to develop the computational model in this work. The author gratefully acknowledges the support of the facilities support from Alabama supercomputing center.

CONTENTS

ABSTRACT.....	ii
DEDICATION.....	iv
LIST OF ABBREVIATIONS AND SYMBOLS	v
ACKNOWLEDGEMENTS.....	viii
LIST OF TABLES	xiii
LIST OF FIGURES	xv
CHAPTER.I. INTRODUCTION.....	1
1.1 Motivation for dual fuel low temperature combustion.....	1
1.2 Why investigate cyclic combustion variation in dual fuel low- temperature combustion?.....	3
1.3 Why develop a dual fuel low temperature combustion CFD model?	5
1.4 Organization of Dissertation.....	5
1.5 References	7
CHAPTER.II. IMPACT OF METHANE ENERGY FRACTION (MEF) ON EMISSIONS, PERFORMANCE AND CYCLIC VARIABILITY IN LOW LOAD DUAL FUEL COMBUSTION AT EARLY INJECTION TIMINGS	8
2.1 Abstract.....	8
2.2 Introduction	9
2.3 Experimental setup	13
2.4 Experimental procedure.....	16

2.5	Impact of MEF on dual fuel ignition, combustion, performance and emissions.....	18
2.6	Impact of MEF on cyclic variations	32
2.7	Conclusions	38
2.8	Acknowledgments	39
2.9	References	40
Appendix I		47
Appendix II.....		50
CHAPTER.III. IMPACT OF LOW REACTIVITY FUEL TYPE ON PERFORMANCE, EMISSIONS AND CYCLIC VARIATIONS IN DUAL FUEL LOW TEMPERATURE COMBUSTION		
		54
3.1	Abstract.....	54
3.2	Introduction	55
3.3	Objective of the present work.....	60
3.4	Experimental setup	61
3.5	Experimental procedure.....	66
3.6	Result and discussion	70
3.6.1	Ensemble-Averaged Results.....	70
3.6.2	Cyclic In-Cylinder Pressure and AHRR Results.....	80
3.6.2.1	Zero-Dimensional Chemical Kinetic Analysis.....	84
3.6.3	Cyclic Behavior of Various Combustion Parameters.....	87
3.7	Conclusions	110
3.8	Acknowledgements	113
3.9	References	114
CHAPTER.IV. NUMERICAL INVESTIGATION OF DUAL FUEL ENGINE COMBUSTION AT EARLY INJECTION TIMINGS FOR LOW LOAD OPERATION		
		120

4.1	Abstract.....	120
4.2	Introduction	121
4.3	Numerical background	129
4.3.1	Governing equations.....	130
4.3.1.1	Mass and momentum transport	130
4.3.1.2	Equation of state	131
4.3.1.3	Energy transport	132
4.3.1.4	Species transport.....	133
4.3.1.5	Passive transport.....	133
4.3.2	Numerical approach.....	134
4.3.2.1	Finite volume.....	134
4.3.2.2	PISO algorithm.....	134
4.3.2.3	Time-step control.....	136
4.3.2.4	Turbulence modeling.....	137
4.3.2.4.1	RNG k- ϵ turbulence model.....	139
4.3.2.5	Spray model.....	141
4.3.2.6	Combustion model.....	147
4.3.2.7	Emission models.....	150
4.3.2.8	Gridding Methodology	151
4.4	CFD model, initial and boundary setup.....	152
4.4.1	Computational resource.....	152
4.4.2	Initial Condition.....	152
4.4.2.1	Inlet Species Mass Fraction.....	152
4.4.3	Initial and boundary condition sweep.....	160

4.4.3.1	In-cylinder grid size variation	160
4.4.3.2	Fuel temperature variation.....	162
4.4.3.3	KH time constant Sweep	164
4.4.3.4	Schmidt number variation	166
4.4.3.5	Computational consecutive cycle to cycle variation	169
4.4.3.5.2	Mechanism comparison.....	175
4.4.3.6	Diesel quantity variation.....	179
4.5	Result and discussion	184
4.5.1	Effect of methane on diesel	187
4.5.2	Model Validation and In-cylinder combustion characterization.....	194
4.5.3	Combustion and emission characteristics.....	206
4.5.3.1	Combustion characterization	206
4.5.3.2	Emission characterization.....	224
4.6	Spray targeting study	234
4.6.1	Spray included angle sweep	234
4.6.2	Spray targeting study with different number of nozzles	251
4.6.3	Spray targeting study with two sets of half spray include angle in the same injector at 310 SOI.....	263
4.7	Conclusions	273
4.8	References	276
CHAPTER.V. RECOMMENDATIONS FOR FUTURE WORK.....		283
5.1	Recommendation for Future Work.....	283

LIST OF TABLES

Table 2.1	Engine specifications and operating conditions	15
Table 2.2	Details of Experimental Measurements devices.....	16
Table 2.3	Operating conditions	17
Table 2.4	Zero-dimensional PSR simulations at $P = 28$ bar, $T = 810$ K to investigate impact of MEF on dodecane LTHR.....	24
Table 2.5	Crank angle degrees where SOI, EOI and, onset of HTHR occurs for 3.3 and 5 bar BMEP at $N=1500$ rpm, $P_{in}=1.5$ bar (** denotes negligible LTHR)	31
Table 2.6	Accuracies of various sensors	50
Table 2.7	The uncertainties calculated using the methodology described in Eq. A2.4 to A2.9	52
Table 3.1	Engine Specifications (0° refers to gas exchange TDC, 360° refers to compression TDC).....	65
Table 3.2	Details of experimental sensors and their accuracies.	65
Table 3.3	Details of experimental sensors and their accuracies.	66
Table 3.4	Fuel properties [36,37,38]	67
Table 3.5	Zero-Dimensional simulation conditions for n-dodecane (representing diesel), DG (gasoline represented by iso-octane), DM and DP, all for an initial temperature of 780 K and an initial pressure of 28 bar.	86
Table 3.6	CA5 (with 1 std. dev) for DP, DM, DG dual fuel combustion for diesel SOIs from 280 to 330 CAD.	87
Table 3.7	Number of cycles for which CA50 leads CAPMAX.	90
Table 4.1	Coefficients of the spray angle correlation.....	154

Table 4.2	Initial and boundary condition of experimental and computational cases for 1.5 bar boost pressure, 500 bar diesel injection pressure at 5.1 bar IMEP engine load at diesel injection timing 310 CAD.....	161
Table 4.3	Computational model constants	161
Table 4.4	Computational model constants	164
Table 4.5	Computational model constants used in this study.....	165
Table 4.6	Initial and boundary condition of experimental and computational cases for 1.5 bar boost pressure, 500 bar diesel injection pressure at 5.1 bar IMEP engine load at diesel injection timing 320 and 330 CAD	167
Table 4.7	Initial and boundary condition of four cycles at diesel injection timing of 310 CAD	171
Table 4.8	Initial and boundary condition for 1.5 bar boost pressure, 500 bar diesel injection pressure, 80 PES of methane, and 5.1 bar IMEP engine load at diesel injection timing of 310, 310, and 330 CAD	177
Table 4.9	Single Cylinder Research Engine Specification.....	185
Table 4.10	Test condition for methane influence on dodecane.....	188
Table 4.11	Initial and boundary conditions for diesel injection timing of 310, 320, and 330 CAD.....	195
Table 4.12	Computational model constants used in this study.....	195

LIST OF FIGURES

Figure 1.1	Energy consumption by different sector [1]	2
Figure 1.2	Fuel type consumption by the transport sector [1]	3
Figure 1.3	Low-temperature dual fuel engine concept [5]	4
Figure 2.1	Experimental setup of the single cylinder research engine	15
Figure 2.2	Equivalence ratio (measured from engine-out raw emissions data) versus equivalence ratio (measured from air and fuel flow rate ratio) for various MEFs at (a) 3.3 bar and (b) 5.0 bar BMEP, N=1500 rpm, Pin=1.5 bar, SOI = 310 CAD	18
Figure 2.3	In-cylinder pressure histories for various MEFs at (a) 3.3 bar and (b) 5.0 bar BMEP, N=1500 rpm, Pin=1.5 bar, SOI = 310 CAD.....	19
Figure 2.4	MPRR and COVIMEPnet histories for 3.3 and 5.0 bar BMEPs at various MEFs at N= 1500 rpm, Pin = 1.5 bar, SOI = 310CAD.	19
Figure 2.5	AHRR histories for various MEFs at (a) 3.3 bar and (b) 5.0 bar BMEP, N=1500 rpm, Pin=1.5 bar, SOI = 310 CAD.....	21
Figure 2.6	Bulk gas temperature histories and onset of LTHR and onset of HTHR for various MEFs at (a) 3.3 bar and (b) 5.0 bar BMEP, N=1500 rpm, Pin=1.5 bar, SOI = 310 CAD.....	21
Figure 2.7	(Onset of LTHR –EOI) and (onset of HTHR – EOI) histories for various MEFs at (a) 3.3 bar and (b) 5.0 bar BMEP, N=1500 rpm, Pin=1.5 bar, SOI = 310 CAD (please note: there is no appreciable LTHR for 90% MEF at both 3.3 and 5 bar BMEP; therefore there is no data point for LTHR-EOI for both loads at 90% MEF)	22
Figure 2.8	Time evolution of NC12H24O3 and volumetric heat production (Qdotvol) rate histories for various equivalence ratio at Pinitial =28 bar, Tinitial =810K.....	24
Figure 2.9	CA5, CA50 and CA10-90 histories for various MEFs at (a) 3.3 bar and (b) 5.0 bar BMEP, N=1500 rpm, Pin=1.5 bar, SOI = 310 CAD	26

Figure 2.10 Percentage distribution of combustion, indicated fuel conversion efficiencies for various MEFs at 3.3 bar BMEP, N=1500 rpm, Pin=1.5 bar, SOI = 310 CAD	28
Figure 2.11 Percentage distribution of combustion, indicated fuel conversion efficiencies for various MEFs at 5 bar BMEP, N=1500 rpm, Pin=1.5 bar, SOI = 310 CAD	28
Figure 2.12 ISHC, ISCO and ISNO _x histories for various MEFs at (a) 3.3 bar and (b) 5.0 bar BMEP, N=1500 rpm, Pin=1.5 bar, SOI = 310 CAD	31
Figure 2.13 Bulk Temperature histories for various MEFs at (a) 3.3 bar and (b) 5.0 bar BMEP, N=1500 rpm, Pin=1.5 bar, SOI = 310 CAD	32
Figure 2.14 Cycle-to-cycle variations for 1000 consecutive cycles in In-cylinder pressure and AHRR histories for various MEF (%) at 3.3 bar BMEP, N=1500 rpm, Pin=1.5 bar, SOI = 310 CAD	33
Figure 2.15 Cycle-to-cycle variations for 1000 consecutive cycles in In-cylinder pressure and AHRR histories for various MEFs at 5.0 bar BMEP, N=1500 rpm, Pin=1.5 bar, SOI = 310 CAD	33
Figure 2.16 CA5 vs. CA50 for 1000 consecutive cycles for various MEFs at (a) 3.3 bar and (b) 5.0 bar BMEP, N=1500 rpm, Pin=1.5 bar, SOI = 310 CAD	34
Figure 2.17 CAP _{max} vs. P _{MAX} for 1000 consecutive cycles for various MEFs at (a) 3.3 bar and (b) 5.0 bar BMEP, N=1500 rpm, Pin=1.5 bar, SOI = 310 CAD	35
Figure 2.18 Indicated fuel conversion efficiency for 1000 consecutive cycles for various MEFs at (a) 3.3 bar and (b) 5.0 bar BMEP, N=1500 rpm, Pin=1.5 bar, SOI = 310 CAD	37
Figure 2.19 CA50 vs indicated fuel conversion efficiency for 1000 consecutive cycles for various MEFs at (a) 3.3 bar and (b) 5.0 bar BMEP, N=1500 rpm, Pin=1.5 bar, SOI = 310 CAD	37
Figure 3.1 Experimental setup of the single cylinder research engine [12].....	63
Figure 3.2 (a) COVIMEP for DG combustion at various SOIs, (b) COVIMEP for DM and DP combustion at 280 and 330 CAD SOIs for 100, 300, 500 and 1000 consecutive cycles, (c)-COVIMEP for DM and DP combustion at 280 and 330 CAD SOIs at 100 cycle data intervals.....	64

Figure 3.3	3(a-d). Average in-cylinder pressure and AHRR histories for DM, DP, and DG combustion at various SOIs and 5.1 bar IMEP, N=1500 rpm, diesel injection pressure = 500 bar, PES of 80%.	73
Figure 3.4	(a). Maximum pressure rise rate and COV of IMEP (b). CA50 variation at varying SOI for 5.1 bar IMEP, N= 1500 rpm, diesel injection pressure=500 bar, PES =80% for DM, DP and DG dual fuel combustion.	75
Figure 3.5	(a). Combustion efficiency (b). Indicated fuel conversion efficiency variation at varying SOI for 5.1 bar IMEP, N= 1500 rpm, diesel injection pressure=500 bar, PES =80% for DM, DP and DG dual fuel	77
Figure 3.6	(a).ISCO and ISHC (b). ISNOx variation at varying SOI for 5.1 bar IMEP, N= 1500 rpm, diesel injection pressure=500 bar, PES =80% for DM, DP and DG dual fuel	79
Figure 3.7	7(a-f). Cyclic variations in in-cylinder pressure and AHRR histories for 1000 consecutive cycles for DM and DP combustion cases and for 100 consecutive cycles for DG combustion at various SOIs and 5.1 bar IMEP, N=1500 rpm, diesel injection pressure = 500 bar, PES of 80%.	84
Figure 3.8	Time evolution of $\text{NC}_{12}\text{H}_{24}\text{O}_3$ and volumetric heat production (\dot{Q}_{dotvol}) rate histories for various fuel type at $P_{\text{initial}} = 28$ bar, $T_{\text{initial}} = 780$ K.	86
Figure 3.9	CA50 versus CA5 for 1000 consecutive cycles of (a) diesel-methane (b)diesel-propane and 100 consecutive cycles of (c) diesel-gasoline at 5.1 bar IMEP, N= 1500 rpm, diesel injection pressure=500 bar, PFEF =80%, with varying SOI.	88
Figure 3.10	PMAX versus CAPMAX for 1000 consecutive cycles of (a) diesel-methane (b)diesel-propane and 100 consecutive cycles of (c) diesel-gasoline at 5.1 bar IMEP, N= 1500 rpm, diesel injection pressure=500 bar, PES =80%, with varying SOI.	89
Figure 3.11	MPRR versus CAPMAX for 1000 consecutive cycles of (a) diesel-methane (b)diesel-propane and 100 consecutive cycles of (c) diesel-gasoline at 5.1 bar IMEP, N= 1500 rpm, diesel injection pressure=500 bar, PES =80%, with varying SOI.	91
Figure 3.12	Indicated mean effective pressure versus cumulative gross heat release for 1000 consecutive cycles of (a) diesel-methane (b)diesel-propane and 100 consecutive cycles of (c) diesel-gasoline at 5.1 bar IMEP, N= 1500 rpm, diesel injection pressure=500 bar, PES =80%, with varying SOI.	93

Figure 3.13 Indicated mean effective pressure versus CA50 for 1000 consecutive cycles of (a) diesel-methane (b)diesel-propane and 100 consecutive cycles of (c) diesel-gasoline at 5.1 bar IMEP, N= 1500 rpm, diesel injection pressure=500 bar, PES =80%, with varying SOI.	94
Figure 3.14 Indicated fuel conversion efficiency for 1000 consecutive cycles of (a) diesel-methane (b)diesel-propane and 100 consecutive cycles of (c) diesel-gasoline at 5.1 bar IMEP, N= 1500 rpm, Pin = 1.5 bar, PES =80%, with varying SOI.....	97
Figure 3.15 (CA5-TDC) return maps for 1000 consecutive cycles of (a) diesel-methane (b)diesel-propane and 100 consecutive cycles of (c) diesel-gasoline at 5.1 bar IMEP, N= 1500 rpm, diesel injection pressure=500 bar, PES =80%, with varying SOI.....	98
Figure 3.16 CA50-90 versus CA5-50 for 1000 consecutive cycles of (a) diesel-methane (b)diesel-propane and 100 consecutive cycles of (c) diesel-gasoline at 5.1 bar IMEP, N= 1500 rpm, diesel injection pressure=500 bar, PES =80%, with varying SOI.....	99
Figure 3.17 IMEP return maps for 1000 consecutive cycles of (a) diesel-methane (b)diesel-propane and 100 consecutive cycles of (c) diesel-gasoline at 5.1 bar IMEP, N= 1500 rpm, diesel injection pressure=500 bar, PES =80%, with varying SOI.....	101
Figure 3.18 Normal probability plots for 280 injection timing for CA5, CA50 and IMEP.....	104
Figure 3.19 Normal probability plots for 290 injection timing for CA5, CA50 and IMEP.....	105
Figure 3.20 Normal probability plots for 300 injection timing for CA5, CA50 and IMEP.....	106
Figure 3.21 Normal probability plots for 310 injection timing for CA5, CA50 and IMEP.....	107
Figure 3.22 Normal probability plots for 320 injection timing for CA5, CA50 and IMEP.....	108
Figure 3.23 Normal probability plots for 330 injection timing for CA5, CA50 and IMEP.....	109
Figure 4.1 Scheme of the PISO algorithm [49]	136
Figure 4.2 Physical processes for a liquid spray [52]	142

Figure 4.3	Computationally obtained liquid penetration length versus liquid penetration length using Dornotte correlation for diesel injection timing of 310 CAD, 1.5 bar boost pressure, 500 bar diesel injection pressure at 5.1 bar IMEP engine load.....	155
Figure 4.4	Evolution of spray for 310 CAD diesel injection timing, 500bar injection pressure, 80 PES of methane, and 1.5 bar manifold pressure at 5.1 bar IMEP of engine load along with streamtraces representing in-cylinder motion left side is exhaust side and right side is intake side.....	156
Figure 4.5	Swirl ratio evolution over a cycle.....	157
Figure 4.6	Tumble ratio in Y direction evolution over a cycle.....	158
Figure 4.7	Streamtraces representing in-cylinder motion indicating formation of tumble motion.....	159
Figure 4.8	Geometry for SCRE at bottom dead center.....	159
Figure 4.9	Pressure and AHRR histories for various grid size for 310 CAD diesel injection timing, 500bar injection pressure, 80 PES of methane, and 1.5 bar manifold pressure at 5.1 bar IMEP of engine load.....	162
Figure 4.10	Pressure and AHRR histories for various fuel temperature for 310 CAD diesel injection timing, 500bar injection pressure, 80 PES of methane, and 1.5 bar manifold pressure at 5.1 bar IMEP of engine load	163
Figure 4.11	Pressure and AHRR histories for various KH values for 310 CAD diesel injection timing, 500bar injection pressure, 80 PES of methane, and 1.5 bar manifold pressure at 5.1 bar IMEP of engine load.....	165
Figure 4.12	Pressure and AHRR histories for various Schmidt numbers for 320 CAD diesel injection timing, 500bar injection pressure, 80 PES of methane, and 1.5 bar manifold pressure at 5.1 bar IMEP of engine load	168
Figure 4.13	Pressure and AHRR histories for various Schmidt numbers for 330 CAD diesel injection timing, 500bar injection pressure, 80 PES of methane, and 1.5 bar manifold pressure at 5.1 bar IMEP of engine load	169
Figure 4.14	Pressure and AHRR histories for consecutive four computational cycles for 310 CAD diesel injection timing, 500bar injection pressure, 80 PES of methane, and 1.5 bar manifold pressure at 5.1 bar IMEP of engine load.....	172

Figure 4.15 Indicated specific oxides of nitrogen (NO) emission histories for consecutive four computational cycles for 310 CAD diesel injection timing, 500bar injection pressure, 80 PES of methane, and 1.5 bar manifold pressure at 5.1 bar IMEP of engine load.....	173
Figure 4.16 Indicated specific hydrocarbon (HC) emission histories for consecutive four computational cycles for 310 CAD diesel injection timing, 500bar injection pressure, 80 PES of methane, and 1.5 bar manifold pressure at 5.1 bar IMEP of engine load.....	174
Figure 4.17 Indicated specific carbon monoxide (CO) emission histories for consecutive four computational cycles for 310 CAD diesel injection timing, 500bar injection pressure, 80 PES of methane, and 1.5 bar manifold pressure at 5.1 bar IMEP of engine load.....	175
Figure 4.18 Computational Pressure, AHRR and CHR histories using POLIMI_Red mechanism plotted over experimental 1000 consecutive cycles for 500bar injection pressure, 80 PES of methane, 1.5 bar manifold pressure, and 5.1 bar IMEP of engine load at various diesel injection timing of 310, 320 and 330 CAD	178
Figure 4.19 Computational Pressure, AHRR and CHR histories using CSU 186 mechanism plotted over experimental 1000 consecutive cycles for 500bar injection pressure, 80 PES of methane, 1.5 bar manifold pressure, and 5.1 bar IMEP of engine load at various diesel injection timing of 310, 320 and 330 CAD	179
Figure 4.20 Experimental needle lift profile histories for 1000 consecutive cycles for 310 CAD diesel injection timing, 500bar injection pressure, 80 PES of methane, and 1.5 bar manifold pressure at 5,1 bar IMEP of engine load.....	181
Figure 4.21 Computational Pressure histories for various diesel injection mass quantity plotted over experimental 1000 consecutive cycles for 310 CAD diesel injection timing, 500bar injection pressure, 80 PES of methane, and 1.5 bar manifold pressure at 5.1 bar IMEP of engine load	182
Figure 4.22 Computational AHRR histories for various diesel injection mass quantity plotted over experimental 1000 consecutive cycles for 310 CAD diesel injection timing, 500bar injection pressure, 80 PES of methane, and 1.5 bar manifold pressure at 5.1 bar IMEP of engine load	183

Figure 4.23 Computational CHR histories for various diesel injection mass quantity plotted over experimental 1000 consecutive cycles for 310 CAD diesel injection timing, 500bar injection pressure, 80 PES of methane, and 1.5 bar manifold pressure at 5.1 bar IMEP of engine load	184
Figure 4.24 Crank-resolved synthetic injection profile created based on experimental needle lift profile for 5.1 bar IMEP engine load.....	186
Figure 4.25 CFD modeling workflow.....	186
Figure 4.26 Total number of cells in a domain for diesel injection timing of 310 CAD, 1.5 bar boost pressure, 500 bar diesel injection pressure at 5.1 bar IMEP engine load.....	187
Figure 4.27 Comparison of AHRR, dodecane, and methane for a case simulated with methane and without methane as a fuel inside the cylinder for diesel injection timing of 310 CAD, 1.5 bar boost pressure, 500 bar diesel injection pressure	191
Figure 4.28 Dodecane and temperature distribution observed from the top for diesel injection timing of 310 CAD, 1.5 bar boost pressure, 500 bar diesel injection pressure, and 80 PES of methane at 5.1 bar IMEP	192
Figure 4.29 N-dodecane main oxidation pathways [6].....	193
Figure 4.30 Crank angle evolution of NC12-OOQOOH and AHRR histories for the case with methane and case without methane.	193
Figure 4.31 Crank angle evolution of CH3 and AHRR histories for the case with methane and case without methane.	194
Figure 4.32 Computational pressure, AHRR and CHR histories plotted over experimental 1000 consecutive cycles for 500bar injection pressure, 80 PES of methane, 1.5 bar manifold pressure, and 5.1 bar IMEP of engine load at various diesel injection timing of 310, 320 and 330 CAD.....	199
Figure 4.33 Comparison of computational and experimental closed-cycle indicated fuel conversion efficiency (CC_IFCE) for 1.5 bar manifold pressure, 500bar injection pressure, 80 PES of methane, and 5.1 bar IMEP of engine load at various diesel injection timing of 310, 320, and 330 CAD.....	200

Figure 4.34 Comparison of computational and experimental combustion efficiency for 1.5 bar manifold pressure, 500bar injection pressure, 80 PES of methane, and 5.1 bar IMEP of engine load at various diesel injection timing of 310, 320, and 330 CAD	201
Figure 4.35 Comparison of computational and experimental NO emissions for 1.5 bar manifold pressure, 500bar injection pressure, 80 PES of methane, and 5.1 bar IMEP of engine load at various diesel injection timing of 310, 320, and 330 CAD.....	203
Figure 4.36 Comparison of computational and experimental HC emissions for 1.5 bar manifold pressure, 500bar injection pressure, 80 PES of methane, and 5.1 bar IMEP of engine load at various diesel injection timing of 310, 320, and 330 CAD.....	204
Figure 4.37 Comparison of computational and experimental CO emissions for 1.5 bar manifold pressure, 500bar injection pressure, 80 PES of methane, and 5.1 bar IMEP of engine load at various diesel injection timing of 310, 320, and 330 CAD.....	205
Figure 4.38 Computational temperature histories plotted over experimental 1000 consecutive cycles for 500bar injection pressure, 80 PES of methane, 1.5 bar manifold pressure, and 5.1 bar IMEP of engine load diesel at injection timing of 310,320 and 330 CAD	205
Figure 4.39 AHRR, dodecane, and methane crank angle evolution for 1.5 bar boost pressure, 500 bar diesel injection pressure 80 PES of methane, and 5.1 bar IMEP of engine load at diesel injection timing of 310 CAD.....	207
Figure 4.40 AHRR, dodecane, and methane crank angle evolution for 1.5 bar boost pressure, 500 bar diesel injection pressure 80 PES of methane, and 5.1 bar IMEP of engine load at diesel injection timing of 320 CAD.....	208
Figure 4.41 AHRR, dodecane, and methane crank angle evolution for 1.5 bar boost pressure, 500 bar diesel injection pressure 80 PES of methane, and 5.1 bar IMEP of engine load at diesel injection timing of 330 CAD.....	209
Figure 4.42 React ratio v/s temperature colored with methane mass fraction for each computational cell for 1.5 bar boost pressure, 500 bar diesel injection pressure 80 PES of methane, and 5.1 bar IMEP of engine load at diesel injection timing of 310 CAD.....	213

Figure 4.43 React ratio v/s temperature colored with methane mass fraction for each computational cell for 1.5 bar boost pressure, 500 bar diesel injection pressure 80 PES of methane, and 5.1 bar IMEP of engine load at diesel injection timing of 320 CAD.....	214
Figure 4.44 React ratio v/s temperature colored with methane mass fraction for each computational cell for 1.5 bar boost pressure, 500 bar diesel injection pressure 80 PES of methane, and 5.1 bar IMEP of engine load at diesel injection timing of 330 CAD.....	215
Figure 4.45 Equivalence ratio v/s temperature colored with methane mass fraction for each computational cell for 1.5 bar boost pressure, 500 bar diesel injection pressure 80 PES of methane, and 5.1 bar IMEP of engine load at diesel injection timing of 310 CAD.....	218
Figure 4.46 Equivalence ratio v/s temperature colored with methane mass fraction for each computational cell for 1.5 bar boost pressure, 500 bar diesel injection pressure 80 PES of methane, and 5.1 bar IMEP of engine load at diesel injection timing of 320 CAD.....	219
Figure 4.47 Equivalence ratio v/s temperature colored with methane mass fraction for each computational cell for 1.5 bar boost pressure, 500 bar diesel injection pressure 80 PES of methane, and 5.1 bar IMEP of engine load at diesel injection timing of 330 CAD.....	220
Figure 4.48 Temperature distribution observed (isometric view) for 1.5 bar boost pressure, 500 bar diesel injection pressure, and 80 PES of methane at 5.1 bar IMEP at diesel injection timing of 310 CAD.....	222
Figure 4.49 Temperature distribution observed (isometric view) for 1.5 bar boost pressure, 500 bar diesel injection pressure, and 80 PES of methane at 5.1 bar IMEP at diesel injection timing of 320 CAD.....	223
Figure 4.50 Temperature distribution observed (isometric view) for 1.5 bar boost pressure, 500 bar diesel injection pressure, and 80 PES of methane at 5.1 bar IMEP at diesel injection timing of 330 CAD.....	224
Figure 4.51 NO crank angle evolution for 1.5 bar boost pressure, 500 bar diesel injection pressure 80 PES of methane, and 5.1 bar IMEP of engine load at diesel injection timing of 310, 320, and 330 CAD.....	225
Figure 4.52 Methane distribution observed (isometric view) for 1.5 bar boost pressure, 500 bar diesel injection pressure, and 80 PES of methane at 5.1 bar IMEP at diesel injection timing of 310 CAD.....	227

Figure 4.53 Methane distribution observed (isometric view) for 1.5 bar boost pressure, 500 bar diesel injection pressure, and 80 PES of methane at 5.1 bar IMEP at diesel injection timing of 320 CAD.	228
Figure 4.54 Methane distribution observed (isometric view) for 1.5 bar boost pressure, 500 bar diesel injection pressure, and 80 PES of methane at 5.1 bar IMEP at diesel injection timing of 330 CAD.	229
Figure 4.55 CO crank angle evolution for 1.5 bar boost pressure, 500 bar diesel injection pressure 80 PES of methane, and 5.1 bar IMEP of engine load at diesel injection timing of 310, 320, and 330 CAD.	231
Figure 4.56 CO distribution observed (isometric view) for 1.5 bar boost pressure, 500 bar diesel injection pressure, and 80 PES of methane at 5.1 bar IMEP at diesel injection timing of 310 CAD.	232
Figure 4.57 CO distribution observed (isometric view) for 1.5 bar boost pressure, 500 bar diesel injection pressure, and 80 PES of methane at 5.1 bar IMEP at diesel injection timing of 320 CAD.	233
Figure 4.58 CO distribution observed (isometric view) for 1.5 bar boost pressure, 500 bar diesel injection pressure, and 80 PES of methane at 5.1 bar IMEP at diesel injection timing of 330 CAD.	234
Figure 4.59 Representation of half spray included angle.	236
Figure 4.60 Computational pressure, AHRR and CHR histories plotted over experimental 1000 consecutive cycles for diesel injection timing of 310 CAD, 500bar injection pressure, 80 PES of methane, 1.5 bar manifold pressure, and 5.1 bar IMEP of engine load at various diesel half spray included angle.....	238
Figure 4.61 Comparison of closed cycle indicated fuel conversion efficiency (CC_IFCE) for diesel injection timing of 310 CAD, 1.5 bar manifold pressure, 500bar injection pressure, 80 PES of methane, and 5.1 bar IMEP of engine load at various half spray included angle.....	239
Figure 4.62 Comparison of NO emissions for diesel injection timing of 310 CAD, 1.5 bar manifold pressure, 500bar injection pressure, 80 PES of methane, and 5.1 bar IMEP of engine load at various half spray included angle.....	240
Figure 4.63 Comparison of HC emissions for diesel injection timing of 310 CAD, 1.5 bar manifold pressure, 500bar injection pressure, 80 PES of methane, and 5.1 bar IMEP of engine load at various half spray included angle.....	241

Figure 4.64 Comparison of CO emissions for diesel injection timing of 310 CAD, 1.5 bar manifold pressure, 500bar injection pressure, 80 PES of methane, and 5.1 bar IMEP of engine load at various half spray included angle.....	242
Figure 4.65 React ratio v/s temperature colored with methane mass fraction for each computational cell for diesel injection timing of 1.5 bar boost pressure, 500 bar diesel injection pressure 80 PES of methane, and 5.1 bar IMEP of engine load at half spray included angle of 27.5.....	246
Figure 4.66 React ratio v/s temperature colored with methane mass fraction for each computational cell for diesel injection timing of 1.5 bar boost pressure, 500 bar diesel injection pressure 80 PES of methane, and 5.1 bar IMEP of engine load at half spray included angle of 57.5.....	247
Figure 4.67 React ratio v/s temperature colored with methane mass fraction for each computational cell for diesel injection timing of 1.5 bar boost pressure, 500 bar diesel injection pressure 80 PES of methane, and 5.1 bar IMEP of engine load at half spray included angle of 82.5.....	248
Figure 4.68 Methane distribution observed (isometric view) for diesel injection timing of 310 CAD, 1.5 bar boost pressure, 500 bar diesel injection pressure, and 80 PES of methane at 5.1 bar IMEP at half spray included angle of 27.5.....	249
Figure 4.69 Methane distribution observed (isometric view) for diesel injection timing of 310 CAD, 1.5 bar boost pressure, 500 bar diesel injection pressure, and 80 PES of methane at 5.1 bar IMEP at half spray included angle of 57.5.....	250
Figure 4.70 Methane distribution observed (isometric view) for diesel injection timing of 310 CAD, 1.5 bar boost pressure, 500 bar diesel injection pressure, and 80 PES of methane at 5.1 bar IMEP at half spray included angle of 82.5.....	251
Figure 4.71 Computational pressure, AHRR and CHR histories plotted over experimental 1000 consecutive cycles for diesel injection timing of 310 CAD, 500bar injection pressure, 80 PES of methane, 1.5 bar manifold pressure, and 5.1 bar IMEP of engine load at half spray included angle of 57.5 with 12 nozzles, 75 with 12 nozzles, 57.5 with 6 nozzles, 75 with 6 nozzles and 75 with 8 nozzles.....	253

Figure 4.72 Comparison of closed-cycle indicated fuel conversion efficiency (CC_IFCE) for diesel injection timing of 310 CAD, 1.5 bar manifold pressure, 500bar injection pressure, 80 PES of methane, and 5.1 bar IMEP of engine load at half spray included angle of 57.5 with 12 nozzles, 75 with 12 nozzles, 57.5 with 6 nozzles, 75 with 6 nozzles and 75 with 8 nozzles.254

Figure 4.73 Comparison of NO emissions for diesel injection timing of 310 CAD, 1.5 bar manifold pressure, 500bar injection pressure, 80 PES of methane, and 5.1 bar IMEP of engine load at half spray included angle of 57.5 with 12 nozzles, 75 with 12 nozzles, 57.5 with 6 nozzles, 75 with 6 nozzles and 75 with 8 nozzles.255

Figure 4.74 Comparison of HC emissions for diesel injection timing of 310 CAD, 1.5 bar manifold pressure, 500bar injection pressure, 80 PES of methane, and 5.1 bar IMEP of engine load at half spray included angle of 57.5 with 12 nozzle, 75 with 12 nozzle, 57.5 with 6 nozzle, 75 with 6 nozzle and 75 with 8 nozzles.....256

Figure 4.75 Comparison of CO emissions for diesel injection timing of 310 CAD, 1.5 bar manifold pressure, 500bar injection pressure, 80 PES of methane, and 5.1 bar IMEP of engine load at half spray included angle of 57.5 with 12 nozzles, 75 with 12 nozzles, 57.5 with 6 nozzles, 75 with 6 nozzles and 75 with 8 nozzles.257

Figure 4.76 React ratio v/s temperature colored with methane mass fraction for each computational cell for diesel injection timing of 1.5 bar boost pressure, 500 bar diesel injection pressure 80 PES of methane, and 5.1 bar IMEP of engine load at half spray included angle of 57.5 with 6 nozzles.260

Figure 4.77 React ratio v/s temperature colored with methane mass fraction for each computational cell for diesel injection timing of 1.5 bar boost pressure, 500 bar diesel injection pressure 80 PES of methane, and 5.1 bar IMEP of engine load at half spray included angle of 75 with 12 nozzles261

Figure 4.78 Methane distribution observed (isometric view) for diesel injection timing of 310 CAD, 1.5 bar boost pressure, 500 bar diesel injection pressure, and 80 PES of methane at 5.1 bar IMEP at half spray included angle of 57.5 with 6 nozzles.262

Figure 4.79 Methane distribution observed (isometric view) for diesel injection timing of 310 CAD, 1.5 bar boost pressure, 500 bar diesel injection pressure, and 80 PES of methane at 5.1 bar IMEP at half spray included angle of 75 with 12 nozzles.263

Figure 4.80 Two sets of half spray included angle schematics.....	264
Figure 4.81 Computational pressure, AHRR and CHR histories plotted over experimental 1000 consecutive cycles for diesel injection timing of 310 CAD, 500bar injection pressure, 80 PES of methane, 1.5 bar manifold pressure, and 5.1 bar IMEP of engine load at half number of the nozzle with half spray included angle of 57.5 and another half of nozzles with half spray included angle of 75 for 6,8 and 12 number of nozzles.	266
Figure 4.82 Comparison of closed-cycle indicated fuel conversion efficiency (CC_IFCE) for diesel injection timing of 310 CAD, 1.5 bar manifold pressure, 500bar injection pressure, 80 PES of methane, and 5.1 bar IMEP of engine load at half number of the nozzle with half spray included angle of 57.5 and another half of nozzles with half spray included angle of 75 for 6,8 and 12 number of nozzles.	267
Figure 4.83 Comparison of NO emissions for diesel injection timing of 310 CAD, 1.5 bar manifold pressure, 500bar injection pressure, 80 PES of methane, and 5.1 bar IMEP of engine load at half number of the nozzle with half spray included angle of 57.5 and another half of nozzles with half spray included angle of 75 for 6,8 and 12 number of nozzles.	268
Figure 4.84 Comparison of HC emissions for diesel injection timing of 310 CAD, 1.5 bar manifold pressure, 500bar injection pressure, 80 PES of methane, and 5.1 bar IMEP of engine load at half number of the nozzle with half spray included angle of 57.5 and another half of nozzles with half spray included angle of 75 for 6,8 and 12 number of nozzles.	269
Figure 4.85 Comparison of CO emissions for diesel injection timing of 310 CAD, 1.5 bar manifold pressure, 500bar injection pressure, 80 PES of methane, and 5.1 bar IMEP of engine load at half number of the nozzle with half spray included angle of 57.5 and another half of nozzles with half spray included angle of 75 for 6,8 and 12 number of nozzles.	270
Figure 4.86 React ratio v/s temperature colored with methane mass fraction for each computational cell for diesel injection timing of 1.5 bar boost pressure, 500 bar diesel injection pressure 80 PES of methane, and 5.1 bar IMEP of engine load at half number of the nozzle with half spray included angle of 57.5 and another half of nozzles with half spray included angle of 75 for 6 nozzles.	272

Figure 4.87 Methane distribution observed (isometric view) for diesel injection timing of 310 CAD, 1.5 bar boost pressure, 500 bar diesel injection pressure, and 80 PES of methane at half number of the nozzle with half spray included angle of 57.5 and another half of nozzles with half spray included angle of 75 for 6 nozzles.273

CHAPTER I

INTRODUCTION

1.1 Motivation for dual fuel low temperature combustion

According to International Energy Outlook 2020 [1], world energy consumption rises nearly 50% by 2050. Figure 1.1, which is taken from International Energy Outlook 2020 [1] clearly shows that around 25 percent of the total energy consumption will be from the transport sector. Figure 1.2, which is again taken from International Energy Outlook 2020 [1] shows that more than 80% of the transportation sector will still use petroleum and other liquid fuels in the year 2050 as the primary energy source [1]. One can argue to use a diesel engine due to its high fuel conversion efficiency, robustness, and dependability; however, the diesel engine has its disadvantage of producing pollutants like particulate matter (PM) and oxides of nitrogen (NO_x) emissions, which are very difficult to reduce simultaneously without incurring a fuel penalty using conventional combustion strategies. To reduce these pollutants, it is required to use after-treatment devices. These after-treatment devices increase the complexity of maintenance are expensive and have penalties on fuel consumption. This brings the necessity of using advanced combustion strategies to increase efficiency and decrease engine-out pollutants because of the compelling need to reduce the global carbon footprint. Of such advanced combustion strategies that can achieve diesel-like efficiency with low emission is low-temperature dual fuel combustion [2,3]. There are several dual fuel combinations

available like diesel-, propane, gasoline, natural gas (NG)-polyoxymethylene dimethyl ethers (PODE), among others. Out of this natural gas-diesel is a leading choice of fuel combination since the US is an exporter of natural gas, due to widespread availability of natural gas, and forecasted continuous growth of natural gas production [1]. Natural gas (methane is a major constituent of natural gas.)-diesel internal combustion engines offer the opportunity of reducing NO_x and PM emissions simultaneously; however, it has its challenges of high cyclic variation and high hydrocarbon and carbon monoxide emissions at low loads Methane emissions are a major concern since methane has a global warming potential 25 times greater than that of CO₂ over 100 years [4]. Clearly, it is necessary to decrease hydrocarbon and carbon monoxide emissions from diesel-methane dual fuel engines. This dissertation provides insights into the nature of cyclic combustion variations and advances a CFD model to discuss the Spatio-temporal evolution of hydrocarbon and carbon monoxide emissions that might originate in diesel-methane dual fuel combustion, particularly at low loads, and some possible mitigation strategies.

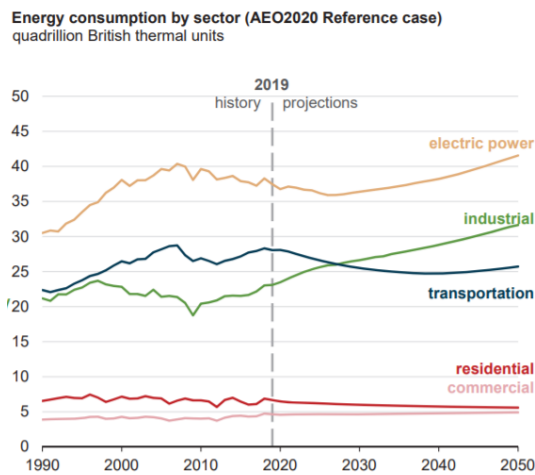


Figure 1.1 Energy consumption by different sector [1]

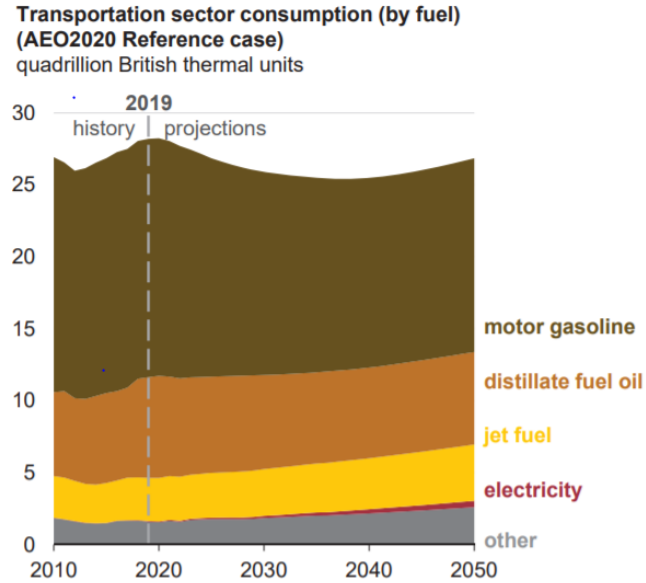


Figure 1.2 Fuel type consumption by the transport sector [1]

1.2 Why investigate cyclic combustion variation in dual fuel low-temperature combustion?

While most conventional combustion processes such as neat diesel combustion can be explained using cycle-averaged cylinder pressure and combustion energy release schedules, advanced combustion strategies such as RCCI and dual fuel LTC exhibit significant cycle to cycle variations which influence engine-out emissions and overall thermal efficiencies. Figure 1.3 shows a cartoon of diesel-methane/NG dual fuel LTC. The figure shows the mechanism by which simultaneously beneficial outcomes - high efficiencies and low NO_x and PM emissions are achieved with dual fuel LTC. Cyclic variations influence these outcomes in the following ways.

- 1) The robustness of distributed ignition centers is influenced by local fluid dynamics, which determines how well the diesel fuel is dispersed in the combustion chamber

2) Faster burn rates are dictated by both robustness of ignition and subsequent reactivity stratification, which depends on local temperatures, and Spatio-temporal distribution of diesel and methane

3) The state of in-cylinder charge influences the fate of how well combustion proceeds, and the ultimate ability to achieve low engine-out emissions

The dissertation uses experimental data and analyses to describe the nature of dual fuel combustion and the nature of cyclic variations in chapters 2 and 3.

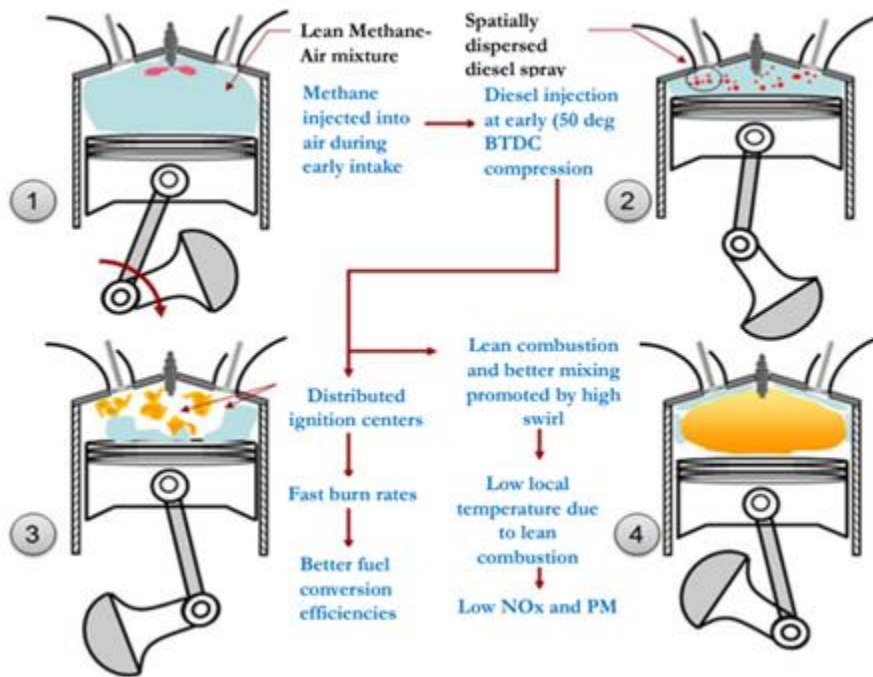


Figure 1.3 Low-temperature dual fuel engine concept [5]

1.3 Why develop a dual fuel low temperature combustion CFD model?

While the first two-thirds of the dissertation presents experimental data analysis to understand the nature of dual fuel LTC and cyclic combustion variations; the complete mechanism of dual fuel combustion including (1) entrainment of methane-air into high pressure diesel spray, (2) subsequent low temperature chemistry of diesel autoignition and (3) the high temperature oxidation of methane, which eventually decides the fate of engine-out emissions can be understood using a validated CFD model. The last part of the dissertation discusses the development and validation of a RANS-based CFD model, which is used to gain useful insights into the aforementioned phenomena. The validated CFD model is further employed for parametric investigations to explore strategies to mitigate unburned HC and CO emissions from dual fuel combustion, particularly at low engine loads.

1.4 Organization of Dissertation

This The dissertation is organized as follows:

- In Chapter 2, the impact of methane energy fraction (MEF) on early injection timing dual fuel ignition and combustion, performance, and emissions at 3.3 and 5.0 bar BMEPs is analyzed. To analyze the impact of MEF on cyclic variations in early injection dual fuel combustion at 3.3 and 5.0 bar BMEPs. The results of this study have been published in the IJER journal titled as “Impact of methane energy fraction on emissions, performance and cyclic variability in low-load dual fuel combustion at early injection timings” [6].
- Chapter 3 of this dissertation investigates the effect of reactivities of different low-reactivity fuels including, methane, propane, and gasoline on average and

cyclic combustion at different diesel SOIs at low load operation. It also characterizes the challenges and opportunities that these fuel combinations present and present possible strategies to mitigate cyclic combustion variations for each fuel combination. The results of this study are under review titled as “Impact of Low Reactivity Fuel Type on Performance, Emissions and Cyclic Variations in Dual Fuel Low Temperature Combustion “

- In Chapter 4, CFD investigation is performed to further explain the nature of dual fuel combustion. In this chapter a validated CFD model is used to obtain insights on, (i) how methane impedes diesel autoignition in dual fuel LTC, (ii) Spray targeting strategies to explore the reduction of engine-out hydrocarbons and carbon monoxide emissions and enhancement of fuel conversion efficiency at low load engine operation.
- Chapter 5 provides recommendations for future work.

1.5 References

1. U.S. Energy Information Administration, "Annual Energy Outlook 2020 with Projections to 2050," 0383(2020), (AEO2020).
<https://www.eia.gov/outlooks/aeo/pdf/aeo2020.pdf>
2. M.M. Abdelaal, A.H. Hegab, Combustion and emission characteristics of a natural gas-fueled diesel engine with EGR, *Energy Convers. Manag.* 64 (0) (2012) 301–312.
3. K.K. Srinivasan, S.R. Krishnan, Y. Qi, Cyclic combustion variations in dual fuel partially premixed pilot-ignited natural gas engines, *J. Energy Resour. Technol. Trans. ASME* (2014) 136(1), <http://dx.doi.org/10.1115/1.4024855>.
4. Jha, P. R., K. K. Srinivasan, and S. R. Krishnan. "Influence of swirl ratio on diesel-methane dual fuel combustion: a CFD investigation." *Internal Combustion Engine Division Fall Technical Conference*. Vol. 58318. American Society of Mechanical Engineers, 2017.
5. Polk AC, Carpenter CD, Scott Guerry EE, et al. Diesel-Ignited Propane Dual Fuel Low Temperature Combustion in a Heavy-Duty Diesel Engine. *ASME. J. Eng. Gas Turbines Power*. 2014;136(9):091509-091509-9. doi:10.1115/1.4027189
6. Jha, P. R., Krishnan, S. R., & Srinivasan, K. K. (2019). Impact of methane energy fraction on emissions, performance and cyclic variability in low-load dual fuel combustion at early injection timings. *International Journal of Engine Research*, 1468087419892380.

CHAPTER II
IMPACT OF METHANE ENERGY FRACTION (MEF) ON EMISSIONS,
PERFORMANCE AND CYCLIC VARIABILITY IN LOW LOAD DUAL FUEL
COMBUSTION AT EARLY INJECTION TIMINGS

2.1 Abstract

The present work experimentally examines the effect of methane (a natural gas surrogate) substitution on early injection dual fuel combustion at representative low loads of 3.3 and 5.0 bar BMEP in a single cylinder, compression ignition engine. Gaseous methane fumigated into the intake manifold at various methane energy fractions (MEF) was ignited using a high pressure diesel pilot injection at 310 CAD. For the 3.3 bar BMEP, MEF sweeps from 50-90% were performed; while at 5.0 bar BMEP, MEF sweeps from 70-90% were performed. It is observed that minimum MEF is limited by maximum pressure rise rate (MPRR) leading to knock and maximum MEF is limited by a high coefficient of variation in netIMEP (COVIMEPnet), which leads to high cyclic variations. For 3.3 bar BMEP, MPRR is 8 bar/CAD at 50% MEF while at 5 bar BMEP, it is 12 bar/CAD at 70% MEF. For 3.3 bar BMEP engine-out NO_x emissions decrease by 43 times when MEF increase from 50% to 90% and it decreases by nearly 46 times when MEF increases from 70% to 90% at 5 bar BMEP. Engine-out UHC emissions increases by nearly 9 times when MEF increases from 50% to 90% at 3.3 bar BMEP and it increases by nearly 5 times when MEF increases from 70% to 90% at 5 bar BMEP.

Engine-out CO emissions increases by nearly 7 times when MEF increases from 50% to 90% at 3.3 bar BMEP and by nearly 5 times when MEF increases from 70% to 90% at 5 bar BMEP. Additionally, cyclic combustion variations at both loads were analyzed to obtain further insights into the combustion process and identify opportunities to further improve fuel conversion efficiencies at low load operation.

2.2 Introduction

According to international energy outlook 2018, more than 80% of the transportation sector will still use petroleum and other liquid fuels in the year 2040 as a source of energy [1]. It is crucial to use advanced combustion strategies to increase efficiency and decrease engine-out pollutants because of the compelling need to reduce the global carbon footprint. Some of the advanced combustion strategies that are being currently pursued by researchers include, homogeneous charge compression ignition (HCCI) [2, 3], partially premixed combustion (PPC) [4, 5], gasoline compression ignition combustion (GCI) [6, 7], premixed mixture ignition in the end gas region (PREMIER) [8] pre-chamber jet ignition [9,10] and reactivity controlled compression ignition (RCCI) [11]. Most of these advanced combustion strategies experience efficiency-emissions-power density trade-offs and achieving an optimal balance is a challenging engineering exercise. Some work has been performed to achieve high efficiencies in combustion engines utilizing advanced combustion concepts with minimized heat losses using thermal barrier coatings [12, 13, 14, 15]. Johnson et al. [16] has shown computationally, it is possible to achieve brake fuel conversion efficiencies (BTE) of up to 59.5 % in IC engines using both mechanical and thermal regeneration. Similarly, participants in the Super Truck program launched by the United States Department of Energy (USDOE) to improve the

BTEs of heavy duty diesel engines (HDDE) that power 18-wheeler trucks, which account for 70 percent of all freight tonnage in the United States, were able to demonstrate BTEs in excess of 50% on a dynamometer [17]. Encouraged by the performance in Super Truck, a second phase, Super Truck II [18] was announced, which aims to achieve further improvements in BTE of up to 55%. More recently, Achates Power [19] has demonstrated a unique two-stroke, compression ignition engine architecture, which employs the opposed piston concept that greatly minimizes heat transfer losses from the cylinder head to realize 30% increase in BTE compared to similar sized, crank and slider driven conventional engine powertrains. Similarly, Pinnacle Engines using a four-stroke, 110 cc, opposed piston concept were able to greatly reduce NO_x emissions at a reasonable fuel economy [20]. Several researchers have also been using alternative fuels in IC engine like natural gas, propane, ethanol, biodiesel, etc. [21-25] to achieve high thermal efficiency and low engine-out emissions. Natural gas is emerging as a leading choice for alternative fuels because of renewed interest in shale gas extraction, and its utilization is predicted to increase steadily over time and reach 39% of US energy production by 2050 [26]. Natural gas as an alternative fuel for internal combustion engines offers new opportunities for reducing oxides of nitrogen (NO_x) and particulate matter (PM) emissions albeit with persisting challenges vis-à-vis higher unburned hydrocarbon (UHC) and carbon monoxide (CO) emissions. High UHC and CO emissions, particularly at low engine loads, are attributed natural gas trapped in crevices and to lower reactivity of natural gas leading to flame quench [21, 22, 27, 28, 29].

Dual fuel combustion where a highly reactive fuel (usually with higher propensity for autoignition) is used to ignite a predominantly lean, premixed mixture of air and a fuel

with lower reactivity (usually with a lower propensity to auto ignite) such as RCCI [11] and dual fuel low temperature combustion (LTC) with natural gas modes [21] exhibit significant cyclic combustion variations, particularly at high natural gas substitutions [30]. Cyclic variations have been extensively characterized in SI engines. Young [31] presents a detailed literature review on cyclic variations in SI engines, which lists many studies as early as the 1960s. A more practical analysis of SI engine cycle-to-cycle variations was performed by Matekunas [32]. In particular, he found there are fast and slow burn cycles both with lean burn operation and increased spark advance. For lean operation, cyclic variability of combustion was attributed to either inadequate flame propagation or inadequate flame initiation by the spark. A very important conclusion of this study was that not all cycles that registered a successful ignition event resulted in a successful flame propagation event. The ultimate impact of cyclic combustion variability is to produce variations in indicated mean effective pressure (IMEP) so large as to affect drivability. Srinivasan et al. [30] developed Matekunas' idea further in the context of dual fuel engine combustion. They categorized fast-burn, and slow-burn cycles based on crank angle corresponding to maximum firing pressure (CAPmax), maximum firing pressure (Pmax) and crank angle corresponding to 50% cumulative heat release (CA50) or combustion phasing. They found that for micro-pilot ignited natural gas combustion at advanced diesel injection timings e.g. 300 crank angle degrees (CAD), the variations in ignition CAD (CA5) significantly affected combustion phasing (CA50) variations, which eventually led to slow- and fast-burn cycles. Klos et al. [33] investigated sources of combustion instability in diesel-gasoline RCCI combustion and attributed variations in trapped gas temperature, PFI mass, DI mass and EGR% as main causes of combustion

variability. Dong et al. [34] performed cyclic variability of ethanol/diesel and the result showed that combustion was sensitive to a premixed ethanol/diesel ratio, especially at low load conditions. Similarly, Dong et al. [35] compared cyclic variability of gasoline/diesel and ethanol/diesel fuel combustion and found fluctuations in the combustion of premixed fuels contributed to higher cyclic variation. Gong et al. [36] evaluated cycle-to-cycle combustion variations in direct injection spark ignition (DISI) engine fueled with methanol. They found methanol DISI engine cycle-to-cycle combustion is affected by injection and ignition timings, engine load and speed, compression ratio and injector configuration. Similar cycle-to-cycle combustion variations and their impact on different engine operating parameters were studied by several researchers [37-39]. Selim [37] observed cycle variability highly depends on both mass and type of gaseous fuel used. He also observed with increasing engine speed cyclic variability and combustion noise decreases. Tuner et al. [38] indicate that spatial inhomogeneities in in-cylinder charge leads to more stable engine operation and less cyclic variations. Srinivasan et al. [39] postulate, inconsistency in ignition quality arising from inconsistencies in local diesel-air mixing leading to variation in combustion development can be one of the limiting factors for cyclic variation. Jupudi et al. [40] performed CFD simulations for cycle-to-cycle variations in a dual fuel combustion engine. One of their goals was to quantify and prioritize the factors that led to cycle-to-cycle variability. Variability on the start of diesel injection and diesel flow rate were top factors affecting cycle-to-cycle variability. Conventionally cycle-to-cycle variation in an engine is regarded as stochastic in nature. But early research by Kantor [41] and Martin [42] showed that cyclic variations in engines have both stochastic and deterministic

characteristics. Finney et al. [43] emphasize that understanding the deterministic and chaotic patterns in cyclic combustion are essential for both design and control. They also explained that the design of a feedback control loop is possible for controlling deterministic patterns of cyclic combustion. Yao et al. [44] show using simulations that MPRR and COVIMEP at specific loads can be controlled using in-cylinder pressure based closed-loop control algorithm.

The present work experimentally examines the effect of methane (a natural gas surrogate) substitution on early injection timing dual fuel combustion at representative low loads in a single cylinder, compression ignition engine. Specific objectives of this work include:

1. To analyze the impact of methane energy fraction (MEF) on early injection timing dual fuel ignition and combustion, performance and emissions at 3.3 and 5 bar BMEP
2. To analyze the impact of methane energy fraction (MEF) on cyclic variations in early injection dual fuel combustion at 3.3 and 5 bar BMEP

2.3 Experimental setup

The A single cylinder research engine (SCRE) was used to perform all experimental work explained in this paper. Figure 2.1 shows a schematic of the experimental setup of a single cylinder research engine in a test cell. Engine specifications are listed in Table 2.1. The engine was connected to a 250 hp AC regenerative engine dynamometer. Engine speed was controlled using Dyne Systems Inter-Loc V and torque was controlled by supplying an appropriate amount of diesel and methane to have a desired level of fuel split on an energy basis. The methane flow rate was controlled using the electronic

control needle valve (Hanbay, Inc., Model MCM-050AB) to fumigate into the intake manifold of the engine. Diesel was directly injected in-cylinder using Bosch CP3 common-rail diesel injection pump and a solenoid-actuated injector while control of crank angle resolved diesel injection was achieved using a Drivven (National Instruments) stand-alone diesel injection (SADI) driver coupled with CALVIEW software. To provide compressed air to the engine intake manifold, an external air compressor (Atlas Copco Model GA75) and a desiccant air dryer (Atlas Copco Model CD 250) were employed. Kistler model 6052C pressure sensor and a Kistler 5010B type charge amplifier were utilized to obtain in-cylinder pressure measurements and a hall-effect-based needle lift sensor (Wolff Instruments, Inc.) was used to obtain injector needle lift. Both of these sensors were phased with respect to crank angle using an incremental shaft encoder (BEI Model XH25D-SS-3600-ABZC-28V/V-SM18) with a 0.1 crank angle degree (CAD) resolution (i.e., 3600 pulses per revolution) coupled to the engine crankshaft. In this paper absolute crank angle convention will be used; i.e., 0 CAD refers to gas exchange TDC while 360 CAD refers to compression TDC. Table 2 provides details of instruments used to measure important parameters and their make and accuracies. For this experiment engine synchronous data (crank-resolved data such as cylinder pressure and needle lift), was recorded over 1000 consecutive cycles and an intake manifold absolute pressure sensor (SETRA 209) was used to peg the cylinder pressure data at intake valve closure (IVC). Similarly, engine-asynchronous data (i.e., steady state data such as temperatures, mass flow rates, manifold pressures, etc.) were recorded and averaged over 60 s.

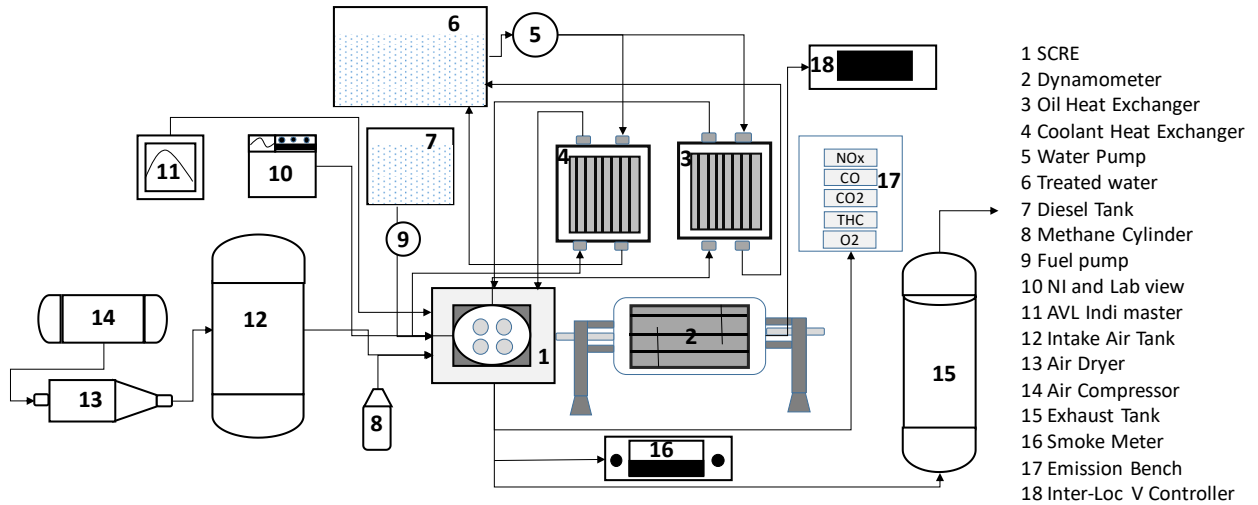


Figure 2.1 Experimental setup of the single cylinder research engine

Table 2.1 Engine specifications and operating conditions

(Note: *0 CAD refers to gas exchange TDC while 360 CAD refers to compression TDC)

Parameter	Value
Engine type	Single cylinder research engine, compression-ignition
Bore × Stroke	128 mm × 142 mm
Connecting rod length	228 mm
Displaced volume	1827 cm ³
Compression ratio (nominal)	17.1: 1
Intake valve open	32 CAD*
Intake valve close	198 CAD*
Exhaust valve open	531 CAD*
Exhaust valve close	14 CAD*
Diesel fuel injection system	CP3 Bosch common rail
Methane fuel system	Fumigation into intake manifold
Maximum speed	1900 rpm
Injector hole diameter	0.197 mm

Table 2.2 Details of Experimental Measurements devices

Data Type	Make/Model	Type	Unit	Accuracy
Temperature intake, exhaust, etc.	Omega	K-type	°C	±0.75% of reading
Air mass flow	Flowmaxx	Sonic orifice	kg/h	±0.1% of reading
Diesel mass flow	Micro Motion	Coriolis	kg/h	0.35% of reading
Methane mass flow	Micro Motion	Coriolis	kg/h	0.56% of reading
Smoke	AVL 415S	Filter	FSN	0.001 of reading
NOx and NO	ESA EGAS 2M	CLD	ppm	<1% of full scale
THC	ESA EGAS 2M	FID	ppm	<0.5% of full scale
CO	ESA EGAS 2M	NDIR	%	<1% of full scale
CO2	ESA EGAS 2M	NDIR	%	<1% of full scale
O2	ESA EGAS 2M	MPA	%	<1% of full scale
Cylinder pressure	Kistler 6052C	Piezoelectric	bar	±0.005 of reading
Pressures (intake, exhaust, etc.)	Setra Model 209	Capacitance	psig	±0.25% of full scale

2.4 Experimental procedure

For diesel-methane dual fuel combustion, methane energy fraction (MEF) sweeps were performed at two loads of 3.3 and 5.0 bar BMEP. For the 3.3 bar BMEP, MEF sweeps from 50-90% were performed while at 5.0 bar BMEP MEF sweeps from 70-90% were performed. The following parameters were kept constant throughout these experiments: engine speed at 1,500 rpm, rail pressure at 500 bar, boost pressure at 1.5 bar, and the start of diesel injection at 310 CAD. Operating conditions are summarized in Table 3. Carbon balance was performed for each experiment and is shown in Figure 2.2 for both 3.3 and 5 bar BMEP. In this Figure, the fuel-air equivalence ratios calculated from fuel and airflow rates entering the engine are compared to the fuel-air equivalence ratio estimated from engine-out raw emissions (SAE J1003). Data is considered of good quality if these measurements fall within 5% of each other. All the values in Figure 2.2

for 5 bar BMEP fall within the ± 5 percent tolerance limit assuring good quality of measured data. An exception is in Figure 2.2a for 90% MEF at 3.3 bar where it can be noted that equivalence ratio (measured from engine-out raw emissions data) and equivalence ratio (measured from air and fuel flow rate) doesn't fall within ± 5 percent band. This is because the measured values of the HC emissions exceeded the operational limit of the HC analyzer (i.e., above 10000 ppm for the FID). As for all other cases this ratio is within ± 5 percent tolerance level so air and fuel flow rate value can be trusted to approximate HC engine out emissions. So, for 90% MEF, HC emissions were recalculated maintaining emissions ϕ within ± 5 percent of the equivalence ratio (ϕ) measured from the air and fuel flow rates. Detailed procedure of this methodology can be found in Raihan [45].

Table 2.3 Operating conditions

Parameter	Value
Engine speed (rpm)	1500
Engine load (bar)	3.3 and 5 (BMEP) or 5 and 7 bar (IMEP)
Rail pressure(bar)	500
Boost pressure (bar)	1.5
Methane energy fraction (%)	50, 60, 70, 80 and 90 for 3.3 bar BMEP 70, 75, 80, 85 and 90 for 5 bar BMEP
Start of injection (CAD)	310
Intake manifold temperature (°C)	35 +/- 5
Oil temperature (°C)	80 +/- 5
Coolant temperature (°C)	80 +/- 5
EGR (%)	0 (No EGR used)

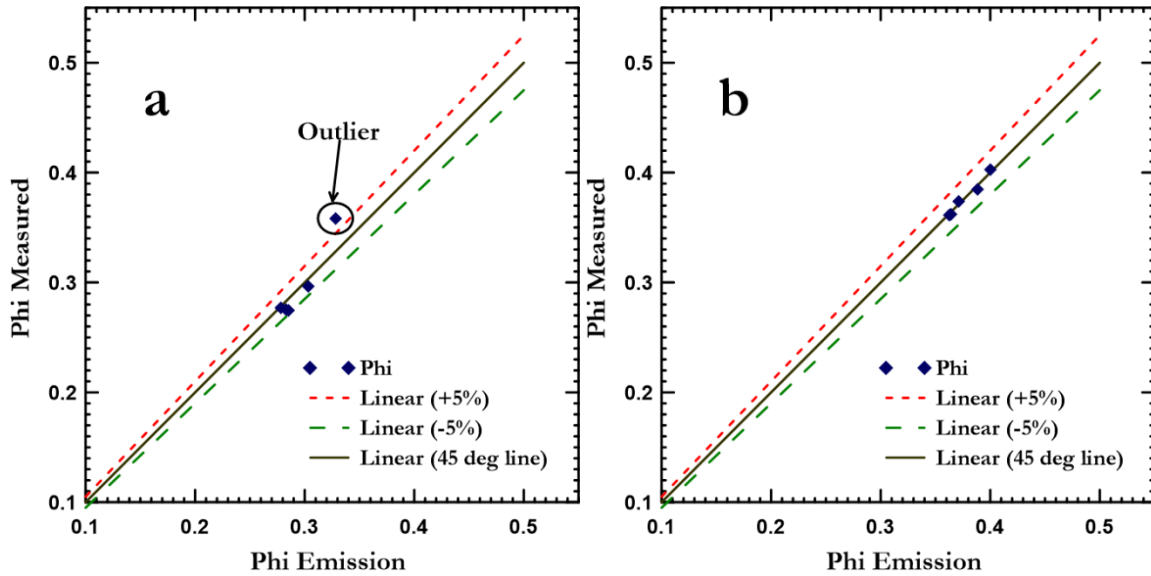


Figure 2.2 Equivalence ratio (measured from engine-out raw emissions data) versus equivalence ratio (measured from air and fuel flow rate ratio) for various MEFs at (a) 3.3 bar and (b) 5.0 bar BMEP, $N=1500$ rpm, $P_{in}=1.5$ bar, $SOI = 310$ CAD

2.5 Impact of MEF on dual fuel ignition, combustion, performance and emissions

Figure 2.3 shows cylinder pressure histories for (a) 3.3 bar and (b) 5 bar BMEP at different methane energy fractions (MEF) at 310 CAD diesel injection timing. For both BMEPs, with a decrease in MEF (i.e. increase in diesel energy fraction (DEF)) magnitude of peak in-cylinder pressure increases from 80 bar at 90% MEF to 121.2 bar at 50% MEF at 3.3 bar BMEP and from 93 bar at 90% MEF to 140 bar at 70% MEF at 5.0 bar BMEP.

Figure 2.4 shows MPRR and COVIMEP_{net} at 3.3 and 5.0 bar BMEP at various MEFs. With an increase in MEF, MPRR decreases, and COVIMEP_{net} increases. For 3.3 bar, MPRR decreases from 8.2 to 2 bar/CAD when MEF increases from 50% to 90%, and COVIMEP_{net} increases from 1.5% to 13.4% when MEF increases from 50% to 90%. At 5 bar BMEP, MPRR decreases from 12 to 2 bar/CAD when MEF increases from 70% to 90%, and COVIMEP_{net} increases from 1.5% to 3.9% when MEF increases from 70% to 90%.

90%. From these observations, maximum diesel energy fraction (DEF) is limited by MPRR leading to knocking-like combustion, and minimum DEF is limited by high COVIMEPnet characterized by high cyclic variability.

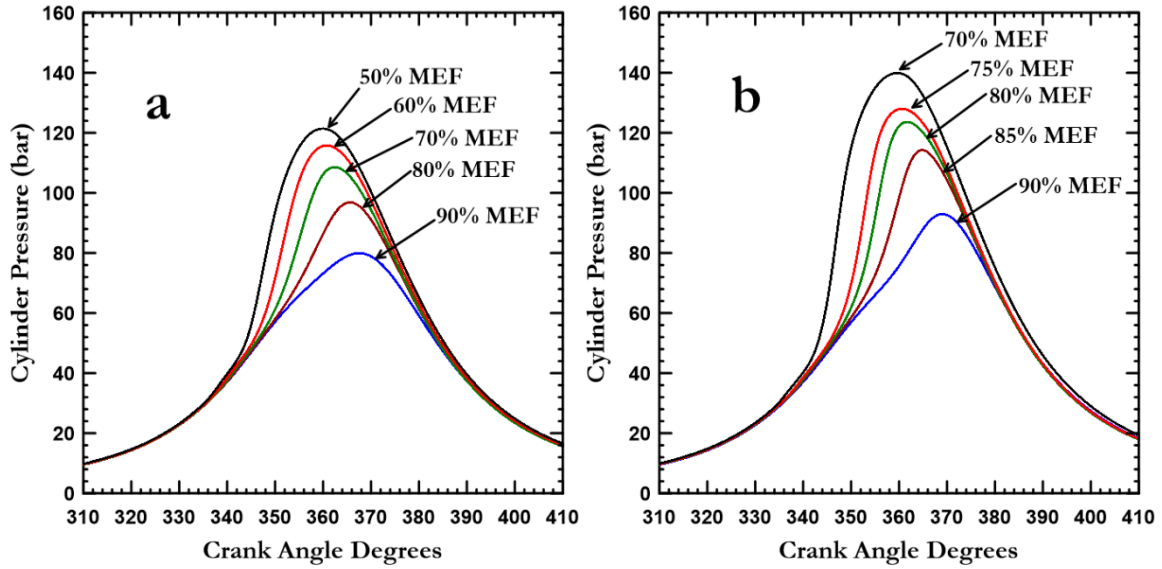


Figure 2.3 In-cylinder pressure histories for various MEFs at (a) 3.3 bar and (b) 5.0 bar BMEP, N=1500 rpm, Pin=1.5 bar, SOI = 310 CAD

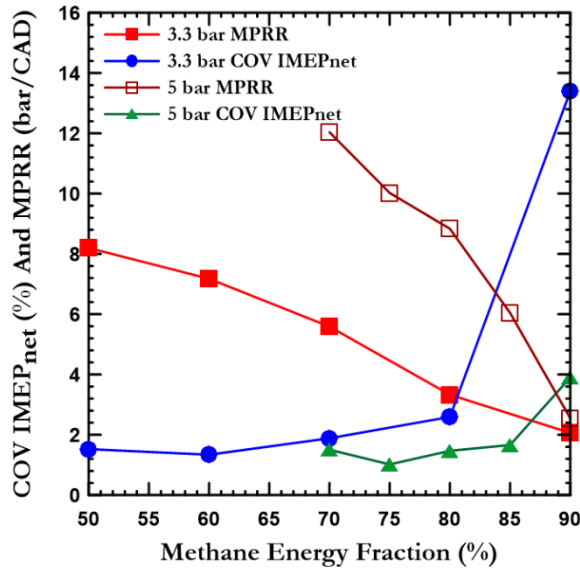


Figure 2.4 MPRR and COVIMEPnet histories for 3.3 and 5.0 bar BMEPs at various MEFs at N= 1500 rpm, Pin = 1.5 bar, SOI = 310CAD.

Figure 2.5 shows the apparent heat release rate (AHRR) trends for both 3.3 and 5.0 bar BMEP at various MEFs at 310 CAD injection timing. AHRRs at all MEFs constitute a distinct high-temperature heat release (HTHR) and low-temperature heat release (LTHR) phase except at 90% MEF at both BMEPs where the LTHR is negligible. In these experiments, the onset of LTHR is defined by the first occurrence of a slope change in AHRR after SOI, and the onset of HTHR is defined by the first occurrence of a slope change in AHRR after LTHR if any. The magnitude of peak LTHR increases with a decrease in MEF. To understand this further crank angle resolved bulk gas temperatures are plotted in Figure 2.6 for both 3.3 bar and 5 bar BMEP. LTHR is a feature of fuels that exhibit a two-stage heat release, e.g., diesel, n-heptane, etc. [18, 29, 46]. In these experiments, LTHR was observed at a temperature range around 750 to 900 K at engine-relevant conditions, which is similar to observations reported by Szybist et al at engine-relevant conditions for diesel and diesel surrogates [47]. In Figure 2.6, with increasing MEF, the onset of LTHR is progressively delayed. Figure 2.7 shows (onset of LTHR – EOI) and (onset of HTHR – EOI) in milliseconds for (a) 3.3 bar and (b) 5 bar BMEP at various MEFs. It is evident from Figure 2.7 that for 3.3 bar BMEP, the shortest time after EOI to the onset of LTHR occurs for 50% MEF; thereafter, the onset of LTHR is delayed with increasing MEF.

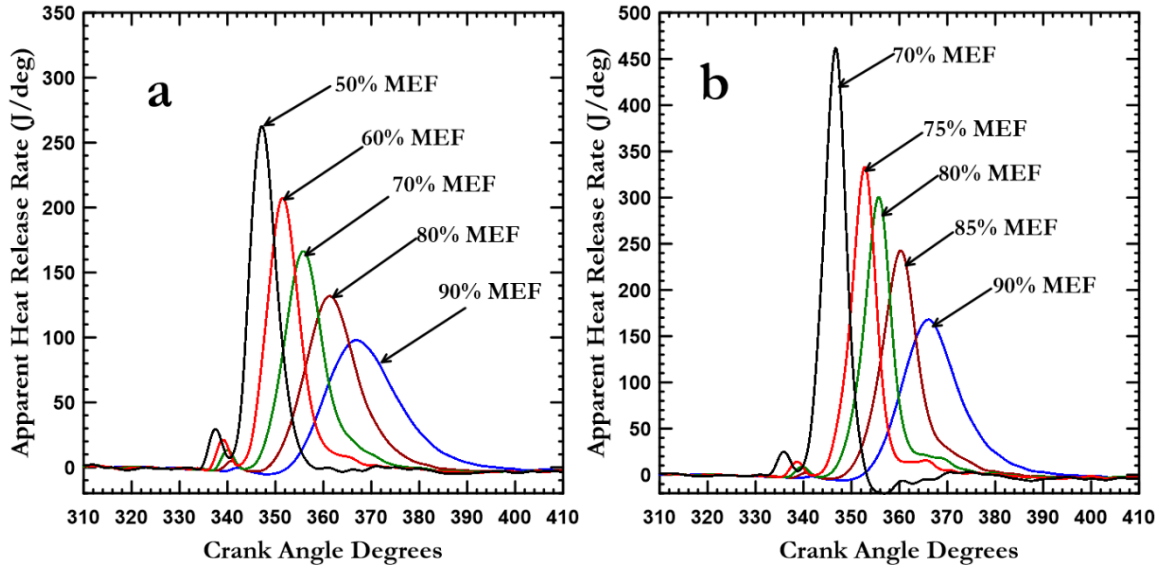


Figure 2.5 AHRR histories for various MEFs at (a) 3.3 bar and (b) 5.0 bar BMEP, N=1500 rpm, Pin=1.5 bar, SOI = 310 CAD

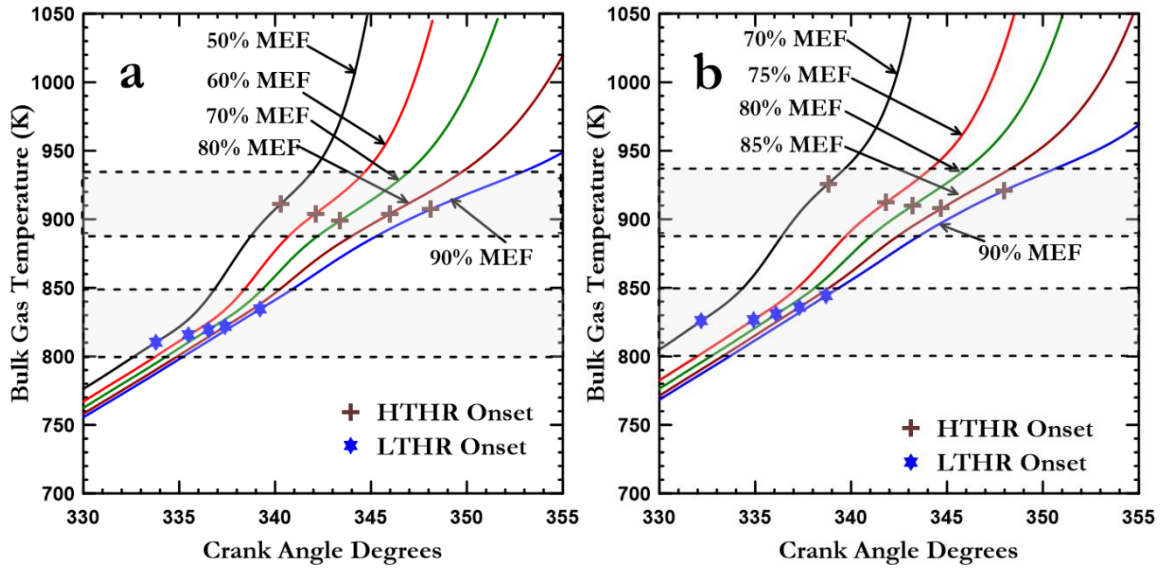


Figure 2.6 Bulk gas temperature histories and onset of LTHR and onset of HTHR for various MEFs at (a) 3.3 bar and (b) 5.0 bar BMEP, N=1500 rpm, Pin=1.5 bar, SOI = 310 CAD.

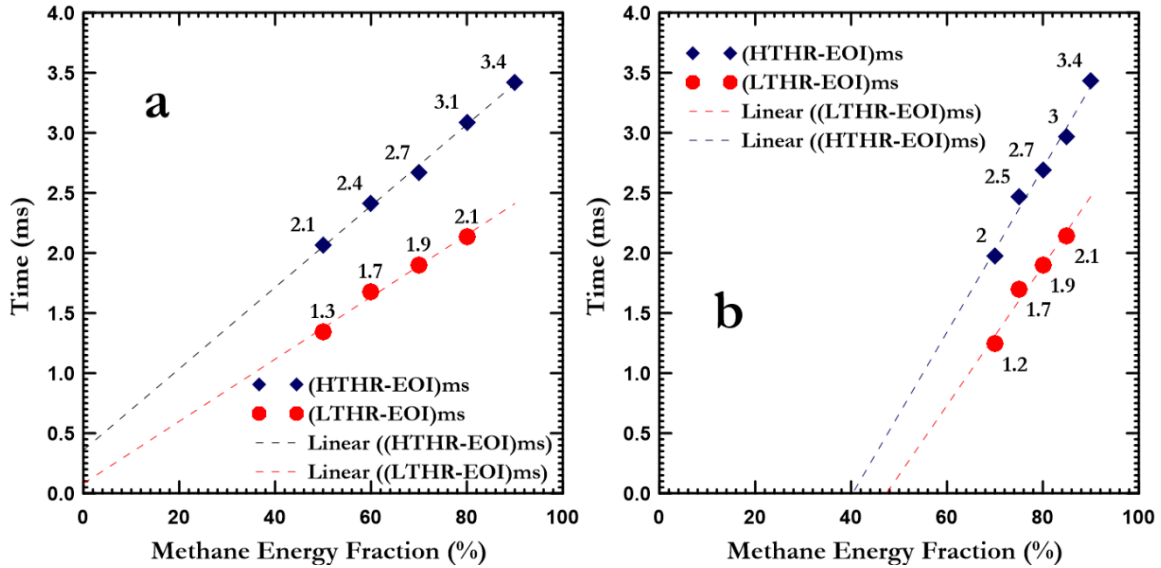


Figure 2.7 (Onset of LTHR –EOI) and (onset of HTHR –EOI) histories for various MEFs at (a) 3.3 bar and (b) 5.0 bar BMEP, N=1500 rpm, Pin=1.5 bar, SOI = 310 CAD (please note: there is no appreciable LTHR for 90% MEF at both 3.3 and 5 bar BMEP; therefore there is no data point for LTHR-EOI for both loads at 90% MEF)

To further analyze the delayed onset of LTHR with increasing MEF, zero-dimensional simulations in a perfectly stirred reactor were performed using the POLIMI_RED mechanism [48] at engine relevant conditions. As indicated in Table 4, four equivalence ratio combinations starting with neat n-dodecane (with a fixed amount of dodecane, indicated by an overall equivalence ratio of 0.3) with progressively increasing amounts of methane addition (reflected by higher overall equivalence ratios) were chosen for these simulations. The simulations were performed at a pressure of 28 bar and temperature of 810 K corresponding to the onset of LTHR from experiments at 3.3 bar and 50% MEF. The POLIMI_RED mechanism with 96 species and 993 reactions reduced from the detailed mechanism POLIMI_TOT with 1407 species [48] was used in our zero-dimensional investigations based on the rationale that it was used recently by Kahila et al. [49] to investigate the dual fuel ignition process in an LES framework

wherein a high pressure n-dodecane spray was injected into a premixed methane-air mixture at different equivalence ratios. They found that the POLIMI_RED mechanism had the relevant reaction pathways that represented the low-temperature methane oxidation process, and therefore could be used without further modification within the dual fuel framework. Their numerical studies further corroborated the experimental investigations by Srna et al. [50], who observed that in dual fuel combustion, the presence of methane delayed the autoignition of diesel fuel. Figure 2.8 shows the time evolution of the volumetric heat production rate (\dot{Q}_{vol}) during the LTHR phase at various equivalence ratios. Three observations are evident from Figure 2.8. First, the onset of volumetric heat release is progressively delayed with the addition of methane, which verifies the observations made by both Srna et al. [50] and Kahila et al. [49] that in dual fuel combustion, methane delays the autoignition of diesel. Second, the concentration of $NC_{12}H_{24}O_3$ is observed to decrease in proportion to methane addition indicating that methane clearly influences the low-temperature n-dodecane decomposition pathway. Third, the magnitude of volumetric heat release is maximum for the neat n-dodecane case (with $\phi = 0.3$) and is observed to decrease in proportion with increasing methane addition. This indicates that while methane may not contribute positively to the heat release during the LTHR period, it does play a significant role in suppressing the magnitude of heat release, all of which appear to be from n-dodecane.

Table 2.4 Zero-dimensional PSR simulations at P = 28 bar, T = 810 K to investigate impact of MEF on dodecane LTHR

	Dodecane equivalence ratio	Overall equivalence ratio	Temperature K	Pressure kPa	Ignition delay s
Case1	0.3	0.3	810	2800	3.28E-03
Case2	0.3	0.4	810	2800	3.66E-03
Case3	0.3	0.5	810 </td <td>2800</td> <td>4.21E-03</td>	2800	4.21E-03
Case4	0.3	0.6	810	2800	4.84E-03

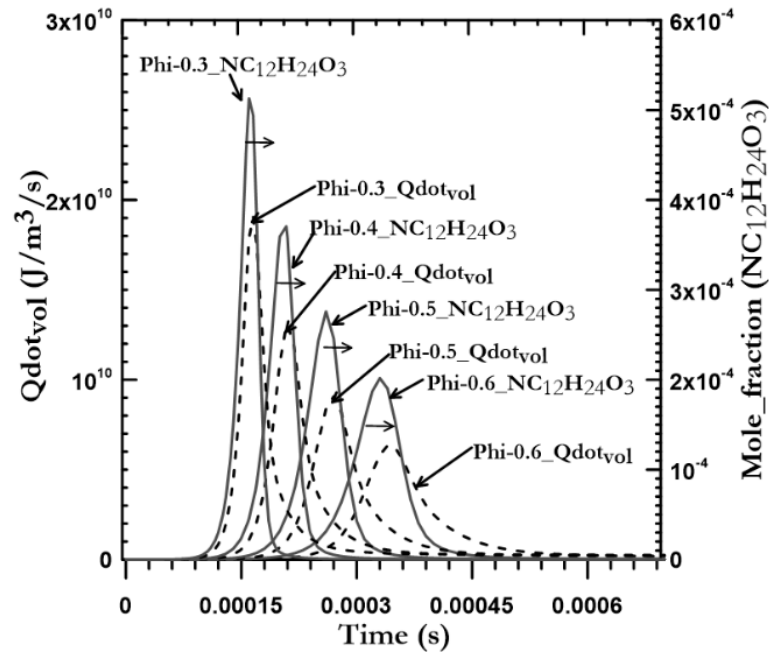


Figure 2.8 Time evolution of NC12H24O3 and volumetric heat production (Qdotvol) rate histories for various equivalence ratio at Pinitial = 28 bar, Tinitial = 810K.

The additional insight from zero-dimensional modeling affords a deeper examination of the nuances of dual fuel combustion. For instance, from Figures 2.6 and 2.7, it is seen that at both engine loads with increasing MEFs the magnitude of LTHR decreases and is accompanied by a commensurate delay in HTHR onset. In Figure 2.7, the (Onset of

LTHR –EOI) and (Onset of HTHR – EOI) lines are converging with decreasing MEF further corroborating the fact that larger LTHR magnitudes result in smaller separation between the onset of LTHR and the onset of HTHR. Another interesting observation from Figure 2.5 is that the peak of HTHR for 90% and 80% MEF at 3.3 bar BMEP occurs after TDC while it occurs before TDC for all other MEFs. Similarly, at 5 bar BMEP the peak of HTHR for 90% MEF occurs after TDC while it occurs before TDCs for all other MEFs. The reason for this behavior is analyzed further in Figure 2.9, where CA5, CA50 and CA5-90 trends for 3.3 and 5 bar BMEPs are discussed. By definition CA5 represents the crank angle corresponding to 5 percent cumulative HTHR and CA50 corresponds to the crank angle corresponding to 50 percent cumulative HTHR. CA5-90 represents the crank angle duration elapsed between CA5 and CA90; we refer to this as combustion duration throughout the rest of the paper. With an increase in DEF, combustion duration (CA5-90) shortens for both BMEPs. This can be attributed to the fact that with more diesel, there is a greater degree of charge stratification, which helps accelerate local reaction rates resulting in faster burn rates. With increasing MEF, the magnitude of LTHR is observed to decrease. As a consequence, CA5 is further removed from the diesel SOI. A delayed CA5 results in a delayed CA50. The other useful observation from Figure 2.9 is the linear behavior of both CA5 and CA50 with increasing MEF. Wagner et al. [51] report the increasing loss of combustion control under RCCI conditions with greater injection advance of the higher reactivity fuel. Since the diesel SOI is held constant at 310 CAD throughout this study, this linear trend of CA5 and CA50 allows for the usage of MEF as a viable control lever (all other factors, including

EGR and boost pressure being constant) to dictate the nature of combustion and perhaps steer it towards higher thermal efficiencies.

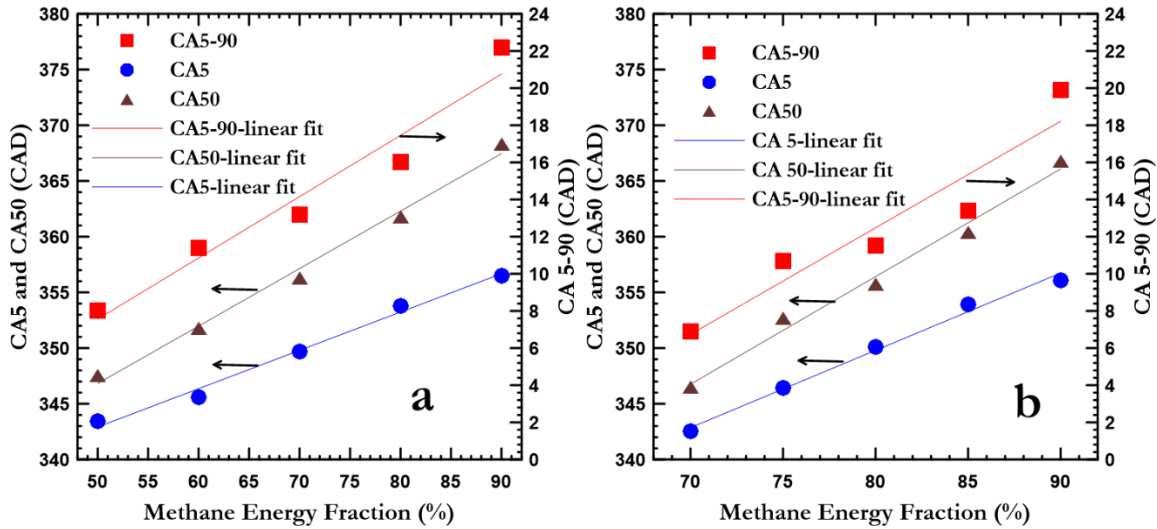


Figure 2.9 CA5, CA50 and CA10-90 histories for various MEFs at (a) 3.3 bar and (b) 5.0 bar BMEP, N=1500 rpm, Pin=1.5 bar, SOI = 310 CAD

Figure 2.10 and Figure 2.11 shows combustion and indicated fuel conversion efficiencies, at 3.3 and 5 bar BMEP, respectively. Combustion efficiency decreases with increasing MEF for both 3.3 and 5 bar BMEP. Since methane delays diesel autoignition, there is a greater residence time for diesel to disperse and mix with the methane-air mixture thereby reducing the degree of in-cylinder charge stratification. This compromised “degree of charge stratification” results in sub-optimal “distributed ignition” leading to slower methane combustion rates and reduced combustion efficiencies. As the load is increased from 3.3 bar to 5 bar BMEP combustion efficiency increases for the same MEF as fuel-air equivalence ratio increases. Indicated fuel conversion efficiencies first increase, attain a maximum value and thereafter either are

invariant at 3.3 bar BMEP or further decrease at 5 bar BMEP with decreasing MEFs. To understand this trend, it is necessary to consider competing effects, viz., CA50 (combustion phasing), CA5-90 (combustion duration), cylinder-averaged heat transfer rates, and relative magnitudes of compression and expansion work. For instance, at 3.3 bar, the IFCE remains at 44% between 50-70% MEF. At these conditions, CA50 occurs early in the compression stroke and combustion is essentially complete in the compression stroke. This implies greater compression work against a rapid combustion that is characterized by very short (CA5-90) burn durations. This also means the bulk of the expansion work occurs when cylinder pressures are relatively high. At the same time, the heat transfer rates are expected to be high since the bulk of the heat transfer occurs close to TDC. Clearly, there is a complex interplay of competing influences with the most dominant effect being that of the relatively high magnitude of the expansion work, which likely outweighs the negative effects of both increased heat transfer and compression work. Similar observations are in order at 5 bar BMEP with one notable exception. The IFCE is observed to decrease from 46% to 44% when MEF decreases from 75% to 70%. At this condition, the MPRRs are extremely high resulting in “knocking-like” combustion. Therefore, heat transfer rates are expected to be erratic at this condition resulting in reduced IFCE. On the other hand, the IFCE trends are intuitive at high MEFs at both loads and can be attributed to poor combustion efficiencies.

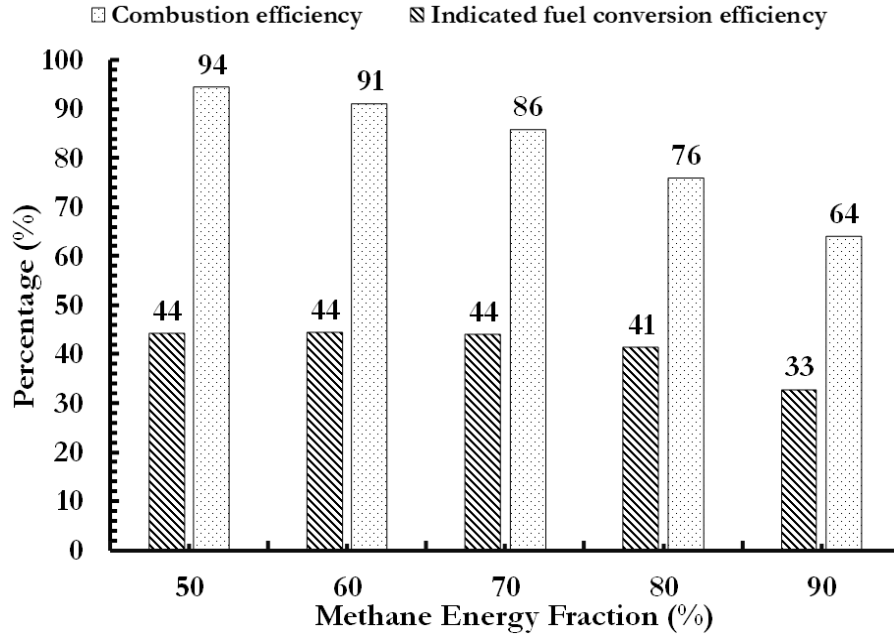


Figure 2.10 Percentage distribution of combustion, indicated fuel conversion efficiencies for various MEFs at 3.3 bar BMEP, N=1500 rpm, Pin=1.5 bar, SOI = 310 CAD

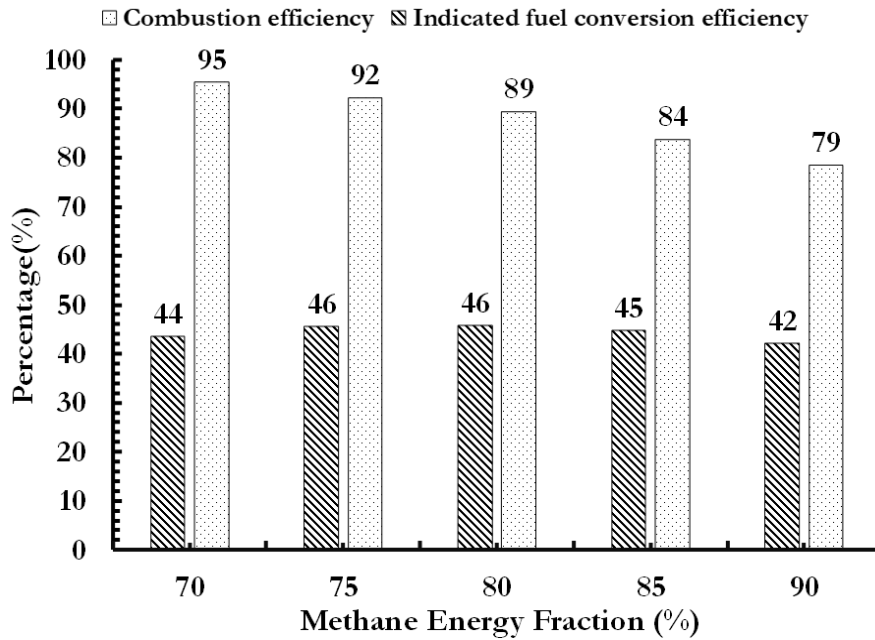


Figure 2.11 Percentage distribution of combustion, indicated fuel conversion efficiencies for various MEFs at 5 bar BMEP, N=1500 rpm, Pin=1.5 bar, SOI = 310 CAD

Figure 2.12 shows ISHC, ISCO and ISNO_x trends for various MEFs at (a) 3.3 and (b) 5 bar BMEP. For 3.3 bar BMEP ISHC and ISCO increases exponentially with increasing MEF. ISHC increases from 8.8 g/kWh at 50% MEF to 78.3 g/kWh at 90% MEF. Similarly, ISCO increases from 3.8 g/kWh at 50% MEF to 25.5 g/kWh at 90% MEF at 3.3 bar BMEP. Similar trends are observed for ISHC and ISCO for 5 bar BMEP where ISHC increases exponentially from 7.4 g/kWh at 70% MEF to 35.5 g/kWh at 90% MEF and ISCO increases from 1.4 g/kWh at 70 MEF to 7.2 g/kWh at 90% MEF. Unburned methane trapped in the cervices [52,53,54], bulk quenching around cylinder walls [55] and unstable operation (characterized by high COVIMEP_{net} [56, 57]) are the main contributors to high engine-out hydrocarbons in dual fuel combustion. Rapid increase of ISHC for 3.3 bar BMEP from 80% to 90% MEF is correlated with the rapid increase in cyclic combustion variations as represented by a sharp increase in COVIMEP_{net} from 2.6% at 80% MEF to 13.4% at 90% MEF. ISHC for 50% MEF at 3.3 bar BMEP and 70% MEF for 5 bar BMEP are almost the same indicating the majority of ISHC for these two cases can be attributed to crevice-trapped hydrocarbons. To explain this, consider the 70% MEF case at 5 bar BMEP. For this case (1) bulk gas temperatures are high for longer durations as seen in Figure 2.13 (2) cyclic variability is minimum as seen from COVIMEP_{net} in Figure 2.4. These observations indicate that oxidation of hydrocarbons should have occurred if they were within the combustion chamber as evidenced by high combustion efficiencies (94-96%) at this condition; however, in these cases it is very likely that the crevice-trapped hydrocarbons enter the cylinder during the late expansion stroke when the bulk gas temperatures are significantly reduced. Collectively, these observations further lend credence to the fact that crevice-trapped

hydrocarbons are a major source of engine-out hydrocarbon emissions in early injection dual fuel combustion. For both loads, ISCO emissions are observed to increase with increasing MEF. CO formation and oxidation are governed by chemical kinetics. CO formation is an important intermediate step in hydrocarbon combustion and its oxidation requires OH radicals and high bulk gas temperatures [58]. At high MEFs, as seen from Figure 2.13, bulk gas temperatures are considerably lower throughout the expansion process as a consequence engine-out CO emissions are higher.

NO_x formation is dependent on local equivalence ratios, local combustion temperatures and residence times. For both engine loads, ISNO_x emissions decrease exponentially with increasing MEF from 3.44 g/kWh at 50% MEF to 0.08 g/kWh at 90% MEF for 3.3 bar BMEP, as shown in Figure 2.12. The (Onset of HTHR-EOI) decreases with decreasing MEF indicating that the time available for diesel to mix with the in-cylinder charge is reduced. This leads to more robust autoignition of injected diesel, earlier onset of HTHR more stratified, faster combustion. As a consequence of the more stratified combustion, local temperatures are higher; thereby, promoting higher NO_x formation rates. At higher MEFs, diesel is comparatively well dispersed in the in-cylinder charge, which results in less stratified but slower combustion. As a consequence of the reduced stratification, local temperatures are lower, and thereby, result in reduced NO_x formation rates. Another important factor that aids NO_x formation is residence time, i.e., how long (relative to combustion duration) higher temperatures persist. It can be noted from Figure 2.13 and Table 2.5, majority of combustion occurs during the compression phase at lower MEFs resulting in higher local temperatures persisting for relatively longer durations; thereby, resulting in higher ISNO_x emissions.

Table 2.5 Crank angle degrees where SOI, EOI and, onset of HTHR occurs for 3.3 and 5 bar BMEP at N=1500 rpm, Pin=1.5 bar (** denotes negligible LTHR)

MEF	BMEP	SOI	Injection Duration (EOI-SOI)	Onset of LTHR – EOI	Onset of HTHR-EOI
%	bar	CAD	CAD	CAD	CAD
50	3.3	310	11.7	12.1	18.6
60			10.4	15.1	21.7
70			9.4	17.1	24.0
80			8.2	19.2	27.8
90			7.3	**	30.8
70	5.0		11.0	11.2	17.8
75			9.6	15.3	22.2
80			9.0	17.1	24.2
85			8.0	19.3	26.7
90			7.1	**	30.9

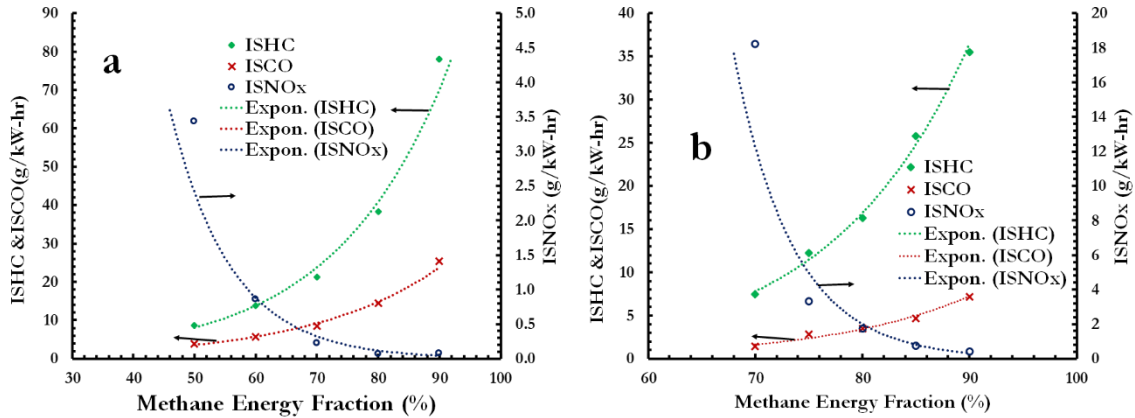


Figure 2.12 ISHC, ISCO and ISNOx histories for various MEFs at (a) 3.3 bar and (b) 5.0 bar BMEP, N=1500 rpm, Pin=1.5 bar, SOI = 310 CAD

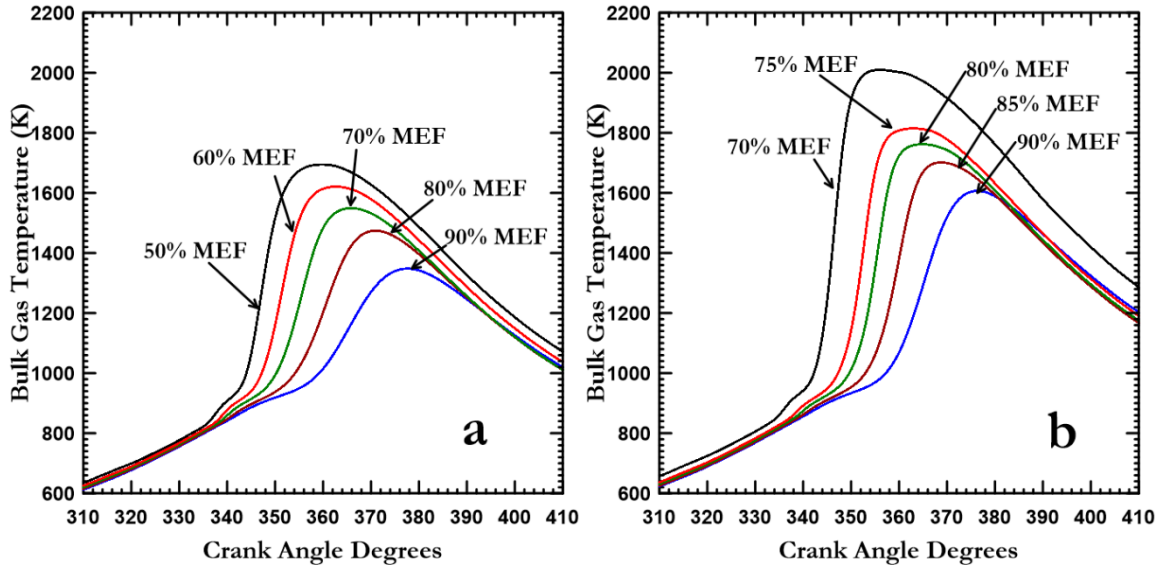


Figure 2.13 Bulk Temperature histories for various MEFs at (a) 3.3 bar and (b) 5.0 bar BMEP, $N=1500$ rpm, $P_{in}=1.5$ bar, $SOI = 310$ CAD

2.6 Impact of MEF on cyclic variations

Figures 2.14 and 2.15 show cycle-to-cycle variations of crank-resolved AHRR and cylinder pressure over 1000 individual cycles at 3.3 bar and 5 bar BMEP, respectively. We can observe from both Figures 2.14 and 2.15, with an increase in MEF cyclic variation increases (as indicated by the smearing of the peak pressure magnitude from engine cycle to another). The increase in cyclic variations with an increase in MEF can be due to a decrease in overall reactivity of charge, as methane's reactivity is lower than that of diesel. We can also observe cycle by cycle variations decrease with increase in engine load from 3.3 bar to 5 bar BMEP. This can be attributed to the fact that with an increase in engine load overall fuel amount increases thus increasing overall fuel reactivity and as a result, in-cylinder temperature increases, which decreases cycle-to-cycle variations.

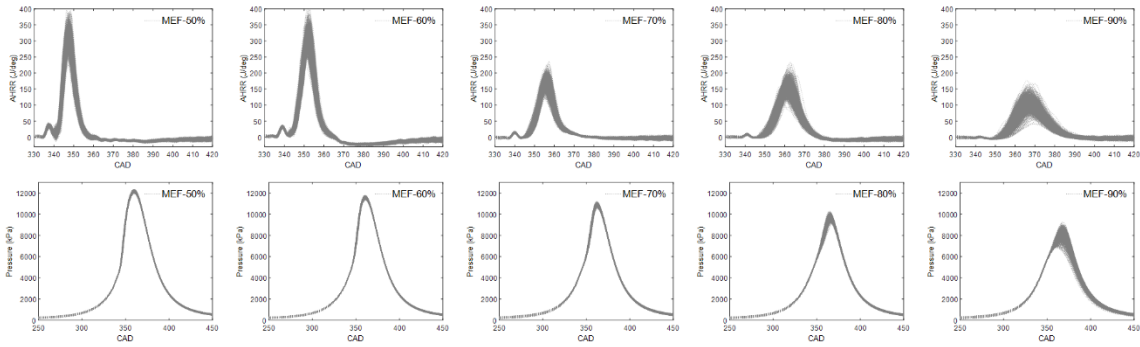


Figure 2.14 Cycle-to-cycle variations for 1000 consecutive cycles in In-cylinder pressure and AHRR histories for various MEF (%) at 3.3 bar BMEP, N=1500 rpm, $P_{in}=1.5$ bar, SOI = 310 CAD

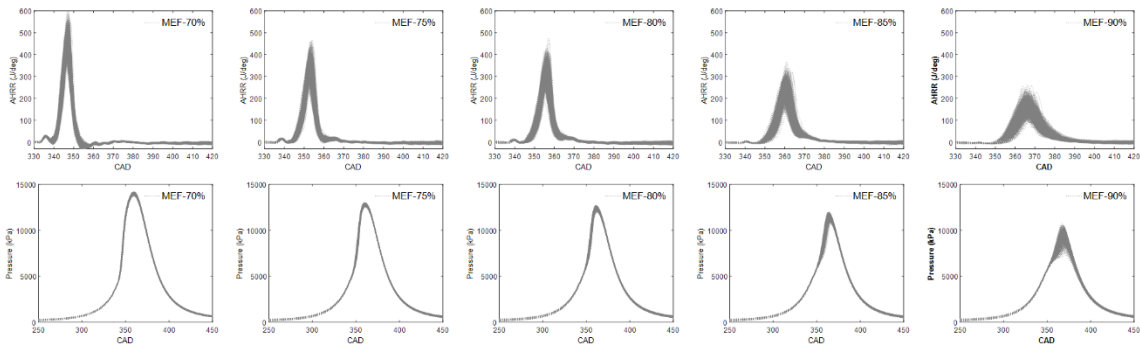


Figure 2.15 Cycle-to-cycle variations for 1000 consecutive cycles in In-cylinder pressure and AHRR histories for various MEFs at 5.0 bar BMEP, N=1500 rpm, $P_{in}=1.5$ bar, SOI = 310 CAD

Figure 2.16 discusses CA5 versus CA50 for both 3.3 bar and 5 bar BMEP over 1000 individual cycles. There are several interesting observations that can be made from Figure 2.16. First, there is a linear correlation between CA5 and CA50 with increasing MEF. This indicates that it is possible to use MEF as a potential feedback-based control variable in a hypothetical closed-loop feedback controller. Second, at the lowest MEF (for both loads), a small change in CA5 registers a small change in CA50 and the separation between CA5 and CA50 is small indicating auto ignition dominated combustion. Whereas, at the highest MEF, the separation between CA5 and CA50 is

significantly large, and in particular, for the same CA5 there are considerable CA50 variations, indicating that due to the relatively smaller amounts of diesel at these conditions, the auto ignition sensitivity is very high, and this impacts subsequent combustion evolution. The primary reason for the reduced cyclic variations at lower MEFs can be attributed to increased auto ignition sites with increasing diesel mass at these conditions.

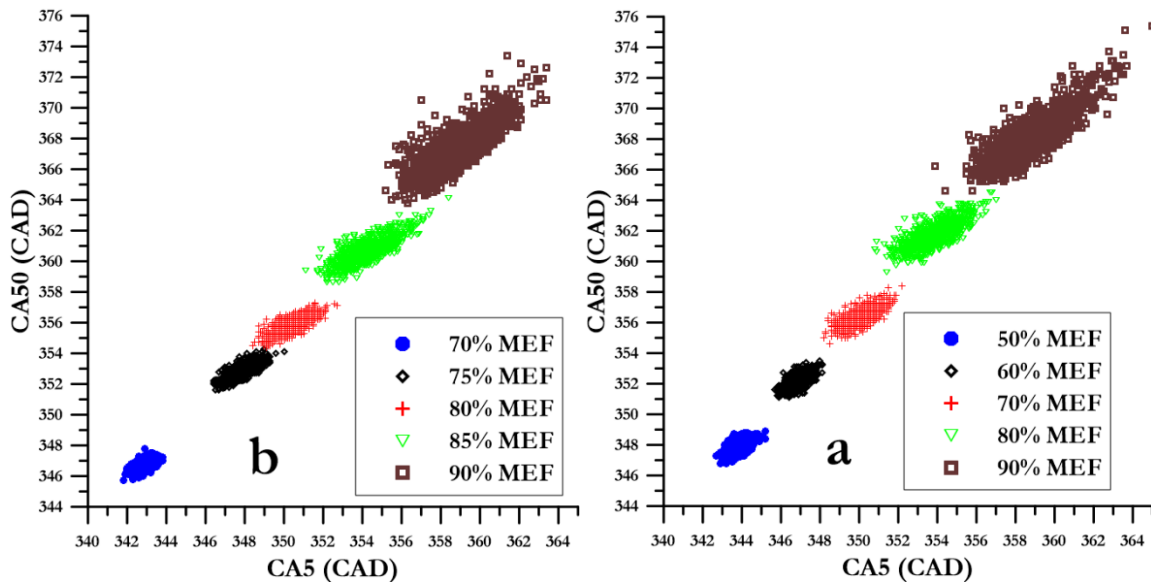


Figure 2.16 CA5 vs. CA50 for 1000 consecutive cycles for various MEFs at (a) 3.3 bar and (b) 5.0 bar BMEP, N=1500 rpm, Pin=1.5 bar, SOI = 310 CAD

Figure 2.17 discusses Pmax versus CAPmax for both 3.3 bar and 5 bar BMEP over 1000 individual cycles. For both BMEPs, at lower MEFs, magnitude of Pmax is higher and variation of Pmax and CAPmax are lowest. Similarly, for high MEFs magnitude of Pmax is lower and variation of Pmax and CAPmax is highest. As described by Matekunas [32] and Srinivasan et al. [39], the occurrence of CA50 before CAPmax with high Pmax magnitudes is a characteristic of fast burning cycles and occurrence of CAPmax before CA50 with low Pmax magnitudes is a characteristic of slow burning

cycles. For 3.3 bar BMEP at lower MEFs (50%, 60%, and 70%) CAPmax predominantly occurs after CA50 indicating a very high population of fast burn cycles. For 80% MEF at 3.3 bar BMEP there may be few cycles which may be slow burning but a majority of the cycles are fast burning cycles as CAPmax occurs between 364 and 367 CAD and CA50 occurs between 360 and 364.5 CAD (see Figure 2.16). For 90% MEF at 3.3 bar BMEP there is a mixture of both fast and slow burning cycles as CAPMax occurs between 361 and 371 CAD and CA50 occurs between 364 to 374 CAD. Similarly, for MEF (70%, 75%, and 80%) at 5 bar BMEP, CAPmax always occurs after CA50 indicating only fast burn cycles. For MEF of 85% at 5 bar BMEP, there may be few cycles which might be slow burning, but majority of the cycles are fast burning as CAPmax occurs between 363 and 367 CAD and CA50 occurs between 358 and 364 CAD. For 90 MEF at 5 bar BMEP, there is a mixture of both fast and slow burning cycles as CAPmax occurs between 366.5 and 373 CAD and CA50 is between 364 and 372.5 CAD.

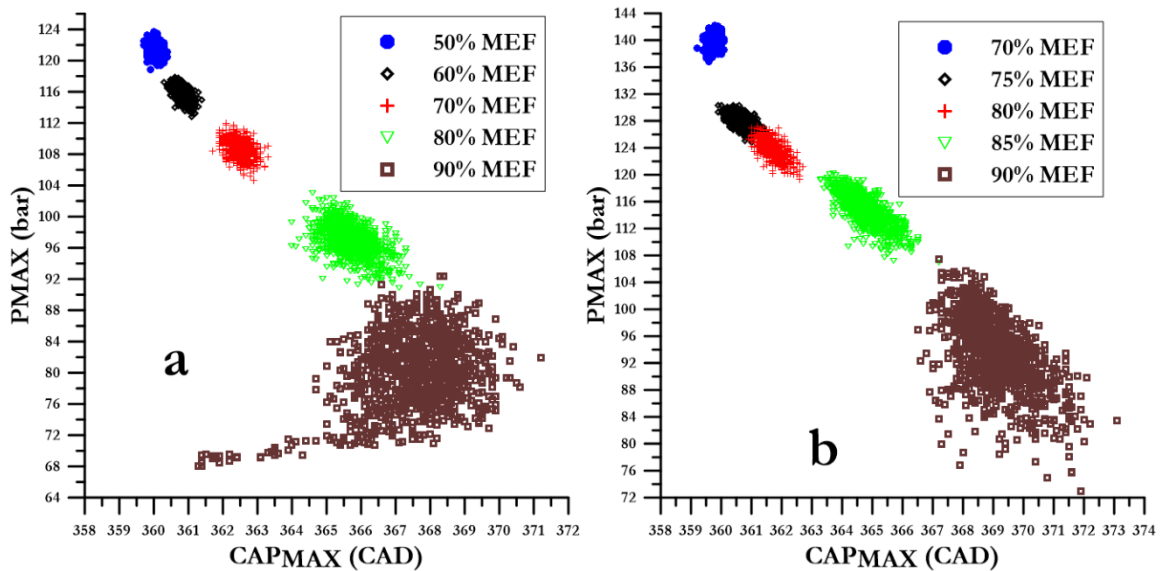


Figure 2.17 CAPmax vs. PMAX for 1000 consecutive cycles for various MEFs at (a) 3.3 bar and (b) 5.0 bar BMEP, N=1500 rpm, Pin=1.5 bar, SOI = 310 CAD

Figure 2.18 is indicated fuel conversion efficiency (IFCE) for (a) 3.3 bar and (b) 5 bar BMEP over 1000 individual cycles and Figure 2.19 is CA50 versus IFCE for (a) 3.3 bar and (b) 5 bar BMEP over 1000 individual cycles. For 3.3 bar BMEP, we can observe variation in IFCE is a maximum and widespread for 90% MEF and noticeable amount for 80% MEF. Variation in IFCE for 3.3 bar BMEP at MEF of 50%, 60% and, 70% is comparatively low. NO_x emissions at 90% and 80% MEF at 3.3 bar BMEP are lowest but HC and CO emission is high, which can most likely be reduced with an increase in IFCE. So, there is a possibility of getting better efficiency and lower emissions for these operating conditions. Similarly, for 5 bar BMEP cycle-to-cycle variation in IFCE is higher at 85% and 90% MEF compared to that at 70%, 75%, and 80% MEF.

In general, it is recommended that CA50 should be phased within 5-11 CAD aTDC [59] for best indicated efficiencies. For example, at 70% MEF 5 bar BMEP, CA50 is phased much before TDC, i.e., 12 to 14 CAD bTDC; therefore, even with shorter combustion duration and comparatively higher combustion efficiencies, IFCEs are lower. Whereas, at 85% MEF although combustion efficiencies are lower, IFCEs are comparable to the 70% MEF case. This is because CA50 is phased appropriately to realize high IFCEs. These observations collectively lend themselves to considering closed cycle IFCE as an effective observer for achieving optimal control of CA50 along with other parameters such as EGR, intake temperature, swirl, multiple injection and others to identify opportunities for high efficiency dual fuel combustion over a wide operating space.

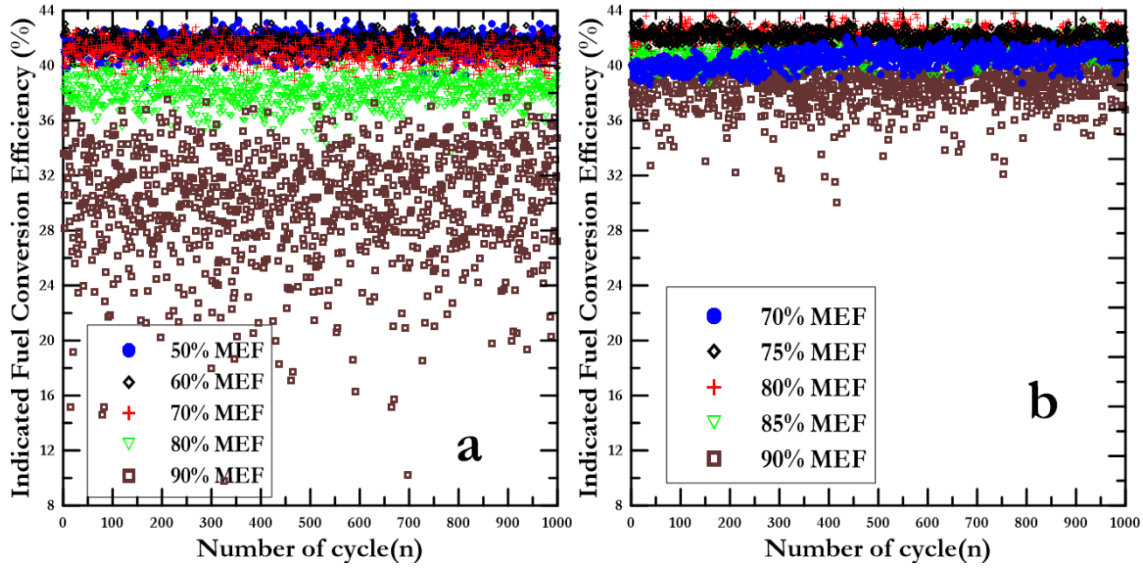


Figure 2.18 Indicated fuel conversion efficiency for 1000 consecutive cycles for various MEFs at (a) 3.3 bar and (b) 5.0 bar BMEP, N=1500 rpm, Pin=1.5 bar, SOI = 310 CAD

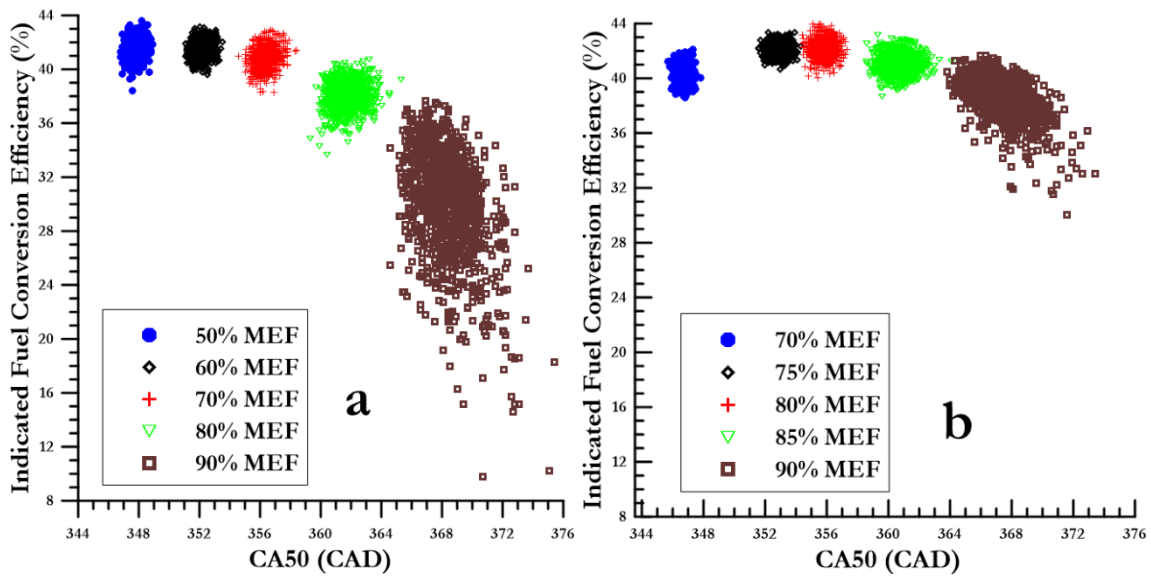


Figure 2.19 CA50 vs indicated fuel conversion efficiency for 1000 consecutive cycles for various MEFs at (a) 3.3 bar and (b) 5.0 bar BMEP, N=1500 rpm, Pin=1.5 bar, SOI = 310 CAD

2.7 Conclusions

The effect of methane substitution on early injection diesel-methane dual fuel combustion in a single cylinder, compression ignition engine was studied. MEF sweep was performed at two respective loads of 3.3 and 5.0 bar BMEP. The following conclusions were drawn from this study.

1. Minimum methane energy fraction (MEF) is limited by maximum pressure rise rate (MPRR) leading to a strong propensity for knock and maximum MEF is limited by a high coefficient of variation in IMEP ($COV_{IMEP_{net}}$), which is indicative of high cycle-to-cycle variations leading to poor combustion.
2. Zero-dimensional PSR simulations of dodecane LTHR process in the presence of methane at engine-relevant conditions show that at lean equivalence ratios methane delays the onset of dodecane LTHR and that while methane may not contribute positively to the heat release during the LTHR period, it does play a significant role in suppressing the magnitude of heat release. This corroborates the observations that increasing MEF delays the onset of LTHR and HTHR, suppresses diesel LTHR magnitudes and increases the separation between onset of LTHR and HTHR at all engine loads reported in this study.
3. The increase in combustion efficiency at low MEFs at both engine loads is countered by competing effects such as increased in-cylinder heat transfer rates and increased gas-exchange work due to early combustion phasing (CA50) that occurs in the compression process. However, the IFCEs at these conditions are almost invariant due to the fact that the bulk of the expansion work occurs at

- higher indicated pressures, which balances the negative influences of increased heat transfer and gas-exchange work.
4. Linear CA5 and CA50 trends allows for the use of MEF as a viable control lever (all other factors, including EGR and boost being a constant) to dictate the nature of combustion and perhaps steer it towards higher thermal efficiencies.
 5. NO_x emissions decrease exponentially and UHC and CO increase exponentially with increasing MEF at both loads.
 6. The auto ignition sensitivity is related to the amount of diesel, which directly affects CA5. Variations in CA5, chemical kinetics, and mixing affects variations CA50.
 7. Analysis of cycle-to-cycle variations indicates that IFCE may be used as an effective monitor to optimize CA50 location while adjusting other engine-operating parameters such as EGR and RGR fraction, intake charge temperature, swirl, multiple injections, etc. to identify opportunities to achieve high efficiency dual fuel combustion over a wide operating space.

2.8 Acknowledgments

“This paper was developed based on partial funding from the Alliance for Sustainable Energy, LLC, Managing and Operating Contractor for the National Renewable Energy Laboratory for the U.S. Department of Energy”

2.9 References

1. U.S. Energy Information Administration, International Energy Outlook 2018.
2. Thring, R., "Homogeneous-Charge Compression-Ignition (HCCI) Engines," SAE Technical Paper 892068, 1989, <https://doi.org/10.4271/892068>.
3. Christensen, M. and Johansson, B., "Supercharged Homogeneous Charge Compression Ignition (HCCI) with Exhaust Gas Recirculation and Pilot Fuel," SAE Technical Paper 2000-01-1835, 2000, <https://doi.org/10.4271/2000-01-1835>.
4. Splitter, D. A., Hanson, R. M., Kokjohn, S. L., Reitz, R. D. Improving engine performance by optimizing fuel reactivity with a dual fuel PCCI strategy. Conference on Thermo and Fluid Dynamic Processes in Diesel Engines, Valencia, Spain, September 2010, 14–17.
5. Manente, V., Johansson, B., and Tunestal, P. Partially Premixed Combustion at High Load using Gasoline and Ethanol, a Comparison with Diesel. SAE Technical Paper 2009-01-0944, 2009.
6. Kalghatgi, G., Risberg, P., and Ångström, H. Partially Pre-Mixed Auto-Ignition of Gasoline to Attain Low Smoke and Low NO_x at High Load in a Compression Ignition Engine and Comparison with a Diesel Fuel," SAE Technical Paper 2007-01-0006, 2007.
7. Stephen Ciatti and Swami Nathan Subramanian. "An Experimental Investigation of Low-Octane Gasoline in Diesel Engines" J. Eng. Gas Turbines Power. 2011;133 (9):092802-092802-11.
8. Azimov, U., Tomita, E., Kawahara, N., & Harada, Y. Premixed mixture ignition in the end-gas region (PREMIER) combustion in a natural gas dual-fuel engine: operating range and exhaust emissions. International Journal of Engine Research, (2011), 12(5), 484–497.

9. Attard, W. and Blaxill, H., "A Single Fuel Pre-Chamber Jet Ignition Powertrain Achieving High Load, High Efficiency and Near Zero NOx Emissions," SAE Int. J. Engines 5(3):734-746, 2012, <https://doi.org/10.4271/2011-01-2023>
10. Vedula, R. T., Song, R., Stuecken, T., Zhu, G. G., and Schock, H., 2017, "Thermal Efficiency of a Dual-Mode Turbulent Jet Ignition Engine Under Lean and Near-Stoichiometric Operation," Int. J. Engine Res., 18(10), pp. 1055–1066
11. Kokjohn, S.L., Hanson, R.M., Splitter, D.A., and Reitz, R.D., "Fuel Reactivity Controlled Compression Ignition (RCCI): A Pathway to Controlled High-Efficiency Clean Combustion," International Journal of Engine Research, Special Issue on Fuel Efficiency, Vol. 12, pp. 209-226, doi:10.1177/1468087411401548, 2011
12. "T. Taymaz, K. Çakir, A. Mimaroglu Experimental study of effective efficiency in a ceramic coated diesel engine J Surf Coat Technol, 200 (2005), pp. 1182-1185"
13. Filipi, Zoran & Prucka, Robert & O'Donnell, Ryan & Hoffman, Mark & Killingsworth, Nick & Powell, Tommy. (2017). Predicting the gas-wall boundary conditions in a thermal barrier coated low temperature combustion engine using sub-coating temperature measurements. International Journal of Powertrains. 6. 125. 10.1504/IJPT.2017.10006633
14. O'Donnell, Ryan & Powell, Thomas & Filipi, Zoran & Hoffman, Mark. (2016). Estimation of Thermal Barrier Coating Surface Temperature and Heat Flux Profiles in a Low Temperature Combustion Engine Using a Modified Sequential Function Specification Approach. Journal of Heat Transfer. 139. 10.1115/1.4035101
15. Powell, Thomas & O'Donnell, Ryan & Hoffman, Mark & Filipi, Zoran. (2017). Impact of a Yttria-Stabilized Zirconia Thermal Barrier Coating on HCCI Engine Combustion, Emissions, and Efficiency. Journal of Engineering for Gas Turbines and Power. 139. 10.1115/1.4036577
16. Johnson, B. and Edwards, C. Exploring the Pathway to High Efficiency IC Engines through Exergy Analysis of Heat Transfer Reduction. SAE Int. J. Engines, 2013 6(1):150-166.
17. National Academies of Sciences, Engineering, and Medicine. 2015. Review of the 21st Century Truck Partnership, Third Report. Washington, DC: The National Academies Press.
18. U.S. Department of Energy's (DOE) SuperTruck II program, 2016.

19. Sharma, A. and Redon, F. Multi-Cylinder Opposed-Piston Engine Results on Transient Test Cycle. SAE Technical Paper 2016-01-1019, 2016.
20. Banerjee, S., Naber, C., Willcox, M., Finney, C. E. A., and Edwards, D. K. (June 19, 2018). "High-Performance Computing and Analysis-Led Development of High Efficiency Dilute Opposed Piston Gasoline Engine." ASME. J. Eng. Gas Turbines Power. October 2018; 140(10): 102803.
<https://doi.org/10.1115/1.4039845>
21. E. Scott Guerry, Mostafa S. Raihan, Kalyan K. Srinivasan, Sundar R. Krishnan, Aamir Sohail, Injection timing effects on partially premixed diesel–methane dual fuel low temperature combustion, Applied Energy Volume 162, 15 January 2016, Pages 99–113.
22. Sundar Rajan Krishnan, Kalyan Kumar Srinivasan, Mostafa Shameem Raihan. The effect of injection parameters and boost pressure on diesel-propane dual fuel low temperature combustion in a single-cylinder research engine. Fuel Volume 184, 15 November 2016, Pages 490–502.
23. Kyle A. Hodges, Andrea Aniello, Sundar Rajan Krishnan, Kalyan Kumar Srinivasan. Impact of propane energy fraction on diesel-ignited propane dual fuel low temperature combustion. Fuel, 209 (2017), pp. 769-775
24. D.H. Qi & C.F. Lee. Combustion and emissions behaviour for ethanol–gasoline-blended fuels in a multipoint electronic fuel injection engine. International Journal of Sustainable Energy, 2016, 35:4, 323-338.
25. Northrop, W., Bohac, S., and Assanis, D. Premixed Low Temperature Combustion of Biodiesel and Blends in a High Speed Compression Ignition Engine. SAE Int. J. Fuels Lubr, 2009. 2(1):28-40.
26. Annual Energy Outlook 2018 with Projections to 2050. U.S. Energy Information Administration, 2018
27. Polk AC, Carpenter CD, Scott Guerry EE, et al. Diesel-Ignited Propane Dual Fuel Low Temperature Combustion in a Heavy-Duty Diesel Engine. ASME. J. Eng. Gas Turbines Power. 2014;136(9):091509-091509-9. doi:10.1115/1.4027189
28. Papagiannakis, R. G., and Hountalas, D. T., 2002, "Experimental Investigation Concerning The Effect of Natural Gas Percentage on Performance and Emissions of a DI Dual Fuel Diesel Engine," Appl. Thermal Eng., 23(3), pp. 353–365
29. Raihan MS, Guerry ES, Dwivedi U, Srinivasan KK, Krishnan SR (2014) Experimental analysis of diesel-ignited methane dual fuel low temperature

- combustion in a single cylinder diesel engine. *Trans ASCE: J Energy Eng* C4014007.
30. Srinivasan KK, Krishnan SR, Qi YY. Cyclic Combustion Variations in Dual Fuel Partially Premixed Pilot-Ignited Natural Gas Engines. *ASME. J. Energy Resour. Technol.* 2013;136(1):012003-012003-10. doi:10.1115/1.4024855.
 31. Young, Michael B. Cyclic Dispersion in the Homogeneous-Charge Spark-Ignition Engine—A Literature Survey. *SAE Transactions* 90 (1981): 49-73.
 32. Matekunas, F., Modes and Measures of Cyclic Combustion Variability. *SAE Technical Paper* 830337, 1983.
 33. Klos, D., & Kokjohn, S. L. Investigation of the sources of combustion instability in low-temperature combustion engines using response surface models. *International Journal of Engine Research* 16, no. 3 (2015): 419-440.
 34. S. Dong, X. Cheng, B. Ou, et al. Experimental and numerical investigations on the cyclic variability of an ethanol/diesel dual-fuel engine *Fuel*, 186 (2016), pp. 665-673
 35. Dong, S., Ou, B., and Cheng, X., Comparisons of the Cyclic Variability of Gasoline/Diesel and Ethanol/Diesel Dual-Fuel Combustion Based on a Diesel Engine, *SAE Technical Paper*, 2017, 2017-01-5001.
 36. C. Gong, K. Huang, Y. Chen, J. Jia, Y. Su, X. Liu Cycle-by-cycle combustion variation in a DISI engine fueled with methanol *Fuel*, 90 (8) (2011), pp. 2817-2819
 37. Selim, M. Y. "Effect of engine parameters and gaseous fuel type on the cyclic variability of dual fuel engines." *Fuel* 84, no. 7-8 (2005): 961-971.
 38. Tunér, M., Karlsson, M., & Mauss, F. Studying HCCI combustion and its cyclic variations versus heat transfer, mixing and discretization using a PDF based approach. No. 2009-01-0667. *SAE Technical Paper*, 2009
 39. Srinivasan K.K., Krishnan S.R., Jha P.R., Mahabadipour H. Cyclic Combustion Variations in Diesel–Natural Gas Dual Fuel Engines. In: Srinivasan K., Agarwal A., Krishnan S., Mulone V. (eds) *Natural Gas Engines. Energy, Environment, and Sustainability*. Springer, Singapore, (2019) pp 329-358 DOI https://doi.org/10.1007/978-981-13-3307-1_12
 40. Jupudi, R., Finney, C., Primus, R., Wijeyakulasuriya, S. et al., "Application of High Performance Computing for Simulating Cycle-to-Cycle Variation in Dual-Fuel Combustion Engines," *SAE Technical Paper*, 2016, 2016-01-0798

41. Kantor JC. A dynamical instability of spark--ignited engines. *Science* 1984; 224: 1233---1235.
42. Martin, J.K., Plee, S.L., and Remboski, D.J., "Burn Modes and Prior-Cycle Effects on Cyclic Variations in Lean-Burn Spark-Ignition Combustion," SAE Technical Paper880201, 1988, doi: 10.4271/880201.
43. Finney, C. E., Kaul, B. C., Daw, C. S., Wagner, R. M., Edwards, K. D., & Green, J. B. Invited Review: A review of deterministic effects in cyclic variability of internal combustion engines. *International Journal of Engine Research*, 2015. 16(3), 366–378.
44. C. Yao, Y. Hu, T. Zhou, et al. Combustion stability control of dieseline PPCI based on in-cylinder pressure signals IFAC-Papers OnLine, 49 (11) (2016), pp. 333-339
45. Raihan, Mostafa Shameem, "A comparative study of diesel ignited methane and propane dual fuel low temperature combustion in a single cylinder research engine," MSSTATE, 2014
46. Shibata, G., Oyama, K., Urushihara, T., and Nakano, T., "The Effect of Fuel Properties on Low and High Temperature Heat Release and Resulting Performance of an HCCI Engine," SAE Technical Paper 2004-01-0553, 2004, <https://doi.org/10.4271/2004-01-0553>
47. J.P. Szybist, A.L. Boehman, D.C. Haworth, H. Koga Premixed ignition behavior of alternative diesel fuel-relevant compounds in a motored engine experiment *Combust Flame*, 149 (1) (2007), pp. 112-128
48. A. Frassoldati, G. D'Errico, T. Lucchini, A. Stagni, A. Cuoci, T. Faravelli, A. Onorati, E. RanziReduced kinetic mechanisms of diesel fuel surrogate for engine CFD simulations *Combust. Flame*, 162 (10) (2015), pp. 3991-4007
49. H. Kahila, A. Wehrfritz, O. Kaario, V. Vuorinen Large-eddy simulation of dual-fuel ignition: diesel spray injection into a lean methane–air mixture *Combust. Flame*, 199 (2019), pp. 131-151
50. A. Srna, M. Bolla, Y.M. Wright, K. Herrmann, R. Bombach, S.S. Pandurangi, Konstantinos Boulouchos , Gilles Bruneaux. Effect of methane on pilot-fuel auto-ignition in dual-fuel engines *Proc Combust Inst*, 37 (4) (2019), pp. 4741-4749, 10.1016/j.proci.2018.06.177

51. Roberts, G., Rousselle, C., Musculus, M., Wissink, M. et al. RCCI Combustion Regime Transitions in a Single-Cylinder Optical Engine and a Multi-Cylinder Metal Engine. *SAE Int. J. Engines*, 2017, 10(5):2392-2413
52. Wu, Z., Rutland, C. J., & Han, Z. (2019). Numerical evaluation of the effect of methane number on natural gas and diesel dual-fuel combustion. *International Journal of Engine Research*, 20(4), 405–423.
<https://doi.org/10.1177/1468087418758114>
53. Konigsson, F. (2012) Advancing the limits of dual fuel combustion, Ph. D. thesis, Royal Inst. Of Tech., Sweden
54. Tamura, M., Sakurai, T, Tai, H. (2001) Study of crevice flow in a gas engine using laser induced fluorescence, SAE 2001-01-0913
55. Shim, E., Park, H, Bae, C., Intake air strategy for low HC and CO emissions in dual-fuel (CNG-diesel) premixed charge compression ignition engine, *Appl. Energy*, Volume 225, 1 September 2018, Pages 1068-1077
56. Srinivasan, K. K., Krishnan, S. R., Singh, S., Midkiff, K. C., Bell, S. R., Gong, W., Fiveland, S. B., and Willi, M. (May 3, 2004). "The Advanced Injection Low Pilot Ignited Natural Gas Engine: A Combustion Analysis." *ASME. J. Eng. Gas Turbines Power*. January 2006; 128(1): 213–218.
57. Srinivasan, K. K., Krishnan, S. R., & Midkiff, K. C. (2006). Improving low load combustion, stability, and emissions in pilot-ignited natural gas engines. *Proceedings of the Institution of Mechanical Engineers, Part D: Journal of Automobile Engineering*, 220(2), 229–239.
<https://doi.org/10.1243/09544070JAUTO104>
58. S. R. Turns, *An Introduction to Combustion: Concepts and Applications*. Second Edition New York, McGraw-Hill, 2000
59. J.A. Caton Combustion phasing for maximum efficiency for conventional and high efficiency engines *Energy Convers Manag*, 77 (2014), pp. 564-576
60. Heywood, J. B. *Internal combustion engine fundamentals* 2nd edition. New York: McGraw-Hill. 2018.
61. Gatowski, J., Balles, E. N., Chun, K., Nelson, F., Ekchian, J., Heywood, J. B. Heat release analysis of engine pressure data. Tech. rep., SAE Technical paper, 1984.
62. Shangming Li. A Temperature-dependent Model of Ratio of Specific Heats Applying in Diesel Engine. Master thesis, NTNU, 2017

63. Egnell, R., "Combustion Diagnostics by Means of Multizone Heat Release Analysis and NO Calculation," SAE Technical Paper 981424, 1998, <https://doi.org/10.4271/981424>.
64. Brunt, M., Rai, H., and Emtage, A., "The Calculation of Heat Release Energy from Engine Cylinder Pressure Data," SAE Technical Paper 981052, 1998, <https://doi.org/10.4271/981052>.

Appendix I

$$MEF = \frac{\dot{m}_m LHV_m}{\dot{m}_d LHV_d + \dot{m}_m LHV_m} \quad (A1.1)$$

$$DEF = \frac{\dot{m}_d LHV_d}{\dot{m}_d LHV_d + \dot{m}_m LHV_m} \quad (A1.2)$$

$$\Phi = \frac{(A/F)_{st-tot}}{\left(\frac{\dot{m}_a}{\dot{m}_d + \dot{m}_m}\right)} \quad (A1.3)$$

$$\eta_c = 1 - \frac{\sum_i x_i Q_{LHV_i}}{\left(\frac{\dot{m}_f}{\dot{m}_f + \dot{m}_a}\right) Q_{LHV_f}} \quad (A1.4)$$

$$AHRR(\theta) = \frac{\gamma}{\gamma-1} P \frac{dV}{d\theta} + \frac{1}{\gamma-1} V \frac{dP}{d\theta} \quad (A1.5)$$

$$\gamma(T) = 1.375 - 6.99 \times 10^{-5} T \quad (A1.6)$$

$$MPRR = \left(\frac{dp}{d\theta}\right)_{max} \quad (A1.7)$$

$$COV_{imep} = \left(\frac{\sigma}{\mu}\right)_{max} \quad (A1.8)$$

$$IFCE = \frac{IP}{\dot{m}_d LHV_d + \dot{m}_m LHV_m} \quad (A1.9)$$

$$m_{res} = \left(\frac{P_{EVC} * V_{EVC}}{T_{exhaust} * R_{EVC}}\right) \quad (A1.10)$$

$$m_{IVC} = m_{res} + m_{air} + m_{ch4} \quad (A1.11)$$

Equation A1.1 and A1.2 define methane energy fraction (MEF) and diesel energy fraction (DEF), respectively. In equation 1 and 2 \dot{m} refers to the mass flow rates of diesel (subscript “d”), gaseous methane fuel (subscript “m”), and air (subscript “a”), and LHV refers to the corresponding fuel lower heating values. The stoichiometric air required for complete oxidation of both diesel and methane into CO₂ and H₂O is defined as the stoichiometric air-fuel ratio $\left(\frac{A}{F}\right)_{st-tot}$. Therefore, $\left(\frac{A}{F}\right)_{st-tot}$ is dependent on the MEF and DEF. A detailed uncertainty analysis accompanying the estimation of indicated fuel conversion efficiency is provided in Appendix II.

Equation A1.4 defines the combustion efficiency. Heywood [60], uses exhaust concentrations of CO, HC, H₂ and PM emissions and their respective lower heating values to calculate combustion efficiency. As gravimetric PM is not measured for these experiments (since they are likely very low as demonstrated by the low FSN values), only the measured CO and HC concentrations and H₂ mass fractions calculated from stoichiometric calculations are used to determine the combustion efficiency. In Equation A1.4, x_i are the mass fractions of HC, CO, and H₂. Q_{LHV_i} are their respective lower heating values, and subscripts “f” and “a” denote fuel and air, respectively. According to Heywood [60], fuel LHV can be used as LHV of HC in the calculation of combustion efficiency in equation A1.4. Since, diesel and methane are used as source of fuel so combined fraction weighted LHV (i.e., mass-fraction-weighted average of 42.6 MJ/kg for diesel and 50 MJ/kg for methane) of these two fuels are used for LHV of HC in equation A1.4. And the lower heating values for CO and H₂ are assumed to be 10.1 MJ/kg and 120 MJ/kg, respectively.

Apparent heat release rate (AHRR) is calculated using Equation A1.5 [60] and the ratio of specific heats (γ) was determined using Equation A1.6 based on global in-cylinder temperature (T), by Gatowski's model [61]. Li's [62] found gamma estimation results by Gatowski's model [61] closest with reference mode than Egnell's model [63] and Brunt's model [64]. Engine geometry values such as compression ratio, bore, stroke, and connecting rod length coupled with engine crankshaft position measurements were used to calculate instantaneous volume (V). The rate of change of volume with respect to crank angle ($dV/d\Theta$) was calculated using crank angle-resolved instantaneous volume data and the rate of change of pressure with respect to crank angle ($dP/d\Theta$) was calculated using crank angle-resolved cylinder pressure data. For cyclic data, each cycle cylinder pressure data was smoothed using 5th order low pass Butterworth filter with a cut of frequency of 4500 Hz. Equation A1.7 defines the maximum pressure rise rate and is the maximum value of the rate of change of pressure with respect to crank angle ($dP/d\Theta$). Equation A1.8 provides a coefficient of variation of IMEP and is calculated over 1000 cycles in this study. In equation A1.8 σ represents standard deviation in IMEP and μ represents mean of IMEP. Equation A1.9 defines indicated fuel conversion efficiency (IFCE) and IP is indicated power. Equation A1.10 is employed to calculate residual gas inside the cylinder. P_{EVC} , V_{EVC} and R_{EVC} are pressure, instantaneous volume and gas constant at Exhaust valve closing. Assuming in-cylinder temperature and exhaust temperature are the same when the exhaust valve closes, the exhaust temperature is used as In-cylinder temperature at exhaust valve closing in equation A1.10 and m_{IVC} in equation A1.11 is trapped mass at IVC and is calculated using air and methane mass from air and methane mass flow rates and residual gas mass is estimated using A1.10.

Appendix II

Allowing a variation of equivalence ratio of 5% due to cycle-to-cycle variations the accuracy of sensors used in measurements are given below.

Table 2.6 Accuracies of various sensors

Measured parameters	Sensor	Units	Accuracy
Engine speed	Hall effect	RPM	± 1 RPM
Cylinder pressure	Piezoelectric	bar	± 0.005 bar
Intake manifold pressure	Absolute pressure	PSIG	± 0.25 % of reading
Airflow rate	Sonic flow nozzle	Kg/hr	± 0.1 % of reading

Now using this information, uncertainty propagation of estimated IFCE is performed for a representative average cycle.

IFCE is given by,

$$\eta = \frac{N * AFS * \sum p dv}{120 * \phi * \dot{M}_a * Q_f} \quad (A2.1)$$

Where N is engine speed, AFS is air-fuel ratio at stoichiometric of a combined fuel, ϕ is air-fuel equivalence ratio, p is pressure and dv is differential volume, \dot{M}_a is air mass flow rate and Q_f is the heating value of a representative hydrocarbon with a similar energy density of a known methane-diesel mixture.

AFS is calculated using the below equation

$$AFS = \frac{34.56(4+Y)}{12.011+1.008*Y} \quad (A2.2)$$

Where Y is hydrogen to carbon ratio in fuel.

And Q_f is calculated using the below equation

$$Q_f = \frac{(\dot{m}_{diesel} Q_{lhv_{diesel}} + \dot{m}_{ch4} Q_{lhv_{ch4}})}{\dot{m}_{diesel} + \dot{m}_{ch4}} \quad (A2.3)$$

Uncertainty in estimated IFCE can be written as,

$$U_\eta = \left[\begin{array}{l} \left(\frac{\partial \eta}{\partial P}\right)^2 (U_P)^2 + \left(\frac{\partial \eta}{\partial (dV)}\right)^2 (U_{(dV)})^2 \\ + \left(\frac{\partial \eta}{\partial AFS}\right)^2 (U_{AFS})^2 + \left(\frac{\partial \eta}{\partial \dot{m}_a}\right)^2 (U_{\dot{m}_a})^2 \\ + \left(\frac{\partial \eta}{\partial \phi}\right)^2 (U_\phi)^2 + \left(\frac{\partial \eta}{\partial Q_f}\right)^2 (U_{Q_f})^2 + \left(\frac{\partial \eta}{\partial N}\right)^2 (U_N)^2 \end{array} \right]^{0.5} \quad (A2.4)$$

Overall uncertainty includes both bias and precision

$$U = \sqrt{(P^2 + B^2)} \quad (A2.5)$$

We can assume $U_{(dV)}$, $U_{(AFS)}$ and $U_{(Q_f)}$ to be 0.

Now derivatives of all other remaining parameters used in equation A2.4 is estimated as follows,

$$\frac{\partial \eta}{\partial P} = \frac{AFS * N * \Sigma dv}{120 * \phi * \dot{M}_a * Q_f} \quad (A2.6)$$

$$\frac{\partial \eta}{\partial \phi} = \frac{AFS * N * \Sigma p dv}{120 * \phi^2 * \dot{M}_a * Q_f} \quad (A2.7)$$

$$\frac{\partial \eta}{\partial \dot{M}_a} = \frac{AFS * N * \Sigma dv}{120 * \phi * \dot{M}_a^2 * Q_f} \quad (A2.8)$$

$$\frac{\partial \eta}{\partial N} = \frac{AFS * N * \Sigma dv}{120 * \phi * \dot{M}_a * Q_f} \quad (A2.9)$$

Table 2.7 The uncertainties calculated using the methodology described in Eq. A2.4 to A2.9

BMEP (bar)	MEF (%)	IFCE (%)	U _{IFCE}
3.3	90	32.8	±1.64
	80	41.3	±2.07
	70	44.0	±2.20
	60	44.4	±2.22
	50	44.2	±2.21
5.5	90	42.1	±2.10
	80	44.7	±2.23
	70	45.7	±2.28
	60	45.5	±2.27
	50	43.5	±2.17

Similar uncertainties in the calculation of IFCE for each cycle can be considered. This indicates that the spread in variation of IFCE for all above cases remains more or less the same.

CHAPTER III
IMPACT OF LOW REACTIVITY FUEL TYPE ON PERFORMANCE, EMISSIONS
AND CYCLIC VARIATIONS IN DUAL FUEL LOW TEMPERATURE
COMBUSTION

3.1 Abstract

In dual fuel combustion, a low reactivity fuel (e.g., methane) is ignited by a higher reactivity fuel (e.g., diesel) in a compression ignition engine. Ensemble-averaged data are sufficient to explain overall behavior for conventional (stable) combustion with a low coefficient of variation of indicated mean effective pressure (COVIMEP). However, advanced combustion strategies such as reactivity-controlled compression ignition (RCCI) and low temperature combustion (LTC) have significant cyclic variations, especially at low loads, which cannot be completely understood with ensemble-averaged data. Characterizing cyclic variations is crucial not only for a better understanding of the combustion process in dual fuel combustion but also to further improve engine efficiency and reduce engine-out emissions. In this study, cyclic variations in dual fuel combustion with diesel ignition of three different low reactivity fuels (methane, propane, and gasoline) are examined. Experiments were performed on a single cylinder research engine (SCRE) at a low load of 5.1 bar indicated mean effective pressure (IMEP). The start of injection (SOI) of diesel was varied from 280 to 330 absolute crank angle degrees (CAD) at an interval of 10 CAD. Engine speed, rail pressure, and boost pressure were all

kept constant at 1500 RPM, 500 bar, and 1.5 bar, respectively. The energy substituted by the low reactivity fuel was fixed at 80 percent of the total energy input. It was found that diesel-methane (DM) and diesel-propane (DP) dual fuel combustion were affected by diesel mixing to a greater extent than diesel-gasoline (DG) dual fuel combustion due to the higher reactivity of gasoline. The magnitude of low temperature heat release was greatest for DG followed by DM and DP for all SOIs. The ignition delay for DG was the shortest, followed by DM and DP. DM and DP exhibited more cyclic variations than DG. Cyclic variations were analyzed by observing the start of combustion (CA5), combustion phasing (CA50), peak cylinder pressure (Pmax), indicated mean effective pressure (IMEP), maximum pressure-rise rate (MPRR), cumulative heat release (CHR), and cumulative gross heat release (GHR). Cyclic variations decreased for DM and DP when SOI was advanced; however, DG cyclic variations remained essentially constant for all SOIs. Earlier SOIs (280, 290, 300, and 310 CAD) for DM and (280, 290, and 300 CAD) for DP dual fuel combustion indicated some prior-cycle effects on the combustion and IMEP (i.e., some level of determinism). By comparison, all SOIs for DG combustion showed a greater probability for stochastic cyclic combustion variations. Finally, the challenges and opportunities in utilizing methane, propane, and gasoline in diesel ignited dual fuel combustion as well as strategies for mitigating cyclic variations were explored.

3.2 Introduction

Dual fuel engine combustion is defined by compression ignition of premixed fuel-air mixture, which is generally a low reactivity (low cetane) fuel, followed by the injection of fuel with higher reactivity (high cetane), which is used as an ignition source. There have been multiple studies performed on different fuel combinations for dual fuel

engine operation such as diesel-methane (DM) [1, 2], diesel-propane (DP) [3, 4], diesel-gasoline (DG) [5, 6], diesel-butane (DB) [7], and biodiesel-CNG (DCNG) [8]. The dual fuel combustion concept is not a recent endeavor, with one of the earliest studies of an engine operating with the dual fuel strategy performed by Riffkin [9] in 1937. Riffkin used town gas in a compression ignition engine, using liquid fuel as a source of ignition. Abundant research has led to improved technology within the field of dual fuel combustion, allowing for the concept to be a potential pathway to reduced engine-out oxides of nitrogen (NO_x) as compared to traditional diesel combustion [1, 10, 11, 12]. The dual fuel concept is not without its challenges, some of which include high cyclic variations and high engine-out hydrocarbons (HC), and carbon monoxide (CO) emissions [13, 14, 15, 16, 17]. Cyclic variations within the internal combustion (IC) engine have been apparent for several decades. Many studies have been performed on both the causes and the effects of these cyclic variations. Soltau [18] studied the cylinder pressure variations in a petrol engine and found that the in-cylinder pressure variation from one cycle to the next was influenced by slight changes in the air-fuel ratio. He also postulated that the fuel conversion efficiency could be increased if the variations from cycle to cycle were eliminated and if all cycles matched the most efficient cycle. Patterson [19] observed that in spark ignited (SI) engines the mixture velocity variation near the spark plug at ignition timing were primary causes of a cycle to cycle variation. One way to reduce such cycle to cycle variations at low loads is to accelerate the rate of combustion within the cylinder. Cole and Mirskey [20] studied the effects of mixture motion on the maximum pressure rise rate (MPRR) by using an air-propane jet in a constant volume cylindrical combustion chamber. Their findings concluded that the MPRR increases with

an increase in mixture jet intensity and that the maximum MPRR was observed for a jet profile with a slightly greater width than the spark plug gap. Barton et al. [21] used an empirical model to study cycle to cycle variations in an SI engine. The study finds that the maximum pressure variation from one cycle to another is affected by the time after ignition required to burn the first 5% of the fuel (CA5) as well as the phasing of the combustion process. A cyclic combustion literature review was performed by Young [22] for SI engines, wherein it is presented that for reduced cyclic variations inside the cylinder, better drivability, potentially better fuel economy, and lower emissions can be achieved. A summary of the parametric effects on cyclic variations within the cylinder, as well as a categorical extent to which these physical factors affect cyclic variations in SI engines, was presented. A swirl study with two separate spark locations in an SI single cylinder engine with a transparent piston crown was performed by Matekunas [23]. A major observation from this study was that the overall flow pattern within the cylinder determines the behavior of cyclic repeatability.

Multiple studies have regarded cyclic combustion in engines to be stochastic in nature [22-24]. Later studies [25-28], however, indicated that there may be some determinism present within the cyclic variations, which could be utilized to develop feedback-based control strategies. Wagner et al. [25] studied the effects of fuel/air ratio, swirl, and the start of injection (SOI) on a single cylinder research engine (SCRE) to gain insight on prior cycle effects within the cycle to cycle combustion dynamics. This was accomplished by using return maps, Shannon entropy, and symbol statistics. The findings indicate that the transition from stochastic behavior to deterministic behavior occurs with a change of equivalence ratio (ϕ) from stoichiometric to lean. Similarly, Daw et al. [26]

discussed the deterministic aspects of the cycle to cycle variations in SI engines operating under high exhaust gas recirculation (EGR) percentages and low equivalence ratio (ϕ) while also using an active control loop by changing the spark timing and the fuel delivery to control combustion stability. Agarwal [27] studied the effects of various parameters (e.g. engine speed and intake temperature) on cyclic variability in different homogenous charge compression ignition engines (HCCI). One finding from this study showed that the behavior of cyclic variations transitioned from stochastic to deterministic as the intake temperature was increased. Finney et al. [28] performed a detailed review of the cycle to cycle combustion variations within SI engines. The focus was to evaluate if cycle to cycle combustion variations has a deterministic structure, which can be used to control combustion. The detailed literature review suggested some type of deterministic feature in the cycle to cycle combustion is present when operating at a very low equivalence ratio (ϕ), high EGR, or any other global transition point.

Dual fuel combustion using diesel as the high reactivity fuel and liquid petroleum gas (LPG) or methane as the low reactivity fuel was studied by Selim [29]. The influence of various parameters such as engine load, compression ratio (CR), SOI of diesel, pilot fuel mass, and engine speed on cyclic combustion variation of dual fuel engines was researched. The study shows that the types of gaseous fuel, SOI, pilot fuel mass, CR, and engine speed all have effects on the cyclic variations. SOIs of 30-35 degrees before top dead center (BTDC) showed minimum cyclic variations, and the variations decrease as the engine speed was increased. Diesel-LPG dual fueling showed higher combustion noise compared to DM. Sun et al [30] studied cyclic variations in diesel-gasoline dual fuel combustion in a medium duty diesel engine. One hundred fifty consecutive cycles

worth of data were taken and showed that parameters such as spray penetration of the diesel, in-cylinder charge motion, fuel air ratio and SOI of the diesel affect the in-cylinder pressure variations. Srinivasan et al. [14] studied cyclic combustion variation in DM dual fuel engine and distinguished fast burn cycles and slow burn cycles based on maximum in-cylinder pressure (P_{MAX}), the crank angle where maximum pressure occurs (CAP_{MAX}) and phasing for 50% mass burnt fraction of charges (CA₅₀). They found cycles with CA₅₀ closer to top dead center (TDC), higher P_{max}, and CAP_{max} away from TDC were fast burned cycles. Conversely, slow burn cycles are identified by CA₅₀ phased away from TDC, reduced P_{max} values, and CAP_{max} phased further from TDC. Wang et al. [31] performed a cyclic variations study on methanol fumigated diesel engine and found that at low load, cyclic variations decrease with higher intake temperature but at high load cyclic variations increase when intake temperature exceeds 75 °C. Three different methanol injection locations in diesel methanol dual fuel engines were studied by Chen et al. [32]. It was discovered there was less variation in combustion when methanol injection is performed in the inlet manifold and inlet duct distal end, compared to the inlet duct near its end. Jamrozik et al. [33] performed experiments on a compression ignition (CI) engine where diesel was injected inside the cylinder and alcohol fuels (methanol and ethanol) were fumigated into the intake manifold. Two hundred consecutive engine cycles were analyzed, and it is concluded that the cyclic variability of a dual fuel engine increased when the energy fraction of alcohol fuel was increased from 20% to 50%. Jha et al. [12] studied DM dual fuel combustion at two different loads and found that the variation in CA₅₀ is caused due to variations in CA₅, chemical kinetics, and mixing inside the cylinder.

To investigate cyclic combustion variations, computation fluid dynamic (CFD) simulations have been utilized by some researchers [34,35] to get more insight into the phenomena. Klos et al. [34] used thousands of CFD simulations in parallel to map operating zones, which were later utilized to create a statistical model that can run hundreds of cycles in series quickly to represent cyclic combustion variations. Fluctuations in trapped gas temperature, port fuel injection (PFI) mass, direct injection (DI) mass and EGR quantity were found to be the main sources of combustion variations from one cycle to another. Similarly, Jupudi et al. [35] performed a CFD study running several cycles in parallel by changing the operating condition at the start of the simulation and used a statistical model to evaluate cyclic variation. It was postulated that to clearly quantify cycle to cycle variations in a natural gas-diesel dual fuel engine, the effects of natural gas stratification and shot to shot variation in diesel injection would also need to be studied.

3.3 Objective of the present work

As evident from the literature review, the nature of cyclic variations in both SI and dual fuel engines have been studied by several researchers. The current paper addresses a crucial knowledge gap in the open literature:

characterization of the impact of low reactivity fuel type on cyclic variations in dual fuel low temperature combustion (LTC). We present a simultaneous comparison of cyclic variations between dual fuel LTC with diesel-methane (DM), diesel-propane (DP), and diesel-gasoline (DG) combinations on the same engine platform under similar operating conditions. All engine operating conditions such as intake temperature, intake pressure, engine load and speed are maintained constant. Diesel fuel injected quantities

are comparable at all operating conditions; therefore, at the same SOI, it can be posited that the fluid dynamic effects responsible for diesel dispersion in the cylinder are similar for DM, DP and DG dual-fuel LTC. Any observable differences in engine combustion and performance are then dictated by the reactivities and chemical properties of the low reactivity fuel (methane, propane, and gasoline) used. The main objectives of this work are to:

1. Investigate the effect of reactivities of different low-reactivity fuels on average and cyclic combustion at different diesel SOIs
2. Compare cyclic variations of a dual fuel engine operation at low load for various diesel SOIs with methane, propane, and gasoline as the low reactivity fuels
3. Characterize the challenges and opportunities that these fuel combinations present and present possible strategies to mitigate cyclic combustion variations for each fuel combination

3.4 Experimental setup

A 1.8-liter single cylinder research engine (SCRE) was used for the experimental work presented in this paper. A detailed list of engine specifications is given in Table 1. A detailed schematic of the engine setup on the testbed is given in Figure 3.1. The engine was connected to a 250 HP AC dynamometer and used a Dyne Systems Inter-Loc V to control speed. The torque, and therefore the load, of the engine, was controlled by changing the fueling rate of the engine. With the engine being operated in a dual fuel operating mode, it is important to be able to both control the amount of both fuels being supplied to the engine. To control the gaseous (methane, propane, gasoline) fueling rate

into the intake manifold, the use of an electronic needle valve from Hanbay Inc. (Model MCM-50AB) was used. Diesel fuel was injected directly into the cylinder through a solenoid injector, which was connected to a Bosch CP3 common rail system. The injection event (timing, duration, and pressure) was controlled via a DRIVEN (National Instruments) stand-alone diesel injection (SADI) driver, which was coupled to National Instruments' CALVIEW software. Pressurized air was supplied to the engine using an Atlas Copco (Model GA75) external air compressor which, before entering the engine, was conditioned using an Atlas Copco heatless desiccant dryer (Model CD 250).

In cylinder pressure was measured using a Kistler model 6052C pressure sensor coupled with a Kistler 5010B type charge amplifier. The injector was fitted with a Hall-effect needle lift sensor from Wolff Instruments. A 0.1 crank angle degree (CAD) resolution BEI shaft encoder (Model XH25D-SS-3600-ABZC-28V/V-SM18) was used to phase both the in-cylinder pressure trace as well as the needle lift with respect to CAD. Various crank angle conventions exist throughout the literature, but for the purposes of this paper the absolute crank angle convention will be used, meaning that 0° refers to gas exchange TDC, and 360° refers to compression TDC. One thousand consecutive engine synchronous data cycles were collected for DM and DP combustion, and 100 consecutive cycles were collected for DG. Figure 3.2 (a) shows COV_{IMEP} for DG at various diesel SOIs for 100 consecutive cycles. Figure 3.2 (b) shows COV_{IMEP} of DM and DP at early and late diesel SOIs for 100, 300, 500, and 1000 consecutive cycles, and Figure 3.2 (c) shows COV_{IMEP} of DM and DP at early and late diesel SOIs for 100 consecutive cycles. DG combustion for diesel SOIs from 280 to 330 CAD has low COV_{IMEP} . From Figures 3.2(b) and 3.2(c) it is clear that for low COV_{IMEP} , the behavior of data from 100

consecutive cycles is similar to the behavior of data from 300, 500, and 1000 consecutive cycles. Therefore, for DG dual fuel combustion cases with low COV_{IMEP} , a dataset of 100 consecutive cycles was considered statistically significant to adequately represent cyclic variations. Intake pressure was measured using a Setra (Model 209) absolute pressure sensor, which was then used to peg the cylinder pressure at intake valve closing (IVC). In a similar fashion, steady state (asynchronous) engine data were collected and averaged over a duration of 60 seconds. Further information on sensors used and their accuracies are provided in Table 2.

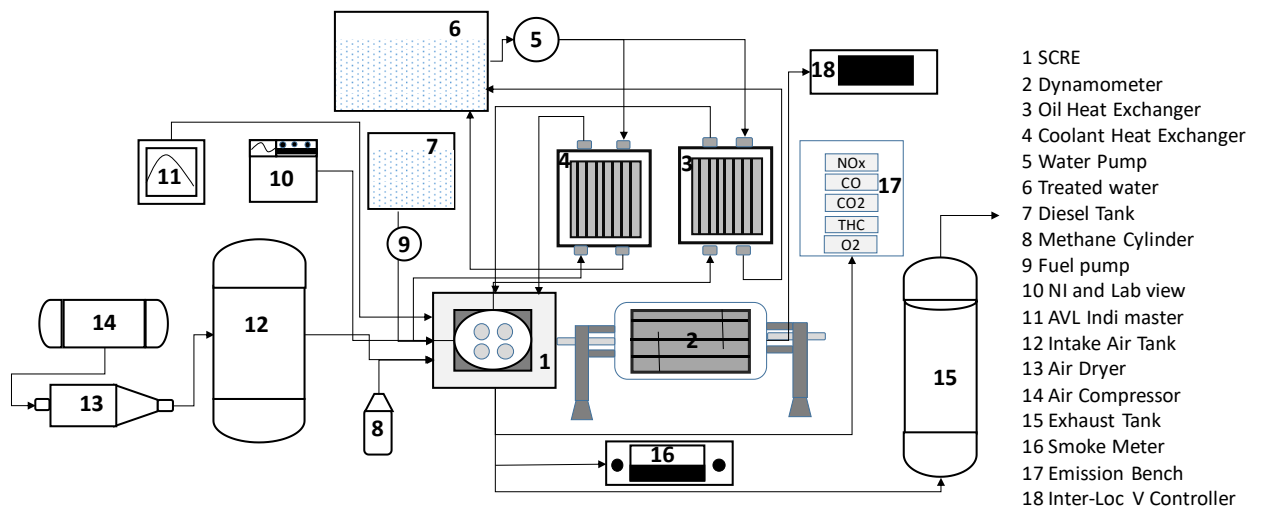


Figure 3.1 Experimental setup of the single cylinder research engine [12].

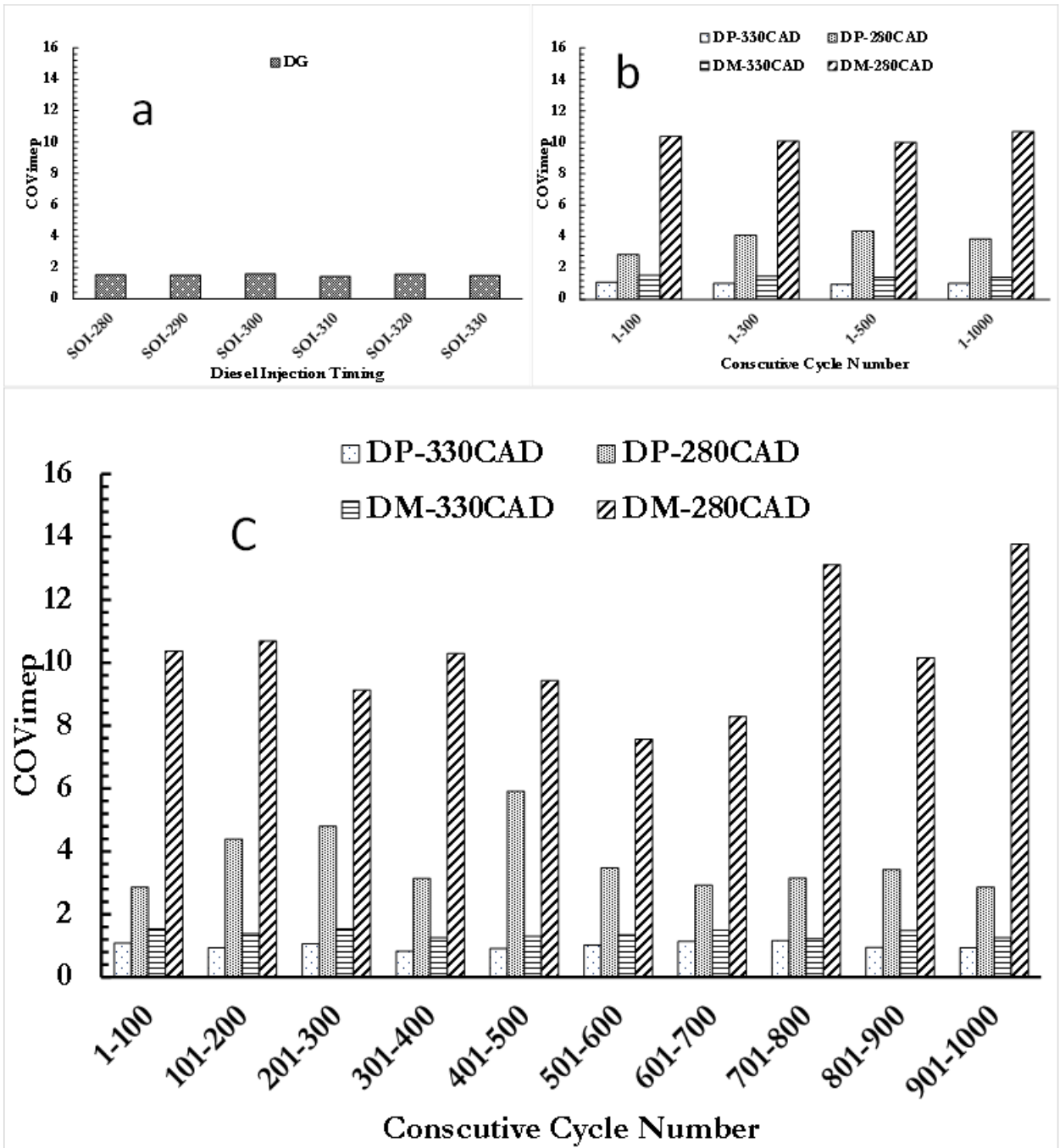


Figure 3.2 (a) COVIMEP for DG combustion at various SOIs, (b) COVIMEP for DM and DP combustion at 280 and 330 CAD SOIs for 100, 300, 500 and 1000 consecutive cycles, (c)-COVIMEP for DM and DP combustion at 280 and 330 CAD SOIs at 100 cycle data intervals.

Table 3.1 Engine Specifications (0° refers to gas exchange TDC, 360° refers to compression TDC).

Parameter	Value
Engine type	Single cylinder research engine, compression-ignition
Bore × Stroke	128 mm × 142 mm
Connecting rod length	228 mm
Displaced volume	1827 cm ³
Compression ratio (nominal)	17.1: 1
Intake valve opening	32°
Intake valve closing	198°
Exhaust valve opening	531°
Exhaust valve closing	14°
Diesel fuel injection system	CP3 Bosch common rail
Low cetane fuel injection system	Fumigation into intake manifold
Maximum speed	1900 rpm
Injector hole diameter	0.197 mm

Table 3.2 Details of experimental sensors and their accuracies.

Data Type	Make/Model	Type	Unit	Accuracy
Temperature intake, exhaust, etc.	Omega	K-type	°C	±0.75% of reading
Air mass flow	Flowmaxx	Sonic orifice	kg/h	±0.1% of reading
Diesel mass flow	Micro Motion	Coriolis	kg/h	0.35% of reading
Methane mass flow	Micro Motion	Coriolis	kg/h	0.56% of reading
Smoke	AVL 415S	Filter	FSN	0.001 of reading
NOx and NO	ESA EGAS 2M	CLD	ppm	<1% of full scale
THC	ESA EGAS 2M	FID	ppm	<0.5% of full scale
CO	ESA EGAS 2M	NDIR	%	<1% of full scale
CO2	ESA EGAS 2M	NDIR	%	<1% of full scale
O2	ESA EGAS 2M	MPA	%	<1% of full scale
Cylinder pressure	Kistler 6052C	Piezoelectric	bar	±0.005 of reading
Pressures (intake)	Setra Model 209	Capacitance	psig	±0.25% of full scale

3.5 Experimental procedure

For DM, DP, and DG dual fuel combustion, a diesel SOI sweep was performed from 280 to 330 CAD in 10 CAD increments at 5.1 bar indicated mean effective pressure (IMEP). For all of these experiments, several parameters were held constant: an engine speed of 1500 RPM, a rail pressure of 500 bar, a boost pressure of 1.5 bar, and a primary fuel energy fraction (methane, propane, gasoline) of 80%. Operating conditions are summarized in Table 3 and fuel properties are summarized in Table 4.

Table 3.3 Details of experimental sensors and their accuracies.

Parameter	Value
Engine speed (rpm)	1500
Engine load (bar)	5.1 (IMEP)
Rail pressure(bar)	500
Boost pressure (bar)	1.5
Low reactivity fuel (methane/propane/gasoline) energy fraction (%)	80
Start of injection (CAD)	280-330 (at an interval of 10CAD)
Intake manifold temperature (°C)	35 ± 5
Oil temperature (°C)	80 ± 5
Coolant temperature (°C)	80 ± 5
EGR	0 %

Table 3.4 Fuel properties [36,37,38]

Parameters	Methane	Propane	Gasoline	Diesel
Chemical formula	CH ₄	C ₃ H ₈	C _n H _{1.87n}	C _n H _{1.8n}
Molecular weight	16	44	~100	~170
Lower heating value (MJ/kg)	50	46.4	43	42.7
Stoichiometric air-to-fuel ratio	17.23	15.67	14.6	14.5
RON	120	112	91-99	
Cetane number	-	-	-	~45
Flammability limits vol. % of gas in air)				
Upper	15	9.5	7.6	7.5
Lower	5	2.2	1.4	0.6

Different combustion parameters used in this paper such as percentage energy substitute (PES), equivalence ratio, combustion efficiency (η_c), apparent heat release rate (AHRR), and specific heat ratio (γ), etc. are defined below.

$$PES = \frac{\dot{m}_{LRF}LHV_{LRF}}{\dot{m}_dLHV_d + \dot{m}_{LRF}LHV_{LRF}} \quad (3.1)$$

$$\Phi = \frac{\left(\frac{A}{F}\right)_{st-tot}}{\left(\frac{\dot{m}_a}{\dot{m}_d + \dot{m}_{LRF}}\right)} \quad (3.2)$$

Equations 3.1 define PES. In Equations 3.1, \dot{m} refers to the mass flow rates of diesel (subscript “d”), low reactivity fuel (subscript “LRF”), and air (subscript “a”), and LHV refers to the corresponding fuel lower heating values. In Equation 3.2, the stoichiometric air required for complete oxidation of both diesel and methane into CO₂ and H₂O is defined as the stoichiometric air-fuel ratio $\left(\frac{A}{F}\right)_{st-tot}$. Therefore, $\left(\frac{A}{F}\right)_{st-tot}$ is dependent on the PES.

$$\eta_c = 1 - \frac{\sum_i x_i Q_{LHV_i}}{\left(\frac{\dot{m}_f}{\dot{m}_f + \dot{m}_a}\right) Q_{LHV_f}} \quad (3.3)$$

Equation 3.3 defines the combustion efficiency. Heywood [36], uses exhaust concentrations of CO, HC, H₂, and PM emissions and their respective lower heating values to calculate combustion efficiency. As gravimetric PM is not measured for these experiments (since they are likely very low as indicated by the low FSN values), only the measured CO and HC concentrations and H₂ mass fractions are calculated from stoichiometric calculations are used to determine the combustion efficiency. In Equation 3.3, x_i are the mass fractions of HC, CO, and H₂. Q_{LHV_i} are their respective lower heating values, and subscripts “f” and “a” denote fuel and air, respectively. According to Heywood [36], fuel LHV can be used as an LHV of HC in the calculation of combustion efficiency in Equation 3. For DM dual fuel engine, diesel and methane combined fraction weighted LHV (i.e., a mass-fraction-weighted average of 42.6 MJ/kg for diesel and 50 MJ/kg for methane) of these two fuels are used for LHV of HC in equation 3. For DP dual fuel engine, combined fraction weighted LHV (i.e., a mass-fraction-weighted average of 42.6 MJ/kg for diesel and 46.4 MJ/kg for propane) of these two fuels are used for LHV of HC in equation 3.3. Similarly, for DG dual fuel engine, combined fraction weighted LHV (i.e., a mass-fraction-weighted average of 42.6 MJ/kg for diesel and 43.4 MJ/kg for gasoline) of these two fuels are used for LHV of HC in equation 3.3. The lower heating values for CO and H₂ are assumed to be 10.1 MJ/kg and 120 MJ/kg, respectively.

$$AHRR(\theta) = \frac{\gamma}{\gamma-1} P \frac{dV}{d\theta} + \frac{1}{\gamma-1} V \frac{dP}{d\theta} \quad (3.4)$$

$$\gamma(T) = 1.375 - 6.99 \times 10^{-5}T \quad (3.5)$$

$$MPRR = \left(\frac{dp}{d\theta} \right)_{max} \quad (3.6)$$

$$COV_{imep} = \left(\frac{\sigma_{imep}}{\mu_{imep}} \right) \quad (3.7)$$

$$IFCE = \frac{IP}{\dot{m}_d LHV_d + \dot{m}_{PF} LHV_{PF}} \quad (3.8)$$

$$M_{Res} = \left(\frac{P_{EVC} * V_{EVC}}{T_{exhaust} * R_{EVC}} \right) \quad (3.9)$$

$$M_{IVC} = M_{Res} + M_a + M_{PF} \quad (3.10)$$

$$Normalized\ IMEP\ (n) = \frac{IMEP(n)}{[Max(IMEP(n=1....1000))]} \quad (3.11)$$

$$Normalized\ CHR\ (n) = \frac{\int_{\theta=SOI}^{\theta=EOI} AHRR(n)d\theta}{[Max(\int_{\theta=SOI}^{\theta=EOI} AHRR(n=1....1000)d\theta)]} \quad (3.12)$$

AHRR is calculated using Equation 3.4 [36] and γ was determined using Equation 3.5 based on global in-cylinder temperature (T), estimated by Gatowski's model [39]. Li [40] found γ estimation results by Gatowski's model closest with reference mode than Egnell's model [41] and Brunt's model [42]. Engine geometry values such as compression ratio, bore, stroke, and connecting rod length coupled with engine crankshaft position measurements were used to calculate instantaneous volume (V). The rate of change of volume with respect to crank angle (dV/d Θ) was calculated using crank angle-resolved instantaneous volume data and the rate of change of pressure with respect to crank angle (dP/d Θ) was calculated using crank angle-resolved cylinder pressure data.

For cyclic data, cylinder pressure data for each cycle was smoothed using a 2nd order low pass Butterworth filter with a cutoff frequency of 2610 Hz. Equation 3.6 defines the maximum pressure rise rate and is the maximum value of the rate of change of pressure with respect to the crank angle ($dP/d\Theta$). Equation 3.7 provides a coefficient of variation of IMEP and is calculated over 1000 cycles in this study. In equation 3.8 σ represents the standard deviation in IMEP and μ represents the mean of IMEP. Equation 3.8 defines indicated fuel conversion efficiency (IFCE) and IP is indicated power. Equation 3.9 is employed to calculate residual gas inside the cylinder. P_{EVC} , V_{EVC} and R_{EVC} are pressure, instantaneous volume and gas constant at Exhaust valve closing. Assuming in-cylinder temperature and exhaust temperature are the same when the exhaust valve closes, the exhaust temperature is used as In-cylinder temperature at the exhaust valve closing in Equation 3.9. MIVC in Equation 3.10 is trapped mass and is calculated using the mass of air inside the cylinder (M_a), mass of primary fuel inside the cylinder (M_{PF}) and residual mass inside the cylinder (M_{Res}). Equation 3.11 and 3.12 define normalized IMEP(n) and CHR(n) of the nth cycle respectively.

3.6 Result and discussion

3.6.1 Ensemble-Averaged Results

Figures 3.3(a-d) represent average pressure and AHRR curves for DM, DP and DG combustion at diesel SOIs of 280, 310, 320, and 330 CAD. The SOI of 280 CAD represents the most premixed combustion process (approaching “HCCI-like” combustion) within this SOI range, the SOI 310 CAD represents dual fuel low temperature combustion (DFLTC), and 320 and 330 CAD SOIs represent partially premixed combustion (PPC). As posited earlier, fluid dynamics effects are similar, and

the diesel injected quantities are comparable for the same diesel SOIs for different low reactivity fuels. Therefore, the major factor responsible for differences in combustion is likely the chemical behavior of the corresponding low reactivity fuel (methane, propane, and gasoline).

The combustion process can be generalized for dual fuel combustion for different types of fuels. For all cases studied in this paper, the temperature and pressure at SOI are too low for diesel to auto ignite. Due to the fact that this is a low swirl engine [43] entrainment and subsequent mixing of the premixed fuel-air mixture into the diesel spray are driven by the diesel jet momentum. Therefore, there is more time available for diesel injected at 280 CAD SOI (compared to 330 CAD SOI) before temperature, pressure, and local equivalence ratios are amenable for autoignition. Since diesel is a two-stage ignition fuel, depending on the behavior of the low reactivity fuel, the low temperature ignition (or LTHR) is either exhibited or suppressed. A distinct LTHR is not observed for 330 CAD SOI for all three low-reactivity fuels. This may be due to reduced time available for diesel to disperse inside the cylinder before temperature and pressure that favor high temperature heat release are met. On the other hand, a distinct LTHR is exhibited for diesel-gasoline combustion for diesel injection timing of 280, 310, and 320 CAD, indicating that gasoline has little or no effect on low temperature diesel ignition. By contrast, very little or no LTHR is exhibited for DP dual fuel combustion for 280, 310, and 320 CAD, indicating that propane suppresses low temperature diesel ignition. Methane clearly shows LTHR for 320 CAD but little or no LTHR for 280 and 310 CAD, indicating methane also suppresses diesel LTHR at the earlier SOIs. Another interesting phenomenon is the change in AHRR shape observed from 320 CAD SOI to 330 CAD

SOI, irrespective of the low reactivity fuel used. While additional analysis is required to fully explain this phenomenon, it may be attributable to the change in diesel distribution inside the cylinder before in-cylinder conditions favor high temperature diesel autoignition.

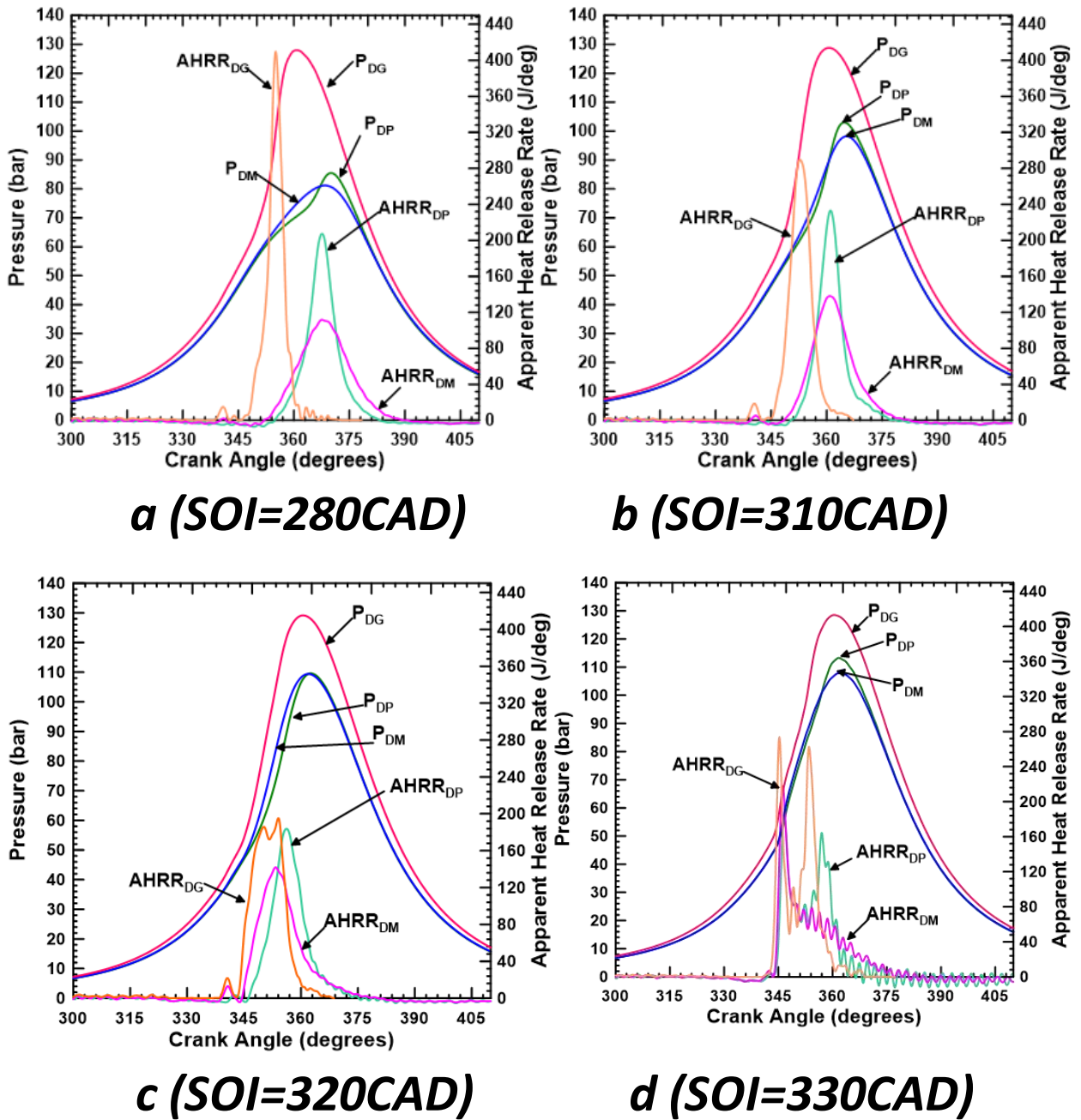


Figure 3.3 3(a-d). Average in-cylinder pressure and AHRR histories for DM, DP, and DG combustion at various SOIs and 5.1 bar IMEP, N=1500 rpm, diesel injection pressure = 500 bar, PES of 80%.

Figure 3.4(a) and 3.4(b) shows MPRR, COV_{IMEP} , and CA50 for DM, DP, and DG dual fuel combustion at several diesel SOIs. To explain engine performance characteristics clarification on how the change in diesel SOIs will impact diesel ignition sources is needed. For diesel SOI 280 there is a long time for diesel to mix with the air/low-reactivity fuel environment. This leads to a less stratified charge at the time when the charge is ready for combustion (i.e. ignition). For diesel SOI 330, however, there is less time to mix, leading to a more stratified charge at the time of ignition and therefore more ignition sources. This transition is gradual over the diesel SOI sweep from 280 to 330. For DG combustion COV_{IMEP} remains more or less constant but for DM and DP, COV_{IMEP} decreases as the diesel SOI is moved towards TDC. This indicates that for DG dual fuel combustion even a small amount of ignition source is sufficient to have better combustion. DP combustion has high COV_{IMEP} for 280 and 290 CAD diesel SOIs, indicating a small amount of ignition source is not sufficient for robust combustion, leading to more variation. DP combustion, therefore, requires both a stronger ignition source and a higher number of ignition sources for stable combustion when compared to DG dual fuel combustion. For DM, except 330 and 320 CAD diesel SOIs, there is high COV_{IMEP} . This suggests that to have stable DM dual fuel combustion, both a stronger ignition source and a larger number of ignition sources are required. For similar strength and similar amount of diesel ignition sources, It can be said that it is more difficult to combust methane compared to propane and gasoline. MPRR for DM and DP combustion increases as the diesel SOI is shifted from 280 to 330 CAD while MPRR mostly decreases for DG combustion. Increases in MPRR from DM and DP dual fuel combustion can be attributed to the fact that as the diesel SOI is shifted from 280 to 330

CAD the number of ignition sources increases leading to faster combustion causing higher MPRR. Another reason for the increase in MPRR can be found within the CA50 plots. For DM and DP dual fuel combustion, as the diesel SOI shifts from 280 to 330 CAD, a corresponding advance in CA50 occurs, CA50 advances, and even occurs before TDC for the latest injection timings, leading to higher MPRR values. The trend for MPRR of DG can also be explained with CA50 trends. For all diesel SOIs tested, CA50 occurs before TDC. CA50 advances as diesel SOIs are shifted from 280 to 320 CAD leading to a decrease of MPRR; however, as the injection timing is further delayed from 320 to 330 CAD, CA50 retards towards TDC leading to a slight increase in MPRR.

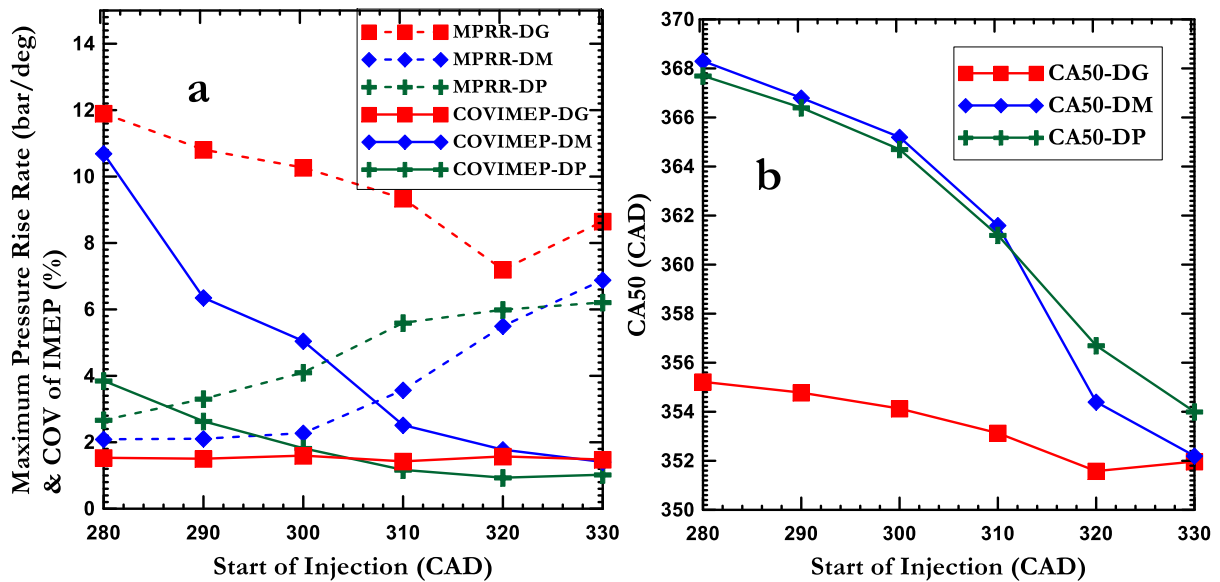


Figure 3.4 (a). Maximum pressure rise rate and COV of IMEP (b). CA50 variation at varying SOI for 5.1 bar IMEP, N= 1500 rpm, diesel injection pressure=500 bar, PES =80% for DM, DP and DG dual fuel combustion.

Figure 3.5(a) and 3.5(b) shows combustion efficiency and indicated fuel conversion efficiency for DM, DP, and DG dual fuel combustion at several diesel SOIs.

Combustion efficiency is insensitive to diesel SOI for DG dual fuel combustion; however, it increases monotonically for DP and first increases and then steadies out for DM dual fuel combustion as diesel SOI is retarded. These trends indicate that DG dual fuel combustion is not affected by relative diesel stratification introduced by changing diesel SOI. Whereas DP dual fuel combustion becomes progressively better with diesel SOI retardation indicating that increasing diesel stratification aids combustion efficiency. A more or less similar trend to DP is observed for DM dual fuel combustion. Indicated fuel conversion efficiency (IFCE) is consistently highest for DP, followed by DG and then DM dual fuel combustion at all diesel SOIs investigated. This is a counterintuitive trend, i.e., an increase in combustion efficiency is not always accompanied by an increase in IFCE. This is explained by combustion phasing or CA50 trends. For the DG case at all diesel SOIs CA50 occurs before TDC. This leads to excessive heat transfer losses near TDC, which leads to a reduction in IFCE. For the DP and DM cases, IFCE seems to be affected by both combustion efficiency a CA50 location. For example, at SOIs advanced beyond 310 CAD, the combustion efficiencies are relatively lower; however, CA50 location is favorable; thereby balancing out IFCE. Similarly, at diesel SOIs retarded beyond 310 CAD, combustion efficiencies are higher, however, CA50 occurs before TDC, which again seems to balance out IFCE.

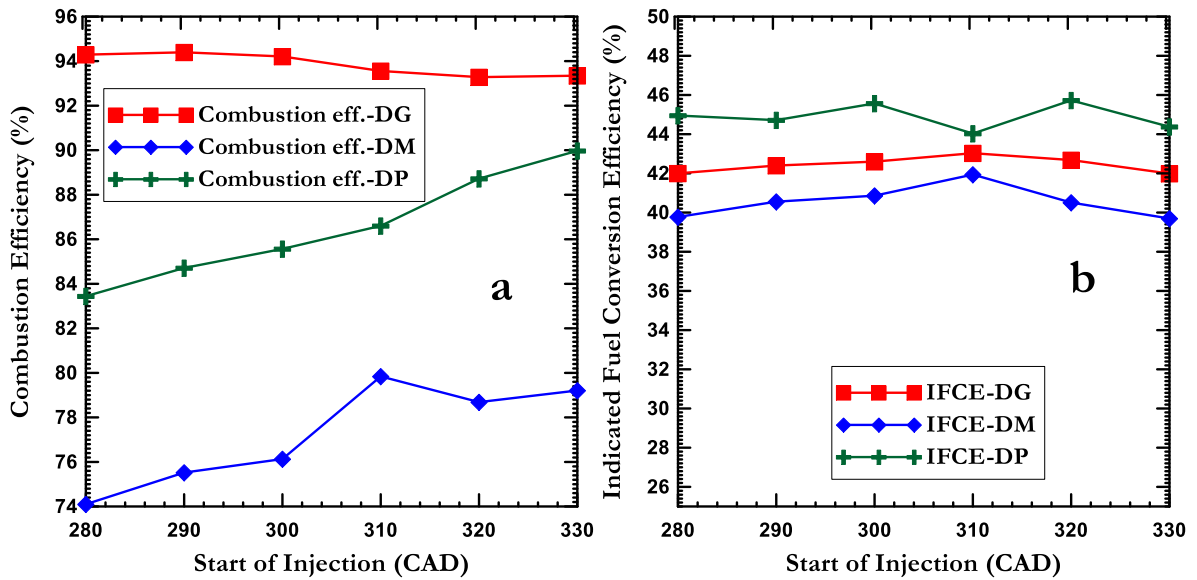


Figure 3.5 (a). Combustion efficiency (b). Indicated fuel conversion efficiency variation at varying SOI for 5.1 bar IMEP, N= 1500 rpm, diesel injection pressure=500 bar, PES =80% for DM, DP and DG dual fuel

Figure 3.6(a) shows ISHC and ISCO trends for DP, DM, and DG dual fuel combustion as a function of diesel SOI. At all SOIs ISHC is highest for DM followed by DP and DG dual fuel combustion. This indicates that the reactivity of the low-reactivity fuel clearly influences engine-out HC emissions. For instance, at 310 CAD, DM combustion has the longest ignition delay. This indicates that all conditions being the same, methane tends to impede diesel reactivity compared to propane and gasoline. As a result, ensuing diesel autoignition centers do not cascade into combusting fronts in the combustion chamber. Therefore, methane is either partially oxidized into CO or remains unreacted in the cylinder, especially at low loads. This manifests as high engine-out HC emissions. Clearly, the scenario is different with propane and gasoline, which are relatively more reactive compared to methane; and therefore have a higher likelihood of

being oxidized. As explained by Krishnan et. al [44], the reason for ISCO from combustion chamber can be attributed to lack of OH radicals, insufficient mixing between high temperature and low temperature regions, insufficient time available for CO oxidation. Consider the ISCO emissions trends for DM cases. At all diesel SOIs there are insufficient OH radicals produced due to the low combustion temperatures; therefore, the primary CO oxidation pathway is unsupported due to lack of OH radicals. Therefore, the only mechanism to oxidize $\text{CO} \rightarrow \text{CO}_2$ is through the slower pathway, which is supported by higher bulk gas temperatures, which occurs at retarded diesel SOIs, e.g., 330 CAD. A similar trend is observed for DP cases; however, with an interesting difference. For diesel SOIs between 280 and 310 CAD CO emissions are higher than HC emissions, but, after 310 CAD the CO emissions are lower than corresponding HC emissions. This is because of the reactivity of propane, i.e., propane or fuel oxidation is faster than CO oxidation at lower temperatures at advanced injection timings, however, as injection timing is retarded, CO oxidation takes preference since it is supported by the higher bulk temperatures as explained before. For the DG case CO emissions are observed to increase when diesel SOI is retarded from 280 to 330 CAD. This is because CA50 occurs earlier and this results in a competition between CO oxidation charge cooling due to cylinder expansion, which freezes CO chemistry.

Figure 3.6(b) shows ISNOx emissions for DG, DM, and DP dual fuel combustion. ISNOx emissions increases with the shift in diesel SOIs from 280 to 330 CAD for DM, DP, and DG dual fuel combustion. This may be attributed to the fact that with a shift in diesel SOIs from 280 to 330 CAD, diesel becomes more stratified leading to diesel autoignition to occur at higher diesel phi leading to higher local temperatures forming

more NOx. ISNOx level is very low for all three DM, DP, and DG dual fuel combustion for diesel SOI 280 to 310 due to better mixing leading to lean diesel air mixture at time of combustion resulting in lower local temperature. Higher ISNOx for 330 diesel SOI for DM and DG compared to DP is due to the fact that the amount of diesel injected to obtain the same engine out load is higher for DM and DG compared to DP as indicated fuel conversion efficiency of DP combustion is better than DM and DG cases. It is to be noted that for all SOIs investigated engine-out soot emissions were low, and therefore not discussed. With this understanding of DM, DP, and DG dual fuel combustion based on ensemble-averaged data, a more detailed analysis of the cyclic variations associated with DM, DP, and DG dual fuel combustion is presented in the following sections.

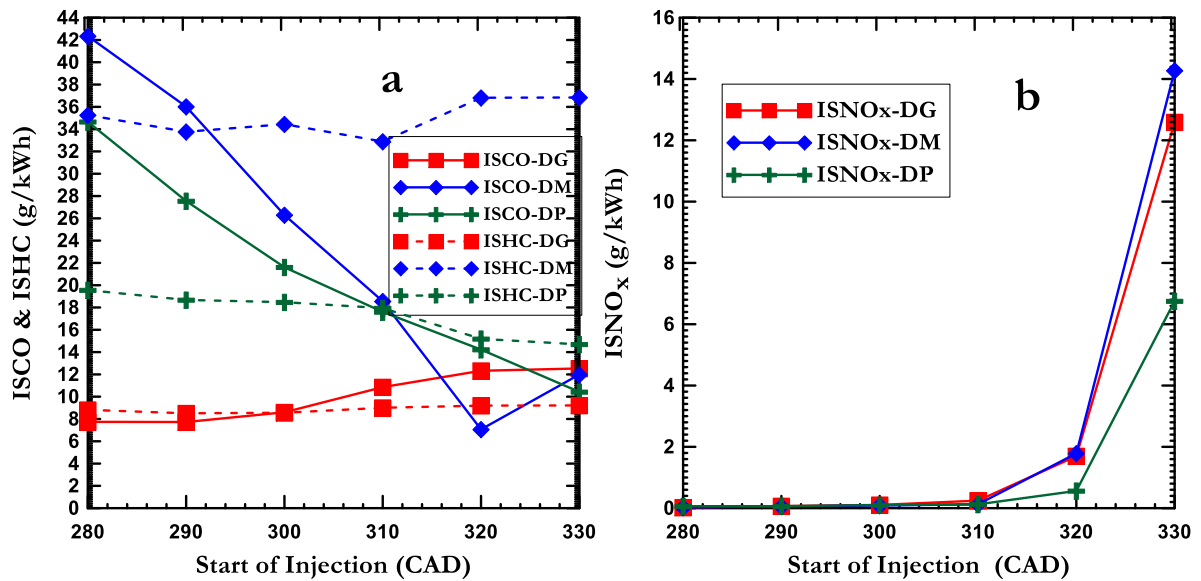


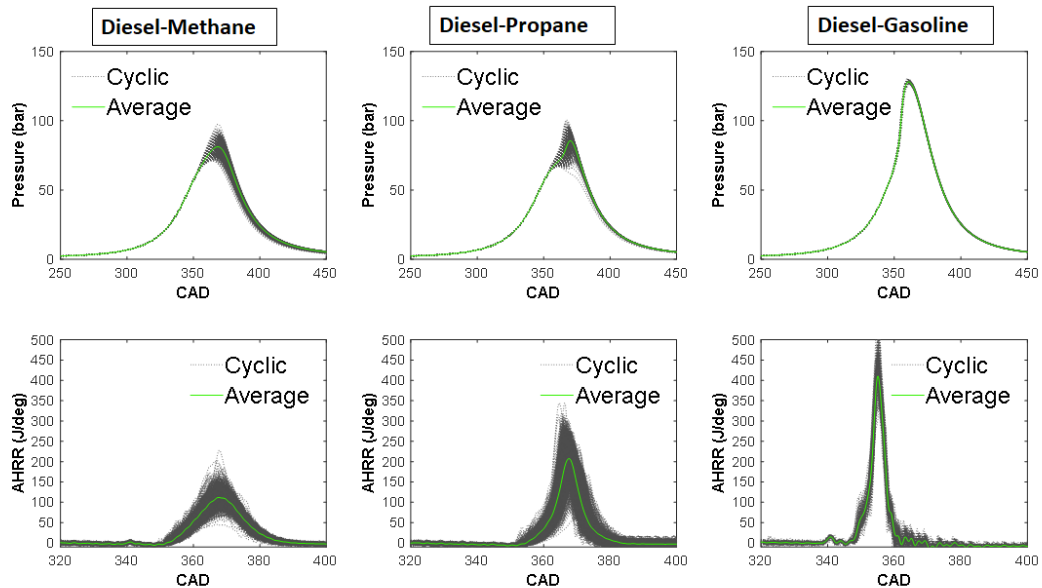
Figure 3.6 (a).ISCO and ISHC (b). ISNO_x variation at varying SOI for 5.1 bar IMEP, N=1500 rpm, diesel injection pressure=500 bar, PES =80% for DM, DP and DG dual fuel

3.6.2 Cyclic In-Cylinder Pressure and AHRR Results

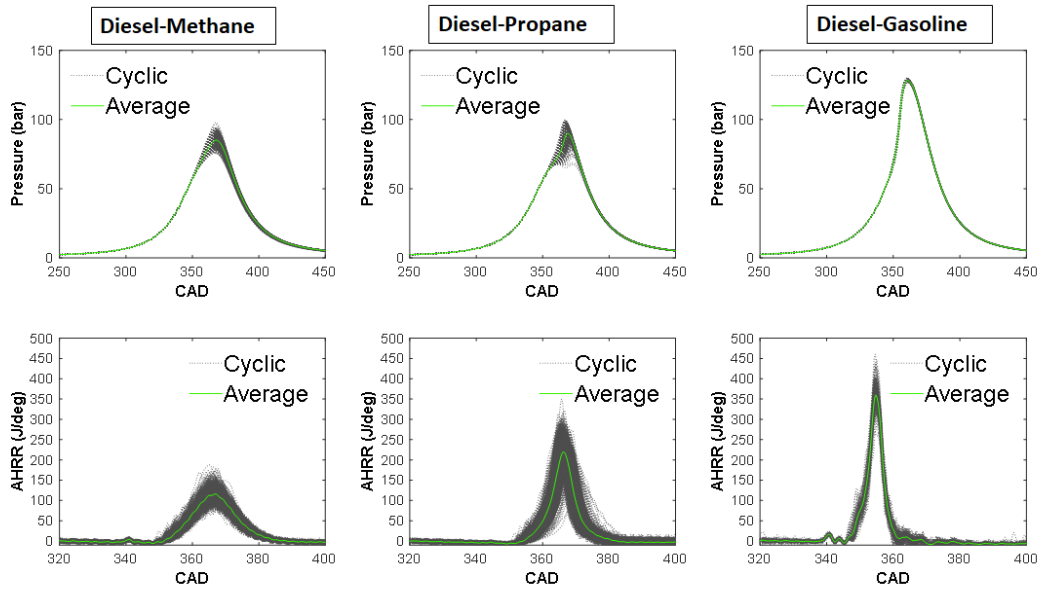
Cyclic pressure and AHRR traces are shown in Figures 3.7 (a-f) for DM, DG, DP dual fuel combustion. Again, engine speed and load were fixed at 1500 rpm and 5.1 bar IMEP, respectively, and the PES value was 80% for all fuel combinations. The only parameter that was allowed to change (apart from the fuel itself) was the diesel SOI, which ranged from 280 to 330 CAD. At the same SOI across all three fueling combinations, the magnitude of peak pressure is greatest for DG, followed by DP and DM in that order. This is an indicator of how well the spatially dispersed diesel autoignition centers are able to activate the surrounding fuel-air mixture, with gasoline being the best of the fuels tested at sustaining continued activation from the diesel ignition centers. Similarly, for the same injection timing across all three fueling combinations, it can be seen that there is very little cyclic variation in the expansion phase of the pressure trace for DG and DP as opposed to DM combustion. It should be noted that there is significant cyclic variation during the combustion phase of diesel-propane combustion. The minimal cyclic variation in the expansion further suggests that it is easier for spatially distributed ignition centers to sustain combustion into the surrounding fuel-air mixture of DG and DP opposed to DM combustion. Another interesting phenomenon is that, when SOI is retarded, the second stage of combustion is dominant in DG first followed by DP. These trends are consistent with the fact that gasoline is more reactive than propane followed by methane. For 330 CAD SOI, there are two distinct peaks in the AHRR trace for DG and DP; this suggests that combustion is likely sustained well after the mass of diesel has been consumed within the cylinder, owing to the higher reactivity of these fuels. No such phenomenon occurs with the DM,

indicating that combustion is hard to sustain in the lean ϕ_{Methane} environment. It can also be seen that the cyclic variations of DG combustion remain more or less constant with varying SOI. Cyclic variations in DM and DP, however, decrease as SOI is retarded from 280 CAD to 330 CAD.

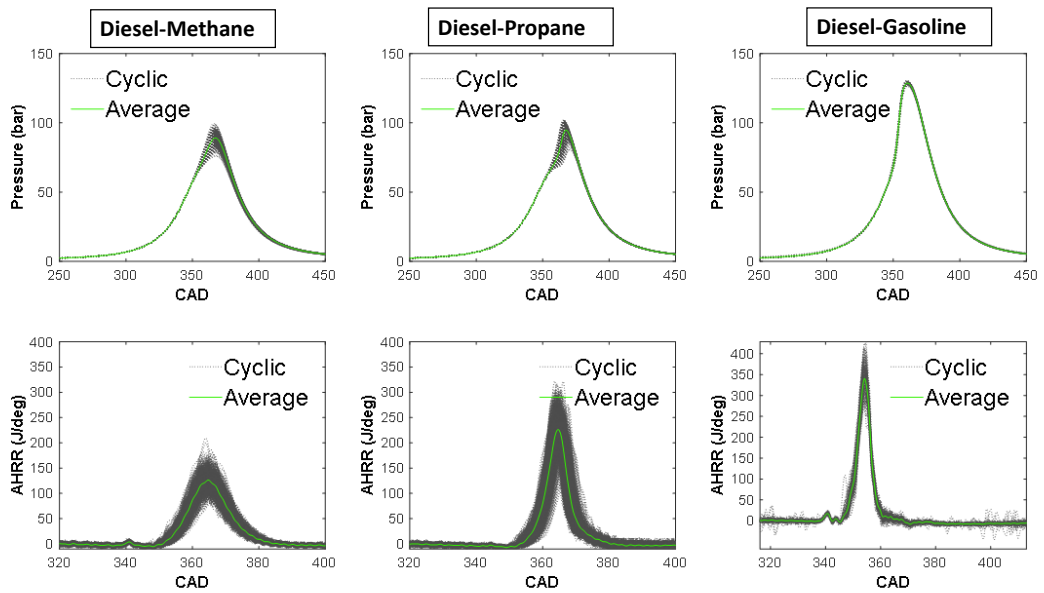
Distinct LTHR and high temperature heat release (HTHR) phases are evident for DM and DG at most SOIs. However, DP exhibits distinct low temperature and high temperature phases only for 320 and 330 CAD SOIs. When LTHR is observed, its magnitude is greater for DG compared to DM and DP. Based on these observations, it can be hypothesized that the low temperature chemistry, which leads to LTHR, is actively suppressed by both propane and methane, with propane suppressing the chemistry more-actively than methane. With LTHR present at all SOIs for DG, gasoline likely had no negative effect, or possibly even enhanced diesel's low temperature chemistry.



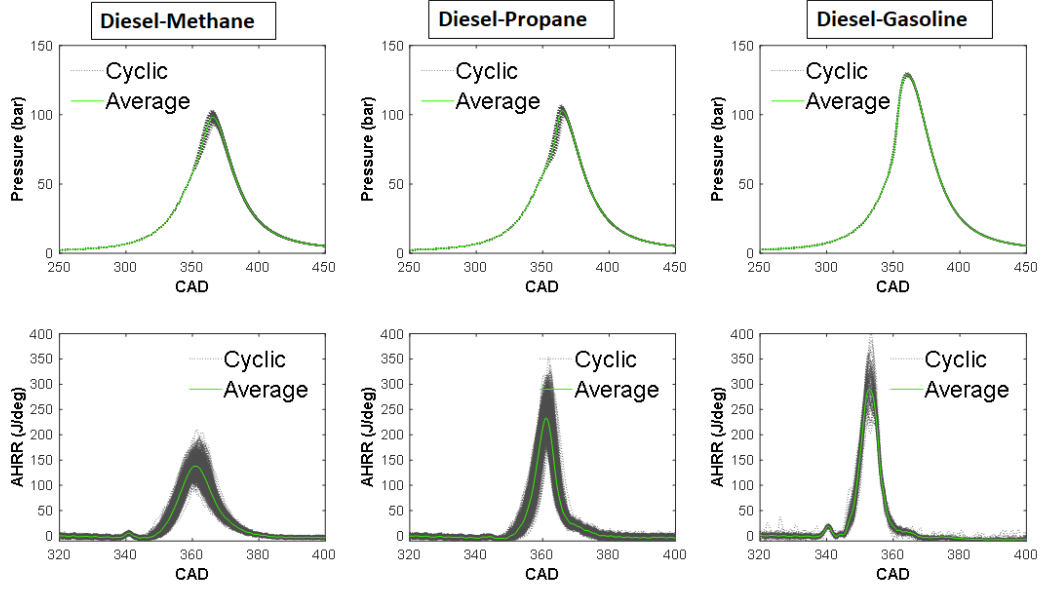
a (SOI=280CAD)



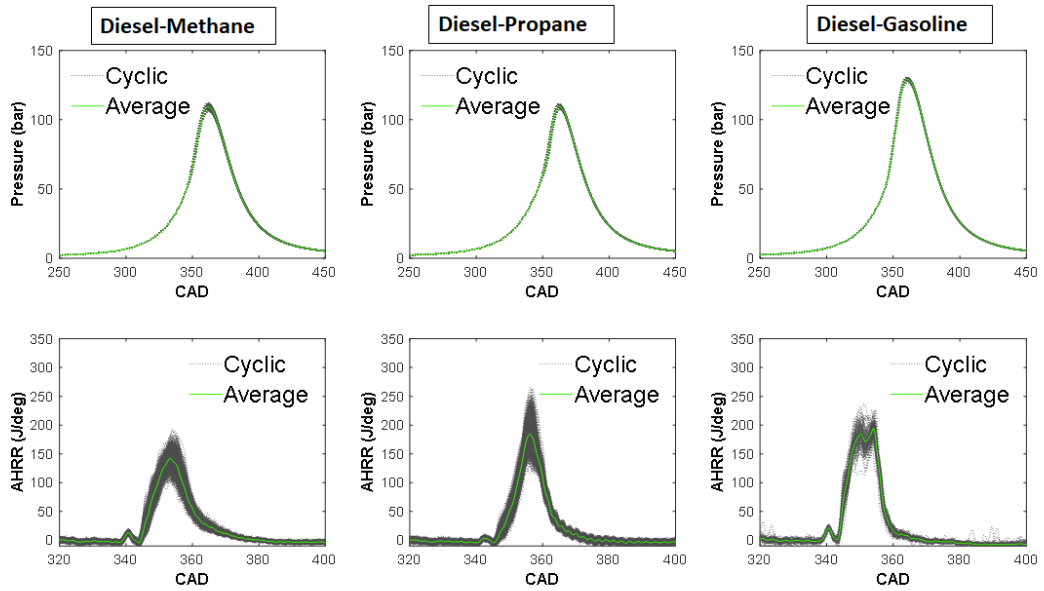
b (SOI=290CAD)



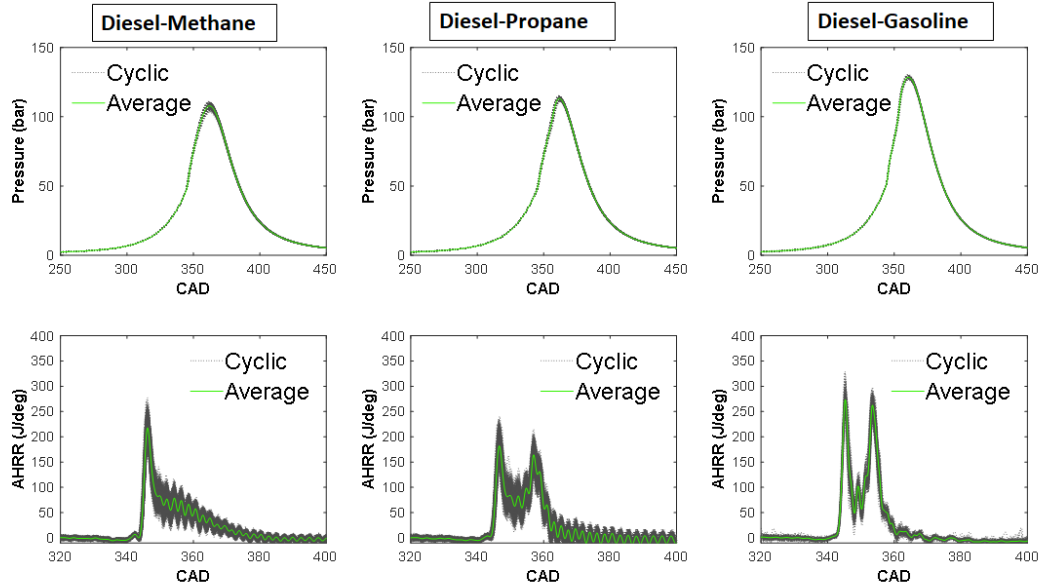
c (SOI=300CAD)



d (SOI=310CAD)



e (SOI=320CAD)



$f(SOI=330CAD)$

Figure 3.7 7(a-f). Cyclic variations in in-cylinder pressure and AHRR histories for 1000 consecutive cycles for DM and DP combustion cases and for 100 consecutive cycles for DG combustion at various SOIs and 5.1 bar IMEP, N=1500 rpm, diesel injection pressure = 500 bar, PES of 80%.

3.6.2.1 Zero-Dimensional Chemical Kinetic Analysis

To further investigate fuel effects on diesel LTHR, a zero-dimensional chemical kinetic analysis is performed. The simulation is performed in a closed homogenous reactor using the “POLIMI_TOT” detailed chemical kinetics mechanism for n-dodecane [45] at engine-relevant conditions. As indicated in Table 5, four different fuel combinations were chosen for these simulations. Diesel is represented by n-dodecane and gasoline is represented by iso-octane. Case 1 was for neat n-dodecane with $\phi = 0.3$. Cases 2 through 4 used a fixed amount of n-dodecane (with $\phi_{\text{dodecane}} = 0.3$) with sufficient addition of iso-octane (representing gasoline), methane, and propane, respectively, to achieve a total equivalence ratio (ϕ_{total}) of 0.5. The simulations were performed at a

pressure of 28 bar and temperature of 780 K, corresponding to the average conditions at the onset of LTHR from experiments for DM, DP, and DG combustion at several SOIs. The POLIMI_TOT mechanism includes more than 450 species and 15000 reactions [45]. This mechanism includes sub-mechanisms for C1 through C16 hydrocarbons. Figure 3.8 shows the time evolution of the volumetric heat production rate (\dot{Q}) during the LTHR phase at various ϕ_{total} values. The following observations are evident from Figure 3.8.

- The onset of volumetric heat release is delayed with the addition of iso-octane, methane, or propane, which suggests that in dual fuel combustion, the addition of low reactivity fuel (regardless of the specific fuel type) delays n-dodecane autoignition.
- The maximum delay in the onset of volumetric heat release is caused by propane, followed by methane and then iso-octane.
- The concentration of n-dodecyl-ketohydroperoxide radical ($\text{NC}_{12}\text{H}_{24}\text{O}_3$) is observed to decrease with the addition of iso-octane, methane, or propane.
- These observations indicate that of the low reactivity fuels investigated, propane has the most effect in both delaying the onset of and suppressing the formation of the ketohydroperoxide radical followed by methane and then iso-octane. As a consequence, propane also suppresses the magnitude of volumetric heat release the most followed by methane and then iso-octane. It is noteworthy that estimated CA5 trends as indicated by the start of high temperature heat release in Table 6 for DP, DM, and DG dual fuel combustion also follow a similar trend. Further analysis of the chemical kinetic pathways for DP, DM, and DG is warranted to understand the reason behind this trend.

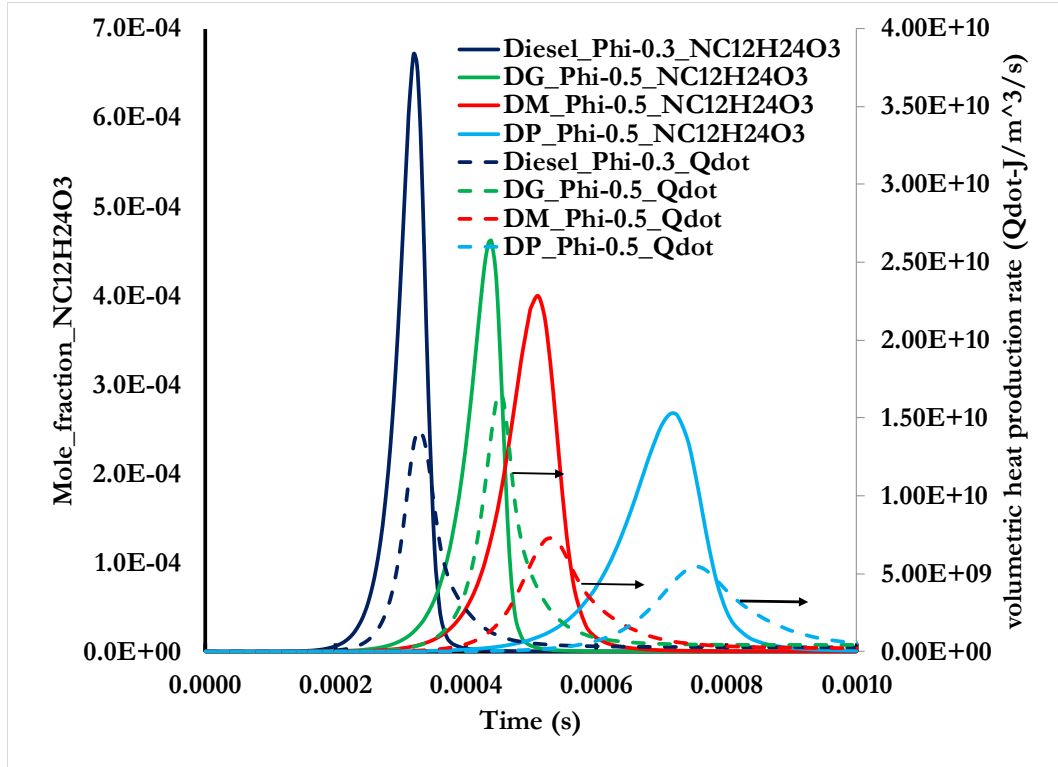


Figure 3.8 Time evolution of NC12H24O3 and volumetric heat production (Qdotvol) rate histories for various fuel type at Pinitial = 28 bar, Tinitial = 780 K.

Table 3.5 Zero-Dimensional simulation conditions for n-dodecane (representing diesel), DG (gasoline represented by iso-octane), DM and DP, all for an initial temperature of 780 K and an initial pressure of 28 bar.

Fuel combination	Diesel equivalence ratio	Overall equivalence ratio	Ignition delay (seconds)
n-dodecane	0.3	0.3	3.35E-03
n-dodecane + iso-octane	0.3	0.5	2.41E-03
n-dodecane + methane	0.3	0.5	4.44E-03
n-dodecane + propane	0.3	0.5	4.10E-03

Table 3.6 CA5 (with 1 std. dev) for DP, DM, DG dual fuel combustion for diesel SOIs from 280 to 330 CAD.

SOI	DP		DM		DG	
CAD	CAD	SD	CAD	SD	CAD	SD
280	360.51	1.41	358.25	1.11	350.53	0.54
290	359.63	1.33	357.16	1.07	349.95	0.59
300	358.76	1.18	356.63	1.05	349.55	0.59
310	355.60	0.98	353.84	0.92	348.57	0.51
320	350.14	0.61	347.48	0.45	345.77	0.29
330	345.94	0.18	345.46	0.16	344.58	0.11

3.6.3 Cyclic Behavior of Various Combustion Parameters

Cyclic variations in CA5 (5% of cumulative heat release) versus cyclic variations in CA50 (50% of cumulative heat release) are shown in Figure 3.9 for DM, DP, and DG at various SOIs. The CA5 variations decrease for all three fueling strategies as the SOI is retarded from 280 to 330 CAD. As SOI is retarded from 280 to 330 CAD, diesel has less time to mix inside the cylinder, which helps to form a stratified mixture with locally diesel rich zones. These zones easily ignite compared to the leaner diesel zones; thereby, decreasing the CA5 variation. CA5 variations are highest in DP followed by DM and then DG. This is attributed to propane suppressing diesel LTHR most. Cyclic CA50 variations decrease for DP and DG cases compared to DM, indicating that once the ignition is established it is easier for combustion to progress throughout the DP and DG mixtures compared to the DM mixtures. In addition, at 330 CAD SOI, regardless of the low reactivity fuel used, low cyclic variations in CA5 do not guarantee smaller variations in CA50. By contrast, higher CA5 variations are always accompanied by higher CA50 variations for DM combustion; however, this is not the case for DP and DG combustion.

For DG combustion, higher CA5 variations are not accompanied by higher CA50 variations and a similar observation can be seen for few cases of DP combustion. The separation between CA5 and CA50 for all three fuel combinations reduces with retarding SOI from 280 CAD to 330 CAD, indicating that cyclic combustion variations are likely dominated by auto-ignition.

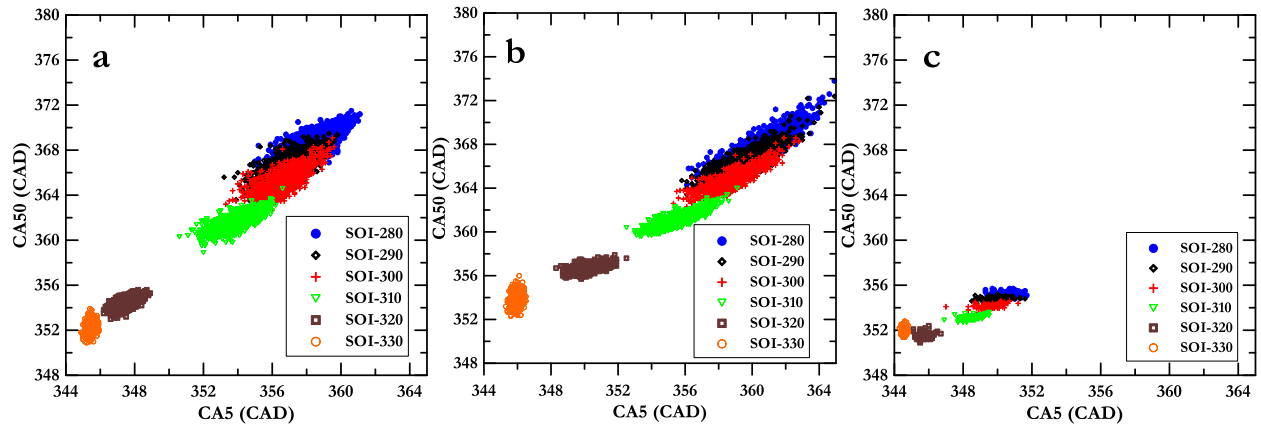


Figure 3.9 CA50 versus CA5 for 1000 consecutive cycles of (a) diesel-methane (b)diesel-propane and 100 consecutive cycles of (c) diesel-gasoline at 5.1 bar IMEP, N= 1500 rpm, diesel injection pressure=500 bar, PFEF =80%, with varying SOI.

Figure 3.10 discusses cyclic variations in P_{MAX} versus cyclic variation in CAP_{MAX} for DM and DP and DG combustion for different SOIs. There is not much variation in the magnitude of P_{MAX} and CAP_{MAX} for DG dual fuel combustion for different SOIs between 280 CAD to 330 CAD. Fast-and slow burn cycles can be discerned through methods put forth by Matekunas [23] and Srinivasan et al. [14] wherein an observation of CA50 and CAP_{MAX} is needed. If CA50 occurs before CAP_{MAX} along with a high magnitude of P_{MAX}, the cycle can be said to be fast-burn, and vice versa for slow-burn cycles. For all SOIs between 280 CAD to 330 CAD for DG, CA50 occurs before CAP_{MAX} with a higher magnitude of P_{MAX}, indicating that all cycles are

fast burn. For DM and DP combustion, there is a wide variation in the magnitude of P_{MAX} and CAP_{MAX} with a change in SOI. For DP combustion, the magnitude of P_{MAX} increases linearly with retarding SOI from 280 CAD to 330 CAD. To further analyze the DM and DP trends, cycles having CA₅₀ occurring before CAP_{MAX} were identified. Table 7 shows the number of cycles for which CA₅₀ occurs before CAP_{MAX}. For DP, virtually all cycles have CA₅₀ occurring before CAP_{MAX}. This indicates that DP combustion has the potential to have all fast burn cycles if the magnitude of P_{MAX} is high enough, irrespective of SOI. For DM combustion, almost half of the cycles at 280 CAD SOI are a slow burn. For 290 and 300 CAD SOIs, there are some cycles which are a slow burn. This analysis shows that SOI plays a key role in achieving fast burn cycles for DM combustion.

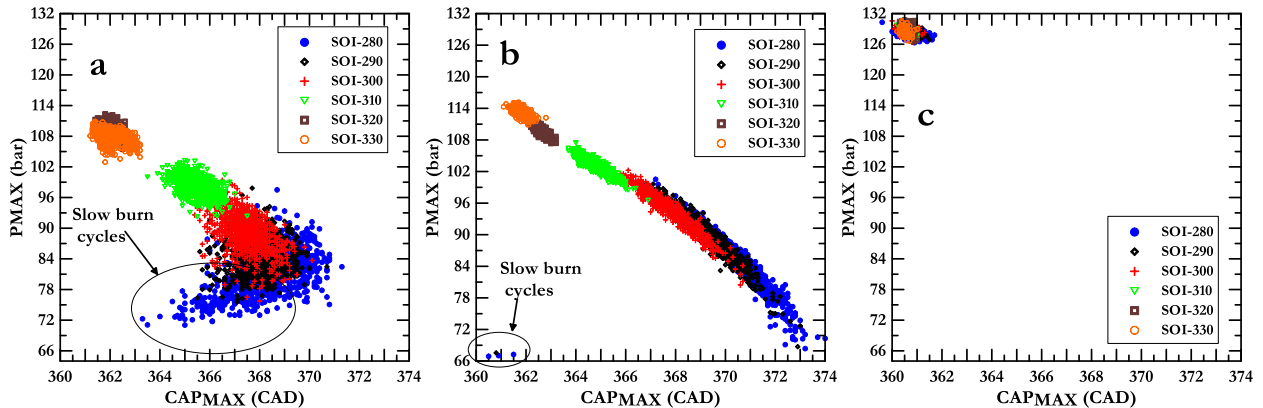


Figure 3.10 P_{MAX} versus CAP_{MAX} for 1000 consecutive cycles of (a) diesel-methane (b)diesel-propane and 100 consecutive cycles of (c) diesel-gasoline at 5.1 bar IMEP, N= 1500 rpm, diesel injection pressure=500 bar, PES =80%, with varying SOI.

Table 3.7 Number of cycles for which CA50 leads CAPMAX.

SOI (CAD)	280	290	300	310	320	330
Diesel-methane	538	881	989	1000	1000	1000
Diesel-propane	997	999	1000	1000	1000	1000
Diesel-gasoline	100	100	100	100	100	100

Figure 3.11 shows the maximum pressure rise rate (MPRR) versus CAP_{MAX} for DM, DP, and DG. The MPRR decreases with SOI retardation from 280 CAD to 330 CAD for DG dual fuel combustion. This is due to high AHRR magnitudes due to the higher reactivity of gasoline, causing most of the combustion to finish before TDC. The trends are reversed for DM and DP dual fuel combustion since methane and propane are less reactive than gasoline and combustion extend beyond TDC. With higher MPRR, maximum pressure occurs close to TDC in all three dual fuel combustion cases. Variation in MPRR is large for DM combustion for the most part compared to DP and DG dual fuel combustion. For DM combustion, the MPRR for SOIs of 280, 290, and 300 CAD clearly show that there are some slow burn cycles; similarly, 280 and 290 CAD SOIs for DP combustion also show some slow burn cycles. The MPRR can be used as an additional indicator to determine slow burn and fast burn cycles along with CA50 phasing, CAP_{MAX} , and PMAX.

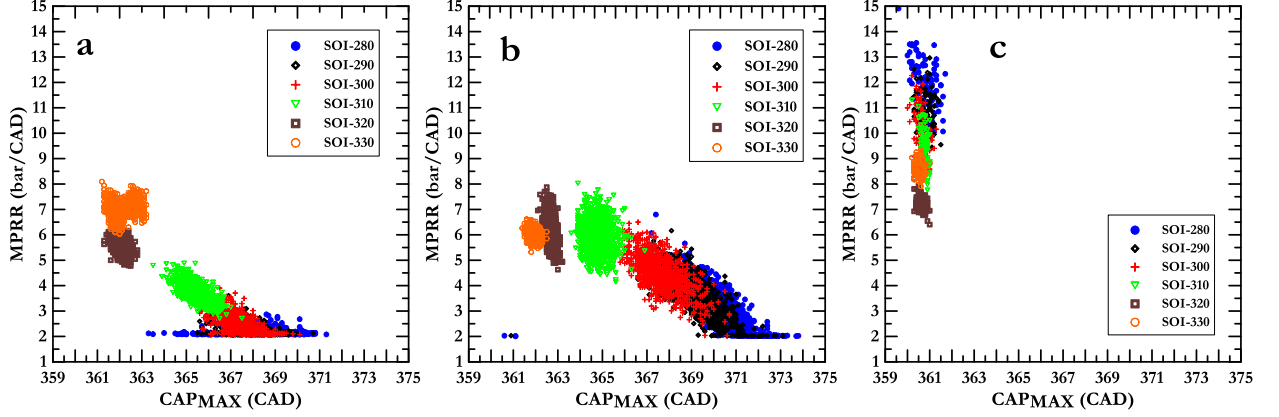


Figure 3.11 MPRR versus CAPMAX for 1000 consecutive cycles of (a) diesel-methane (b) diesel-propane and 100 consecutive cycles of (c) diesel-gasoline at 5.1 bar IMEP, N= 1500 rpm, diesel injection pressure=500 bar, PES =80%, with varying SOI.

Figure 3.12 shows cumulative gross heat release (CGHR) versus indicated mean effective pressure (IMEP) for DM, DP, and DG combustion. Cumulative gross heat release is calculated by first calculating gross heat release and then integrating it from 180 CAD to 540 CAD. To calculate the CGHR, it is necessary to model the heat transfer between the cylinder gas and the cylinder walls. Equation 3.13 is a global heat transfer coefficient provided by Chang et al [46] (also known as the Assanis model) used to calculate GHR:

$$h(t) = \alpha_{scaling} * L(t)^{-0.2} * p(t)^{0.8} * T(t)^{-0.73} * \vartheta_{tuned}(t)^{0.8} \quad (3.13)$$

$$\vartheta_{tuned}(t) = C_1 * \bar{S}_p + \frac{C_2}{6} * \frac{V_d * T_r}{p_r V_r} (p - p_{mot}) \quad (3.14)$$

where p , T , and $\alpha_{scaling}$ are pressure, temperature and a tuning parameter, respectively and ϑ_{tuned} is the characteristic velocity given by Equation 3.14. Details of all constants in Equations 3.13 and 3.14 are provided in Chang et al [46]. This model is adopted since for the range of diesel SOIs chosen the low temperature dual fuel

combustion analyzed in this paper has shared attributes with classical HCCI combustion. CGHR represents the goodness of the combustion process and the IMEP is directly correlated with CGHR. It is clear from IMEP vs. CGHR plots that variations are observed to be a maximum for DM followed by DP, and then DG. For DG, there is not much variation of CGHR and IMEP with a change in SOI. For DP, variations are mainly observed for SOIs of 280 CAD and 290 CAD, and the value of CGHR and IMEP for most cycles for 280 CAD SOI seems to be lower compared to other retarded SOIs. The maximum variations in CGHR and IMEP are observed for DM for 280 CAD SOI. At the same SOI, CGHR and IMEP are observed to reach both their maximum and minimum value. This variation shows the potential to have higher average CGHR and IMEP values in the absence of cyclic variations. For a deeper analysis, 280 CAD SOI was chosen since a similar amount of diesel is injected for all three fuel combinations, and the fluid dynamics (especially of fuel-air mixing) are more or less the same, meaning that the charge mixture should be similar across all of the fuel combinations. At this SOI, it can be seen that the fuel reactivity plays a vital role in cyclic variations. Since gasoline is a high reactivity fuel compared to propane and methane, fewer available ignition centers are enough for combustion to consume almost all of the fuel even at low loads. Similarly, the high temperature reactivity of propane is lower than that of gasoline but higher compared to methane; this means that the available distributed ignition centers are not sufficient to completely consume the fuel properly, causing cyclic variations. Finally, methane is very difficult to combust and to burn completely inside the cylinder. The distributed ignition centers available at 280 CAD SOI for DM are apparently not robust enough; consequently, methane is not burned completely. Due to lower methane fuel

reactivity, the percentage of combustion that occurs in the cylinder with available ignition centers, along with residual gas effects from prior cycles, change combustion from one cycle to another, causing high cyclic variations. This suggests that lower fuel reactivity increases cyclic variations in the absence of sufficiently robust distributed ignition centers within the cylinder, which is the case for DM at 280, 290, and 300 CAD SOIs. For late SOIs, the likely availability of robust diesel ignition centers caused cyclic variations to decrease for DM combustion at 310, 320, and 330 CAD SOIs. This also suggests the potential to increase the CGHR and IMEP if the number and strength of ignition centers are increased, which could reduce cyclic variations and allow more complete combustion in more engine cycles.

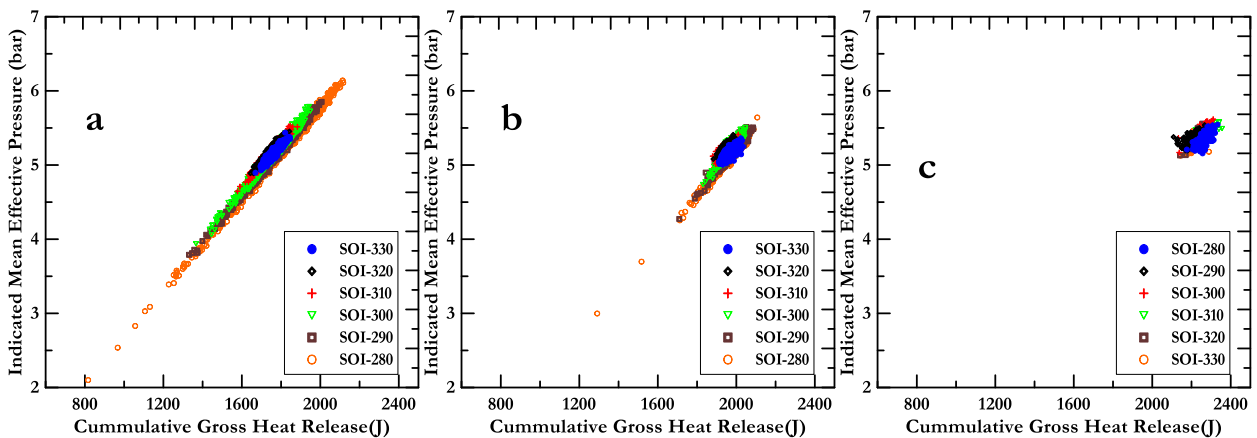


Figure 3.12 Indicated mean effective pressure versus cumulative gross heat release for 1000 consecutive cycles of (a) diesel-methane (b) diesel-propane and 100 consecutive cycles of (c) diesel-gasoline at 5.1 bar IMEP, $N=1500$ rpm, diesel injection pressure=500 bar, PES =80%, with varying SOI.

Figure 3.13 presents IMEP versus CA50 for DM, DP, and DG dual fuel combustion. The location of CA50 is crucial for to ensure good IFCE and it has been suggested that CA50 phasing be between 5-11 CAD after TDC [47] for optimal power

output – efficiency trade-offs. For all SOIs, with DG fueling, CA50 occurs well before TDC, which hinders the ability to extract the maximum power output even with lower cyclic variations. For DP combustion, at SOIs of 300 and 310 CAD, it is observed that even with high cyclic variations, average IMEP is similar to that of 320 and 330 CAD SOIs. This is because CA50 is phased towards the optimum value (mentioned previously as being 5-11 CAD after TDC). Similarly, for DM, the average IMEP for 310 CAD SOI is higher than that of both 320 and 330 CAD SOIs even though cyclic variation for the former is much higher than that of the latter two SOIs. With the elimination of low efficiency cycles and by phasing CA50 correctly, a higher average IMEP can be achieved. Similarly, shifting cycles with minimum variation to the correct CA50 phasing using parameters like intake temperature, swirl, exhaust gas recirculation (EGR), multiple injection events, etc. can help achieve higher IMEP.

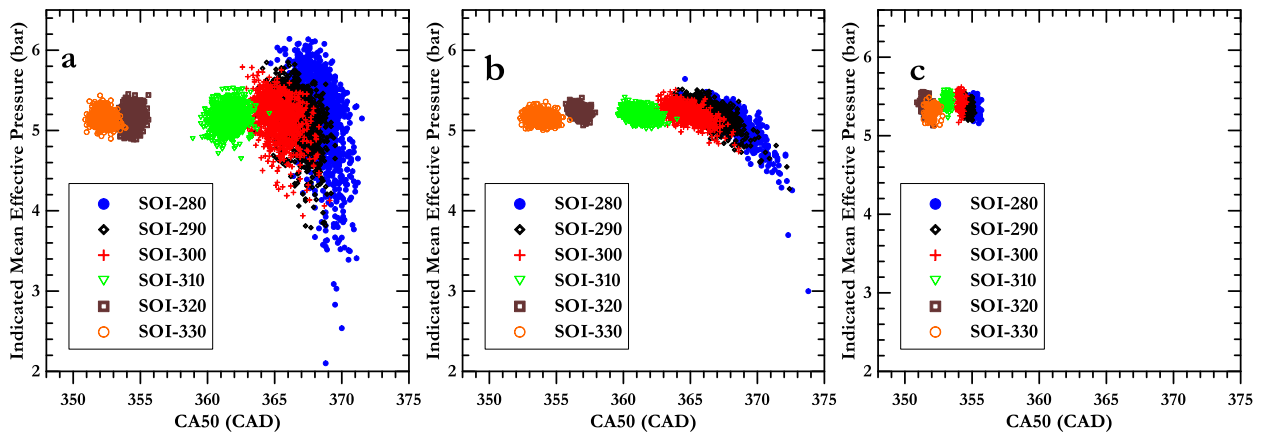


Figure 3.13 Indicated mean effective pressure versus CA50 for 1000 consecutive cycles of (a) diesel-methane (b)diesel-propane and 100 consecutive cycles of (c) diesel-gasoline at 5.1 bar IMEP, N= 1500 rpm, diesel injection pressure=500 bar, PES =80%, with varying SOI.

Figure 3.14 shows cyclic variations in nominal indicated fuel conversion efficiency (Nom-IFCE¹) for 5.1 bar IMEP for DM and DP and DG dual fuel combustion. It is clear from the plots that Nom-IFCE variations are observed to be a maximum for DM followed by DP, and then DG. For DG there is not much variation of Nom-IFCE with changes in injection timing. For the DP case, the variations are mainly observed for diesel SOIs 280 CAD and 290 CAD and are lower for 280 CAD than retarded injection timings. For DM, variations in Nom-IFCE for 280 CAD diesel SOIs are a maximum; at the same injection timing, IFCE fluctuates between the maximum and minimum values. This variation shows the potential to have higher average IFCE if the high cyclic variations are eliminated. For a deeper analysis, an injection timing of 280 CAD was chosen since a similar amount of diesel is being injected in all three fueling strategies, and the fluid dynamics are more or less the same meaning that the charge mixture should be similar across all of the fueling strategies. At this injection timing, it can be seen that the fuel reactivity plays a vital role in controlling cyclic variations. Since gasoline is a high reactivity fuel compared to propane and methane, fewer available ignition sources are sufficient for combustion to consume almost all of the fuel even at low loads as evidenced by virtually no slow burn cycles; however, the overall magnitude is lowest since combustion is complete even before TDC, which means there are significant heat transfer losses. One way to increase the efficiencies would be to employ aggressive EGR, which would ensure combustion is phased appropriately. For the DP case, the residence

¹ Nom-IFCE is defined as the ratio of gross indicated work for i^{th} cycle to the nominal fuel energy input averaged over i cycles. Since cyclic mass flow rate of both diesel and the low reactivity fuel is not available for each of the i cycles, the nom-IFCE is a good relative indicator of the efficiency of the overall work extraction for the closed cycle relative to a nominal amount of fuel energy.

times to disperse diesel into the propane-air mixture are of a similar magnitude as that of the DG case, however, propane has been shown to inhibit diesel's autoignition tendency most. In addition, its reactivity is lower than that of gasoline; therefore, the robustness of distributed diesel ignition is slightly compromised. This is seen from the combustion extending well beyond TDC. By this time, propane has had a chance to react and this works favorably. As a result, despite propane's negative effect on diesel autoignition, higher efficiencies are possible with a few slow burn cycles. Finally, methane being the least reactive of the three fuels is very difficult to combust, and it needs perfect conditions to burn completely inside the cylinder. As pointed out in the zero dimensional simulations, methane also tends to delay diesel autoignition. Interestingly, this tendency was identified by Srna et al. [48]. Due to these reasons combined with methane's poor reactivity, and residual gas effects from prior cycles, leads to high cyclic variations. These observations suggest that spatio-temporal distribution of diesel autoignition centers is a critical parameter to compensate for the reactivity differences of the low reactivity fuel. Therefore, diesel SOI emerges as a crucial control parameter in minimizing cyclic variations in low temperature DM and DP dual fuel combustion.

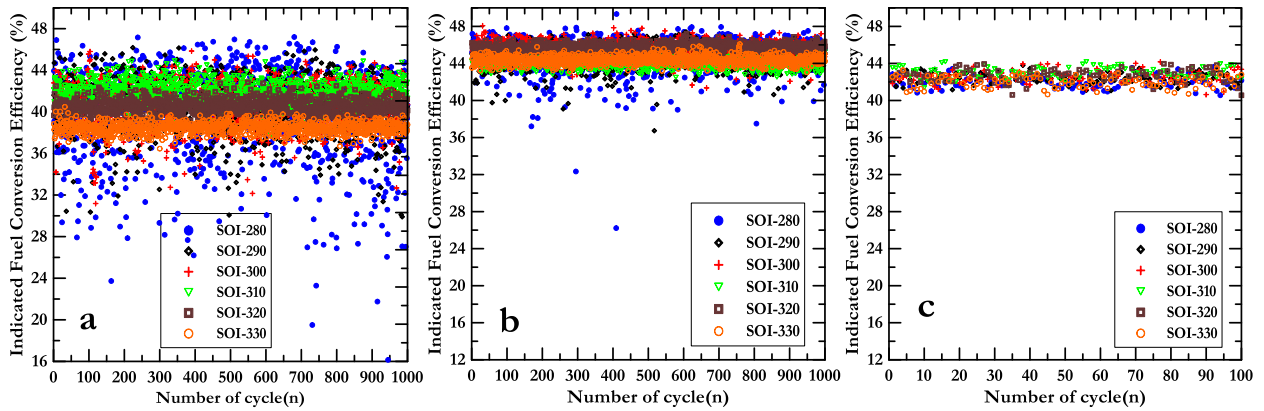


Figure 3.14 Indicated fuel conversion efficiency for 1000 consecutive cycles of (a) diesel-methane (b)diesel-propane and 100 consecutive cycles of (c) diesel-gasoline at 5.1 bar IMEP, N= 1500 rpm, $P_{in} = 1.5$ bar, PES =80%, with varying SOI.

To further explain combustion behavior in DM, DP, and DG dual fuel combustion, a return map for the difference between CA5 and TDC (i.e., CA5-TDC) is shown in Figure 3.15 [49]. A negative value in this return map indicates CA5 occurs before TDC and a positive value indicates CA5 occurs after TDC, with a value of 0 indicating that CA5 occurs at TDC. The return map compares this parameter between a given cycle “n” and the following cycle “n+1.” One common observation in DM, DP, and DG dual fuel combustion is that with SOI retardation from 280 CAD to 330 CAD, CA5 becomes more consistent from one cycle to the next as shown by the decrease in the dispersion of the CA5-TDC return map. This is due to the following factors:

- High temperature and pressure inside the combustion chamber at the start of diesel injection as SOI is retarded from 280 CAD to 330 CAD.
- At 280 CAD SOI, diesel has enough time to mix with the surrounding fuel-air mixture, resulting in a lower diesel equivalence ratio when the mixture is at an appropriate temperature and pressure for ignition to occur, thereby resulting in CA5 variations.

- At 330 CAD SOI diesel has a much shorter time to mix completely; however, it does have just enough time to evaporate and form a proper ignitable mixture, resulting in consistent autoignition, and therefore, lower CA5 cyclic variations.

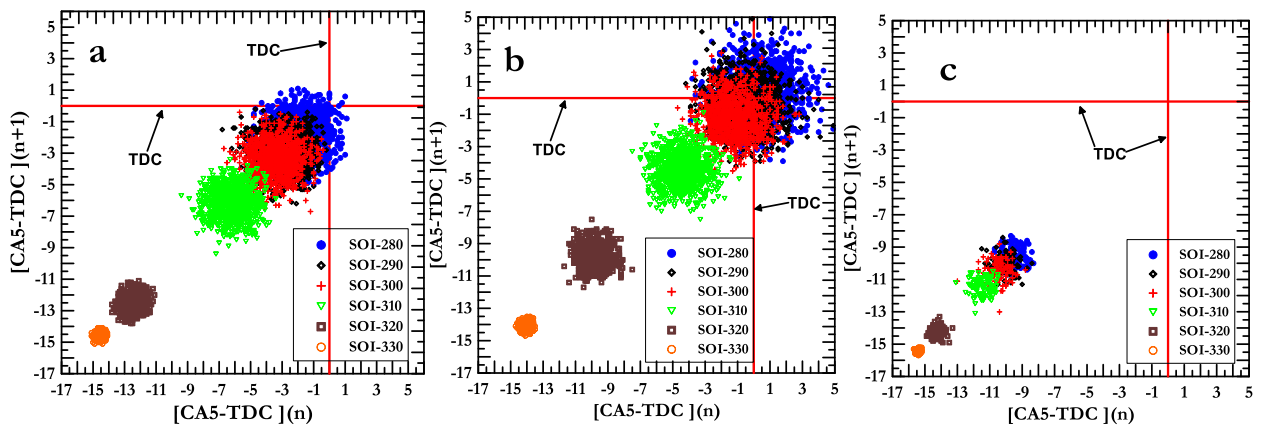


Figure 3.15 (CA5-TDC) return maps for 1000 consecutive cycles of (a) diesel-methane (b)diesel-propane and 100 consecutive cycles of (c) diesel-gasoline at 5.1 bar IMEP, N= 1500 rpm, diesel injection pressure=500 bar, PES =80%, with varying SOI.

Figure 3.15. (CA5-TDC) return maps for 1000 consecutive cycles of (a) diesel-methane (b)diesel-propane and 100 consecutive cycles of (c) diesel-gasoline at 5.1 bar IMEP, N= 1500 rpm, diesel injection pressure=500 bar, PES =80%, with varying SOI.

As mentioned before, fluid dynamic effects can be expected to be relatively similar at a given SOI, since the engine operating conditions across all three fueling combinations were constant. This also means that CA5 variations are mainly based on the chemical properties of the fuel. For the same diesel SOIs across all three fueling combinations, DP combustion shows a delay in the onset of combustion compared to DM and DG. One of the factors that could be responsible for the delay is that propane inhibits diesel's low temperature chemistry more compared to methane, which in turn slows

down the rate of reaction compared to DG dual fuel combustion. As discussed earlier, additional chemical kinetic investigations are needed to determine why propane delays the start of combustion when compared to methane; and such investigations are beyond the scope of this paper.

Figure 3.16 shows CA5-50 duration versus CA50-90 duration plotted for DM and DP, and DG combustion. At all SOIs for DP and DG dual fuel combustion, the CA50-90 duration is faster than the CA5-50 duration, indicating that once the ignition is established it is easy for combustion to progress to completion within the cylinder. For DM at SOIs of 320 and 330 CAD, it is observed that CA50-90 variations are elongated due to difficulty in sustained combustion at low loads. Interestingly, CA5-50 and CA50-90 for 310 CAD SOI are nearly the same, indicating a strong likelihood that diesel ignition centers are well dispersed, sustaining the spread of combustion.

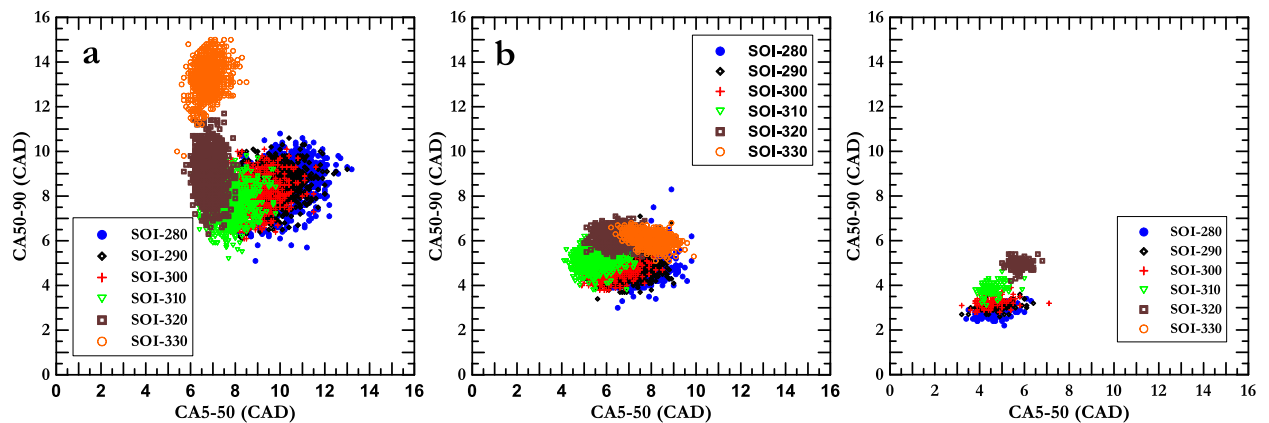


Figure 3.16 CA50-90 versus CA5-50 for 1000 consecutive cycles of (a) diesel-methane (b)diesel-propane and 100 consecutive cycles of (c) diesel-gasoline at 5.1 bar IMEP, N= 1500 rpm, diesel injection pressure=500 bar, PES =80%, with varying SOI.

Figure 3.17 shows the normalized IMEP “first order” return map (i.e., for the n^{th} cycle compared to the $(n+1)^{\text{th}}$ cycle) for various SOIs for all three fueling combinations.

IMEP provides global information about the combustion event inside the cylinder and can be used for statistical analysis. [28]. A time series return map for such engine global parameters can be useful to get low dimensional relations between two successive combustion events. Finney [28] states that cycles which do not have any relation between prior and current cycles are expected to display a “shot gun pattern” with a centroid that falls on a 45-degree line as drawn from the origin of the graph. The cycles which exhibit some determinism will show some structure and deviation from the fixed-point region within the return map. For the DG return map, it can be observed that the IMEP pattern exhibits a slight dispersion, similar to a shotgun blast, about the 45-degree line passing through the origin, indicating that there is a strong likelihood of stochastic behavior. For DP dual fuel combustion, a deviation from the 45-degree line and an incipient triangular structure is seen for SOIs of 280,290, and 300 CAD; however, for SOIs for 310,320, and 330 CAD a shot gun type pattern is seen. This indicates that a low dimensional determinism likely exists for DP combustion for SOIs of 280, 290, and 300 CAD under these operating conditions. Similarly, for DM dual fuel combustion for SOIs of 280, 290, 300, and 310 CAD, the IMEP return map shows deviations from the 45-degree line and a more distinct, larger structure; however, at 320 and 330 CAD SOIs, a shotgun pattern is seen. Some low dimensional determinism may be present for diesel SOIs of 280, 290, 300, and 310 CAD. This behavior seen in both DP and DM may be due to slow burn cycles followed by fast burn cycles (and vice versa) present in combustion at those particular SOIs, leading to prior cycle effects and some associated determinism.

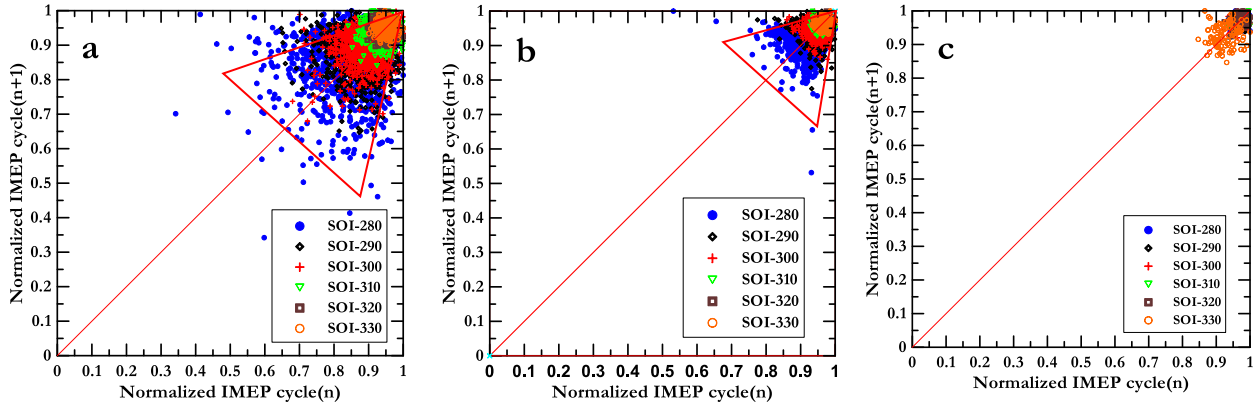


Figure 3.17 IMEP return maps for 1000 consecutive cycles of (a) diesel-methane (b) diesel-propane and 100 consecutive cycles of (c) diesel-gasoline at 5.1 bar IMEP, N=1500 rpm, diesel injection pressure=500 bar, PES =80%, with varying SOI.

Finally, to further analyze these cyclic variations for different SOIs and fuel combinations, a statistical approach was adopted using a normal probability plot. Within a normal probability plot, the distribution of the experimental data is compared to a known distribution (in this case, a normal distribution). A plot is then made of the probability vs. the data value. If the data points fall on a straight line (the red lines shown in Fig. 18-23) that denotes a normal distribution, then the experimental data could be represented by a normal distribution, and therefore, are stochastic in nature. If, however, there is a deviation, then the data may have some degree of determinism to it [50, 51].

Normal probability plots of onset of combustion (CA5), combustion phasing (CA50), and indicated mean effective pressure (IMEP) are shown at 280, 290, 300, 310, 320, and 330 CAD injection timings in Figures 3.18 -3.23 for all fueling combinations. This graphical representation shows that not all variables analyzed follow normal distributions. This deviation from a normal distribution is indicative of data containing some degree of determinism. Consider the normal probability plot for CA5 for different SOIs. It was observed earlier that as the SOI is retarded closer to TDC, there is greater

consistency in the start of combustion. For SOIs between 280 and 320 CAD SOI for DM, DP, and DG, CA5 follows the normal reference line, meaning that the onset of combustion can be said to significant stochasticity. For the SOI of 330 CAD for DM, DP, and DG, the actual CA5 data had a much narrower x-axis range compared to the advanced SOIs, and more importantly, there is very little alignment along the normal probability distribution line. This indicates there is some determinism in the start of combustion for 330 CAD for all three fuel combinations. A similar normal probability plot analysis of combustion phasing (CA50) for DM, DP, and DG at SOIs from 280 to 330 CAD indicates that the data are mostly aligned to the normal distribution reference line, confirming that the cyclic combustion phasing distribution is stochastic in nature.

Next, a normal probability plot analysis for IMEP for different SOIs for DM, DP, and DG is performed. For DG for SOIs from 280-320 CAD, the IMEP data are aligned with the normal reference line, indicating stochasticity. This behavior was also seen previously, from IMEP return maps of DG exhibiting the “shotgun pattern” structure that would be expected with a predominantly stochastic dataset. For the SOI of 330 CAD, there is a deviation from the reference line, indicating some determinism is present in the dataset. However, this information was not clear from just the return map analysis alone. For both DM and DP for SOIs from 280-300 CAD, the normal probability plots of IMEP have some deviation from the reference line, indicating some determinism in the dataset. But for the rest of the SOIs, the IMEP data align with the reference line for both DM and DG combustion, indicating stochasticity. From these normal distribution plots, it is clear that some determinism is present in IMEP for 310 CAD SOI for DM combustion previously observed using IMEP return map analysis. Again, this method does not

indicate the degree to which there is determinism, but it gives evidence that determinism exists within the 280-300 CAD SOI range for DM and DP combustion, at least from the perspective of IMEP.

The normal probability plot analysis provides another tool for researchers to analyze combustion data on a cyclic basis, and when combined with other cyclic analysis techniques on the basis of deterministic/stochastic behavior, it can provide both an added layer of corroboration as well as a slightly more quantitative viewpoint, the caveat being that it is still not a purely quantitative technique.

SOI: 280 CAD

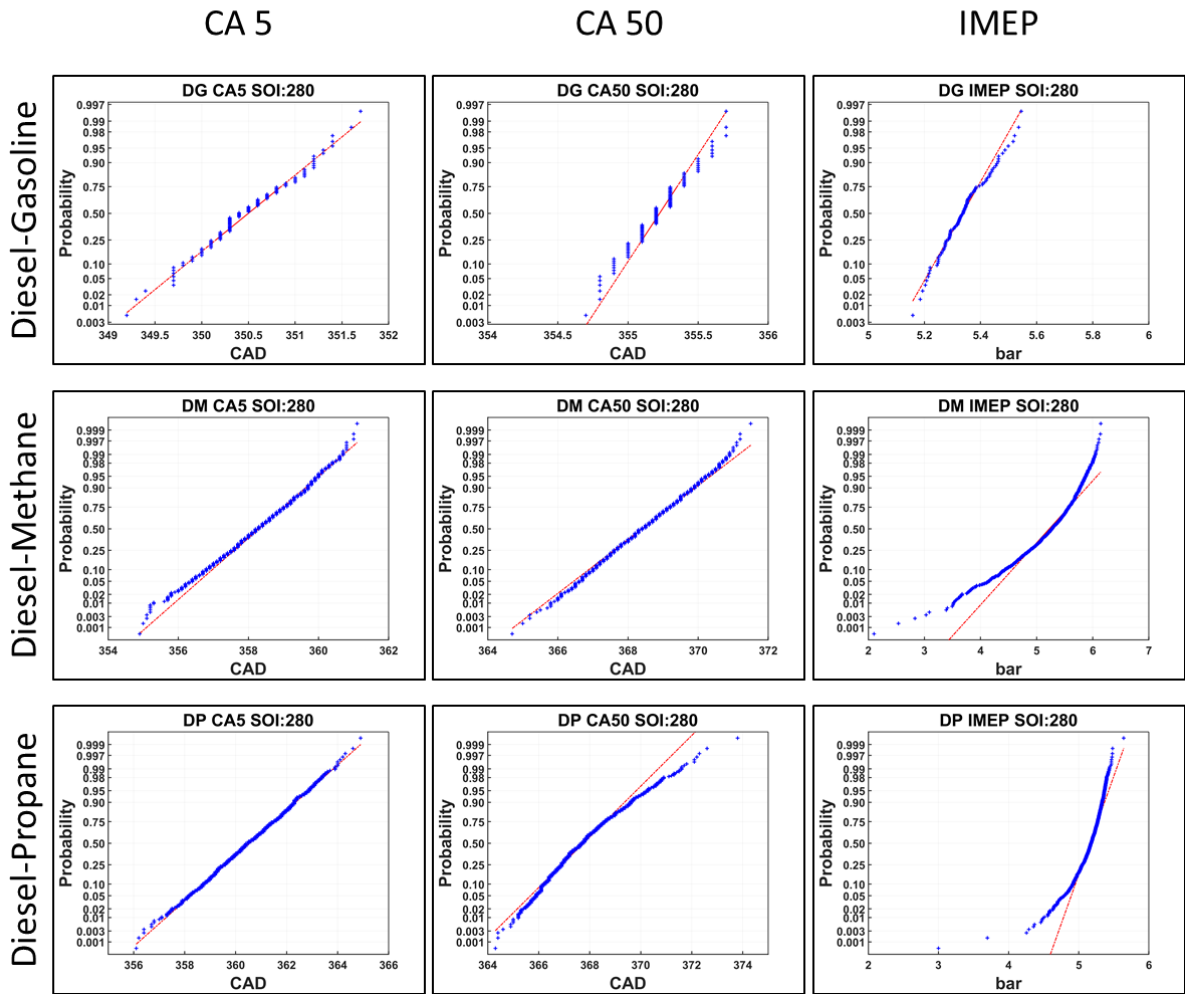


Figure 3.18 Normal probability plots for 280 injection timing for CA5, CA50 and IMEP

SOI: 290 CAD

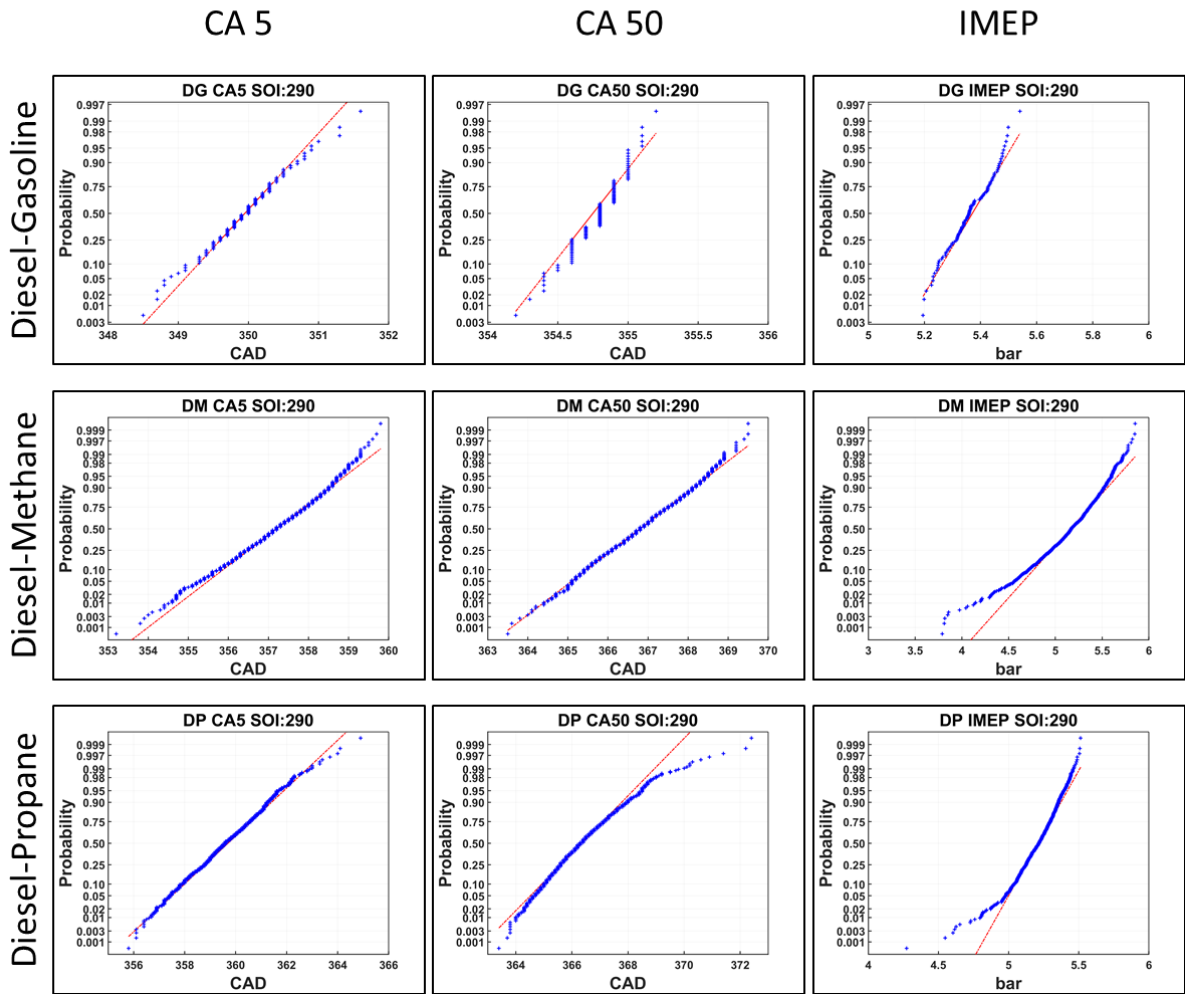


Figure 3.19 Normal probability plots for 290 injection timing for CA5, CA50 and IMEP

SOI: 300 CAD

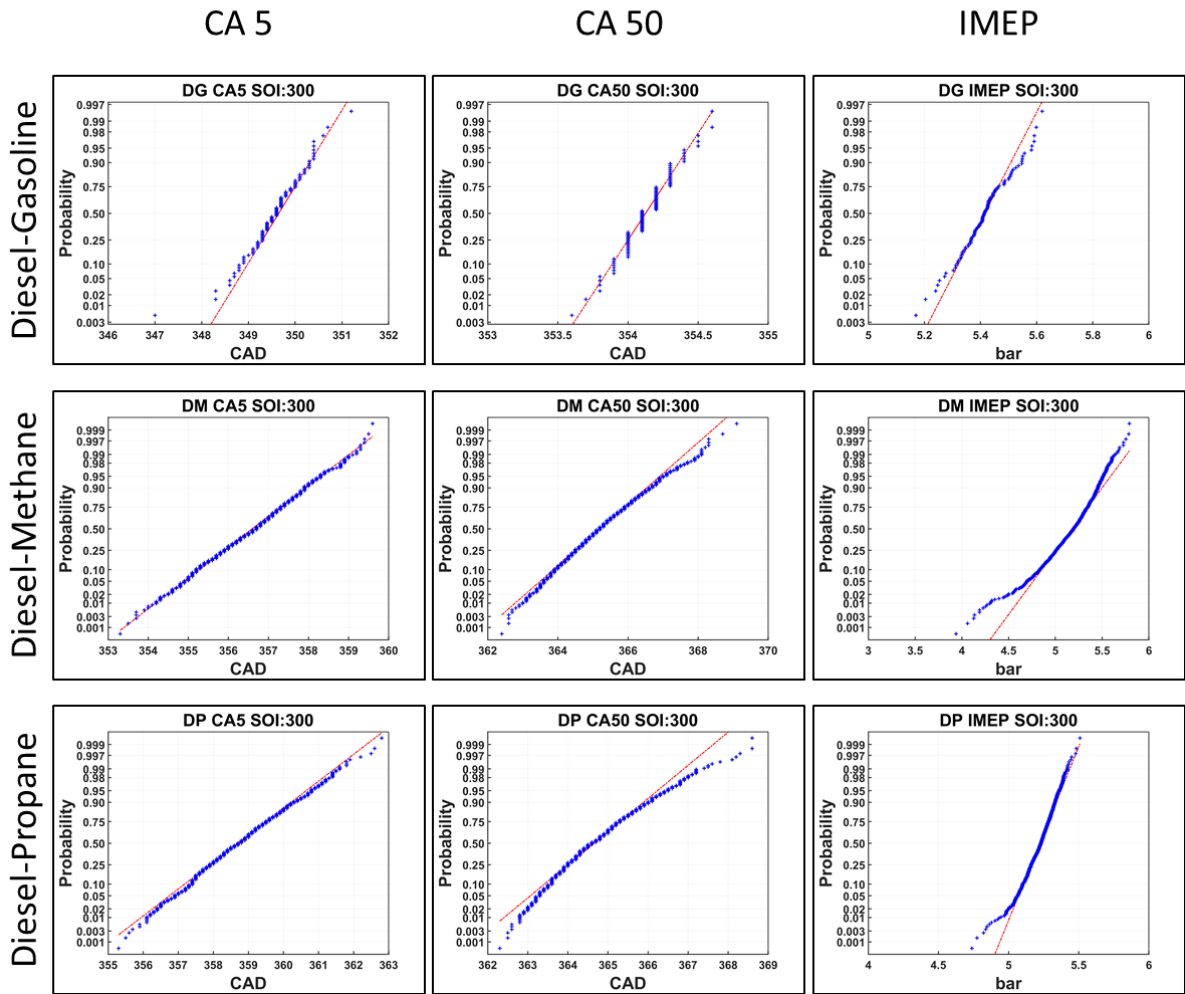


Figure 3.20 Normal probability plots for 300 injection timing for CA5, CA50 and IMEP

SOI: 310 CAD

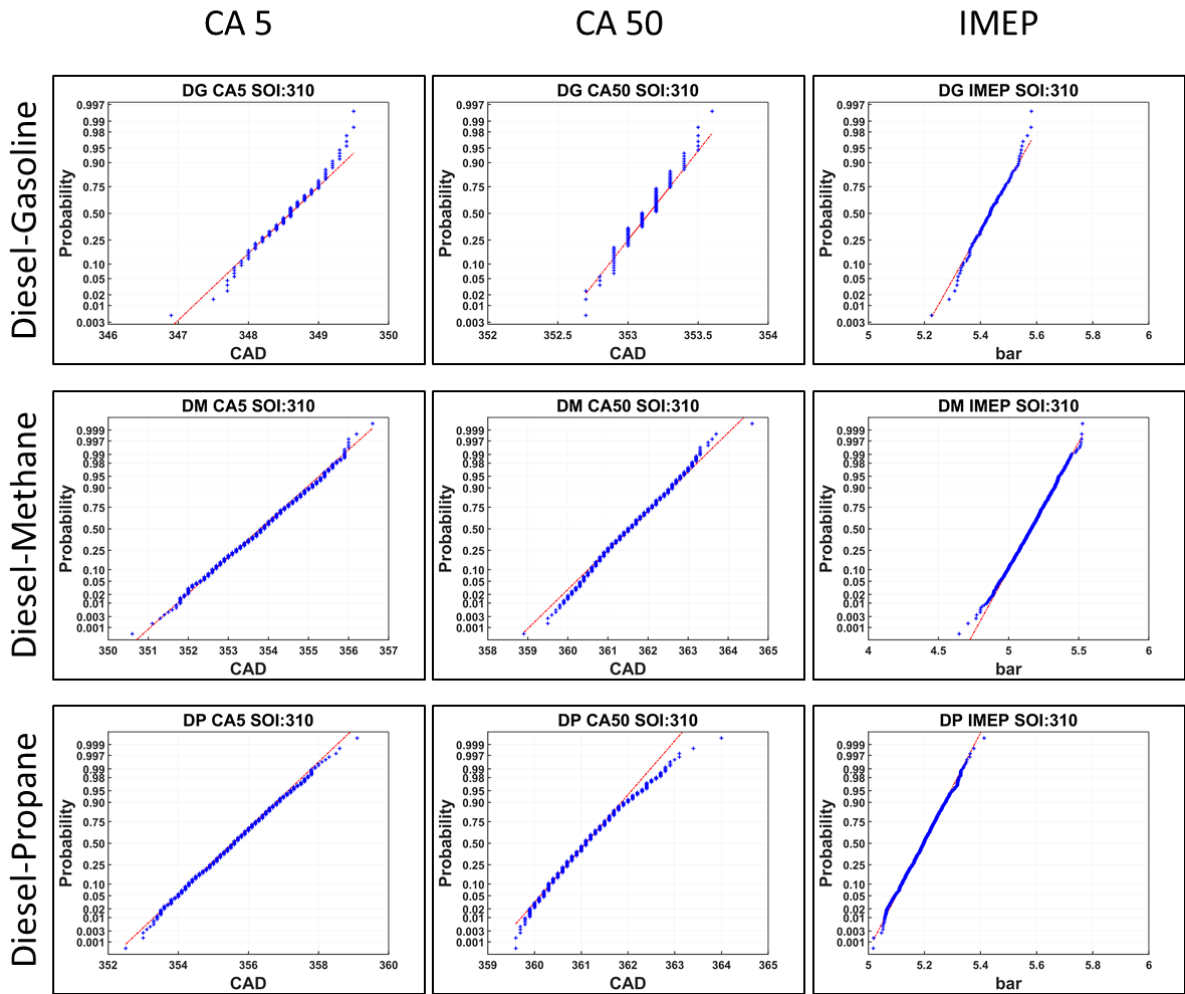


Figure 3.21 Normal probability plots for 310 injection timing for CA5, CA50 and IMEP

SOI: 320 CAD

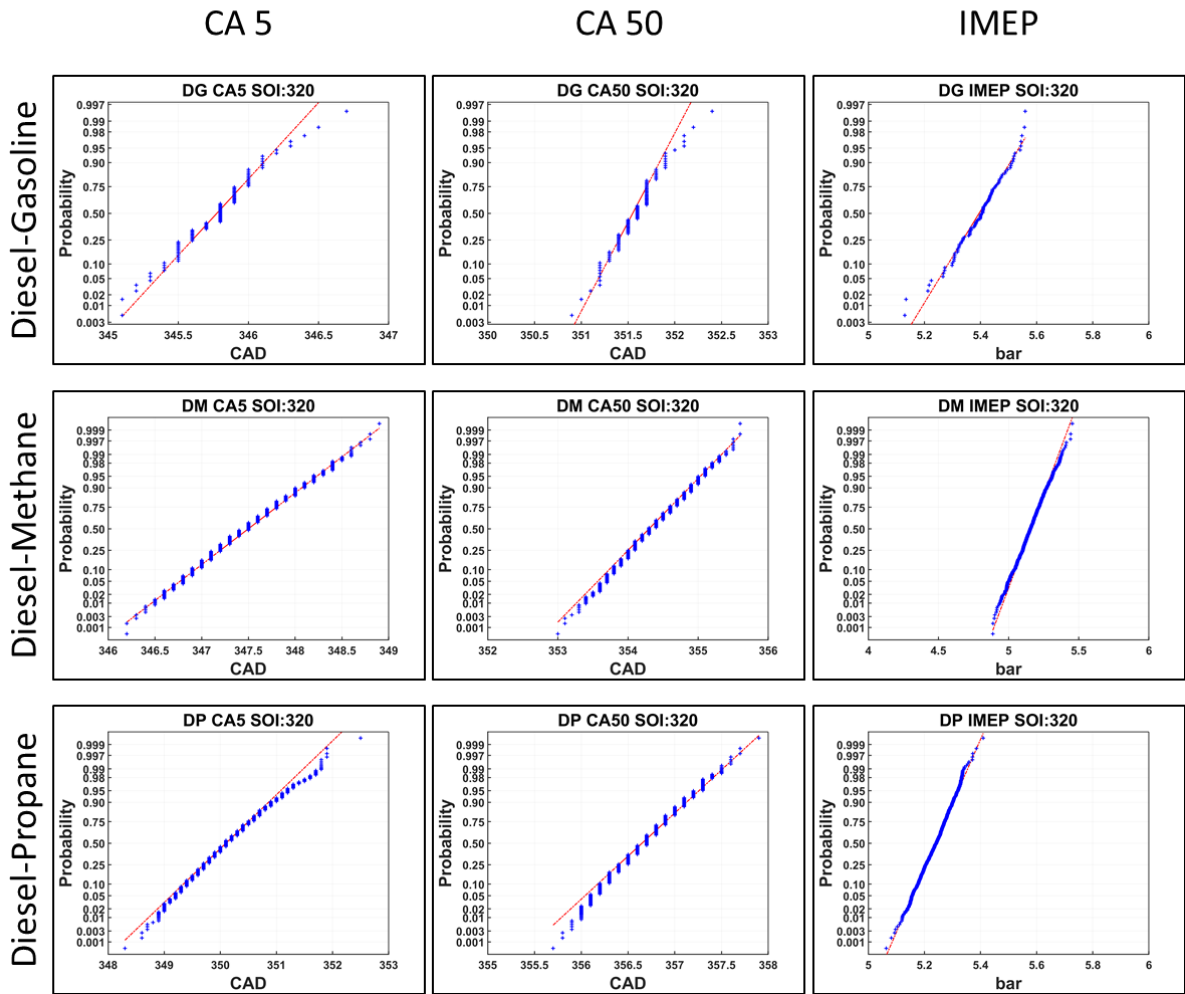


Figure 3.22 Normal probability plots for 320 injection timing for CA5, CA50 and IMEP

SOI: 330 CAD

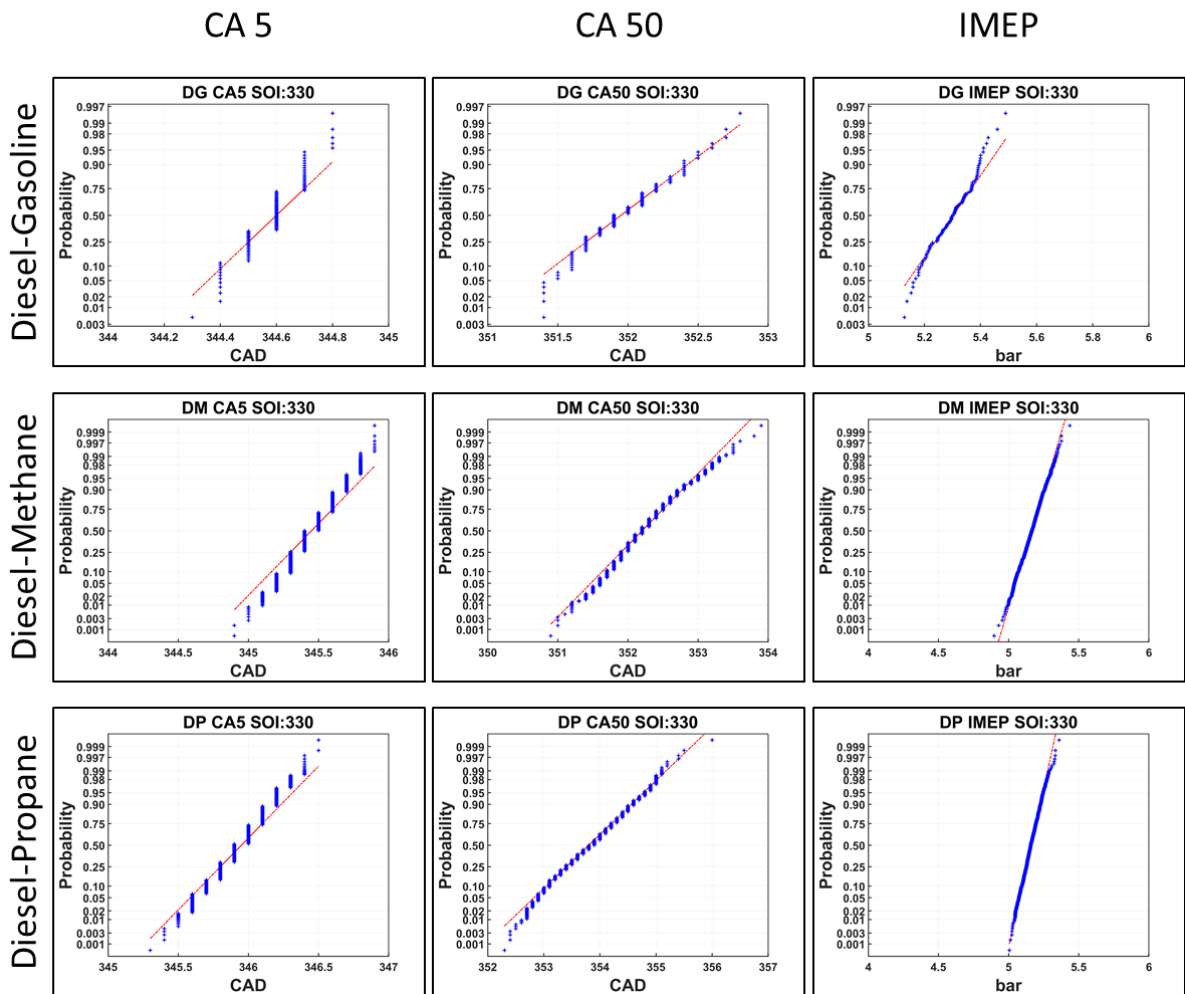


Figure 3.23 Normal probability plots for 330 injection timing for CA5, CA50 and IMEP

3.7 Conclusions

The impact of reactivity of different low-reactivity fuels (methane, propane, and gasoline) on diesel-ignited dual fuel low temperature combustion, especially cyclic variations at low engine load, was characterized at a constant engine speed of 1500 rpm. Since the engine platform remained the same and the engine aggregate in-cylinder fluid dynamics remain similar for the corresponding diesel SOIs when switching low reactivity fuels, any variations in combustion behavior likely stem from the type of low reactivity fuel used. Diesel SOI was varied from 280 CAD to 330 CAD. The main conclusions obtained are as follows:

- There is change in AHRR shape observed from 320 CAD SOI to 330 CAD SOI, irrespective of the low reactivity fuel used which can be attributable to the change in diesel distribution inside the cylinder before in-cylinder conditions favor high temperature diesel autoignition.
- For DG combustion COV_{IMEP} remains more or less constant but for DM and DP, COV_{IMEP} decreases as the diesel SOI is moved towards TDC. This indicates that for DG dual fuel combustion even a small amount of ignition source is sufficient to have better combustion while for DP and DM combustion requires both a stronger ignition source and a higher number of ignition sources for stable combustion.
- Combustion efficiency is insensitive to diesel SOI for DG dual fuel combustion; however, it increases monotonically for DP and first increases and then steadies out for DM dual fuel combustion as diesel SOI is retarded. This indicates that DG dual fuel combustion is not affected by relative diesel stratification introduced by changing diesel SOI. Whereas DP and DM dual fuel combustion becomes

progressively better with relative diesel stratification introduced by changing diesel SOI.

- Indicated fuel conversion efficiency (IFCE) is consistently highest for DP, followed by DG and then DM dual fuel combustion at all diesel SOIs investigated. The increase in combustion efficiency is not always accompanied by an increase in IFCE. For better IFCE, CA50 location needs to be at favorable location after TDC.
- ISNO_x increases with shifting diesel SOIs from 280 to 330 CAD for all three fuel combinations (DM, DP and DG), This is mainly due to more diesel stratification leading to diesel autoignition to occur at higher diesel phi leading to higher local temperature forming more NO_x.
- For DM and DP ISCO emissions decrease as diesel SOI is shifted from 280 to 330 CAD. Since for this condition, the only mechanism to oxidize CO → CO₂ is through the slower pathway, which is supported by higher bulk gas temperatures, which occurs at retarded diesel SOIs, e.g., 330 CAD. For DG case CO emissions are observed to increase when diesel SOI is retarded from 280 to 330 CAD. This is because CA50 occurs earlier and this results in a competition between CO oxidation charge cooling due to cylinder expansion, which freezes CO chemistry.
- At all SOIs ISHC is highest for DM followed by DP and DG dual fuel combustion. This indicates that the reactivity of the low-reactivity fuel clearly influences engine-out HC emissions. Lower reactivity of methane results in high engine-out HC emissions while propane and gasoline are more reactive compared to methane yielding low engine-out HC emissions.

- Using zero-dimensional simulations of n-dodecane, the presence of methane, propane, and iso-octane (representing gasoline) at engine-relevant conditions shows that at lean equivalence ratios, methane, propane, and iso-octane all delay the onset of n-dodecane LTHR. Methane and propane also suppress volumetric heat release while iso-octane slightly enhances the magnitude of low temperature heat release.
- In dual fuel combustion, it is easier for the spatially distributed ignition centers to sustain combustion into the surrounding fuel-air mixture for gasoline, followed by propane, and then methane.
- Higher CA5 variations are not accompanied by corresponding higher variations in CA50 in DG combustion but CA5 variations are always accompanied by higher variations in CA50 for DM and some cases of DP combustion.
- A linear correlation was observed between CA5 and CA50 for DM and DP combustion but not for DG combustion, indicating that the combustion phasing (CA50) can be controlled via commanded SOI for both DM and DP combustion, but not controlled as easily for DG combustion.
- No slow burn cycles were observed for DG combustion for any diesel SOI investigated. For early SOIs, many more slow burn cycles were observed for DM combustion than for DP combustion. This indicated that slow burn cycles in DM and DP combustion can be controlled by optimizing SOI.
- Since gasoline is more reactive than propane and methane; fewer diesel ignition centers can apparently sustain combustion, thus decreasing cyclic combustion variations in DG combustion. By comparison, a robust spatial distribution of

diesel ignition centers is required for decreasing cyclic combustion variations and to achieve more complete combustion for DM and DP.

- DP exhibited longer ignition delays compared to DM and DG for the same diesel SOIs. This is likely due to propane inhibiting diesel LTHR causing slower reaction rates and a slower rate of temperature increase inside the cylinder
- Normalized IMEP first order return maps for DG show stochastic behavior for all diesel SOIs. Similar IMEP return maps for DP for SOIs of 310, 320, and 330 CAD show stochastic behavior as well but some level of determinism may be present for diesel SOIs of 280, 290 and 300 CAD. Similarly, normalized IMEP return maps for DM for diesel SOIs of 320, and 330 CAD show stochastic behavior but again, some determinism may be present for diesel SOIs of 280, 290 300 and 310 CAD.
- Normal probability plots of IMEP provide more evidence to suggest deterministic behavior at early diesel SOIs for DM and DP combustion. On the other hand, for DG combustion, the normal probability plots of IMEP indicate stochastic behavior with very little (or no) determinism.

3.8 Acknowledgements

The author(s) acknowledge the Alliance for Sustainable Energy, LLC, Managing and Operating Contractor for the National Renewable Energy Laboratory for the US Department of Energy for partial funding for the development of this article.

3.9 References

1. Krishnan, S. R., Srinivasan, K. K., Singh, S., Bell, S. R., Midkiff, K. C., Gong, W., Fiveland, S. B., and Willi, M., 2004, "Strategies for Reduced NO_x Emissions in Pilot-Ignited Natural Gas Engines," *ASME J. Eng. Gas Turbines Power*, 126(3), pp. 665–671.
2. A.P. Carlucci, D. Laforgia, et al. Combustion and emissions control in diesel–methane dual fuel engines: the effects of methane supply method combined with variable in-cylinder charge bulk motion *Energy Convers Manage*, 52 (2011), pp. 3004-3017
3. Polk, A. C., Carpenter, C. D., Scott Guerry, E., Dwivedi, U., Kumar Srinivasan, K., Rajan Krishnan, S., and Rowland, Z. L. (April 18, 2014). "Diesel-Ignited Propane Dual Fuel Low Temperature Combustion in a Heavy-Duty Diesel Engine." *ASME. J. Eng. Gas Turbines Power*. September 2014; 136(9): 091509. <https://doi.org/10.1115/1.4027189>
4. Gibson, C. M., Polk, A. C., Shoemaker, N. T., Srinivasan, K. K., and Krishnan, S. R. (April 20, 2011). "Comparison of Propane and Methane Performance and Emissions in a Turbocharged Direct Injection Dual Fuel Engine." *ASME. J. Eng. Gas Turbines Power*. September 2011; 133(9): 092806. <https://doi.org/10.1115/1.4002895>
5. Choi, D., Jung, H., Chi, Y., and Joo, S., "Diesel/Gasoline Dual Fuel Powered Combustion System based on Diesel Compression Ignition Triggered Ignition Control," *SAE Technical Paper 2013-01-1718*, 2013, <https://doi.org/10.4271/2013-01-1718>.
6. J. Benajes, A. García, J. Monsalve-Serrano, et al. Achieving clean and efficient engine operation up to full load by combining optimized RCCI and dual-fuel diesel-gasoline combustion strategies *Energy Convers Manage*, 136 (2017), pp. 142-151

7. Stewart, J., Clarke, A., & Chen, R. (2007). An experimental study of the dual-fuel performance of a small compression ignition diesel engine operating with three gaseous fuels. *Proceedings of the Institution of Mechanical Engineers, Part D: Journal of Automobile Engineering*, 221(8), 943–956. <https://doi.org/10.1243/09544070JAUTO458>
8. K. Ryu Effects of pilot injection pressure on the combustion and emissions characteristics in a diesel engine using biodiesel–CNG dual fuel *Energy Convers. Manag.*, 76 (2013), pp. 506-516
9. J. Riffkin, Town gas as a fuel in the compression ignition engines, *Gas Oil Power*, 32 (35), 1937.
10. Huang, Z., Ji, L., Han, D., Yang, Z., & Lu, X. (2013). Experimental study on dual-fuel compound homogeneous charge compression ignition combustion. *International Journal of Engine Research*, 14(1), 23–33. <https://doi.org/10.1177/1468087412440908>
11. M.M. Abdelaal, A.H. Hegab, Combustion and emission characteristics of a natural gas-fueled diesel engine with EGR, *Energy Convers. Manag.* 64 (0) (2012) 301–312
12. Jha, P. R., Krishnan, S. R., & Srinivasan, K. K. (2019). Impact of methane energy fraction on emissions, performance and cyclic variability in low-load dual fuel combustion at early injection timings. *International Journal of Engine Research*. <https://doi.org/10.1177/1468087419892380>
13. K.A. Hodges, A. Aniello, S.R. Krishnan, K.K. Srinivasan Impact of propane energy fraction on diesel-ignited propane dual fuel low temperature combustion *Fuel*, 209 (2017), pp. 769-775
14. Srinivasan, K. K., Krishnan, S. R., and Qi, Y. (September 12, 2013). "Cyclic Combustion Variations in Dual Fuel Partially Premixed Pilot-Ignited Natural Gas Engines." *ASME. J. Energy Resour. Technol.* March 2014; 136(1): 012003. <https://doi.org/10.1115/1.4024855>
15. R.G. Papagiannakis, C.D. Rakopoulos, D.T. Hountalas, D.C. Rakopoulos Emission characteristics of high speed, dual fuel, compression ignition engine operating in a wide range of natural gas/diesel fuel proportions *Fuel*, 89 (2010), pp. 1397-1406

16. Karim, G., Liu, Z., and Jones, W., "Exhaust Emissions from Dual Fuel Engines at Light Load," SAE Technical Paper 932822, 1993, <https://doi.org/10.4271/932822>.
17. D.C. Rakopoulos, C.D. Rakopoulos, E.G. Giakoumis, R.G. Papagiannakis, D.C. Kyritsis Experimental-stochastic investigation of the combustion cyclic variability in HSDI diesel engine using ethanol–diesel fuel blends *Fuel*, 87 (2008), pp. 1478-1491
18. Soltau, J. P. (1960). Cylinder Pressure Variations in Petrol Engines. Proceedings of the Institution of Mechanical Engineers: Automobile Division, 14(1), 99–117. https://doi.org/10.1243/PIME_AUTO_1960_000_014_02
19. Patterson, D., "Cylinder Pressure Variations, A Fundamental Combustion Problem," SAE Technical Paper 660129, 1966, <https://doi.org/10.4271/660129>.
20. Cole, D. and Mirsky, W., "Mixture Motion - Its Effect on Pressure Rise in a Combustion Bomb: A New Look at Cyclic Variation," SAE Technical Paper 680766, 1968, <https://doi.org/10.4271/680766>.
21. R. K. Barton, S. S. Lestz, W. E. Meyer, "An Empirical Model for Correlating Cycle-by-Cycle Cylinder Gas Motion and Combustion Variations of a Spark Ignition Engine," SAE Paper No. 710163, 1971.
22. Young, Michael B. "Cyclic dispersion in the homogeneous-charge spark-ignition engine—a literature survey." SAE Transactions (1981): 49-73.
23. Matekunas, Frederic A. "Modes and measures of cyclic combustion variability." SAE transactions (1983): 1139-1156.
24. Ozdor, Nir, Mark Dulger, and Eran Sher. "Cyclic variability in spark ignition engines a literature survey." SAE transactions (1994): 1514-1552.
25. Wagner, R. M., et al. "Prior-Cycle Effects in Lean Spark Ignition Combustion - Fuel/Air Charge Considerations." SAE Transactions, vol. 107, 1998, pp. 1574–1584. JSTOR,
26. Daw, C. S., et al. "Controlling Cyclic Combustion Variations in Lean-Fueled Spark-Ignition Engines." AIP Conference Proceedings. Vol. 622. No. 1. American Institute of Physics, 2002.
27. Agarwal, Avinash Kumar. Experimental investigation on intake air temperature and air-fuel ratio dependence of random and deterministic cyclic variability in a

- homogeneous charge compression ignition engine. No. 2011-01-1183. SAE Technical Paper, 2011.
28. Finney, Charles EA, et al. "Invited review: a review of deterministic effects in cyclic variability of internal combustion engines." *International Journal of Engine Research* 16.3 (2015): 366-378.
 29. Selim, Mohamed YE. "Effect of engine parameters and gaseous fuel type on the cyclic variability of dual fuel engines." *Fuel* 84.7-8 (2005): 961-971.
 30. Sun, Jiafeng, Joshua A. Bittle, and Timothy J. Jacobs. "Cyclic Variability in Diesel/Gasoline Dual-Fuel Combustion on a Medium-Duty Diesel Engine." ASME 2013 Internal Combustion Engine Division Fall Technical Conference. American Society of Mechanical Engineers Digital Collection, 2013.
 31. Wang, Q., Wang, B., Yao, C., Liu, M., Wu, T., Wei, H. and Dou, Z., 2016. Study on cyclic variability of dual fuel combustion in a methanol fumigated diesel engine. *Fuel*, 164, pp.99-109.
 32. Chen, Z., Yao, C., Yao, A., Dou, Z., Wang, B., Wei, H., Liu, M., Chen, C. and Shi, J., 2017. The impact of methanol injecting position on cylinder-to-cylinder variation in a diesel methanol dual fuel engine. *Fuel*, 191, pp.150-163.
 33. Jamrozik, A., Tutak, W., Gnatowska, R. and Nowak, Ł., 2019. Comparative analysis of the combustion stability of diesel-methanol and diesel-ethanol in a dual fuel engine. *Energies*, 12(6), p.971.
 34. Klos, D. and Kokjohn, S.L., 2015. Investigation of the sources of combustion instability in low-temperature combustion engines using response surface models. *International Journal of Engine Research*, 16(3), pp.419-440.
 35. Jupudi, R.S., Finney, C.E., Primus, R., Wijeyakulasuriya, S., Klingbeil, A.E., Tamma, B. and Stoyanov, M.K., 2016. Application of high performance computing for simulating cycle-to-cycle variation in dual-fuel combustion engines (No. 2016-01-0798). SAE Technical Paper.
 36. Heywood JB. *Internal combustion engine fundamentals*. 2nd ed. New York: McGraw-Hill, 2018.
 37. Stewart, J., Clarke, A., & Chen, R. (2007). An experimental study of the dual-fuel performance of a small compression ignition diesel engine operating with three gaseous fuels. *Proceedings of the Institution of Mechanical Engineers, Part D*:

38. Engineering ToolBox, (2003). Gases - Explosion and Flammability Concentration Limits. [online] Available at: https://www.engineeringtoolbox.com/explosive-concentration-limits-d_423.html [27 3. 2020].
39. Gatowski J, Balles EN, Chun K, Nelson F, Ekchian J and Heywood JB. Heat release analysis of engine pressure data. SAE technical paper 841359, 1984.
40. Li S. A temperature-dependent model of ratio of specific heats applying in diesel engine. Master thesis, NTNU, Trondheim, 2017.
41. Egnell R. Combustion diagnostics by means of multizone heat release analysis and NO calculation. SAE technical paper 981424, 1998, <https://doi.org/10.4271/981424>
42. Brunt M, Rai H and Emtage A. The calculation of heat release energy from engine cylinder pressure data. SAE technical paper 981052, 1998, <https://doi.org/10.4271/981052>
43. Jha, P.R.; Srinivasan, K.K.; Krishnan, S.R. Influence of Swirl Ratio on Diesel-Methane Dual Fuel Combustion: A CFD Investigation. In Proceedings of the ASME 2017 Internal Combustion Engine Division Fall Technical Conference, Seattle, WA, USA, 15–18 October 2017.
44. Sundar Rajan Krishnan, Kalyan Kumar Srinivasan, Mostafa Shameem Raihan, The effect of injection parameters and boost pressure on diesel-propane dual fuel low temperature combustion in a single-cylinder research engine, fuel, volume 184, 2016, Pages 490-502, ISSN 0016-2361, <https://doi.org/10.1016/j.fuel.2016.07.042>.
45. Frassoldati A, D’Errico G, Lucchini T, Stagni A, Cuoci A, Faravelli T, et al. Reduced kinetic mechanisms of diesel fuel surrogate for engine CFD simulations. Combust Flame 2015; 162(10): 3991–4007.
46. Chang, J., Güralp, O., Filipi, Z., Assanis, D. et al. New Heat Transfer Correlation for an HCCI Engine Derived from Measurements of Instantaneous Surface Heat Flux. SAE Technical Paper. 2004, 2004-01-2996.
47. Caton JA. Combustion phasing for maximum efficiency for conventional and high efficiency engines. Energy Convers Manage 2014; 77: 564–576.

48. Srna, A., Bolla, M., Wright, Y. M., et al., Effect of methane on pilot fuel auto-ignition in dual-fuel engines, Proc. Of Comb. Inst., Vol. 37, Iss. 4., 2019, pp. 4741-4769.
49. Srinivasan KK, Krishnan SR, Jha PR and Mahabadipour H. Cyclic combustion variations in diesel–natural gas dual fuel engines. In: Srinivasan K, Agarwal A, Krishnan S and Mulone V (eds) Natural gas engines. Energy, environment, and sustainability. Singapore: Springer, 2019, pp.329–358.
50. NIST/SEMATECH e-Handbook of Statistical Methods. <<http://www.itl.nist.gov/div898/handbook/>>; 2008.
51. Maurya, R.K. and Agarwal, A.K., 2013. Experimental investigation of cyclic variations in HCCI combustion parameters for gasoline like fuels using statistical methods. Applied energy, 111, pp.310-323.

CHAPTER IV

NUMERICAL INVESTIGATION OF DUAL FUEL ENGINE COMBUSTION AT EARLY INJECTION TIMINGS FOR LOW LOAD OPERATION

4.1 Abstract

The present work focuses on the development and validation of a CFD simulation of diesel-methane dual fuel combustion in a single-cylinder research engine (SCRE). The validated model is used to provide insight about dual fuel combustion at low loads and subsequent parametric studies are performed to explore strategies for unburned hydrocarbon and carbon monoxide emissions. The computational campaign consisted of evaluating three different diesel injection timings of 310, 320, and 330 CAD at a methane percent energy substitution of 80%, 5.1 bar IMEP, 500 bar diesel injection pressure, and 1.5 bar manifold pressure. Combustion, performance, and emissions results are presented and compared with experimental data. The model's ability to capture combustion and emissions trends is demonstrated by good agreement with experimental data. The validated model is further utilized to provide insights into the nature of dual fuel combustion, particularly, the effect of methane on diesel autoignition. Various spray targeting strategies are explored for the reduction of hydrocarbons and carbon monoxide emissions and enhancement of fuel conversion efficiencies at low engine load operation. Analysis of the computational results showed that the onset of both low-temperature heat release and high-temperature heat release of dodecane is delayed by methane. For early

diesel injection in a dual fuel engine at low load, initial high-temperature combustion comes from dodecane combustion followed by combustion of methane. Most of the methane that does not get consumed resided in crevices and areas near the piston top and liner. For diesel injection timing of 310 CAD, spray targeting revealed that two sets of included angles, 105 degrees, and 150 degrees, with 8 nozzles seem to simultaneously reduce NO, CO, and HC by 60%, 12%, and 11%, respectively while increasing closed-cycle indicated fuel conversion efficiencies (CC_IFCE) by 2.6% relative to the baseline for this study, which is the 8 hole nozzle with 150 degrees included angle.

4.2 Introduction

The internal combustion engine is one of the major contributors to the global greenhouse footprint. Due to the greenhouse effects from the exhaust gases of the internal combustion (IC) engine, regulation has been put in place to decrease carbon footprint and emissions from the internal combustion engine. There are several advanced combustion strategies proposed to reduce carbon footprint and emissions from the internal combustion engine [1,2,3]. Dual fuel combustion is one such advanced combustion strategy that has the potential to have a diesel engine-like efficiency and bring down carbon footprint and reduce emissions. There have been several dual fuel combinations like diesel-natural gas[4], diesel -hydrogen[5], diesel-methane[6], diesel-propane[7], diesel -gasoline[8], biodiesel-methane[9], DME-methane[10],

Dual fuel combustion involves the combustion of two different fuels, one with high reactivity and another with low reactivity. Typically, reactivity is characterized by octane and cetane numbers. A high octane number fuel exhibits high resistance to

autoignition, while a high cetane number fuel exhibits a high propensity for autoignition. In conventional dual fuel combustion, a small amount of high reactivity fuel (diesel in this case) is injected to start the combustion process in the low reactivity fuel. The ensuing heat release shape can be considered to consist of three overlapping components according to Karim [11]. The first component is due to the combustion of the diesel fuel, the second is due to the entrainment of methane fuel present near the ignition zone, and the third is due to the pre-ignition reaction activity and flame propagation [11]. In dual fuel combustion, diesel is typically the high reactivity fuel, and methane (a major constituent of natural gas) the low reactivity fuel. Natural gas is an attractive choice and a good substitute for fossil fuels due to the widespread availability of natural gas and the continuous growth in natural gas production in the US and the low H/C ratio [12]. US natural gas production has exceeded the national consumption rate and started exporting natural gas from the year 2017 [12]. Natural gas has a high octane rating which indicates that it has high knock-resistance, which allows it to be used in a diesel engine with a high compression ratio, unlike gasoline. Another advantage of dual fueling, which has been stated several times in literature is that existing diesel engines can be used directly with minor modifications in hardware and software. In this case, diesel is directly injected inside the engine cylinder using a high-pressure, common-rail fuel injection system. There are two main ways in which methane can be introduced in the combustion chamber one using high-pressure direct injection of methane [13] and another by injecting methane fuel inducted in the intake manifold[4,14]. The emissions trends of such diesel methane dual fuel combustion at low engine load also needs to be discussed. Due to predominantly lean equivalence ratios of the natural-gas air mixture, post-combustion

temperatures are likely low; as a result, NO_x emissions are expected to be lower than for corresponding neat diesel operation[6,15,16]. For a well-calibrated dual fuel engine, particulate matter (PM) formation is also generally low generally due to the fact that diesel injected has enough time to mix due to long ignition delay times and the predominantly lean natural-gas equivalence ratios. Carbon monoxide (CO) and hydrocarbon (HC) emissions at low engine loads are generally high[6,16]. The increase in HC and CO emissions is due to the inability to sustain combustion due to lean fuel-air ratios, fuel trapped inside crevices, and quench layer within the cylinder. Due to the lower carbon-to-hydrogen (C/H) ratio the CO₂ emissions decrease. But, the risk of methane slip exists, which is usually mitigated by appropriate design of diesel oxidation catalyst in the after-treatment system

To eliminate or to reduce the high HC and CO emissions at low loads a thorough understanding of the in-cylinder combustion mechanics of diesel methane dual fuel combustion is required. Computational fluid dynamics (CFD) simulations can be used as an alternative to experiments to understand the complex physics of combustion in dual fuel engines and perform a parametric study to find optimal operating space quickly and cheaply.

In diesel methane dual fuel combustion, diesel auto ignites due to compression, which combusts surrounding air methane mixture and helps to combust the rest of the fuel air mixture inside the cylinder. Methane has a high octane number which gives good anti-knock properties, but this also slows the progress of the combustion process at low engine loads inside the combustion chamber. This pushes most of the

combustion to occur after the top dead center (TDC) where CO and HC chemistry freezes and leading to high HC and CO emissions. Therefore, a proper understanding of diesel-assisted methane ignition is required to eliminate this problem. So, to develop a better understanding of this process, it is better to start from the ignition process itself. Most studies have found methane increases the ignition delay of diesel [17,18]. Several studies were performed to study the effects of methane on diesel auto-ignition [19,20,21,22]. Masouleh et al. [19] numerically studied ignition characteristics of n-dodecane and methane mixture. Their study shows that n-dodecane decomposition in presence of methane is delayed by methane. They also observed that the ratio of dodecane to methane was a critical parameter to determine the extent of the delay. Ignition delay decreases with an increase in n-dodecane to methane ratio. Kahila et al. [20] studied diesel spray injection into a lean methane air mixture using Engine Combustion Network (ECN) Spray A configuration. Their finding concluded n-dodecane combustion in methane air mixture as a volumetric process. They also observed n-dodecane low and high-temperature chemistry are inhibited by methane throughout the combustion process. Their sensitivity analysis of n-dodecane combustion in air methane mixture revealed that early n-dodecane decomposition is affected by methane consuming OH radical and forming methyl radical (CH₃) which in turn activates other inhibition reactions influencing n-dodecane low and high-temperature chemistry. Similarly, Srna et al. [21] studied the ignition behavior of n-dodecane micro pilot spray in a lean methane air mixture using laser diagnostics on a rapid compression expansion machine (RCM). For low and high-temperature ignition detection they utilized CH₂O-PLIF and OH* chemiluminescence, respectively. They observed methane postpones cool flame

reactions, which leads to delaying high-temperature reactions. More recently Park et al.[22] studied the micro-pilot ignition process and their study revealed that low-temperature ignition does not expand over the entire spray region for non-methane cases but for methane cases, it spreads over the entire spray and even outside of the spray envelop. This increases the flame surface area when methane is present.

With this understanding of the effects of methane on diesel autoignition characteristics, we can focus our attention on the full engine simulation study performed. There have been several modeling and simulation performed on dual fuel engines like diesel-natural gas [23], diesel -LPG [24], dimethyl ether -natural gas [25], etc. . For this paper, we will concentrate our attention on numerical studies done on diesel-natural gas/methane engines. Several numerical studies [26,27] have been performed to understand complex combustion phenomena occurring inside dual fuel combustion. Different combustion model has been utilized by different researchers to study dual fuel combustion of the diesel-natural gas engine. Singh et al. [28] utilized a characteristic-time diesel combustion model to compare simulation results with experiments for pilot ignited natural gas dual fuel engines. Their focus was to explain experimentally observed emission and combustion behavior. Singh et al. [29] later utilized G-equation based model to investigate dual fuel partially premixed compression ignition engines. They were able to capture emission and combustion trends of dual fuel engines using diesel pilot as ignition source with natural gas air mixture inside cylinder. Similarly, Jha et al. [30] used SAGE combustion modeling to capture diesel-methane conventional dual fuel combustion and proposed to increase the swirl ratio to reduce HC and CO emissions at low engine loads. Elder et al [31] utilized Extended Coherent Flame Model with the 3

Zones approach (ECFM-3Z) to model diesel ignited gas engine dual fuel combustion. They found reasonable agreement between simulation and experimental results. This shows various combustion modeling approaches can be utilized to model dual fuel combustion.

Combustion and emission characteristics of diesel-methane dual fuel engines were computationally explored by Dai et al. [32]. They categorized the combustion region in the dual fuel engine for various diesel injection timings and concluded at such low loads dual fuel combustion was not supported by turbulent flame propagation but sequential local autoignitions. Aniello et al. [33] also numerically studied diesel methane dual fuel combustion at low load in an SCRE at different injection timings. Their finding concluded at such low load and low diesel concentration charge is not able to sustain combustion leading to high hydrocarbon and carbon monoxide emissions. A similar diesel injection timing sweep was performed experimentally and computationally by Yousefi et al. [34] on diesel-natural gas dual fuel engines. They observed OH spatial distribution more uniform with advanced diesel injection timings indicating predominant premixed combustion mode. Gharehghani et al. [35] studied the effects of mixture formation on diesel combustion phenomena in a dual fuel mode operation at different swirl and tumble ratios. They concluded turbocharging enhances the swirl ratio, angular momentum which improves quality and leads to higher percentage utilization of natural gas which brings down emissions and improves fuel efficiency. Fakhari et al.[36] studied the effects of temperature and pressure at inlet valve closing (IVC) on diesel-natural gas combustion and found an increase in pressure and temperature at IVC increases thermal efficiency. They also observed ringing intensity (RI) increases with an increase in

temperature at IVC while it decreases with an increase in pressure at IVC. Bartolucci et al. [37] simulated multiple pilot diesel injection for diesel methane dual fuel low-temperature combustion (LTC) for a single-cylinder research engine (SCRE). The study found that stable combustion is not sustained for post-injection during expansion stroke at low load conditions and low diesel concentrations.

The computational study can also be utilized to optimize new hardware design changes' impact on performance and emissions. Cameretti et al.[38] studied diesel-natural gas dual fuel engine using one-dimensional and a three-dimensional code to optimize engine performance and emissions. They proposed that a one-dimensional study can be performed to see the overall behavior of the engine by changing different parameters like boost pressure, fuel injection, inducted mass flow, and others while three-dimensional results can be used to explain why such behaviors occur utilizing boundary condition from the one-dimensional study. Since lots of parameters influence the operation of dual-fuel engine operation, this tool utilizing one-dimensional and three-dimensional can be utilized with a limited computational effort to reach a final optimized configuration. Donateo et al. [39] computationally performed an optimization process on compression ratio, injector hole position, and diesel fuel (quantity, pressure, and injection timing). They used an optimized point to perform a piston bowl geometry study and observed for a better spread of combustion in the squish region to improve engine performance and emissions. Similarly, Shojae et al [40] using CFD code studied the effects of injection angle and bowl depth on engine performance and exhaust emissions. They found that both NO emissions and indicated power increase with an increase in piston bowl center depth.

Kakaee et al. [41] utilize both LES and RANS approaches to study RCCI combustion of a diesel-natural gas diesel engine and found a good level of agreement between LES and RANS for prediction of cylinder pressure and heat release rate. A similar study on RCCI engine with RANS and LES was performed by Liu et al. [42] and their study found both LES and RANS predicted similar heat release features and chemical pathways. These studies suggest RANS simulation is relevant to get a bulk picture of the engine combustion process considering the computational expense.

Accurately capturing dual fuel combustion process requires hundreds of species and thousands of reactions. But, including hundreds of species and thousands of reactions can be computationally very expensive. For practical purposes, several researchers have reduced the full chemical kinetics mechanism and have developed reduced chemical kinetic mechanisms for dual fuel combustion. For example, Hockett et al. [43] using a direct relation graph method optimized the chemical kinetic mechanisms available for n-heptane and natural gas to be used for simulating dual fuel combustion. This mechanism has 141 species and 709 reactions and was able to predict experimentally obtained results. Similarly, Rahimi et al. [44] using a genetic algorithm-based approach optimized the chemical kinetic mechanisms available for n-heptane and natural gas to be used for simulating dual fuel combustion. This reduced mechanism included 76 chemical species and 464 reactions. A good prediction for a large bore medium speed diesel-natural gas dual fuel combustion was obtained using the Rahimi mechanism by Wijeyakulasuriya et al. [45]. In this work POLIMI_RED mechanism [46] has been used, which includes 96 chemical species and 993 reactions and has been derived from POLIMI total mechanism. It has been used by several researchers [20, 47,48] and their findings suggest that all the

relevant reaction pathways for low temperature and high-temperature oxidation of diesel and methane are present in POLIMI_RED mechanism, and therefore it could be used without further modification within the dual-fuel framework.

In this work, we have developed a numerical model suited for diesel-methane dual fuel combustion which is able to capture the combustion features and trends for different diesel injection timings (310,320, and 330 CAD). The main objective of this chapter are:

- Explore the impact of methane on diesel autoignition and provide insights into nature of dual fuel combustion at advanced injection timings at low load conditions.
- Investigate spatio-temporal evolution of oxides of nitrogen, hydrocarbon, and carbon monoxide emissions at low load operation in dual fuel engines
- Perform parametric investigations to explore strategies to mitigate unburned HC and CO emissions from dual fuel combustion at low engine loads.

4.3 Numerical background

CONVERGECFD 3.0 software was used to perform full engine cycle simulation of diesel-methane dual fuel combustion in a single cylinder research engine (SCRE).

Since engine simulation consists of moving parts like piston, intake, and exhaust valves, generating a suitable computational grid is critical to obtaining good predictions.

CONVERGE CFD automatically generates the appropriate orthogonal structured grid at runtime for a given set of grid and control parameters. This automatic grid generation feature was very helpful in setting up moving boundary problems such as those encountered in internal combustion engines and saved a lot of time. Simulation was

performed on full geometry due to asymmetric nature of piston using RANS approach due to large number of computational cells involved.

4.3.1 Governing equations

The equations for conservation of mass, momentum, and energy, turbulence, and the transport of passive scalars and species are solved to resolve the reactive flow dynamics.

4.3.1.1 Mass and momentum transport

The compressible form of the mass conservation is:

$$\frac{\partial \rho}{\partial t} + \frac{\partial u_i}{\partial x_i} = S \quad (4.1)$$

The compressible form of the momentum transport equation is:

$$\frac{\partial \rho u_i}{\partial t} + \frac{\partial \rho u_i u_j}{\partial x_j} = -\frac{\partial P}{\partial x_i} + \frac{\partial \sigma_{ij}}{\partial x_j} + S_i \quad (4.2)$$

where the viscous tensor (σ_{ij}) is given by:

$$\sigma_{ij} = \mu \left(\frac{\partial u_i}{\partial x_j} + \frac{\partial u_j}{\partial x_i} \right) + \left(\mu' - \frac{2}{3} \mu \right) \left(\frac{\partial u_k}{\partial x_k} \right) \delta_{ij} \quad (4.3)$$

When a turbulent model is activated the viscosity is represented by total viscosity which is made up by two terms:

$$\mu_{tot} = \mu_{mol} + C_\mu \rho \frac{k^2}{\varepsilon} \quad (4.4)$$

In the above equations ρ is the density, u is the velocity, S is the source term due to evaporation, gravitational acceleration, spray, or mass sources, P is the pressure, μ is the viscosity, μ' is the dilatational viscosity and δ_{ij} is the Kronecker delta function, μ_{mol} is the molecular viscosity, C_μ is the turbulent model constant, k is the turbulent kinetic energy and ε is the turbulent dissipation.

4.3.1.2 Equation of state

Equation of state is required to have a well-defined and closed problem for a compressible flow. Momentum and mass transport are coupled with equation of state and utilized to find density, pressure and temperature. Ideal gas, Redlich-Kwong (RK), Redlich-Kwong-Soave (RKS), and Peng-Robinson (PR) are some of the available options in CONVERGE for equation of state.

The well-known ideal gas equation of state is:

$$\frac{P}{\rho} = \frac{R}{W} T \quad (4.5)$$

where R is the universal gas constant, W the molecular weight and T the absolute temperature. The general form of equation of state (RK, RKS, PR), which represent real gas can be written as follows:

$$P = \frac{RT}{v - b} - \frac{a}{v^2 + uvb + wb^2} \quad (4.6)$$

where R is the universal gas constant, W is the molecular weight, and u , w , a and b are coefficients of the RK, RKS and PR equations of state.

4.3.1.3 Energy transport

The energy conservation equations for a compressible flow is given by:

$$\begin{aligned} \frac{\partial \rho e}{\partial t} + \frac{\partial u_j \rho e}{\partial x_j} = & -P \frac{\partial u_j}{\partial x_j} + \sigma_{ij} \frac{\partial u_i}{\partial x_j} + \frac{\partial}{\partial x_j} \left(K \frac{\partial T}{\partial x_j} \right) \\ & + \frac{\partial}{\partial x_j} \left(\rho D \sum_m h_m \frac{\partial Y_m}{\partial x_j} \right) + S \end{aligned} \quad (4.7)$$

where e is the specific internal energy, K is the thermal conductivity, T is the local temperature, D is the mass diffusion coefficient, h_m is the specific enthalpy and Y_m is the mass fraction of species m . When the turbulent model is activated the conductivity is replaced by the turbulent conductivity which is given by

$$K_t = K + c_p \frac{\mu_t}{Pr_t} \quad (4.8)$$

where c_p is specific heat at constant pressure, μ_t is the turbulent viscosity and Pr_t is the turbulent Prandtl number.

In the global energy transport equation in addition to the classic convection and diffusion terms, there are 4 more terms.

- I) First-term is a pressure work term, $-P \frac{\partial u_j}{\partial x_j}$ to account for compression and expansion
- II) The second term is a viscous dissipation term $\sigma_{ij} \frac{\partial u_i}{\partial x_j}$ takes into account the production of heat due to the kinetic energy dissipations
- III) The third term is the species diffusion term $\frac{\partial}{\partial x_j} \left(\rho D \sum_m h_m \frac{\partial Y_m}{\partial x_j} \right)$ accounts for the energy transport due to species diffusion

- IV) The fourth term is a source term that is added to account for user-specified energy sources and dissipations.

4.3.1.4 Species transport

The compressible form of the species conservation equation is:

$$\frac{\partial \rho_m}{\partial t} + \frac{\partial \rho_m u_j}{\partial x_j} = \frac{\partial}{\partial x_j} \left(\rho D \frac{\partial Y_m}{\partial x_j} \right) + S_m \quad (4.9)$$

$$Y_m = \frac{\rho_m}{\rho} \quad (4.10)$$

$$D = \frac{\nu}{Sc} \quad (4.11)$$

$$D_t = \frac{\nu_t}{Sc_t} \quad (4.12)$$

In the above equations, u is the velocity, ρ is the density, ρ_m is the density of species m , S_m is the source term, Y_m is the mass fraction of species m , D is the mass diffusion coefficient and Sc is the Schmidt coefficient. When a turbulent model is activated the mass diffusion coefficient is replaced by the turbulent mass diffusion coefficient (D_t), Sc_t is the turbulent Schmidt number, S_m is the generation term per unit of volume by chemical reactions.

4.3.1.5 Passive transport

Some implemented features in CONVERGE as soot and NO_x models require the definition of passives and a passive transport equation. The solution of this transport equation does not affect the solution of other ones. Its conventional form is the following equation:

$$\frac{\partial \rho \phi}{\partial t} + \frac{\partial \rho u_i \phi}{\partial x_i} = \frac{\partial}{\partial x_i} \left(\rho D \frac{\partial \phi}{\partial x_i} \right) + S \quad (4.13)$$

$$D = \frac{\nu}{Sc} \quad (4.14)$$

where u is the velocity, S is the source term, D is the mass diffusion coefficient, ρ is the density, Sc is the Schmidt number, and ϕ is the passive scalar.

4.3.2 Numerical approach

4.3.2.1 Finite volume

Conservation equations are solved numerically using the finite volume method. One of the advantages of doing so is that this method conserves transported quantities for regular or irregularly shaped cells. All the values are stored at the center of each computational cell by CONVERGE. Where values are required at cell surfaces, they are obtained either by simple cell averaging or upwind scheme.

$$\phi_{i+\frac{1}{2}} = \frac{1}{2} \phi_i + \frac{1}{2} \phi_{i+1} \quad (4.15)$$

$$\phi_{i+\frac{1}{2}} = \phi_i \quad (4.16)$$

Evenly interpolated surface values can be obtained using Equation 1 and an upwind scheme can be obtained using Equation 2.

4.3.2.2 PISO algorithm

The Pressure Implicit with Splitting of Operators (PISO) algorithm is used for pressure and velocity coupling in CONVERGE. The PISO algorithm starts with a predictor step where the momentum equation is solved, and the pressure is corrected and

re-applied to the momentum equation. After the momentum predictor and the first corrector step are completed, other transport equations are solved in series after that. If a second corrector is applied to solve pressure, momentum is updated with a new pressure value. And with this new updated value all other transport equations are re-solved.

Predictor step is shown below where the superscript * means most up-to-date and n is the previous know values:

$$\frac{\rho^n u_i^* - \rho^n u_i^n}{dt} = -\Delta_i p^* + H_i^n \quad (4.17)$$

Corrector step is shown below where ρ^* , and u_i^{**} are new unknowns

$$\frac{\rho^* u_i^{**} - \rho^n u_i^*}{dt} = -\Delta_i p^{**} + H_i^n \quad (4.18)$$

Additional details of the PISO algorithm can be found in CONVERGE 3.0 manual [49] and Issa's papers. [50] The Figure 4.1 below shows a representation of PISO algorithm.

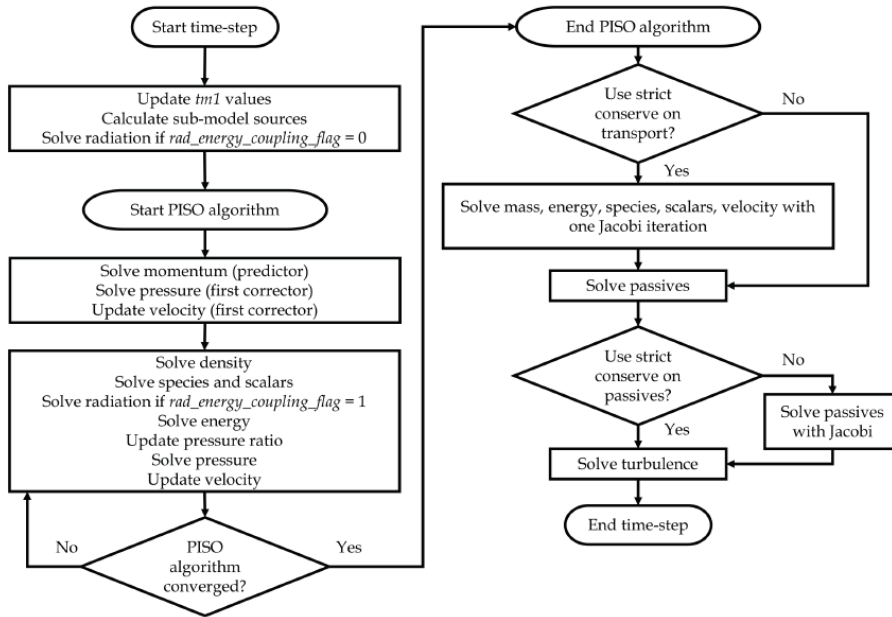


Figure 4.1 Scheme of the PISO algorithm [49]

4.3.2.3 Time-step control

To obtain stable, accurate, and computationally inexpensive results, it is necessary to use the appropriate Courant-Friedrichs-Lewy (CFL) number. The CFL number determines the number of cell solutions that will move forward for a given time step. There are two different settings in CONVERGE for time-step control. It has been found that variable time step is more stable and permit to reduce the computational time compared to fixed time method. So, for this work, a variable time-step is used. Mathematical representations of the speed of sound CFL number, the convective CFL number, and the diffusive CFL number are given below:

$$CFL_v = v \frac{\Delta t}{\Delta x^2} \quad (4.19)$$

$$CFL_u = u \frac{\Delta t}{\Delta x} \quad (4.20)$$

$$CFL_{mach} = c \frac{\Delta t}{\Delta x} \quad (4.21)$$

where, c is the speed of sound, u is the cell velocity, ν is the viscosity, Δt is the time-step and Δx is the grid spacing. While using variable time step method if the solution does not after specified number of iterations, then the time step is reduced [49]. The time step can be limited by specifying the maximum number of iterations for each governing equation and the maximum CFL number. There are also time step restrictions for sub-models. For example, the time step for spray evolution and chemical reactions in the spray sub-model and chemical reaction sub model is calculated using the following equation:

$$dt_{spray} = \min \left\{ \frac{\Delta x}{parcel_{velocity}} \right\} * mult_dt_spray \quad (4.22)$$

The spray parcel travels only one-time step when $mult_dt_spray=1$. In the same way, the dt is controlled during the chemical reactions of combustion:

$$dt_{chem} = dt_{prev} * \min \left\{ \frac{T}{\Delta T} \right\} * mult_dt_chem \quad (4.23)$$

Where the $mult_dt_chem$ is a parameter that controls the maximum change in the temperature in a single time step.

4.3.2.4 Turbulence modeling

Mixing of species, momentum, and energy are greatly affected by turbulence. So good turbulence model is necessary to obtain good results for dual fuel engine combustion simulation. To solve the energy cascade up to the smallest Kolmogorov scale

where it is dissipated the solver must have a discretized domain of the same order of magnitude, which increases the total number of computational cells causing it to be computationally expensive. For this work, Renormalization Group (RNG) k- ϵ turbulence model is used which is a two-equation Reynolds-Averaged Navier Stokes (RANS) turbulence model. Keeping computational expense in mind, this is used in scenarios where it is critical to obtain spatially resolved results. In this model, the actual velocity is decomposed into two velocity components: the ensemble averaged velocity and the fluctuating velocity as given below

$$u_i = \bar{u}_i + u'_i \quad (4.24)$$

where u_i is the actual velocity, \bar{u}_i is the average value and u'_i is the fluctuating component. Substituting the RANS decomposition into the Navier-Stokes equations leads to the following equations for mass and momentum transport:

$$\frac{\partial \bar{\rho}}{\partial t} + \frac{\partial \bar{\rho} \tilde{u}_j}{\partial x_j} = 0 \quad (4.25)$$

$$\begin{aligned} & \frac{\partial \bar{\rho} \tilde{u}_j}{\partial t} + \frac{\partial \bar{\rho} \tilde{u}_i \tilde{u}_j}{\partial x_j} \\ &= -\frac{\partial \bar{P}}{\partial x_i} + \frac{\partial}{\partial x_j} \left[\mu \left(\frac{\partial \tilde{u}_i}{\partial x_j} + \frac{\partial \tilde{u}_j}{\partial x_i} \right) - \frac{2}{3} \mu \frac{\partial \tilde{u}_k}{\partial x_k} \delta_{ij} \right] \\ &+ \frac{\partial}{\partial x_j} (-\bar{\rho} \widetilde{u'_i u'_j}) \end{aligned} \quad (4.26)$$

where the Favre average is defined for velocity as

$$\tilde{u}_i \triangleq \frac{\overline{\rho u_i}}{\bar{\rho}} \quad (4.27)$$

The introduction of RANS decomposition leads to an additional term called the Reynolds stresses that represent the effects of turbulence and introduces six unknown variables. [51] The Reynolds stresses τ_{ij} is given by

$$\tau_{ij} = -\bar{\rho} \widetilde{u'_i u'_j} \quad (4.28)$$

4.3.2.4.1 RNG k- ε turbulence model

For the present work the RNG k- ε is chosen over the standard k- ε model because the standard k- ε model is usually less accurate to model flows with high deformation rates. In the RNG k- ε model the turbulent normal stress values are constraints to ensure the non-negative value. This results in turbulent kinetic energy from the k- ε model always has a physically realistic value. For the RNG k- ε model, the Reynolds stress is given by

$$\tau_{ij} = -\bar{\rho} \widetilde{u'_i u'_j} = 2\mu_t S_{ij} - \frac{2}{3} \delta_{ij} \left(\rho k + \mu_t \frac{\partial \tilde{u}_i}{\partial x_j} \right) \quad (4.29)$$

The turbulent kinetic energy, k , is defined as

$$k = \frac{2}{3} \widetilde{u'_i u'_i} \quad (4.30)$$

The turbulent viscosity, μ_t , is defined as

$$\mu_t = C_\mu \rho \frac{k^2}{\varepsilon} \quad (4.31)$$

where k is the turbulent kinetic energy, μ_t is the turbulent viscosity, ε is the dissipation of turbulent kinetic and C_μ is the model constant that can tune for different flows. The mean strain rate tensor S_{ij} is given by:

$$S_{ij} = \frac{1}{2} \left(\frac{\partial \tilde{u}_i}{\partial x_j} + \frac{\partial \tilde{u}_j}{\partial x_i} \right) \quad (4.32)$$

The turbulent diffusion and turbulent conductivity terms that account for mass transport and energy transport, respectively, are given by the following equations:

$$D_t = \left(\frac{1}{Sc_t} \right) \mu_t \quad (4.32)$$

$$K_t = \left(\frac{1}{Pr_t} \right) \mu_t c_p \quad (4.33)$$

Where D_t is the turbulent diffusion, K_t is the turbulent conductivity, Sc_t is the turbulent Schmidt number and Pr_t is the turbulent Prandtl number. The transport equations for turbulent kinetic energy(k) and dissipation of turbulent kinetic energy(ε) are written as follows:

$$\frac{\partial \rho k}{\partial t} + \frac{\partial \rho u_i k}{\partial x_i} = \tau_{ij} \frac{\partial u_i}{\partial x_j} + \frac{\partial}{\partial x_j} \left(\frac{\mu + \mu_t}{Pr_k} \frac{\partial k}{\partial x_j} \right) - \rho \varepsilon + \frac{C_s}{1.5} S_s \quad (4.34)$$

$$\begin{aligned} \frac{\partial \rho \varepsilon}{\partial t} + \frac{\partial (\rho u_i \varepsilon)}{\partial x_i} &= \frac{\partial}{\partial x_j} \left(\frac{\mu + \mu_t}{Pr_\varepsilon} \frac{\partial \varepsilon}{\partial x_j} \right) + C_{\varepsilon 3} \rho \varepsilon \frac{\partial u_i}{\partial x_i} \\ &+ \left(C_{\varepsilon 1} \frac{\partial u_i}{\partial x_i} \tau_{ij} - C_{\varepsilon 2} \rho \varepsilon + C_s S_s \right) \frac{\varepsilon}{k} + S - \rho R \end{aligned} \quad (4.35)$$

where S_s is the source term from interaction with the spray and S is the user-specified source term. In the previous equation $C_{\varepsilon 1}$, $C_{\varepsilon 2}$ and $C_{\varepsilon 3}$ are model constant that account for compression and expansion and R is:

$$R = \frac{C_{\mu}\eta^3(1 - \eta/\eta_0) \varepsilon^2}{(1 + \beta\eta^3) k} \quad (4.36)$$

$$\eta = \frac{k}{\varepsilon} |S_{ij}| = \frac{k}{\varepsilon} \sqrt{2S_{ij}S_{ij}} \quad (4.37)$$

4.3.2.5 Spray model

In dual fuel engine, combustion diesel is directly injected into the cylinder at high pressures to ignite lean methane-air mixtures. So, it is necessary to correctly model the spray breakdown to evaporation process. Sprays play an important role in the mixing of fuel and air. Spray increases the surface area of injected diesel for rapid evaporation and combustion. It eventually affects ignition behavior and the overall combustion process of the engine combustion process. Once diesel is injected into the cylinder it goes through many processes like a breakup, collision, and coalescence until evaporation. The process of different processes taking place to spray is represented in Figure 4.2 [52].

When diesel is injected into the cylinder, there are numerous forces like aerodynamic forces, surface shear forces, centrifugal forces, and electrostatic forces acting against its momentum force. When this force leads to oscillation and perturbation to the liquid jet, it leads to the breakup of liquids into small droplets. This process is referred to as a primary breakup. The primary breakup is followed by the secondary breakup. Secondary breakup is the breakup of larger droplets formed during the primary breakup into smaller droplets due to disruptive force acting on it. These droplets may undergo collision and coalescence. These droplets may evaporate and mix with the surrounding air or air fuel mixture to form a combustible charge if the surrounding temperature is high enough. These charges combust under favorable conditions. We will

discuss the main process in a spray model as a breakup, collision, coalescence, and evaporation below:

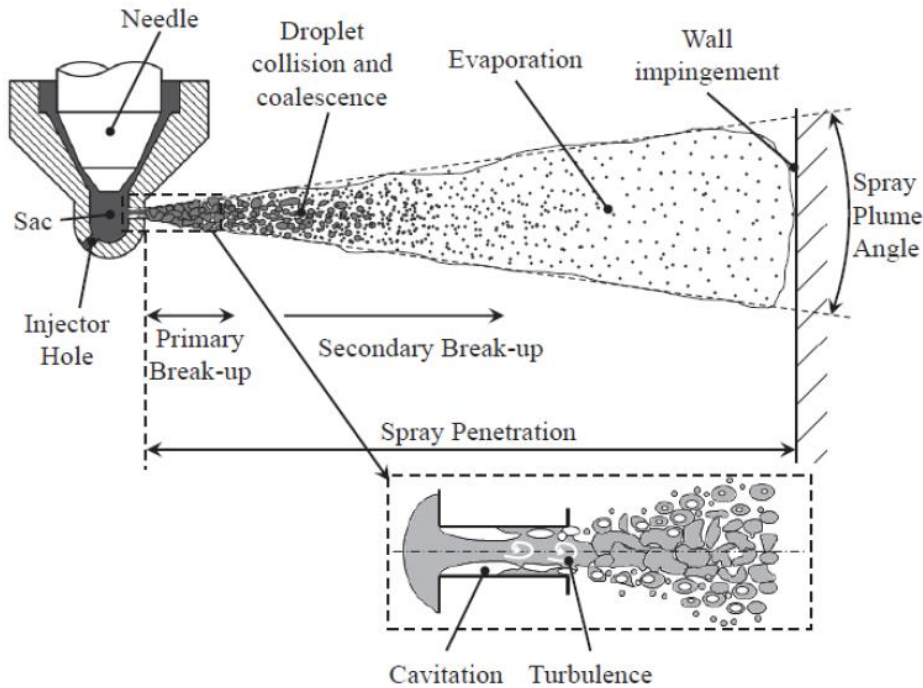


Figure 4.2 Physical processes for a liquid spray [52]

The Lagrangian approach is applied to solve the dynamics of the spray breakup from injection up to vaporization for liquid spray. Since in the Lagrangian approach each particle is tracked individually it can be computationally expensive. To reduce computational expenses, a group of identical drops with the same radius, temperature, and velocity is represented as a parcel in CONVERGE.

DIESEL2 from the CONVERGE library is chosen as the single-component liquid species for all simulations performed in this work. Viscosity, surface tension, the heat of vaporization, vapor pressure, conductivity, density, and specific heat as a function of critical temperature are obtained from CONVERGE library.

For modeling spray evolution, the blob injection approach is utilized. In this approach, the initial drop size is set equal to the real nozzle hole diameter. The spray rate shape, total injected mass, injection duration, injection pressure, and the discharge coefficient determine the instantaneous velocity of incoming spray from the nozzle. Flow contraction may occur while fuel flows through the nozzle hole. This is considered by introducing a contraction coefficient.

$$C_a = \frac{C_d}{C_v} \quad (4.38)$$

Where C_a is the area contraction coefficient, C_d is the discharge coefficient and C_v is the velocity contraction coefficient which is dynamically calculated based on the injection pressure at that time. The above equation suggests that when the effective area of the nozzle decreases the magnitude of drop velocities increases. Equation of motion is utilized to obtain drop velocity which is governed by the sum of drag and gravitational body forces:

$$\rho_l V_d \frac{dv_i}{dt} = F_{drag,i} + F_{g,i} \quad (4.39)$$

$$F_{drag,i} = C_D A_f \frac{\rho_g |U_i|}{2} U_i \quad (4.40)$$

$$F_{g,i} = \rho_l V_d g_i \quad (4.41)$$

In the above equations ρ_l is the liquid density, V_d is the drop volume, C_D is the drag coefficient, A_f is the drop's frontal area, ρ_g is the gas density and U_i is the drop-gas relative velocity. It is important to determine the drag coefficient for accurate spray

modeling. A dynamic drag model is used for all simulations performed in this work in which the drop shape varies per a distortion parameter, y . The Taylor Analogy Breakup (TAB) model [53] is used to determine this distortion parameter.

The drag coefficient is given by

$$C_D = C_{D,sphere}(1 + 2.632y) \quad (4.42)$$

where y is drop distortion from the TAB model and is given as

$$y(t) = We_c + e^{-t/t_d} \left[(y(0) - We_c) \cos(\omega t) + \frac{1}{\omega} \left(\frac{dy}{dt}(0) + \frac{y(0) - We_c}{t_d} \right) \sin(\omega t) \right] \quad (4.43)$$

Where,

$$We_c = \frac{C_f}{C_k C_b} We_g \quad (4.44)$$

$$We_g = \frac{\rho_g u^2 r_0}{\sigma} \quad (4.45)$$

$$\frac{1}{t_d} = \frac{C_d}{2} \frac{\mu_l}{\rho_l r_0^2} \quad (4.46)$$

$$\omega^2 = C_k \frac{\sigma}{\rho_l r_0^3} - \frac{1}{t_d} \quad (4.47)$$

Where We_g is the weber number which represents the ratio of the aerodynamic forces to the surface tension forces. ω is droplet oscillation frequency, C_k , C_f , C_d , and C_b are constants, σ is liquid surface tension, ρ_l is the liquid phase density

$C_{D,sphere}$ value is implemented according to drop Reynolds number from the equation below:

$$C_{D,sphere} = \begin{cases} 0.424 & Re \geq 100 \\ \frac{24}{Re} \left(1 + \frac{1}{6} Re^{\frac{2}{3}}\right) & Re \leq 1000 \end{cases} \quad (4.48)$$

In this work to model spray breakup, a modified Kelvin-Helmholtz and Rayleigh-Taylor (KH-RT) droplet breakup model is utilized. In the KH-RT model, the primary breakup of the intact liquid core is predicted by the KH instability model and both KH and RT instabilities are utilized to predict the secondary breakup of each droplet. The RT break-up model only affects drops beyond the break-up length. In the modified KH-RT model, the RT breakup model affects all drops outside the intact liquid core of the jet.

In the KH model, nozzle hole diameter d_0 is taken as the initial diameter of the parcel. Stability analysis for the liquid jet is performed for relatively large injected blobs. For other parcels and resulting drops, the breakup is calculated by assuming that the breakup drop radius r_c is proportional to the wavelength of the fastest-growing unstable surface wave as reported on the liquid jet stability analysis made by Reitz and Bracco [54]. More details of this model can be found in Reitz and Bracco [54].

$$r_c = B_0 \Lambda_{KH} \quad (4.49)$$

where B_0 is a model constant and Λ_{KH} is the wavelength. B_0 value is generally set to 0.61 as shown by Reitz's studies [55]. To calculate the rate of change of drop radius in a parent parcel the following equations are utilized:

$$\frac{dr_p}{dt} = -\frac{r_p - r_c}{\tau_{KH}} \quad (4.50)$$

Where,

$$\tau_{KH} = \frac{3.726B_1r_p}{\tau_{KH}\Omega_{KH}} \quad (4.51)$$

In above equations, τ_{KH} is the breakup time, B_1 is the breakup time constant related to the initial disturbance level on the liquid jet and its value is dependent on type of injector used and Ω_{KH} is the maximum grow rate found by Reitz[55]. Breakup of parcel leads to the creation of new child parcels into the domain when the fragment masses is enough to establish a new parcel. The normal velocity on the child parcel is determined by the following equation:

$$v_n = C_1 \Lambda_{KH} \Omega_{KH} \quad (4.52)$$

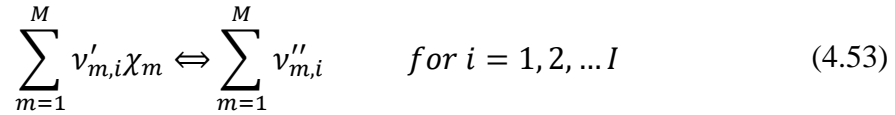
Where C_1 is a model constant.

Due to the high number of parcels, as a result of the breakup, the probability of collision and coalescence between them needs to be taken into account. For all the simulations performed in this work, the no time counter (NTC) collision model of Schmidt and Rutland [56] is used. In the NTC model, the outcome of droplet collision can be grazing collision or coalescence. The temperature and size of the droplet are conserved and the velocity changes for the grazing collision while the size, temperature, and velocity of the droplet are updated and removed from the original parcel in the coalescence. Since fuel is injected quite early in the compression process, this leads to fuel interacting with liner or piston so proper care should also be taken to account for drop-wall interactions. This directly affects the total mass of combustible fuel available in the combustion chamber with an opportunity to participate in the ensuing combustion

process. The rebound/slide model is used for spray wall interaction, details of which can be found in Naber and Reitz, 1988 [57].

4.3.2.6 Combustion model

For this work SAGE model [58] is activated to solve chemical kinetics of the combustion process. SAGE model is a detailed chemical kinetics solver that calculate the reaction rate for each elementary component while the CDF solver solves the transport equations. A multi-step chemical reaction mechanism [59] can be written in the following way:



where $v'_{m,r}$ and $v''_{m,r}$ are the stoichiometric coefficients for the reactants and the products, for a species m and a reaction i ; I is the total number of reactions and χ_m is the chemical symbol for species m . Consequently, for the m species the net production rate is:

$$\dot{\omega}_m = \sum_{i=1}^I v_{m,i} q_i \quad \text{for } m = 1, 2, \dots, M \quad (4.54)$$

$$v_{m,i} = v''_{m,i} - v'_{m,i} \quad (4.55)$$

$$q_i = k_{f_i} \prod_{m=1}^M [X_m]^{v'_{m,i}} - k_{r_i} \prod_{m=1}^M [X_m]^{v''_{m,i}} \quad (4.56)$$

where M is the total number of species, q_i is the rate-of-progress parameter for the i th reaction, $[X_m]$ is the molar concentration of species m , and k_{f_i} and k_{r_i} are the forward and reverse rate coefficients for reaction i .

The forward reaction rate is evaluated using the Arrhenius law:

$$k_{f_i} = A_i T^{b_i} e^{(-E_i/RT)} \quad (4.57)$$

where A_i is the pre-exponential factor, b_i is the temperature exponent, E_i is the activation energy and R is the universal gas constant.

The reverse rate coefficient is calculated by CONVERGE via the equilibrium coefficient K_{c_i} which is determined from the thermodynamic properties:

$$k_{r_i} = \frac{k_{f_i}}{K_{c_i}} \quad (4.58)$$

$$K_{c_i} = K_{p_i} \left(\frac{P_{atm}}{RT} \right)^{\sum_{m=1}^M \nu_{m,i}} \quad (4.59)$$

The equilibrium constant K_{p_i} is obtained in the following way:

$$K_{p_i} = \exp \left(\frac{\Delta S_i^0}{R} - \frac{\Delta H_i^0}{R} \right) \quad (4.60)$$

where Δ is the change that occurs in entropy (S) and enthalpy (H) passing from reactants to products in the i^{th} reaction:

$$\frac{\Delta S_i^0}{R} = \sum_{m=1}^M \nu_{m,r} \frac{S_m^0}{R} \quad (4.61)$$

$$\frac{\Delta H_i^0}{R} = \sum_{m=1}^M \nu_{m,i} \frac{H_m^0}{RT} \quad (4.62)$$

For a given computational cell with the chemical kinetic equation discussed above, the mass and energy conservation can be solved as follow:

$$\frac{d[X_m]}{dt} = \dot{\omega}_m \quad (4.63)$$

For constant volume combustion,

$$\frac{dT}{dt} = \frac{V \frac{dP}{dt} - \sum_m (\bar{h}_m \dot{\omega}_m)}{\sum_m ([X_m] \bar{c}_{p,m})} \quad (4.64)$$

For constant pressure combustion,

$$\frac{dT}{dt} = \frac{(\dot{Q}/V) - \sum_m (\bar{h}_m \dot{\omega}_m)}{\sum_m ([X_m] \bar{c}_{p,m})} \quad (4.65)$$

Where \dot{Q} is the heat release rate, V is the volume, \bar{h}_m is the molar specific enthalpy and $\bar{c}_{p,m}$ is the molar constant pressure specific heat of species m.

At each time step, the species concentrations are updated using the equation provided above. Chemical kinetics are solved in a given computational cell only above a certain temperature and minimum mole fraction of CO, H₂ and the hydrocarbon species. To expedite the chemical kinetics calculation, multi-zone modeling is utilized to solve combustion calculations. For single fuel combustion, SAGE utilizes a two-dimensional

zoning strategy in which cells are grouped based on similar temperature and equivalence ratio. For dual fuel combustion, a three-dimensional zoning strategy is utilized in which similar temperature, equivalence ratio, and diesel mass fraction are considered for grouping cells. For two cells to be grouped in the same zone, they should meet the criteria of temperature and pressure along with the cube root of the specified chemical mass fraction in both cells should be less than $Y_i^{1/3}$. More details about the multi-zone modeling approach can be found in the CONVERGE manual [49].

4.3.2.7 Emission models

Most pollutant species as CO, UHC, NO, and CO₂ are calculated from the chemical kinetics in the combustion model. Some calculations of some pollutants like soot and NO passive method of calculation can also be utilized. For soot production, the Hiroyasu model of soot formation and Nagle-Strickland-Constable (NSC) model for soot oxidation are activated. The total mass of soot in a cell can be computed by considering the rate of soot mass formation minus the rate of soot mass oxidation as follows:

$$\frac{dM_s}{dt} = \frac{dM_{sf}}{dt} - \frac{dM_{so}}{dt} \quad (4.66)$$

where,

$$\frac{dM_{sf}}{dt} = A_{sf} P^{0.5} \exp\left(-\frac{E_{sf}}{R_u T}\right) M_{form} \quad (4.67)$$

where P is the cell pressure, T is the cell temperature, R_u is the universal gas constant, E_{sf} is the activation energy for soot formation, A_{sf} is the Arrhenius pre-exponential factor and M_{form} is the mass of soot formation species.

NO can also be calculated passively using Zel'dovich mechanism. For this work, both active and passive method is utilized. For active NO calculation reactions involving NO formation are taken from the Chalmers mechanism and added to the POLIMI_RED mechanism. The extended Zel'dovich mechanism [60] involves the following set of reactions:



The rate of formation of NO can be written in the following way:

$$\begin{aligned} \frac{d[NO]}{dt} = & k_{R1,f}[O][N_2] - k_{R1,r}[NO][N] + k_{R2,f}[N][O_2] \\ & - k_{R2,r}[NO][O] + k_{R3,f}[N][OH] - k_{R3,r}[NO][H] \end{aligned} \quad (4.71)$$

4.3.2.8 Gridding Methodology

CONVERGE uses a modified cut-cell Cartesian grid generation method to automatically generate the computational grid at runtime [49]. CONVERGE requires only surface geometry represented as a closed triangulated surface. CONVERGE provides complete user control over the mesh resolution by easily changing the global mesh resolution and the local mesh resolution by providing additional files to control fixed embedding, Adaptive Mesh Refinement (AMR), and grid scaling [49].

In this work, AMR and fixed embedding are utilized to obtain finer mesh where and when required to get better accuracy at a reasonable computational cost. The base

grid is taken to be 6 mm in all three directions. Fixed embedding is applied to the intake valve angle, exhaust valve angle, spray region, and the entire cylinder region. Fixed embedding leads to a cell size of 0.375 for intake valve angle, exhaust valve angle, spray region, and 1.4 mm in-cylinder region. Now cylinder region is locally resolved to add higher grid resolution in the regions where property gradients are significant by using adaptive mesh refinement (AMR). In this study, AMR is employed in passive data, species data, temperature field, and velocity field. The embedding is controlled using the equation provided below. This leads to a minimum grid size of 0.375 where required.

$$dx_{embed} = \frac{dx_{base}}{2^{embed_scale}} \quad (4.72)$$

4.4 CFD model, initial and boundary setup

4.4.1 Computational resource

The CFD simulations in the present work were performed on HPC of Alabama supercomputer Authority and the Firepower cluster. Alabama supercomputer authority is a state-funded entity. Firepower cluster is a new facility at the University of Alabama with 14 compute nodes, each node has 48 cores (7204 AMD EPYC processors) totaling 672 computational cores.

4.4.2 Initial Condition

4.4.2.1 Inlet Species Mass Fraction

The initial mass fractions of methane, oxygen, nitrogen, carbon dioxide, and water are given by:

$$MF_{ch4} = \frac{M_{ch4}}{S_s} \quad (4.73)$$

$$MF_{o2} = \frac{M_{o2}}{S_s} \quad (4.74)$$

$$MF_{n2} = \frac{M_{n2}}{S_s} \quad (4.75)$$

$$MF_{co2} = \frac{M_{co2}}{S_s} \quad (4.76)$$

$$MF_{h2o} = \frac{M_{h2o}}{S_s} \quad (4.77)$$

Where MF_{ch4} is the mass flow rate of methane into the cylinder, MF_{o2} is the mass flow rate of oxygen into the cylinder, MF_{n2} is the mass flow rate of nitrogen into the cylinder, MF_{co2} is the mass flow rate of carbon dioxide into the cylinder, MF_{h2o} is the mass flow rate of water vapor into the cylinder and S_s is the total mass flow rate of all species into the cylinder. Since air was dried before supplying to the cylinder, MF_{h2o} is set to 0 and similarly MF_{co2} being at a negligible amount in air is also set to 0 for this study.

Spray cone angle was calculated using the below correlation obtained from Dernote et. al. [61].

spray cone angle (θ)

$$\tan \frac{\theta}{2} = A \left(\frac{\rho_a}{\rho_f} \right)^B \Delta P^C f(v) \quad (4.78)$$

Where,

$$f(v) = \exp(D\Delta P^E v) \quad (4.79)$$

Here ρ_a is the density of the air inside the cylinder, ρ_f is the density of fuel being injected, v is fuel viscosity, ΔP is pressure difference at which liquid is being injected into cylinder and chamber pressure, and A, B, C, D, and E are constants provided in Table4.1.

Table 4.1 Coefficients of the spray angle correlation

A	B	C	D	E
0.24	0.24	0.08	-0.24	-0.58

Similarly, spray penetration correlation was obtained from Dernotte et. al. [61] paper and compared with the computational result and shown for diesel injection timing of 310 CAD, 80 PES of methane and 5.1 bar IMEP is shown in Figure 4.3.

Liquid penetration length is given by the below correlation from Dernotte et. al. [61] paper.

$$S = C_v \left(\frac{\sqrt{\frac{2\Delta P}{\rho_f}}}{\left[1 + \left(\frac{aC_v}{D_0} \right) \left\{ \frac{\left[\tan\left(\frac{\theta}{2}\right) \sqrt{2\Delta P \cdot \rho_a} \right]}{\rho_f} \right\} t \right]^{1.1}} \right)^{\frac{1}{2.2}} t \quad (4.80)$$

Where, ρ_a is the density of the air inside the cylinder, ρ_f is the density of fuel being injected, θ is spray cone angle, D_0 is nozzle hole diameter, C_v is discharge coefficient, ΔP is pressure difference at which liquid is being injected into the cylinder and chamber pressure and t is time.

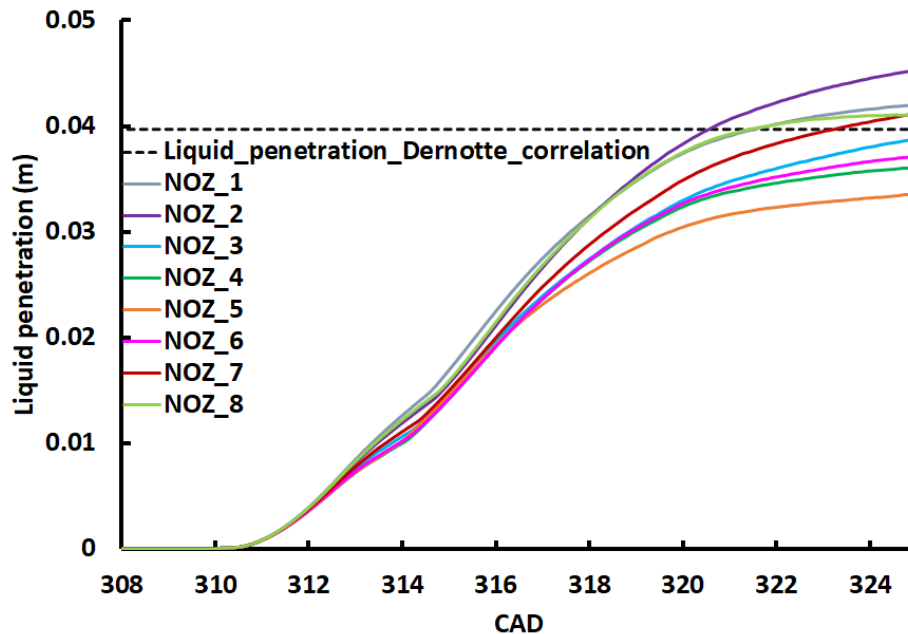


Figure 4.3 Computationally obtained liquid penetration length versus liquid penetration length using Dornette correlation for diesel injection timing of 310 CAD, 1.5 bar boost pressure, 500 bar diesel injection pressure at 5.1 bar IMEP engine load.

The steady state liquid penetration length predicted from the CFD simulation is close to estimates from Dornette et al's co-relation. However, one more thing to note is liquid length is very different for each nozzle. This indicates that spray is asymmetric. This asymmetry is caused by in-cylinder motion affecting the spray from each nozzle differently.

Figure 4.4 shows the evolution of spray and fluid motion inside the cylinder. To represent fluid motion inside cylinder streamtraces are drawn. Streamtraces represents particle path at a specified location in a vector field. Streamtraces were drawn passing from slice obtained parallel to head and around 10 mm below the cylinder head. We can

observe that in-cylinder charge is moving from the left side (exhaust side) to the right side (intake side) pushing the spray more towards the right side. Since diesel injection starts at 310 CAD and ends at 318 CAD, effects of spray advection are seen more after the end of injection due to in-cylinder fluid motion.

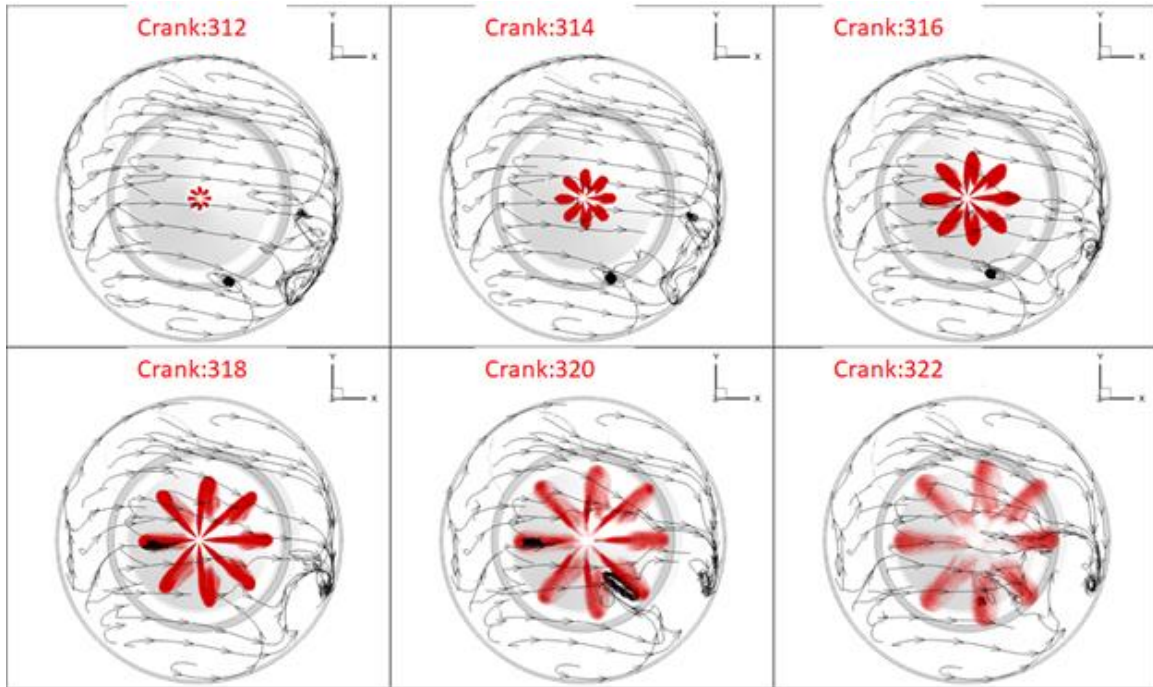


Figure 4.4 Evolution of spray for 310 CAD diesel injection timing, 500bar injection pressure, 80 PES of methane, and 1.5 bar manifold pressure at 5.1 bar IMEP of engine load along with streamtraces representing in-cylinder motion left side is exhaust side and right side is intake side

To further investigate this swirl ratio and tumble ratio in the y-direction are plotted and shown in Figure 4.5 and Figure 4.6 respectively. The swirl ratio is a dimensionless quantity, and for this application can be defined as the ratio of the angular momentum of the fluid flow inside the cylinder to the crankshaft rotational velocity [60]. Similarly, for this application, the tumble ratio in the y-direction is calculated by

evaluating the ratio of the angular speed of the fluid flow inside the cylinder in the y-direction to the angular speed of the crankshaft. Both the swirl ratio and tumble ratio in the y-direction are evaluated about the center of mass. We can observe it is a low swirl engine from the swirl ratio plot at the same time we can see a high tumble ratio in Y-direction.

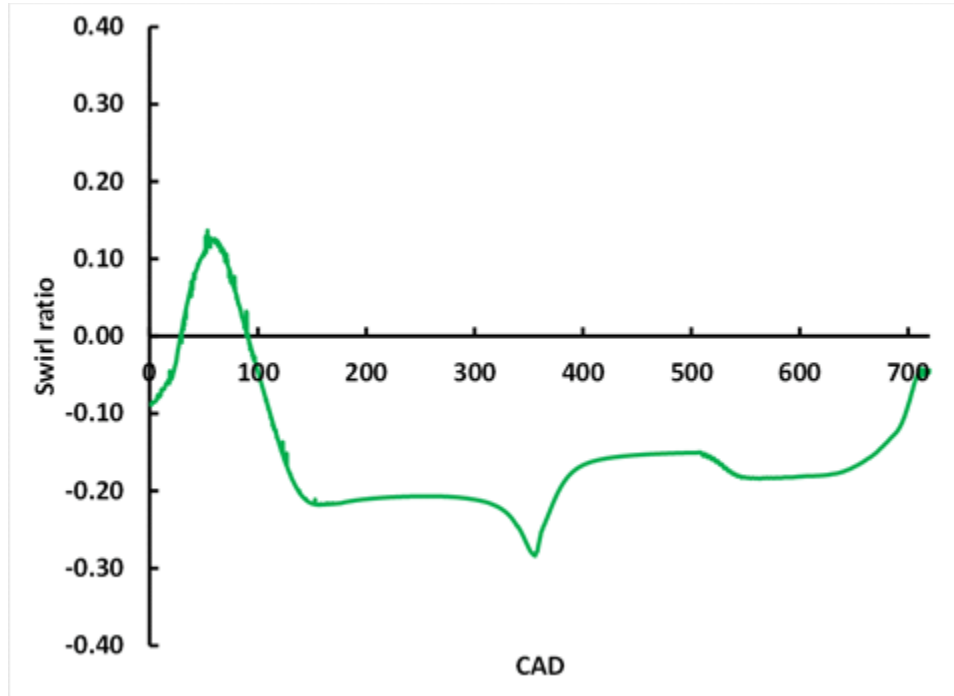


Figure 4.5 Swirl ratio evolution over a cycle

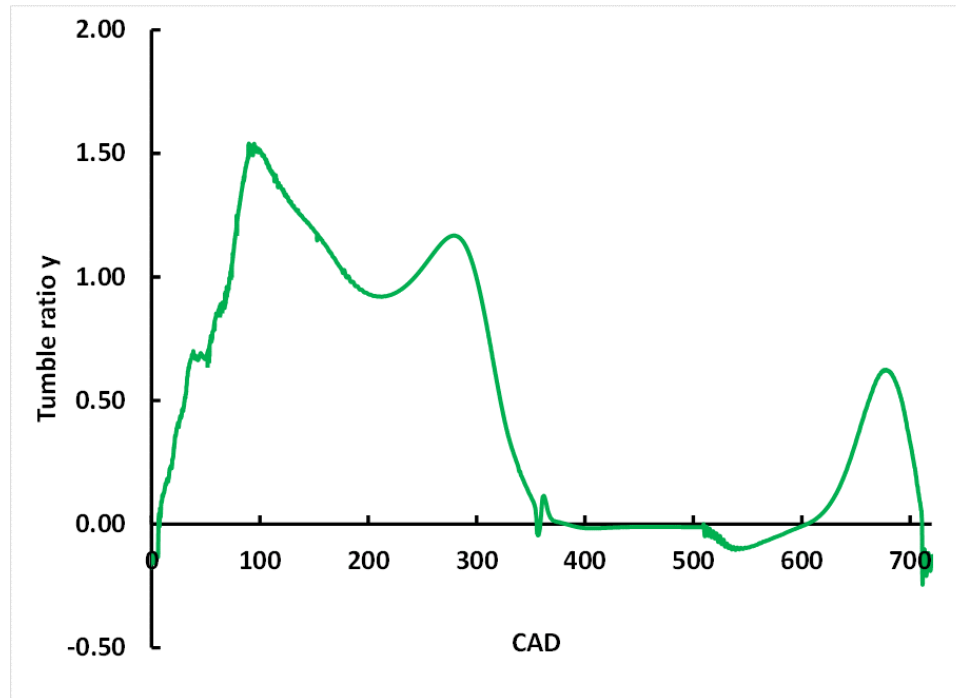


Figure 4.6 Tumble ratio in Y direction evolution over a cycle

Streamtraces are plotted and shown in Figure 4.7. It is clear from Figure 4.7 that there is high tumble motion which is generally observed in a spark-ignited engine, not in a conventional diesel engine. This tumble motion may be a result of box type intake and exhaust runner assumption² as shown in Figure 4.8. Future work may be required to evaluate the effect of such an assumption instead of using an actual intake and exhaust runner.

² This assumption was necessary since the single cylinder engine was designed from a six cylinder engine for which there was no CAD drawings available. As a result, intake and exhaust runner dimensions were approximated using a box type configuration



Figure 4.7 Streamtraces representing in-cylinder motion indicating formation of tumble motion

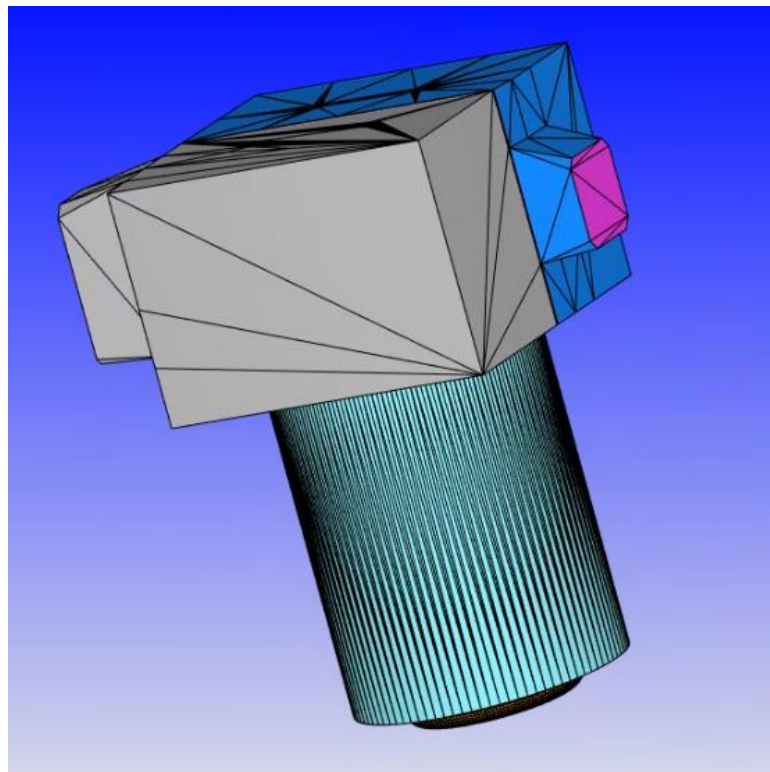


Figure 4.8 Geometry for SCRE at bottom dead center

4.4.3 Initial and boundary condition sweep

Computational results depend on accuracy of initial and boundary conditions. This work also depends on the type of chemical kinetics mechanism used since combustion phenomena involve reaction rates, which depend on the chemical kinetics mechanism used. In this section, we will study the impact of some parameters on the computational results.

4.4.3.1 In-cylinder grid size variation

Initial and boundary condition for this study is shown in Table 4.2 and computational model constants are shown in Table 4.3. It's well understood that grid size influences the computational error due to discretization error. It also influences computational time. Effects of grid size on the in-cylinder region were studied by changing embedding level and AMR which leads to a minimum grid size of 0.7 mm, 0.35 mm, and 0.175 mm. Pressure and AHRR are plotted for various minimum grid size in Figure 4.9. These simulations are performed for diesel injection timing of 310 CAD, 1.5 bar boost pressure, 500 bar diesel injection pressure, 80 PES of methane, and 5.1 bar IMEP engine load. It can be observed that results change drastically with a change in minimum grid size from 0.7 mm to 0.35 mm. There is a minimum change in pressure and AHRR when the minimum grid size is changed from 0.35 mm to 0.175 mm. Therefore, it is deemed that "grid convergence" is achieved and considering the computational time and accuracy, 0.35mm minimum grid size is chosen for this work.

Table 4.2 Initial and boundary condition of experimental and computational cases for 1.5 bar boost pressure, 500 bar diesel injection pressure at 5.1 bar IMEP engine load at diesel injection timing 310 CAD

Parameters	Sim_SOI= 310	Exp_SOI= 310
Engine Speed (rpm)	1500	1500
Exhaust Valve Opening (CAD)	509	509
Exhaust Valve Closing (CAD)	711	711
Inlet Valve Opening (CAD)	6	6
Inlet Valve Closing (CAD)	177	177
Intake Manifold Pressure (bar)	1.50	1.50
Intake Manifold Temperature (K)	317	312
Trapped Mass (kg)	0.00278	0.0028
Piston Temperature (K)	460	
Cylinder Head Temperature (K)	450	
Cylinder Liner Temperature (K)	410	
Injection duration (CAD)	8	8
Diesel fueling (kg/cycle)	1.062e-05	1.062e-05
Methane Fueling (kg/cycle)	3.56E-05	3.65e-05
Start of injection (CAD)	310	310
Compression ratio	17.1	17.1

Table 4.3 Computational model constants

Combustion Model	SAGE
Breakup	KH-RT
KH break up model time	2
RT breakup model time	0.1
NOx Model	Extended Zel'dovich mechanism
CD	Calculated using spray rate calculator in converge
Spray Included angle (CAD)	72.5
$K(m^2/s^2)$	3.0
$E(m^2/s^3)$	280
Fuel temp (T)	411
Mass diffusivity variable	4.16e-06
Nozzle location	0.6 mm
Mechanism	POLIMI_Reduced

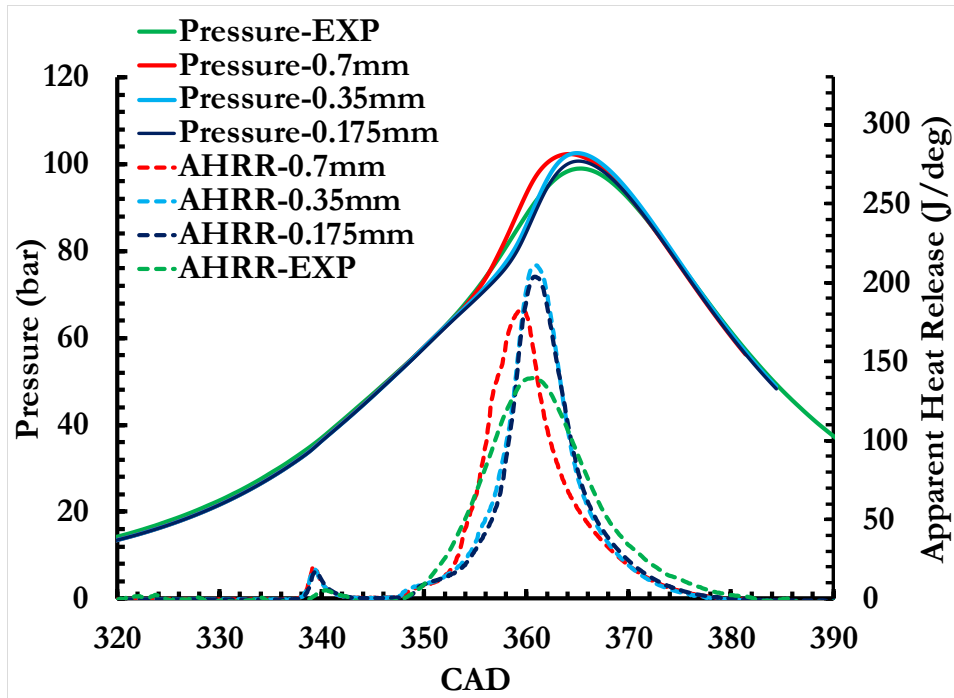


Figure 4.9 Pressure and AHRR histories for various grid size for 310 CAD diesel injection timing, 500bar injection pressure, 80 PES of methane, and 1.5 bar manifold pressure at 5.1 bar IMEP of engine load

4.4.3.2 Fuel temperature variation

Initial and boundary condition for this study is shown in Table 4.2 and computational model constants are shown in Table 4.4. Injected fuel temperature was not measured. So, it makes sense to see the impact of fuel temperature on computational results. Diesel injection temperature is of more importance as a small amount of diesel is only injected and according to [62] since a small amount of diesel is injected in dual fuel combustion, nozzle tip temperatures tend to run high due to insufficient fuel cooling. This indicates high diesel injection temperatures can be expected. So, to study the impact of diesel injection temperature, two cases were simulated with a temperature of 343 K and

411K. These simulations are performed for diesel injection timing of 310 CAD, 1.5 bar boost pressure, 500 bar diesel injection pressure, 80 PES of methane, and 5.1 bar IMEP engine load. Pressure and AHRR results are shown in Figure 4.10. There is a slight shift in combustion as the fuel temperature is increased from 343 K to 411 K. But, globally speaking, fuel temperature has minimum effects on AHRR and pressure at low load and early diesel injection condition. For all simulations in this study, fuel temperature is considered as 411 K considering that only a small amount of diesel is being injected per cycle.

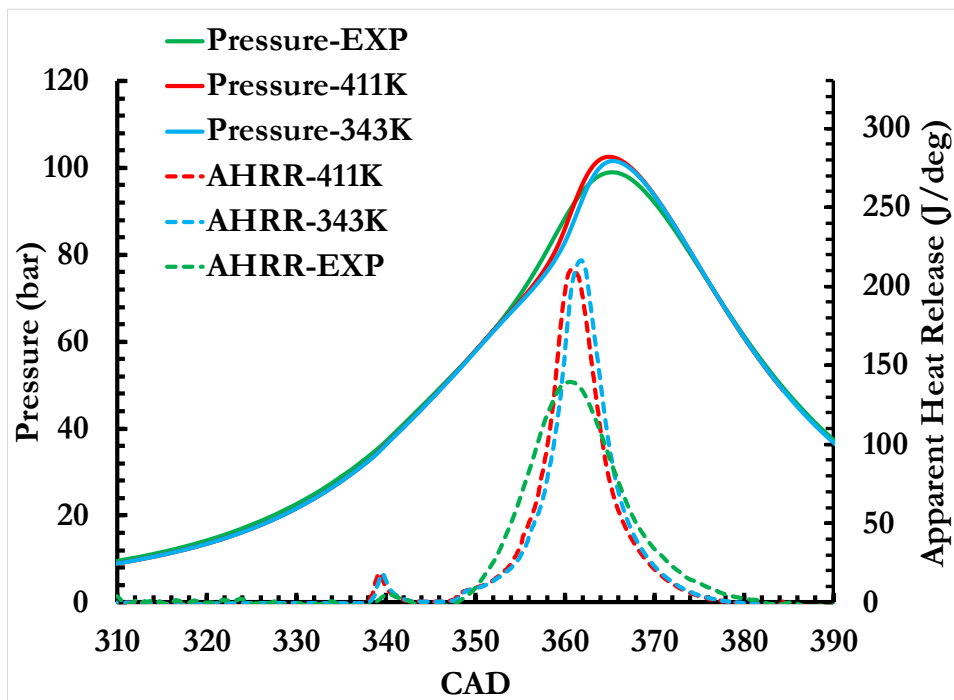


Figure 4.10 Pressure and AHRR histories for various fuel temperature for 310 CAD diesel injection timing, 500bar injection pressure, 80 PES of methane, and 1.5 bar manifold pressure at 5.1 bar IMEP of engine load

Table 4.4 Computational model constants

Combustion Model	SAGE
Breakup	KH-RT
KH break up model time	2
RT breakup model time	0.1
NOx Model	Extended Zel'dovich mechanism
CD	Calculated using spray rate calculator in converge
Spray Included angle (CAD)	72.5
$K(m^2/s^2)$	3.0
$E(m^2/s^3)$	280
Fuel temp	343 and 411
Mass diffusivity variable	4.16e-06
Nozzle location	0.6 mm
Mechanism	POLIMI_Reduced

4.4.3.3 KH time constant Sweep

Initial and boundary condition for this study is shown in Table 4.2 and Computational model constants are shown in Table 4.5. Since the KH time constant value recommended by CONVERGE [49] is 7. Simulations was performed at 310 CAD with $KH = 2$ and $KH = 7$ and Pressure and AHRR comparison is shown in Figure 4.11. We can observe that change in this value does not change anything drastically and for the rest of the simulations KH value of 7 is adopted

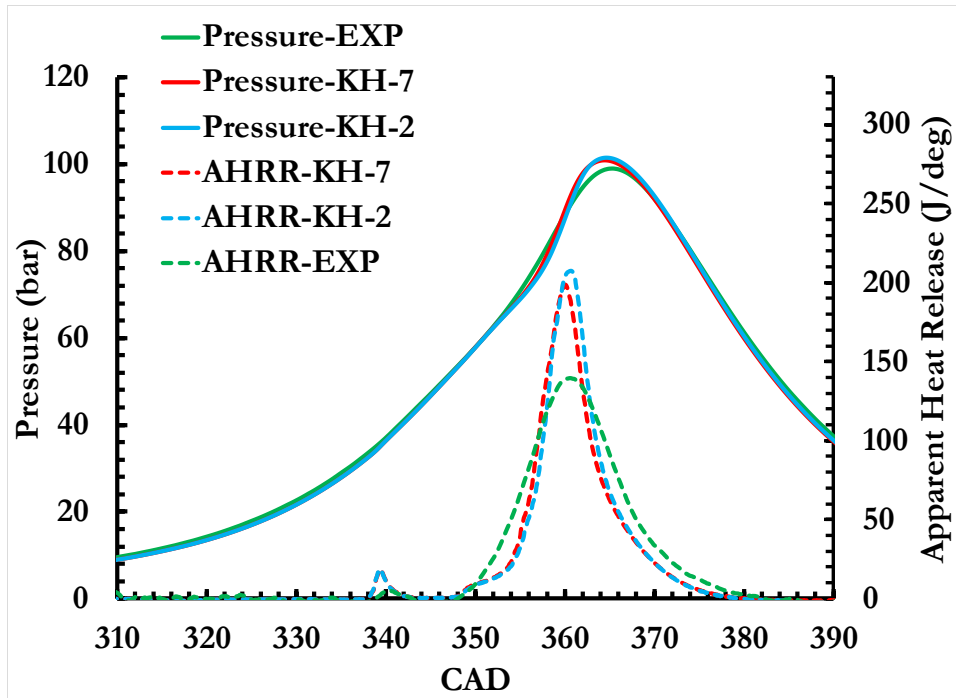


Figure 4.11 Pressure and AHRR histories for various KH values for 310 CAD diesel injection timing, 500bar injection pressure, 80 PES of methane, and 1.5 bar manifold pressure at 5.1 bar IMEP of engine load

Table 4.5 Computational model constants used in this study

Combustion Model	SAGE
Breakup	KH-RT
KH break up model time	7
RT breakup model time	0.1
NOx Model	Extended Zel'dovich mechanism
CD	Calculated using spray rate calculator in converge
Spray Included angle (CAD)	72.5
$K(m^2/s^2)$	3.0
$E(m^2/s^3)$	280
Fuel temp	411
Mass diffusivity variable	4.16e-06
Nozzle location	0.6 mm
Mechanism	POLIMI_Reduced

4.4.3.4 Schmidt number variation

Initial and boundary condition for this study is shown in Table 4.6 and Computational model constants are shown in Table 4.5. While using the RANS approach to model turbulent flow, the turbulent Schmidt number is used in the turbulent mass coefficient term as discussed in the turbulent modeling section (section number). In turbulent flows, the Schmidt number is defined as the ratio of momentum diffusivity to mass diffusivity. According to the author's best knowledge, there is no universally accepted Schmidt number value for engine simulation. Moreover, Schmidt numbers vary locally [63] but it is common practice to use a single value of Schmidt number in engine combustion simulations. CONVERGE manual [49] suggests using Schmidt number value of 0.78. To see the effects of Schmidt number two value of 0.85 (higher than 0.78) and 0.6 (lower than 0.78) were chosen. These simulations are performed for 1.5 bar boost pressure, 500 bar diesel injection pressure, 80 PES of methane, 5.1 bar IMEP engine load, and diesel injection timing of 320 CAD and 330CAD. Figure 4.12 shows pressure and AHRR variation with a change in Schmidt number for diesel injection timing of 320 CAD. Similarly, Figure 4.13 shows pressure and AHRR variation with a change in Schmidt number for diesel injection timing of 330 CAD. It can be observed basically for early injection timing change in Schmidt number seems to change global combustion characteristics. It was also observed that the change in Schmidt number changed NO emissions value in all cases. For all the simulations in this study, the Schmidt number of 0.78 was selected as recommended by CONVERGE manual [49].

Table 4.6 Initial and boundary condition of experimental and computational cases for 1.5 bar boost pressure, 500 bar diesel injection pressure at 5.1 bar IMEP engine load at diesel injection timing 320 and 330 CAD

Parameters	Sim_SOI= 320	Exp_SOI= 320	Sim_SOI= 330	Exp_SOI= 330
Engine Speed (rpm)	1500	1500	1500	1500
Exhaust Valve Opening (CAD)	509	509	509	509
Exhaust Valve Closing (CAD)	711	711	711	711
Inlet Valve Opening (CAD)	6	6	6	6
Inlet Valve Closing (CAD)	177	177	177	177
Intake Manifold Pressure (bar)	1.50	1.50	1.50	1.50
Intake Manifold Temperature (K)	317	309	317	308
Trapped Mass (kg)	0.00279	0.0028	0.00278	0.0028
Piston Temperature (K)	460		460	
Cylinder Head Temperature (K)	450		450	
Cylinder Liner Temperature (K)	410		410	
Injection duration (CAD)	8.3	8.3	8.5	8.5
Diesel fueling (kg/cycle)	1.12E-05	1.14E-05	1.15e-05	1.16E-05
Methane Fueling (kg/cycle)	3.69E-05	3.741E-05	3.81E-05	4.002E-05
Start of injection (CAD)	320	320	330	330
Compression ratio	17.1	17.1	17.1	17.1

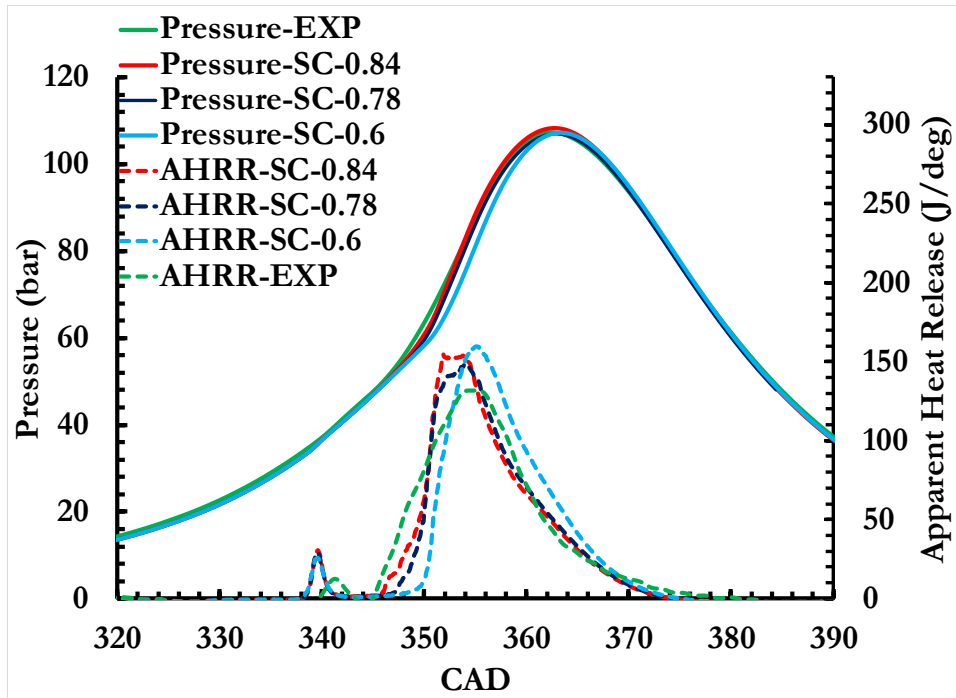


Figure 4.12 Pressure and AHRR histories for various Schmidt numbers for 320 CAD diesel injection timing, 500bar injection pressure, 80 PES of methane, and 1.5 bar manifold pressure at 5.1 bar IMEP of engine load

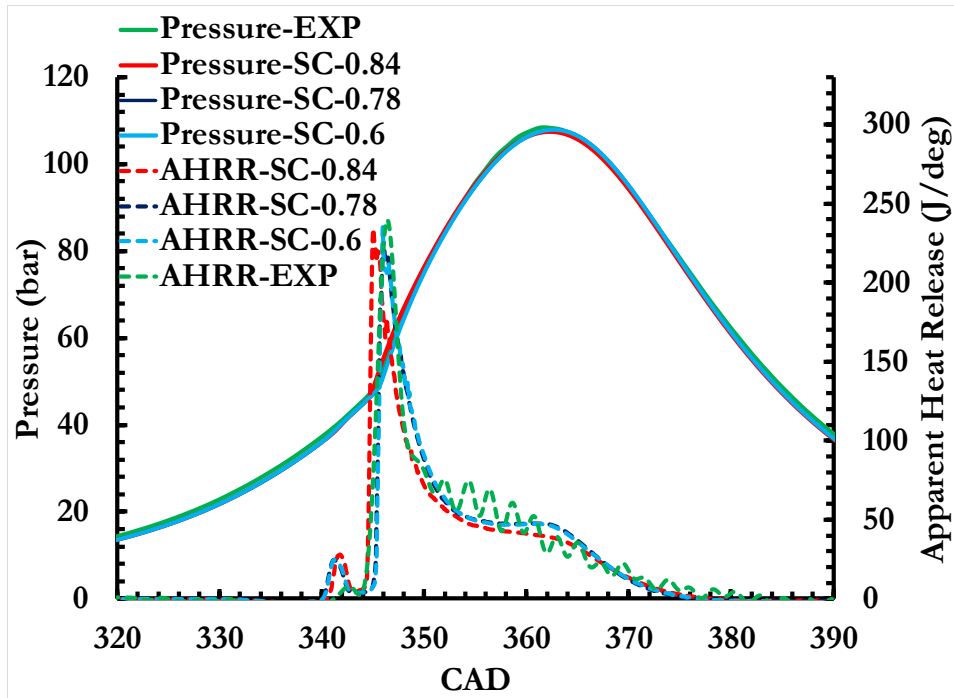


Figure 4.13 Pressure and AHRR histories for various Schmidt numbers for 330 CAD diesel injection timing, 500bar injection pressure, 80 PES of methane, and 1.5 bar manifold pressure at 5.1 bar IMEP of engine load

4.4.3.5 Computational consecutive cycle to cycle variation

For effects of initial conditions to wash out (e.g. initial in-cylinder residual gas fraction, in-cylinder temperature, and so on), it requires few cycles of simulation before simulation results can be used. To find out when the effects of such initial conditions are washed out, four cycles of simulations are performed for diesel injection timing of 310 CAD, 1.5 bar boost pressure, 500 bar diesel injection pressure, 80 PES of methane, and 5.1 bar IMEP engine load. Table 4.7 shows the initial and boundary condition for each cycle against experimental values and computational model constants are shown in Table 4.5. We can observe there is a slight change in trapped mass, methane mass, and power output from one cycle to another cycle. There is a jump in the change in trapped mass, methane mass, and power output from the first cycle to the

second but has small changes from the second cycle to the third and fourth. Figure 4.14 shows the pressure and AHRR variation from one cycle to another cycle. Both pressure and AHRR show a big change from the first cycle to the second but not many global changes can be seen from the second cycle to the third and fourth. With this observation, we can say results don't change much after the second cycle and any data after the second cycle can be presented to compare against the experimental. To further analyze cycle to cycle results variations in emissions data was also analyzed. Figure 4.15 to 4.17 shows NO, HC and CO emission respectively for different cycles. There is a change in NO, HC, and CO emissions from one cycle to another. Ideally, it will be great to run many cycles and average their emission results and present. But considering computational expenses it is not practical, so last cycle emissions results will be analyzed in this study.

Table 4.7 Initial and boundary condition of four cycles at diesel injection timing of 310 CAD

Parameters	Cycle1	Cycle2	Cycle3	Cycle4	Experimental
Engine Speed (rpm)	1500	1500	1500	1500	1500
Indicated Power (kW)	11.42	11.71	11.70	11.78	11.27
Exhaust Valve Opening (CAD)	509	509	509	509	509
Exhaust Valve Closing (CAD)	711	711	711	711	711
Inlet Valve Opening (CAD)	6	6	6	6	6
Inlet Valve Closing (CAD)	177	177	177	177	177
Intake Manifold Pressure (bar)	1.50	1.50	1.50	1.50	1.50
Intake Manifold Temperature (K)	317	317	317	317	312
Trapped Mass (kg)	0.00281	0.002795	0.002787	0.002787	0.00281
Piston Temperature (K)	460	460	460	460	-
Cylinder Head Temperature (K)	450	450	450	450	-
Cylinder Liner Temperature (K)	410	410	410	410	-
Injection duration (CAD)	8	8	8	8	8
Diesel fueling (kg/cycle)	1.058e-05	1.058e-05	1.058e-05	1.058e-05	1.062e-05
Methane Fueling (kg/cycle)	3.56E-05	3.58E-05	3.56E-05	3.56E-05	3.65e-05
Start of injection (CAD)	310	310	310	310	310
Compression ratio	17.1	17.1	17.1	17.1	17.1

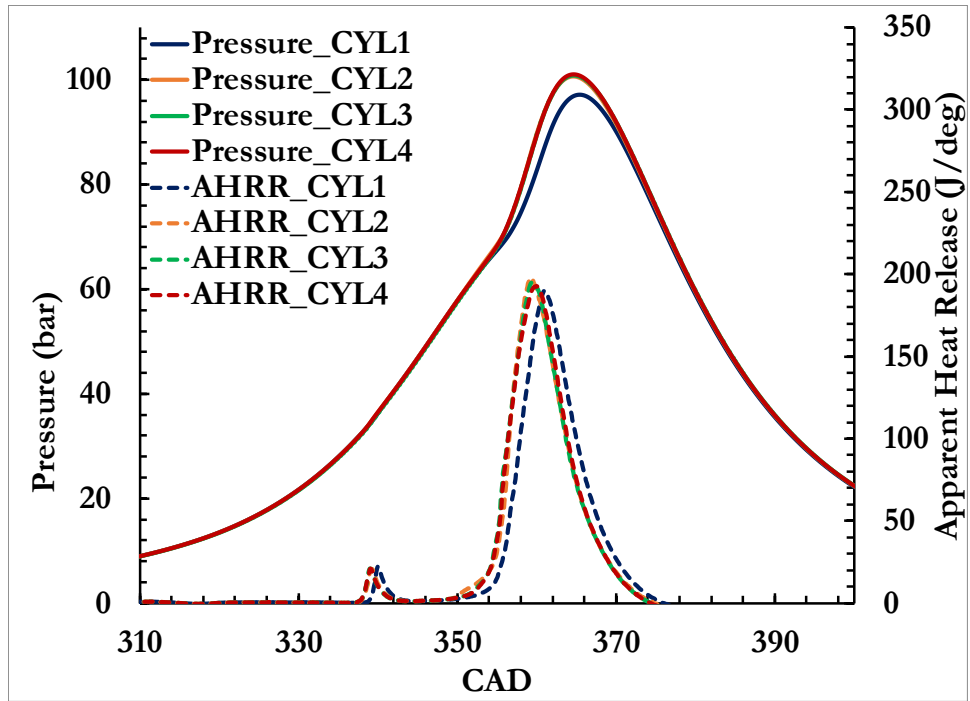


Figure 4.14 Pressure and AHRR histories for consecutive four computational cycles for 310 CAD diesel injection timing, 500bar injection pressure, 80 PES of methane, and 1.5 bar manifold pressure at 5.1 bar IMEP of engine load

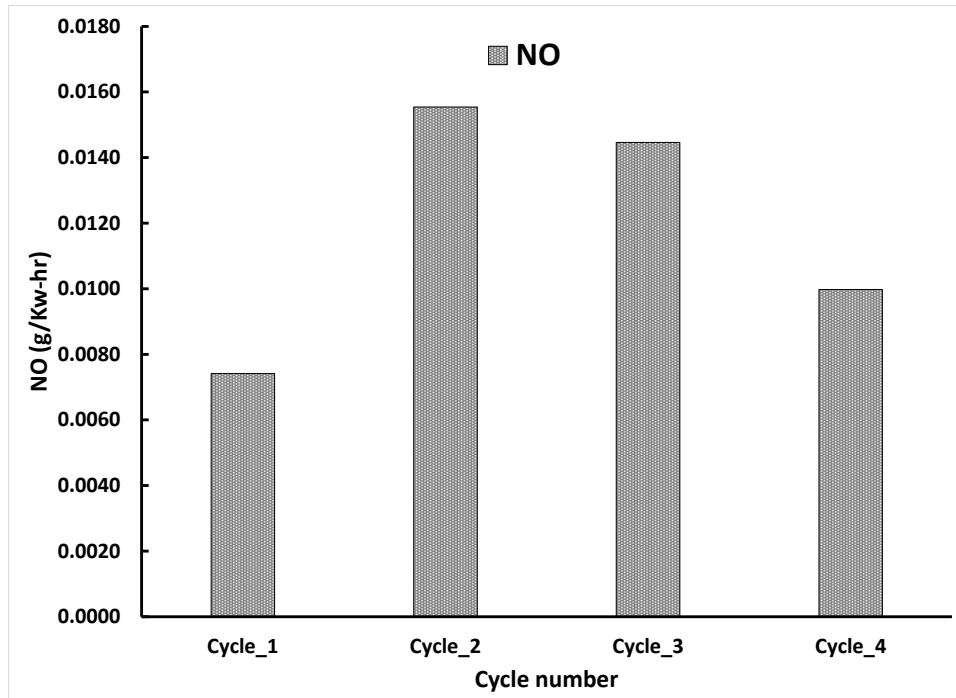


Figure 4.15 Indicated specific oxides of nitrogen (NO) emission histories for consecutive four computational cycles for 310 CAD diesel injection timing, 500bar injection pressure, 80 PES of methane, and 1.5 bar manifold pressure at 5.1 bar IMEP of engine load

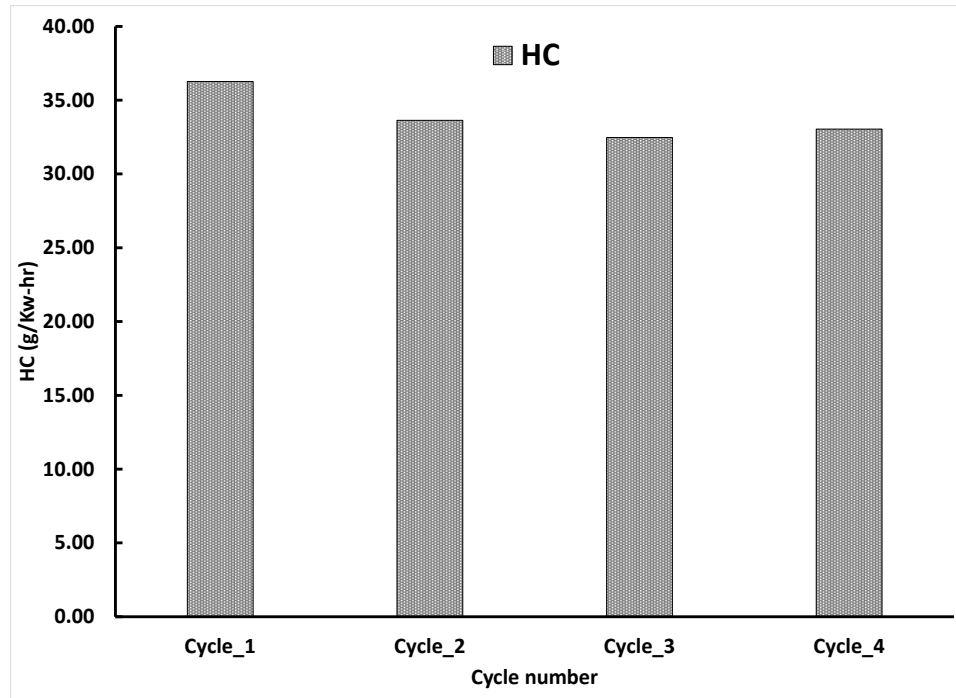


Figure 4.16 Indicated specific hydrocarbon (HC) emission histories for consecutive four computational cycles for 310 CAD diesel injection timing, 500bar injection pressure, 80 PES of methane, and 1.5 bar manifold pressure at 5.1 bar IMEP of engine load

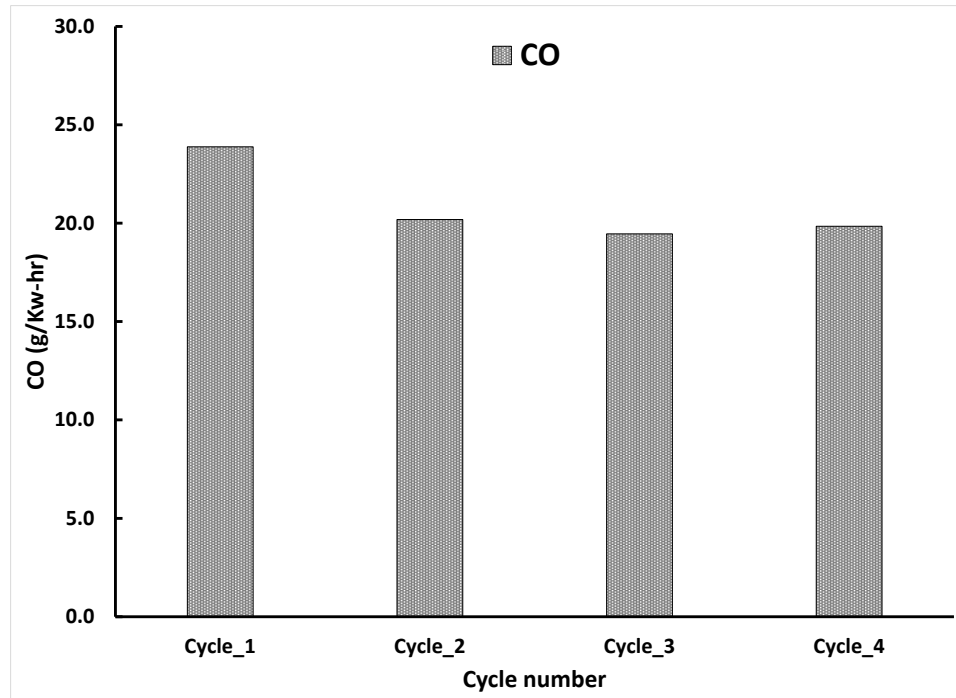


Figure 4.17 Indicated specific carbon monoxide (CO) emission histories for consecutive four computational cycles for 310 CAD diesel injection timing, 500bar injection pressure, 80 PES of methane, and 1.5 bar manifold pressure at 5.1 bar IMEP of engine load

4.4.3.5.2 Mechanism comparison

For the combustion processes to be completely modeled it requires hundreds of species and thousands of reactions. Keeping computational time in mind, it is not practical to use such a complete mechanism. We need a reduced mechanism that can properly capture the combustion process inside the cylinder in reasonable time with accepted accuracy. For this purpose, we have opted two mechanisms, POLIMI_RED mechanism [46] which includes 96 chemical species and 993 reactions and been derived from POLIMI total mechanism and CSU 186 mechanism develop by Hockett [64] which include 186 chemical species and 901 reactions. Table 4.8 show initial and boundary condition used for 1.5 bar boost pressure, 500 bar diesel injection pressure, 80 PES of

methane, and 5.1 bar IMEP engine load at varying diesel injection timing of 310, 320, and 330 CAD computational model constants are shown in Table 4.5. Figure 4.18 shows in-cylinder pressure, AHRR and cumulative heat release (CHR) plotted against experimentally obtained cyclic data for varying diesel injection timing using the POLIMI mechanism. Similarly, Figure 4.19 shows in-cylinder pressure, AHRR, and cumulative heat release (CHR) plotted against experimentally obtained cyclic data for varying diesel injection timing using CSU 186 mechanism. Both the mechanism is able to capture trend when diesel injection timing is changed from 310 CAD to 320 CAD and finally 330 CAD. One interesting thing to note is that change in AHRR shape from diesel injection timing of 320 CAD to diesel injection timing of 330 CAD is captured by both the mechanisms. Upon analysis of CHR, we can observe that start of high-temperature heat release is predicted slightly earlier for CSU mechanism compared to POLIMI_RED mechanism. With the uncertainty in the cylinder wall, piston, liner temperature, injection profile, it can be said that each mechanism does a good job in predicting the trends. POLIMI_RED mechanism is able to consistently capture pressure, AHRR, and CHR for all three-diesel injection timings while CSU mechanism underpredicts the CHR due to early start of high-temperature heat release. POLIMI_RED mechanism is computationally less expensive than CSU 186 mechanism due to the lower number of species transport. With all these considerations, POLIMI_RED mechanism is opted to perform all the simulations of this work.

Table 4.8 Initial and boundary condition for 1.5 bar boost pressure, 500 bar diesel injection pressure, 80 PES of methane, and 5.1 bar IMEP engine load at diesel injection timing of 310, 310, and 330 CAD

Parameters	Sim_SOI= 310	Exp_SOI= 310	Sim_SOI= 320	Exp_SOI= 320	Sim_SOI= 330	Exp_SOI= 330
Engine Speed (rpm)	1500	1500	1500	1500	1500	1500
Exhaust Valve Opening (CAD)	509	509	509	509	509	509
Exhaust Valve Closing (CAD)	711	711	711	711	711	711
Inlet Valve Opening (CAD)	6	6	6	6	6	6
Inlet Valve Closing (CAD)	177	177	177	177	177	177
Intake Manifold Pressure (bar)	1.50	1.50	1.50	1.50	1.50	1.50
Intake Manifold Temperature (K)	317	312	317	309	317	308
Trapped Mass (kg)	0.00278	0.0028	0.00279	0.0028	0.00278	0.0028
Piston Temperature (K)	460		460		460	
Cylinder Head Temperature (K)	450		450		450	
Cylinder Liner Temperature (K)	410		410		410	
Injection duration (CAD)	8	8	8.3	8.3	8.5	8.5
Diesel fueling (kg/cycle)	1.062e-05	1.062e-05	1.12E-05	1.14E-05	1.15e-05	1.16E-05
Methane Fueling (kg/cycle)	3.56E-05	3.65e-05	3.69E-05	3.741E-05	3.81E-05	4.002E-05
Start of injection (CAD)	310	310	320	320	330	330
Compression ratio	17.1	17.1	17.1	17.1	17.1	17.1

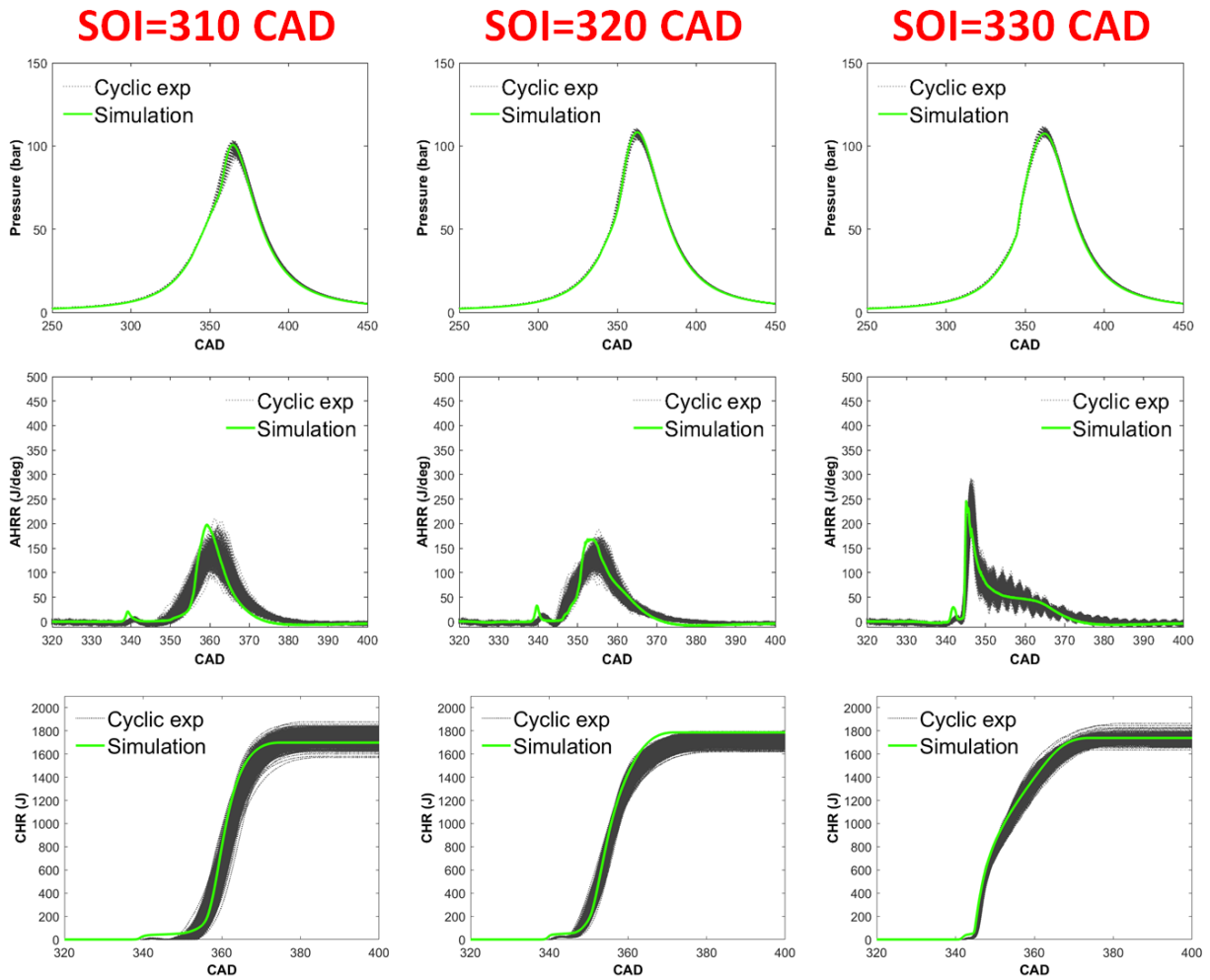


Figure 4.18 Computational Pressure, AHRR and CHR histories using POLIMI_Red mechanism plotted over experimental 1000 consecutive cycles for 500bar injection pressure, 80 PES of methane, 1.5 bar manifold pressure, and 5.1 bar IMEP of engine load at various diesel injection timing of 310, 320 and 330 CAD

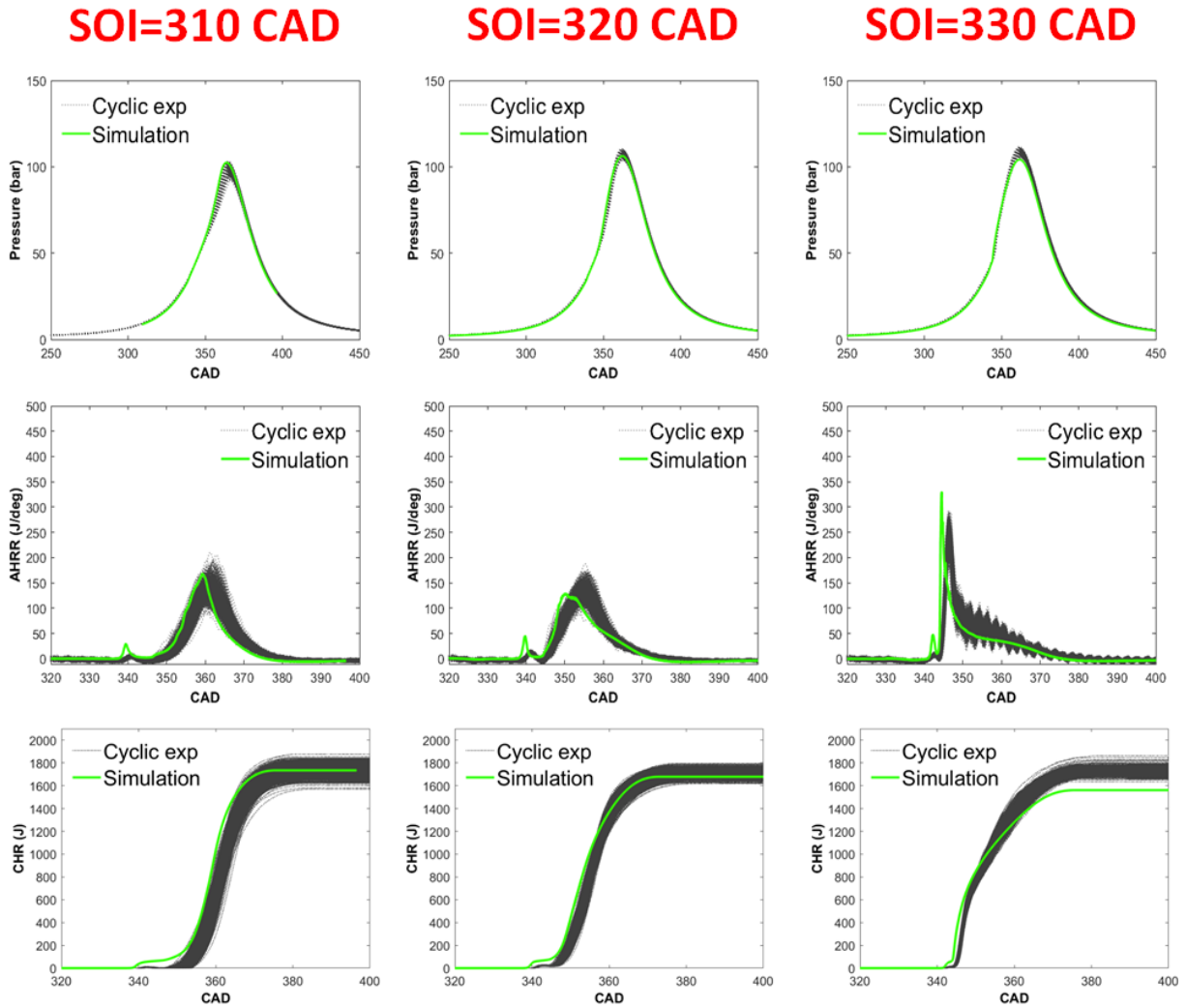


Figure 4.19 Computational Pressure, AHRR and CHR histories using CSU 186 mechanism plotted over experimental 1000 consecutive cycles for 500bar injection pressure, 80 PES of methane, 1.5 bar manifold pressure, and 5.1 bar IMEP of engine load at various diesel injection timing of 310, 320 and 330 CAD

4.4.3.6 Diesel quantity variation

For dual fuel combustion low amount of diesel is injected and, in such case, injector needle is not even fully open. As reported by the several researchers there is

variation in diesel quantity from one shot to another and it is higher for injection when the injector is not even fully open [65,66]. For the cases analyzed in this work, experimental data for such variation is not available. And it is very difficult to quantify such variation from one shot to another shot. In absence of such data, a needle lift profile was utilized to quantify the variation of diesel injected from one cycle to another cycle. Needle lift data for 1000 cycles are presented in Figure 4.20 for diesel injection timing of 310 CAD, 1.5 bar boost pressure, 500 bar diesel injection pressure, 80 PES of methane, and 5.1 bar IMEP engine load. The area under each needle lift profile was calculated and the coefficient of variation of the area under each needle lift curve was calculated and found to be 3.2 percent. So, diesel quantity from average measured quantity was increased and decreased by 3.2 percent and with this diesel, quantity simulation was performed for diesel injection timing of 310 CAD, 1.5 bar boost pressure, 500 bar diesel injection pressure, 80 PES of methane, and 5.1 bar IMEP engine load. Pressure, AHRR, and CHR result from engine simulation with the variation of diesel quantity are plotted on top of 1000 consecutive experimental data in Figures 4.21, 4.22, and 4.23 respectively. We can observe peak pressure is high with higher diesel quantity injected and low with lower diesel quantity injected. Similarly, the fluctuation is observed for AHRR and CHR. It is evident from this exercise that a small variation in diesel quantity has observable effects on engine performance. This observation suggests that one of the reasons for cyclic variability may be due to cycle to cycle variation in diesel injection quantity. For all the simulations performed in this work, diesel injection quantity kept to the average value recorded by the Coriolis flowmeter. Also, there is a lot of cycle to cycle

variation observed for cases analyzed in this work, it makes sense to compare computational results with cyclic data instead of average data.

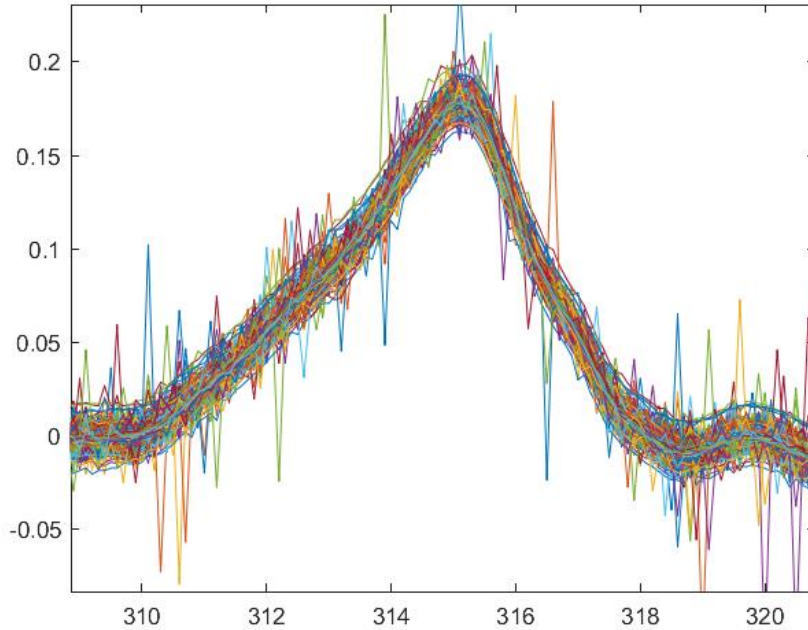


Figure 4.20 Experimental needle lift profile histories for 1000 consecutive cycles for 310 CAD diesel injection timing, 500bar injection pressure, 80 PES of methane, and 1.5 bar manifold pressure at 5,1 bar IMEP of engine load

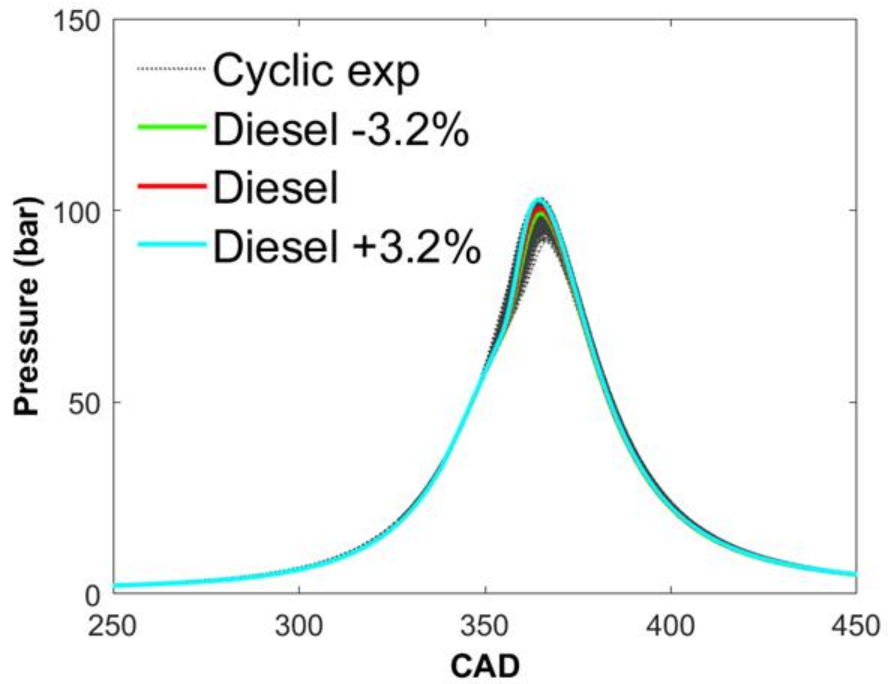


Figure 4.21 Computational Pressure histories for various diesel injection mass quantity plotted over experimental 1000 consecutive cycles for 310 CAD diesel injection timing, 500bar injection pressure, 80 PES of methane, and 1.5 bar manifold pressure at 5.1 bar IMEP of engine load

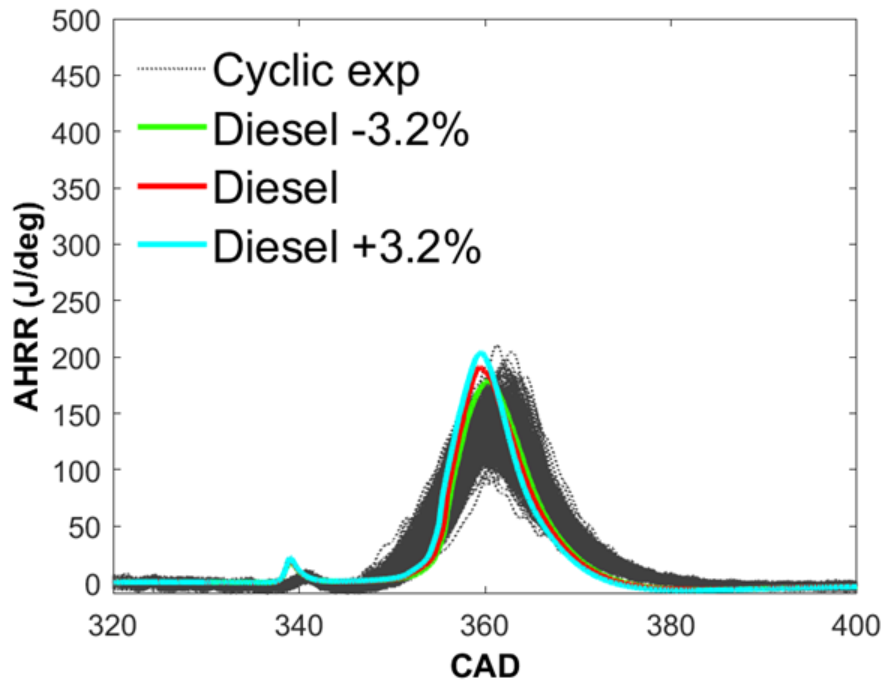


Figure 4.22 Computational AHRR histories for various diesel injection mass quantity plotted over experimental 1000 consecutive cycles for 310 CAD diesel injection timing, 500bar injection pressure, 80 PES of methane, and 1.5 bar manifold pressure at 5.1 bar IMEP of engine load

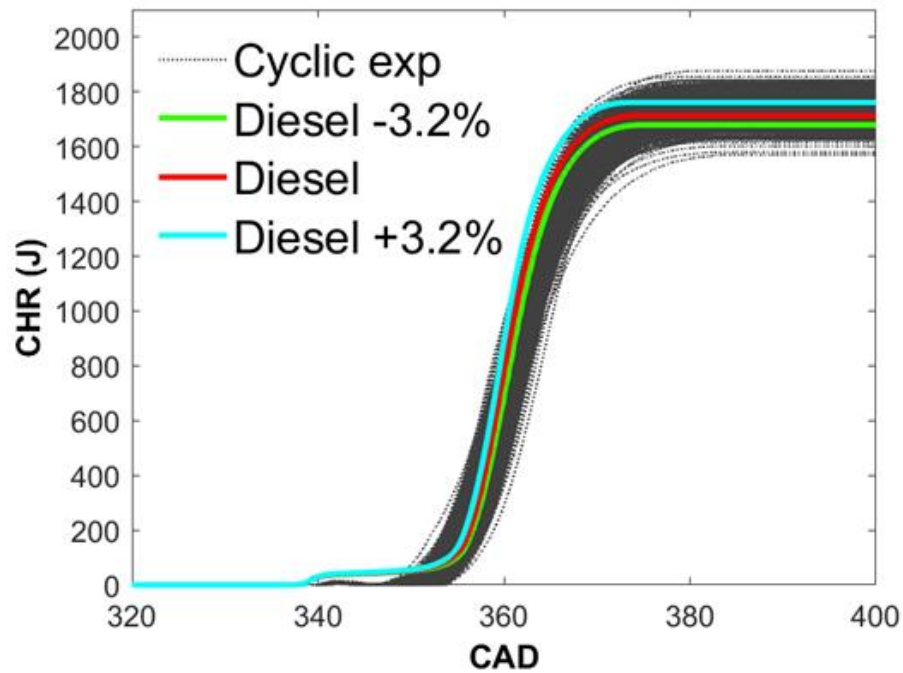


Figure 4.23 Computational CHR histories for various diesel injection mass quantity plotted over experimental 1000 consecutive cycles for 310 CAD diesel injection timing, 500bar injection pressure, 80 PES of methane, and 1.5 bar manifold pressure at 5.1 bar IMEP of engine load

4.5 Result and discussion

For this work, a single-cylinder research engine (SCRE) is used for all experiments and computational simulations are performed on this engine geometry. The specifications of the SCRE are given in Table 4.9. Fuel injection profile from experiments was not available, so a ramp up and ramp down injection profile was created based on experimentally measured needle lift profiles. A typical injection profile is shown in Figure 4.24. Figure 4.25 shows the CFD workflow. CAD model of the piston was created using a scanned piston. A flat cylinder head was assumed for this purpose.

CAD model of intake and exhaust valve was created using measurements and box type assumption was taken for intake and exhaust runner. Multiple full cycle simulation was performed so that the effects of initial condition opted was minimized. SOI 310, 320, and 330 CAD at 5.1 bar IMEP experiments were simulated for model calibration and validation.

Table 4.9 Single Cylinder Research Engine Specification

Parameter	Value
Bore	128 mm
Stroke	142 mm
Connecting rod	228 mm
Compression ratio used for simulations	17.1:1
Combustion Chamber Geometry	Mexican hat
Diesel fuel injection system	Bosch CP3 common rail
Injector nozzle hole diameter	0.197 mm
Number of nozzle holes	8
Methane fueling	Fumigation into manifold
Maximum Engine speed (rpm)	1900

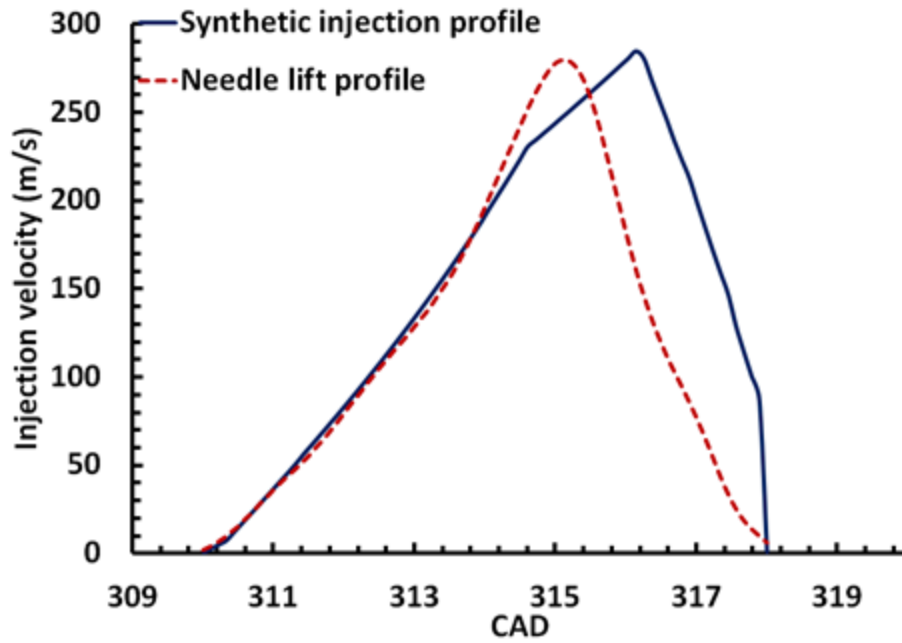


Figure 4.24 Crank-resolved synthetic injection profile created based on experimental needle lift profile for 5.1 bar IMEP engine load

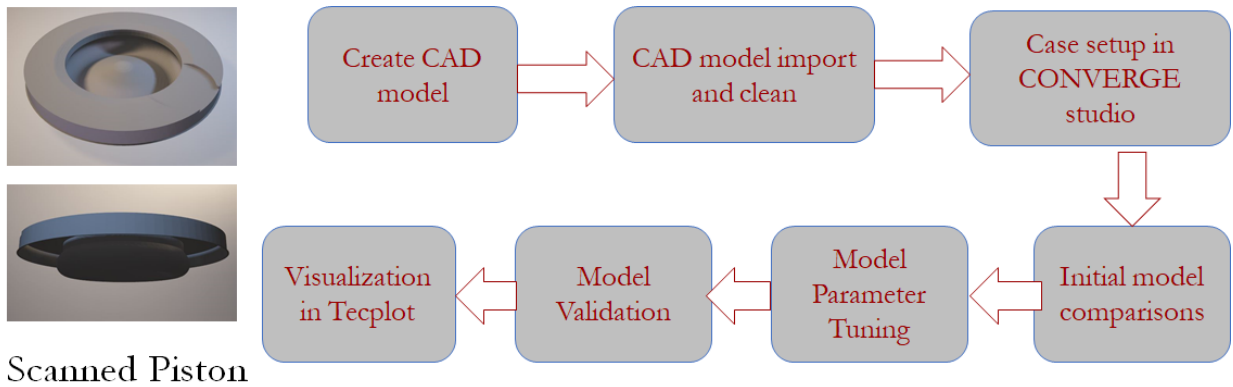


Figure 4.25 CFD modeling workflow

The minimum number of cells is as low as 777663 near the top dead center in the compression stroke before diesel injection while the maximum number of cells is as high as 3616528 in the expansion phase. The number of cells with respect to crank angle for 80 PES, 310 CAD diesel injection timing for diesel-methane dual fuel combustion case is shown in Figure 4.26.

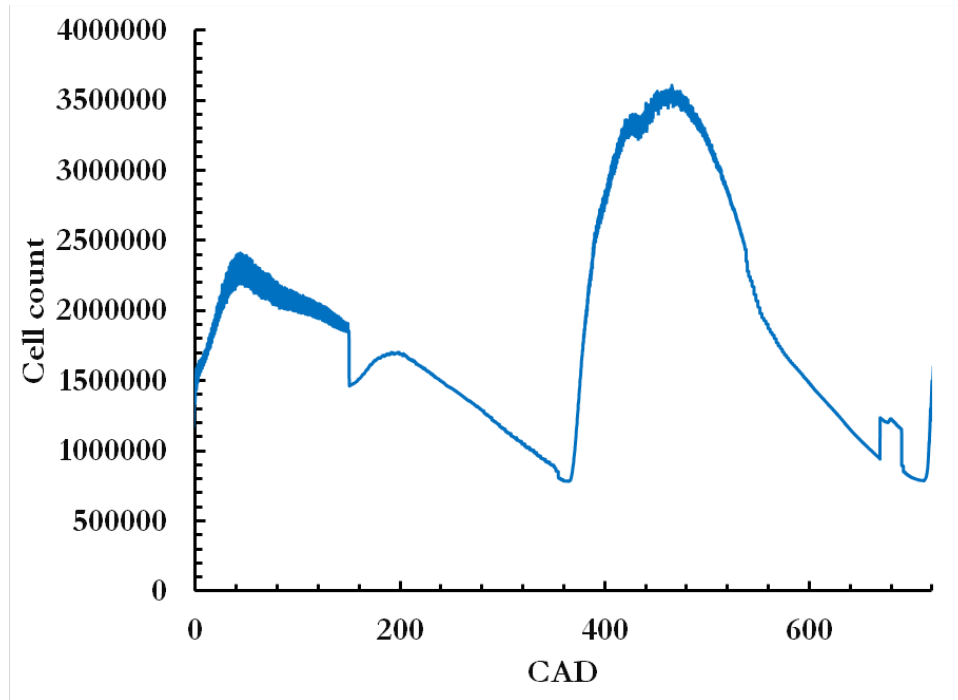


Figure 4.26 Total number of cells in a domain for diesel injection timing of 310 CAD, 1.5 bar boost pressure, 500 bar diesel injection pressure at 5.1 bar IMEP engine load

4.5.1 Effect of methane on diesel

Various researchers [18,20] have shown methane delays the pilot fuel autoignition process. The 3D computational model discussed before is used to study the effect of methane on diesel autoignition. Diesel is represented by dodecane (gas phase) chemical species for all the studies. Two cases were simulated named as “Methane_case” and “No-

methane_case” cases to elaborate on the effect of methane on dodecane autoignition.

Details of the simulation conditions for these cases are shown in Table 4.10.

Table 4.10 Test condition for methane influence on dodecane

Cases	Methane energy fraction	Dodecane energy fraction	Engine speed	Diesel injection timing	Diesel injection pressure	Boost pressure
Methane_case	80	20	1500 rpm	310 CAD	500 bar	1.5 bar
No-methane_case	0	100	1500 rpm	310 CAD	500 bar	1.5 bar

Figure 4.27 shows the apparent heat release rate for both cases along with methane and dodecane species evolution over the engine crank angle. It can be observed that the onset of low-temperature heat release is delayed by the addition of methane suggesting methane delays dodecane autoignition. Similarly, the high temperature of heat release is also delayed by the addition of methane. The interesting thing to note is that the amount of delay in high-temperature combustion is in a similar amount observed for low-temperature combustion, this suggests a delay in low-temperature combustion is extended to high-temperature combustion. A similar observation was made by Srna et al [21]. Figure 4.27 also shows that dodecane decomposition itself is delayed with the addition of methane. It also suggests that all the low-temperature heat release is coming from dodecane. It also gives us the idea that initial high-temperature combustion comes from dodecane combustion followed by combustion of methane. Most of the methane decomposition starts after high-temperature combustion starts. It can be also observed that dodecane combustion starts first followed by methane combustion around by dodecane leading to combustion of methane in the vicinity.

Figure 4.28 shows dodecane and temperature contours for methane case. Dodecane contours are presented for 339 and 347 CAD. This gives us an idea of the distribution of dodecane inside the cylinder. Temperature contours are for selected piston positions of 350, 353, 353, 357, 359, and 363 CAD. As observed in Figure 4.27 when high-temperature heat release starts around 350 CAD, high-temperature activity is seen in-cylinder as indicated in Figure 4.28. Such high-temperature activity is grows in size to 353 CAD. The interesting thing to note is these high-temperature activities are happening only in the regions where dodecane has decomposed. This indicates dodecane auto-ignition has occurred and has raised the temperature of the surrounding fuel-air mixture. At 356 CAD additional combustion activity is seen to occur where the instance of first high-temperature activity was observed at 350 CAD. This indicates methane surrounding dodecane is heated up and combusts. Similar activity is observed at 357 CAD more methane surrounding the area where initial heat release occurred start participating in the combustion process. At 359 and 363 CAD we can observe the progress of combustion towards other regions of the combustion chamber. This gives us an idea about how the combustion process occurs in diesel methane dual-fuel engine at low loads.

To further understand this phenomenon, we need to investigate the evolution of different species. Figure 4.29 shows the main pathways for dodecane oxidation[67]. Figure 4.30 shows the apparent heat release rate for both cases along with n-dodecyl-ketohydroperoxide radical (NC12-OOQOOH) concentration, which marks the start of low temperature heat release. It can be seen that NC12-OOQOOH is delayed with the addition of methane. It can also be seen that the total concentration of NC12-OOQOOH species production is also decreased. These observations indicate that methane

influences the ignition chemistry of dodecane. Kahila et. al. [20] suggested methane addition influences the chemical pathways and production and consumption rate of species like RO_2 , OH , CH_3 , HO_2 , amongst others. Figures 4.31(a) and 4.31(b) shows the crank-resolved evolution of CH_3 radical along with apparent heat release rate. Figure 4.31(b) is a “zoomed-in” representation of Figure 4.31(a) We can observe from Figure 4.31(a) that the evolution of CH_3 radical is delayed with the introduction of methane. But the zoomed-in representation shows that the formation of CH_3 radical starts first in the “methane_case”. This indicates that species like H , OH , and others that may be formed due to the initial decomposition of dodecane are consumed by methane to form CH_3 radical. This phenomenon delays dodecane decomposition until enough H and OH are available. To better understand this, we need the rate of production and consumption of these chemical species. Unfortunately, the CONVERGE code does not output the rate of production and consumption of species. This exercise needs to be done in the future to precisely answer the influence of methane on dodecane.

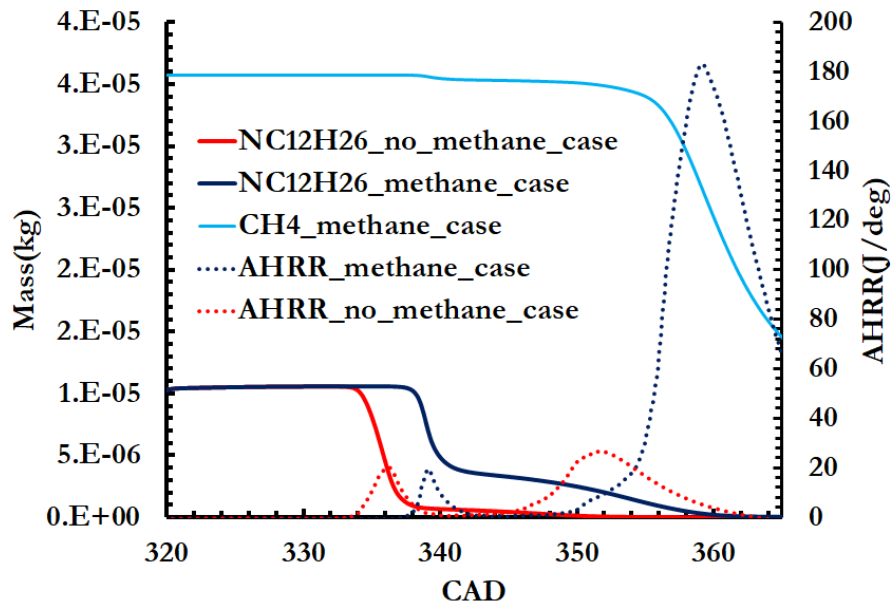


Figure 4.27 Comparison of AHRR, dodecane, and methane for a case simulated with methane and without methane as a fuel inside the cylinder for diesel injection timing of 310 CAD, 1.5 bar boost pressure, 500 bar diesel injection pressure

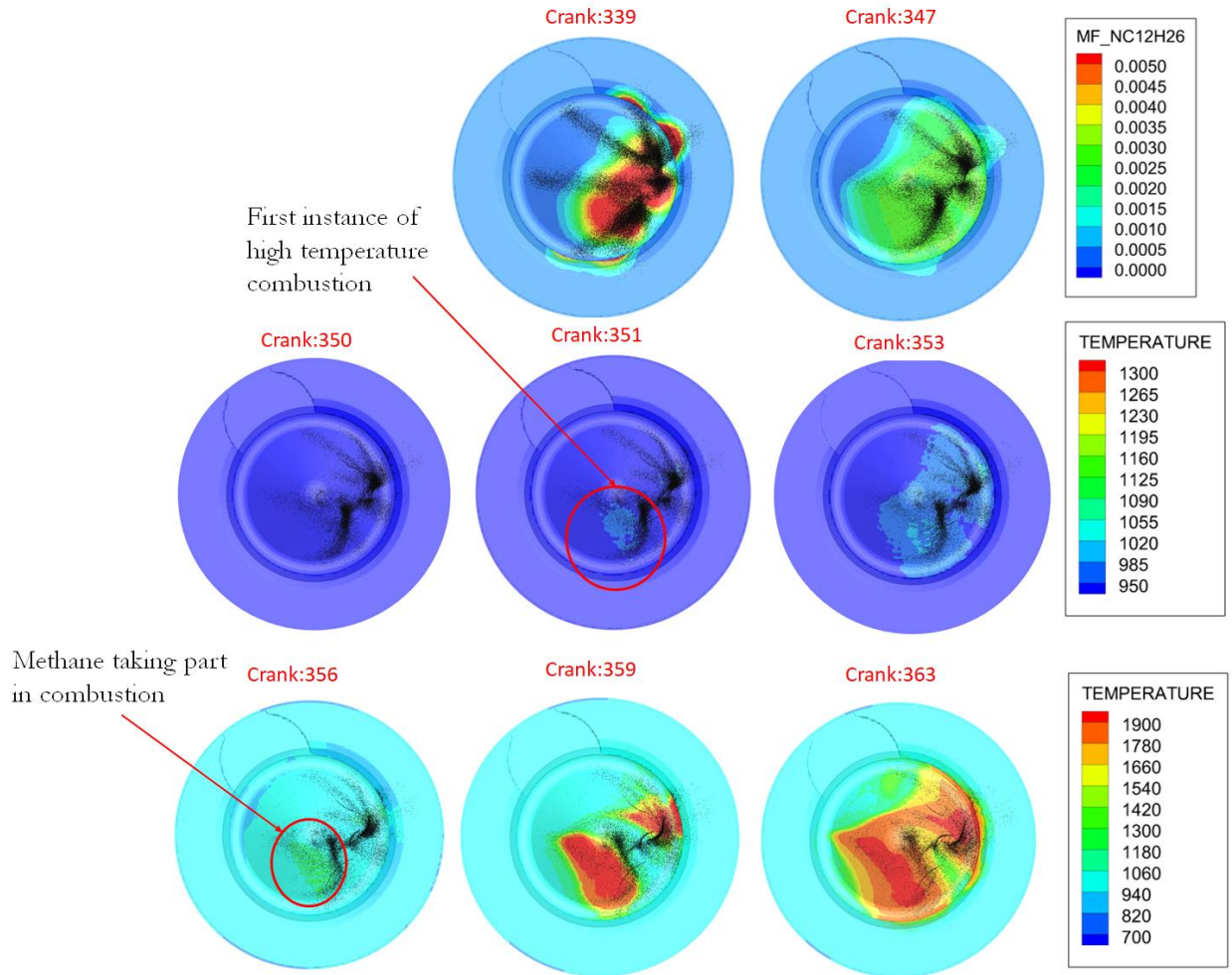


Figure 4.28 Dodecane and temperature distribution observed from the top for diesel injection timing of 310 CAD, 1.5 bar boost pressure, 500 bar diesel injection pressure, and 80 PES of methane at 5.1 bar IMEP

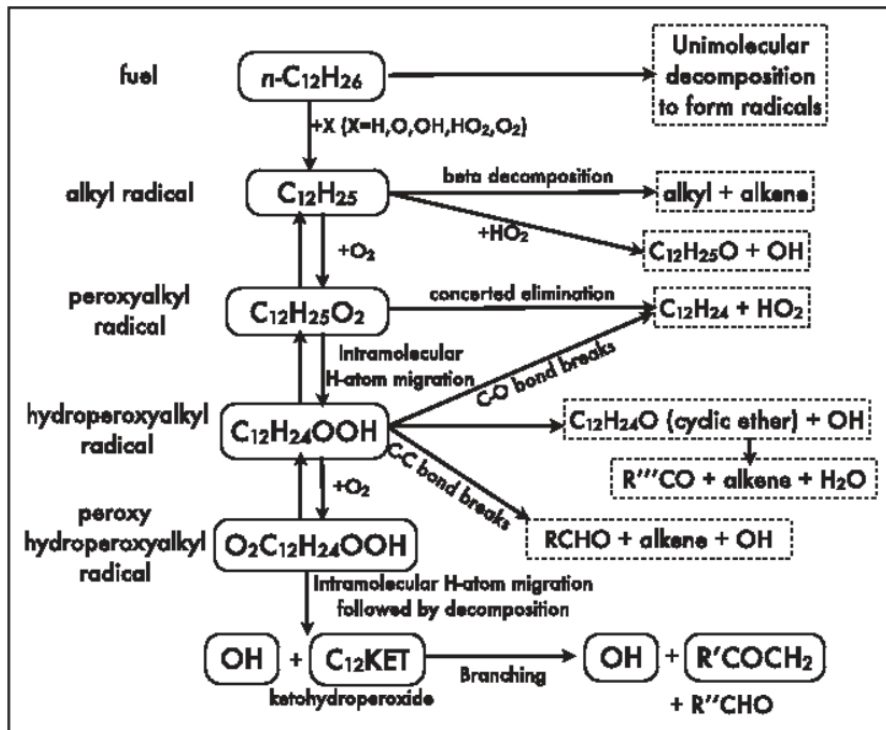


Figure 4.29 N-dodecane main oxidation pathways [6]

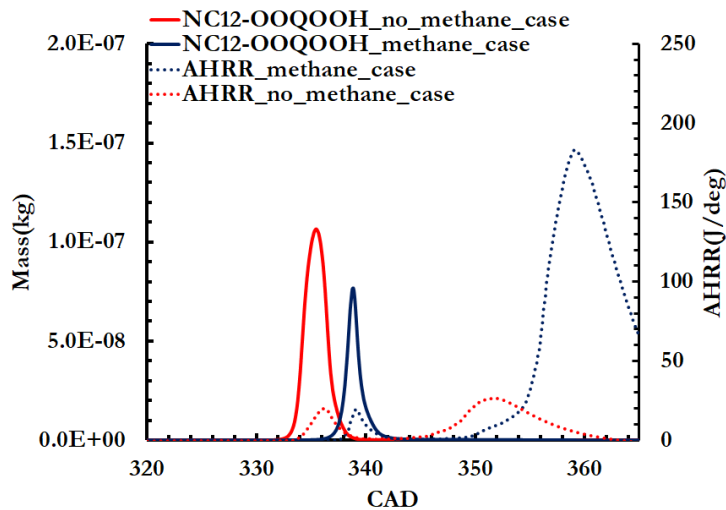


Figure 4.30 Crank angle evolution of NC12-OOQOOH and AHRR histories for the case with methane and case without methane.

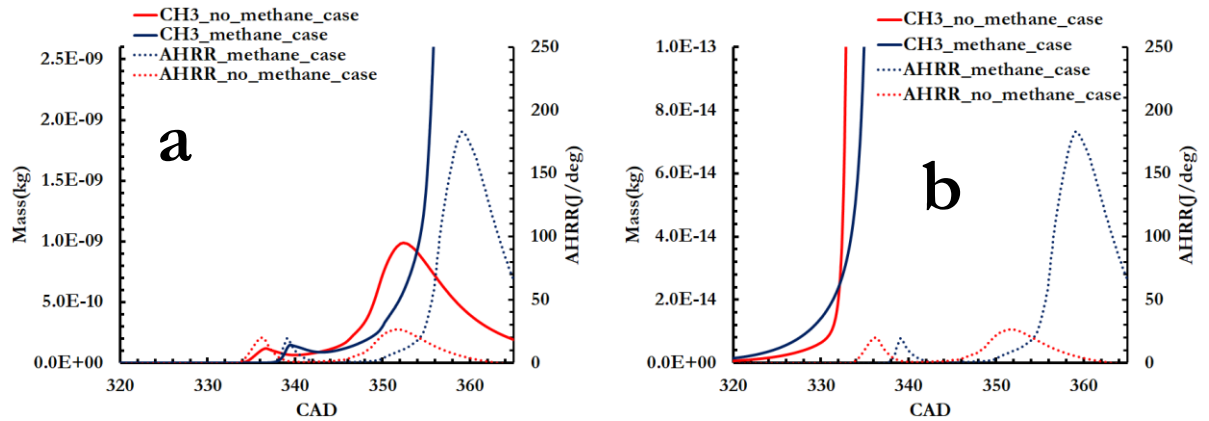


Figure 4.31 Crank angle evolution of CH3 and AHRR histories for the case with methane and case without methane.

4.5.2 Model Validation and In-cylinder combustion characterization

Computational results are validated against experimental measurements. For validation computationally obtained pressure, apparent heat release rate (AHRR), Cumulative heat release (CHR), combustion efficiency (η_{comb}), closed-cycle indicated fuel conversion efficiency (CC_IFCE), NO emissions, HC emissions, and CO emissions compared with the experimental results. The computational model was calibrated for diesel methane dual fuel combustion for 1.5 bar boost pressure, 500 bar diesel injection pressure, 80 PES of methane, and 5.1 bar IMEP engine load at varying diesel injection timing of 310, 320, and 330 CAD. Along with model validation combustion characterization of these dual fuel combustion cases is also performed. Table 4.11 shows all initial conditions and boundary conditions used in the present study and compared against experimental results. Similarly, Table 4.12 shows all model calibration parameters used in this study and kept they were kept same throughout all cases.

Table 4.11 Initial and boundary conditions for diesel injection timing of 310, 320, and 330 CAD

Parameters	Sim_SOI= 310	Exp_SOI= 310	Sim_SOI= 320	Exp_SOI= 320	Sim_SOI= 330	Exp_SOI= 330
Engine Speed (rpm)	1500	1500	1500	1500	1500	1500
IMEP (bar)	5.18	5.15	5.15	5.16	5.24	5.11
Exhaust Valve Opening (CAD)	509	509	509	509	509	509
Exhaust Valve Closing (CAD)	711	711	711	711	711	711
Inlet Valve Opening (CAD)	6	6	6	6	6	6
Inlet Valve Closing (CAD)	177	177	177	177	177	177
Intake Manifold Pressure (bar)	1.50	1.50	1.50	1.50	1.50	1.50
Intake Manifold Temperature (K)	317	312	317	309	317	308
Trapped Mass (kg)	0.00278	0.0028	0.00279	0.0028	0.00278	0.0028
Piston Temperature (K)	460		460		460	
Cylinder Head Temperature (K)	450		450		450	
Cylinder Liner Temperature (K)	410		410		410	
Injection duration (CAD)	8	8	8.3	8.3	8.5	8.5
Diesel fueling (kg/cycle)	1.062e-05	1.062e-05	1.12E-05	1.14E-05	1.15e-05	1.16E-05
Methane Fueling (kg/cycle)	3.56E-05	3.65e-05	3.69E-05	3.741E-05	3.81E-05	4.002E-05
Start of injection (CAD)	310	310	320	320	330	330
Compression ratio	17.1	17.1	17.1	17.1	17.1	17.1

Table 4.12 Computational model constants used in this study

Combustion Model	SAGE
Breakup	KH-RT
KH break up model time	7
RT breakup model time	0.1
NOx Model	NOx mechanism from Chalmer's mechanism
CD	Calculated using spray rate calculator in converge
Spray Included angle (CAD)	75
Spray cone angle (CAD)	24
$K(m^2/s^2)$	3.0
$E(m^2/s^3)$	280
Fuel temp	411
Mass diffusivity variable	4.16e-06
Nozzle location	0.6 mm
Mechanism	POLIMI_Reduced

Different combustion parameters used in this paper such as percentage energy substitute (PES), equivalence ratio(Φ), combustion efficiency (η_{comb}), closed cycle indicated fuel conversion efficiency (CC_IFCE), apparent heat release rate (AHRR), closed cycle indicated power (CC_IP), and specific heat ratio (γ), etc. are defined below.

$$PES = \frac{\dot{m}_m LHV_m}{\dot{m}_d LHV_d + \dot{m}_m LHV_m} \quad (4.81)$$

In Equation 4.81, \dot{m} refers to the mass flow rates of diesel (subscript “d”), methane (subscript “m”), and LHV refers to the corresponding fuel lower heating values.

$$\eta_{comb} = \frac{\int_{soc}^{eoc} \frac{dQ_{chem}}{d\theta} d\theta}{\Sigma(m_i Q_{lHV_i})} \quad (4.82)$$

Equation 4.82 defines the combustion efficiency. Q_{LHV_i} are their respective lower heating values of fuel used. For diesel and methane combined fraction weighted LHV (i.e., a mass-fraction-weighted average of 42.7 MJ/kg for diesel and 50 MJ/kg for methane) of these two fuels are used for LHV in Equation 4.82.

$$AHRR(\theta) = \frac{\gamma}{\gamma-1} P \frac{dV}{d\theta} + \frac{1}{\gamma-1} V \frac{dP}{d\theta} \quad (4.83)$$

$$\gamma(T) = 1.375 - 6.99 \times 10^{-5} T \quad (4.84)$$

$$MPRR = \left(\frac{dp}{d\theta} \right)_{max} \quad (4.85)$$

$$CC_IFCE = \frac{CC_IP}{\dot{m}_d LHV_d + \dot{m}_P LHV_P} \quad (4.86)$$

Experimental AHRR is calculated using Equation 4.83 [60] and γ was determined using Equation 4 based on global in-cylinder temperature (T), estimated by Gatowski's model [68]. The rate of change of volume with respect to crank angle ($dV/d\Theta$) was calculated using crank angle-resolved instantaneous volume data and the rate of change of pressure with respect to crank angle ($dP/d\Theta$) was calculated using crank angle-resolved cylinder pressure data. Equation 5 defines the maximum pressure rise rate and is the maximum value of the rate of change of pressure with respect to the crank angle ($dP/d\Theta$). Equation 6 defines closed cycle indicated fuel conversion efficiency (CC_IFCE) and CC_IP is closed cycle indicated power. It is to be noted that the CFD_AHRR (CFD apparent heat release rate) and CC_IFCE are obtained by passing the CFD cylinder pressure through the same equations (4.83,4.84, 4.86). This allows for direct comparison of simulation and experimental AHRR and CC_IFCE.

Figure 32 shows in-cylinder pressures, apparent heat release rates, and cumulative heat release of computationally predicted and experimental data (for 1000 consecutive cycles) for 1.5 bar boost pressure, 500 bar diesel injection pressure, 80 PES of methane, and 5.1 bar IMEP at diesel injection timing of 310, 320, and 330 CAD. As indicated earlier there is a great deal of cyclic variability at low engine load for diesel-methane dual fuel combustion at high methane substitutions. So, for all comparisons report cyclic experimental data. The in-cylinder pressures are predicted well and fall within the cyclic band. Model is able to predict both onset and trends of low-temperature heat release (also known as cool flame heat release) and high-temperature heat release for different diesel injection timings. But the magnitude of the low-temperature heat release

is over predicted in all cases and can be attributed to uncertainty in injection profile (which were not measured experimentally), reduced chemical kinetics, uncertainty in boundary temperatures, and other parameters. Despite all the uncertainties, the computational model is able to predict the change in AHRR shape occurring from diesel injection timing of 320 to 330 CAD. Also, the start of combustion (SOC) is well captured for all three cases analyzed. Simulated cumulative heat release (CHR) follows the trends of experimentally obtained results and peak CHR value lies within the experimentally obtained band. The initial discrepancy in CHR is due to the difference in low-temperature temperature heat release predictions.

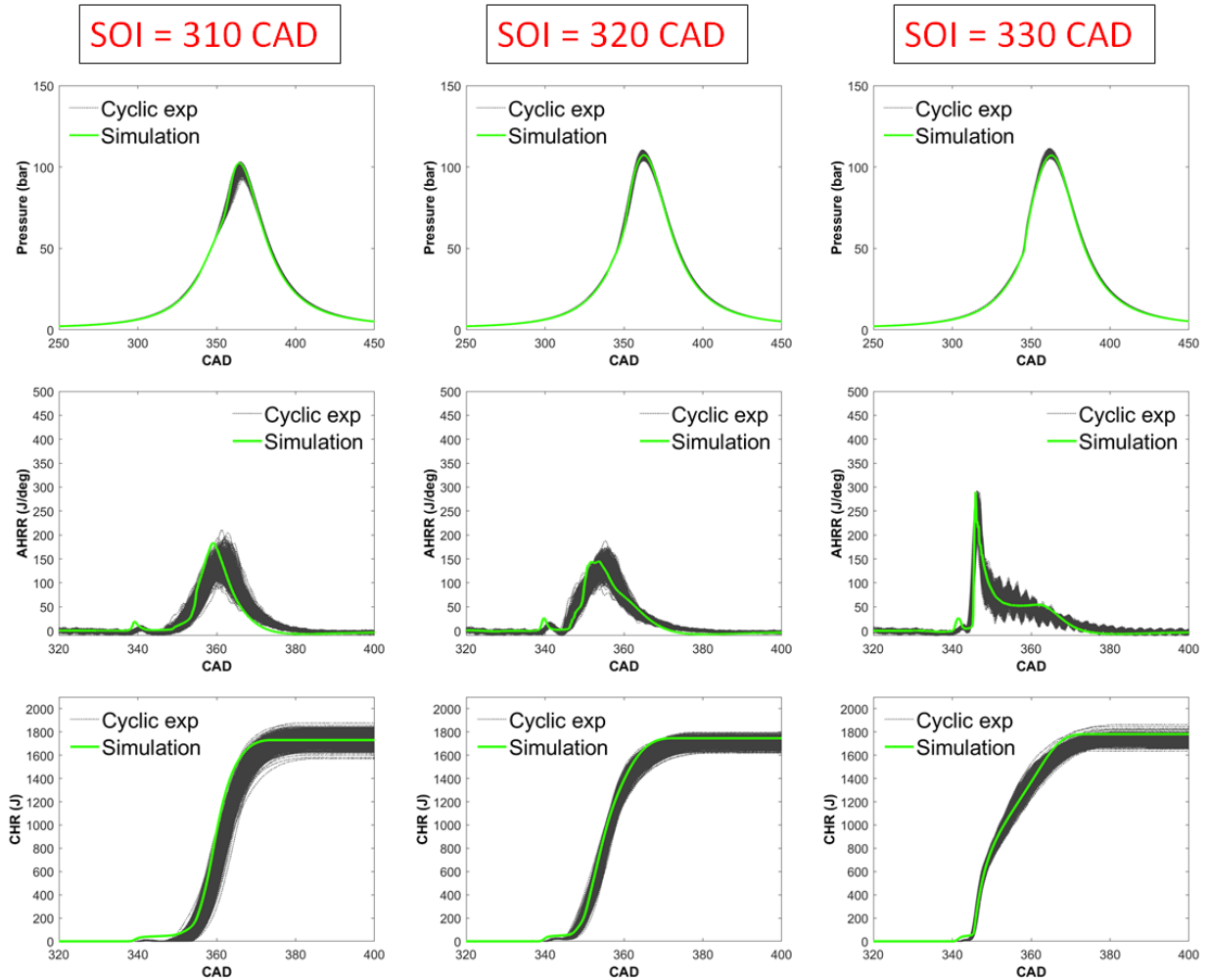


Figure 4.32 Computational pressure, AHRR and CHR histories plotted over experimental 1000 consecutive cycles for 500bar injection pressure, 80 PES of methane, 1.5 bar manifold pressure, and 5.1 bar IMEP of engine load at various diesel injection timing of 310, 320 and 330 CAD

Figures 4.33 and 4.34 show close cycle indicated fuel conversion efficiency and combustion efficiency comparisons. Indicated power in both the simulated and experimental case is obtained only for intake valve closing (IVC) to exhaust valve opening (EVO). It can be observed that the model can predict both the CC_IFCE and

combustion efficiency value reasonably well. From all these observations we can say there is a reasonable match between predicted and experimental AHRR and CHR.

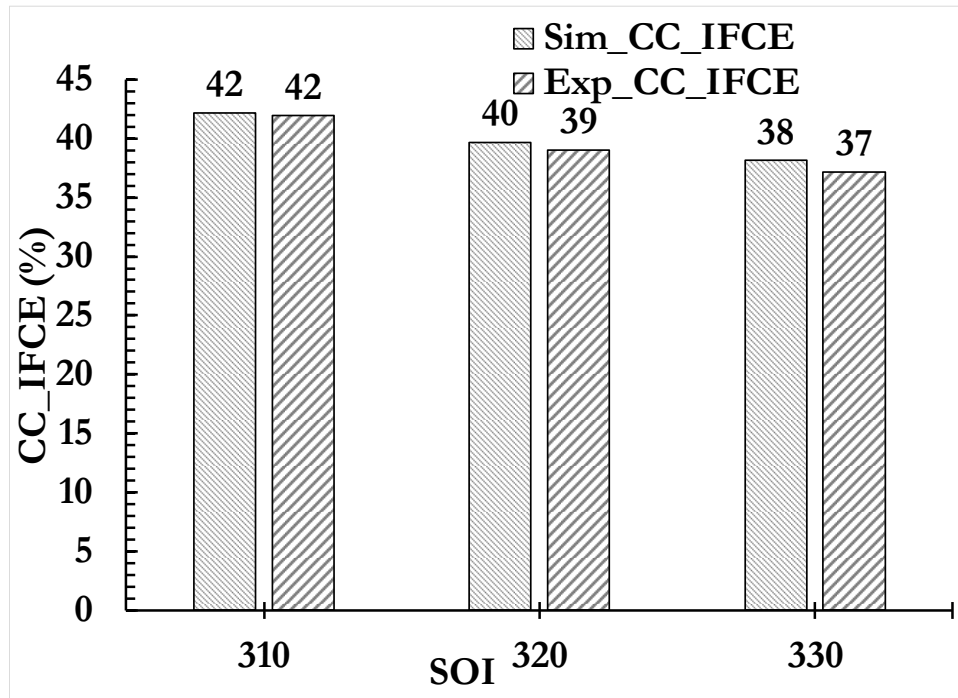


Figure 4.33 Comparison of computational and experimental closed-cycle indicated fuel conversion efficiency (CC_IFCE) for 1.5 bar manifold pressure, 500bar injection pressure, 80 PES of methane, and 5.1 bar IMEP of engine load at various diesel injection timing of 310, 320, and 330 CAD

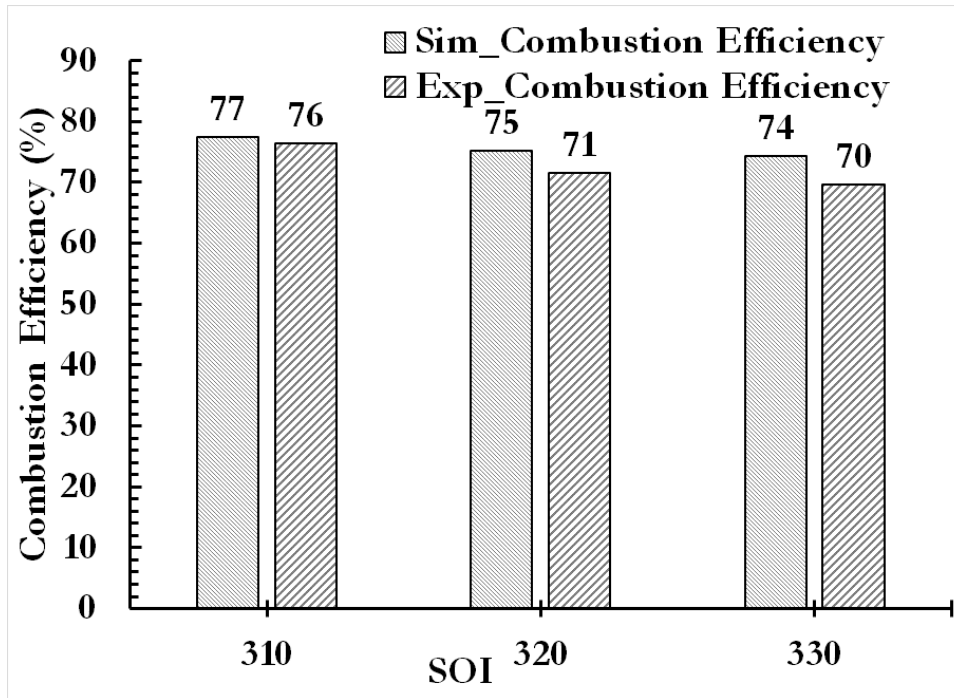


Figure 4.34 Comparison of computational and experimental combustion efficiency for 1.5 bar manifold pressure, 500bar injection pressure, 80 PES of methane, and 5.1 bar IMEP of engine load at various diesel injection timing of 310, 320, and 330 CAD

Figures 4.35, 4.36, and 4.37 show NO, HC, and CO emissions comparison between simulation and experiment. Since we are comparing emissions from second computational cycles with engine-out average emissions from the experiment, there is bound to be some variability, but we are mainly concerned about the model's ability to capture experimental trends. We can visually observe from Figure 4.35 that NO emissions values are well captured both quantitatively and qualitatively by the model. It is able to capture the exponential growth of NO emissions that are seen experimentally when diesel injection timing is shifted from 310 CAD to 330 CAD. From Figure 4.36 we can see the model can capture the HC trends. The model prediction at 310 CAD is very close to the experimental value but there is a discrepancy at for 320 and 330 CAD. This

is likely due to the high cyclic variations in combustion, which leads to partial and total misfire cycles. In such cycles, the partially burned or unburned methane escapes the engine, and this is measured by the emissions bench. A small percentage of such cycles is sufficient to throw off the emissions measurements. A RANS based CFD model captures the average trend and cannot capture cyclic variations. As a consequence, the simulation model under-predicts experimental measurements. Model is able to predict CO emissions trends as shown in Figure 4.37. CO emission in the experiment decreases from diesel injection timing of 310 CAD to 320 CAD and then increases, which is well captured by the model. CO emissions are governed by chemical kinetics and the rate of CO oxidation depends on the bulk gas temperature [69]. As seen from the Figure 4.38 the cylinder-averaged bulk gas temperature from the CFD model is within the cyclic variation band of the experimental cylinder averaged bulk gas temperatures at 310, 320 and 330 CAD. Clearly the rate of CO oxidation from one cycle to another is different based on the observed cyclic variations in cylinder-averaged bulk gas temperatures. As a result, engine-out CO emissions can be expected to be different from one cycle to another. Therefore, while the RANS model is able to capture experimental trends the discrepancy with experimental trends is attributable to high cyclic variations, Considering all the uncertainties, overall, the pressure, AHRR, CHR, η_{comb} , CC_IFCE, NO emissions, HC emissions, and CO emissions comparisons confirm the ability of the open cycle CFD model to predict diesel methane dual fuel combustion at low loads for different diesel injection timings. Therefore, we can use this model with reasonable confidence to perform a parametric investigation to identify different strategies for the reduction of HC and CO emissions at low engine loads.

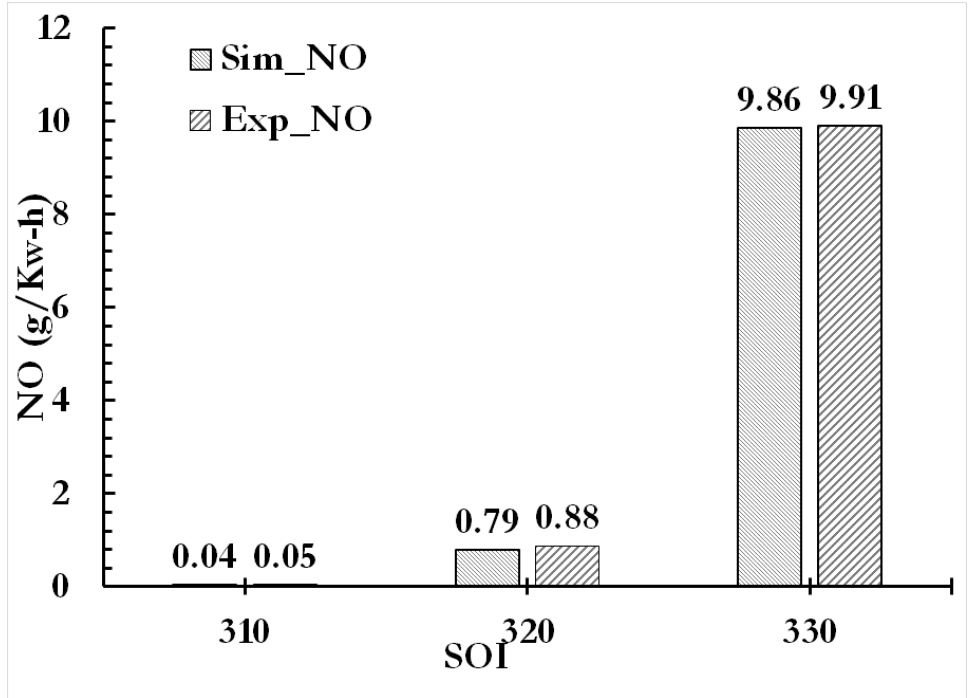


Figure 4.35 Comparison of computational and experimental NO emissions for 1.5 bar manifold pressure, 500bar injection pressure, 80 PES of methane, and 5.1 bar IMEP of engine load at various diesel injection timing of 310, 320, and 330 CAD

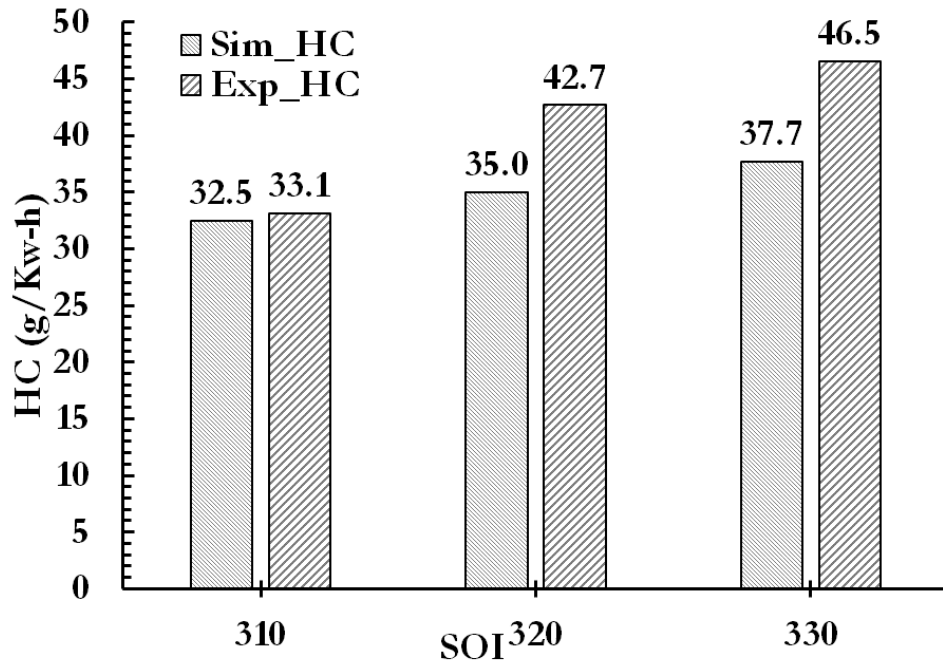


Figure 4.36 Comparison of computational and experimental HC emissions for 1.5 bar manifold pressure, 500bar injection pressure, 80 PES of methane, and 5.1 bar IMEP of engine load at various diesel injection timing of 310, 320, and 330 CAD

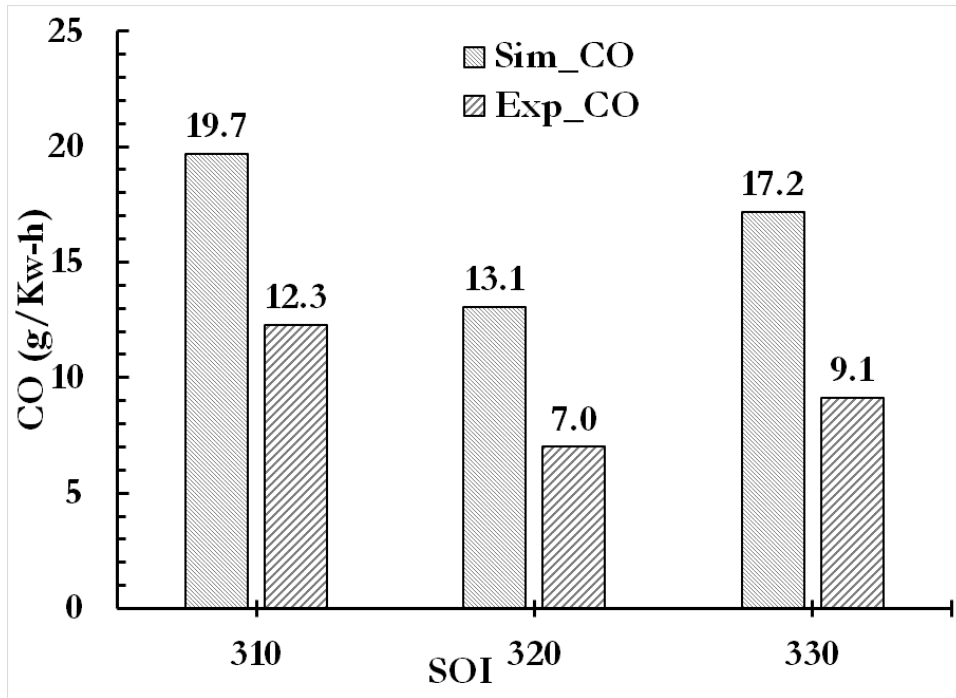


Figure 4.37 Comparison of computational and experimental CO emissions for 1.5 bar manifold pressure, 500bar injection pressure, 80 PES of methane, and 5.1 bar IMEP of engine load at various diesel injection timing of 310, 320, and 330 CAD

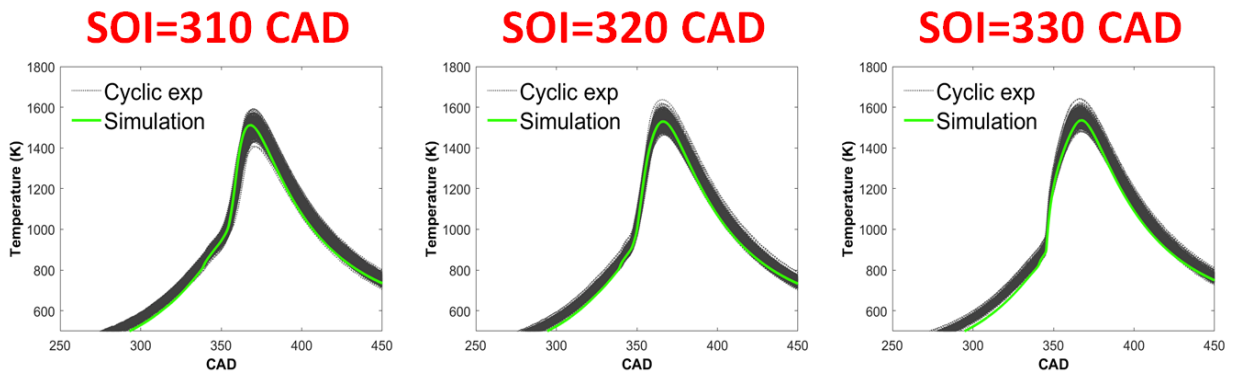


Figure 4.38 Computational temperature histories plotted over experimental 1000 consecutive cycles for 500bar injection pressure, 80 PES of methane, 1.5 bar manifold pressure, and 5.1 bar IMEP of engine load diesel at injection timing of 310,320 and 330 CAD

4.5.3 Combustion and emission characteristics

In this section, we will analyze in-cylinder combustion and emission results for the validated case of diesel injection timing of 310, 320, and 330 CAD for 1.5 bar manifold pressure, 500 bar diesel injection pressure, 80 PES of methane at 5.1 bar IMEP.

4.5.3.1 Combustion characterization

Figures 4.39, 4.40, and 4.41 shows AHRR, methane, and dodecane evolution inside the cylinder for diesel injection timing of 310, 320, and 330 CAD, respectively. Dodecane is chemical species representing diesel in this study. Experimental ignition delay time for diesel SOI 310 CAD is 42 CAD, 320 CAD is 28 CAD, and 330 CAD is 16 CAD. The experimental ignition delay time is defined as the difference between the start of combustion, crank angle where 5% of cumulative heat release (CA5) is achieved and diesel SOI. CA5 for diesel SOI of 310 CAD, 320, and 330 CD are 352, 348, and 346 CAD respectively. It can be observed that combustion starts early when diesel injection is retarded from 310 CAD to 330 CAD. From Figures 39, 40, and 41 it is clear that diesel injection timing of 310 has maximum time to mix inside the cylinder and 330 has minimum time to mix. It is also observed from Figures 4.39, 4.40, and 4.41 is that the initial rate of combustion is slower for diesel injection timing of 310 CAD and the initial rate of combustion increases as the diesel injection timing is retarded towards 330 CAD. One more thing evident from Figures 4.39,4.40 and 4.41 is that majority of dodecane decomposed into other molecules before high-temperature heat release starts and the decomposition process is faster for retarded injection timing. Similarly, most methane does not take part in combustion until the start of high-

temperature heat release and the initial rise in high-temperature heat release in all cases is mainly coming from diesel combustion.

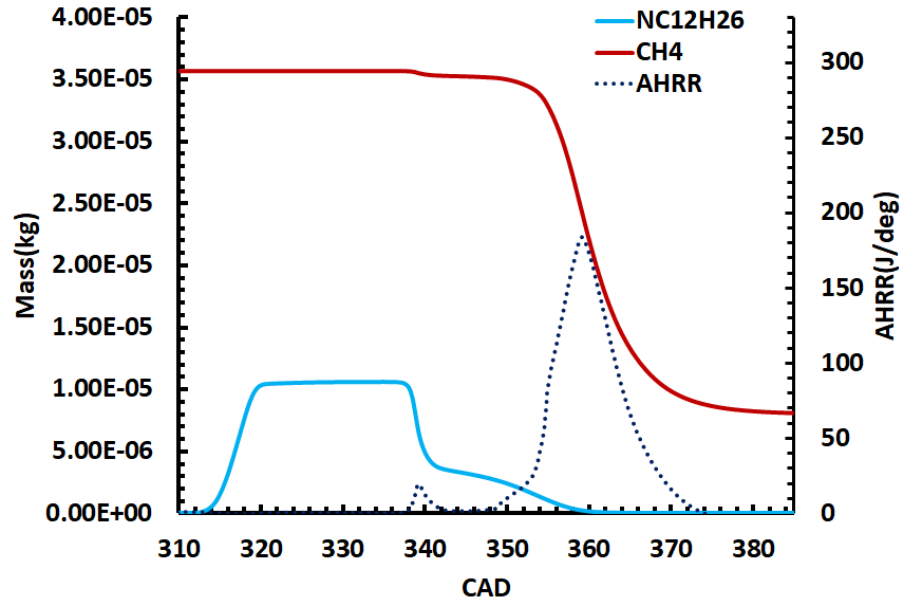


Figure 4.39 AHRR, dodecane, and methane crank angle evolution for 1.5 bar boost pressure, 500 bar diesel injection pressure 80 PES of methane, and 5.1 bar IMEP of engine load at diesel injection timing of 310 CAD

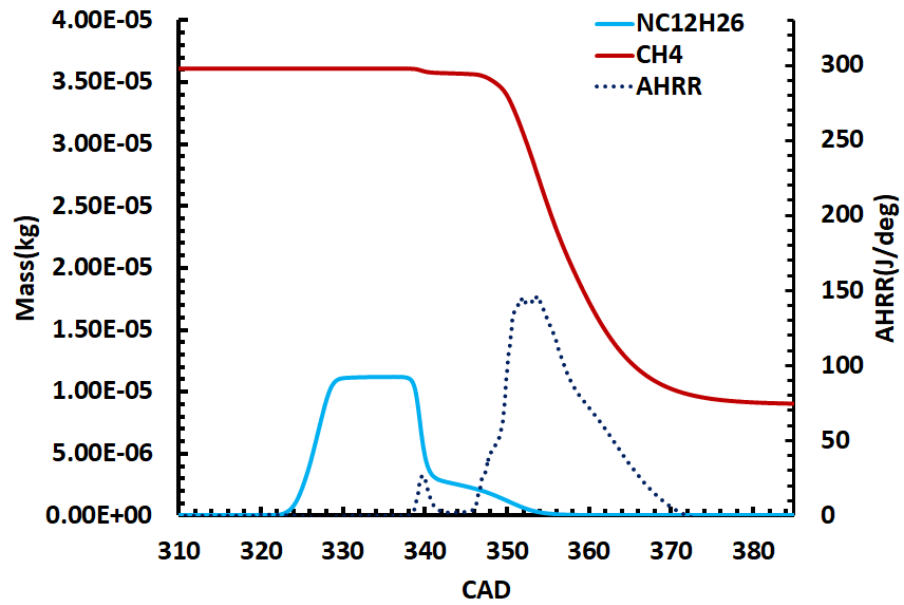


Figure 4.40 AHRR, dodecane, and methane crank angle evolution for 1.5 bar boost pressure, 500 bar diesel injection pressure 80 PES of methane, and 5.1 bar IMEP of engine load at diesel injection timing of 320 CAD

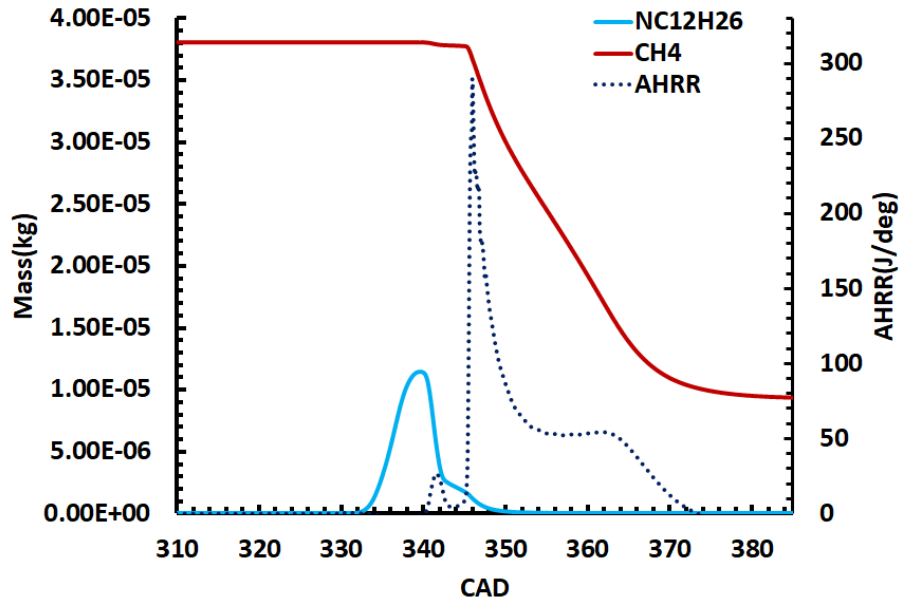


Figure 4.41 AHRR, dodecane, and methane crank angle evolution for 1.5 bar boost pressure, 500 bar diesel injection pressure 80 PES of methane, and 5.1 bar IMEP of engine load at diesel injection timing of 330 CAD

So, to clearly understand the distribution of diesel inside the cylinder and explain the above-observed phenomena, react ratio v/s temperature is plotted for each computational cell. React ratio is an equivalence ratio that doesn't include CO₂ and H₂O in the calculation [49]. It is defined in Equation 4.87 below:

$$\phi_R = \frac{2\sum N_{C_i} + \frac{1}{2}\sum N_{H_i}}{\sum N_{O_i}} \quad (4.87)$$

Where “i” is all species except CO₂ and H₂O

Figures 4.42, 4.43, and 4.44 show react ratio v/s temperature colored by methane mass fraction for diesel injection timing of 310, 320, and 330 CAD, respectively. Since

methane is fumigated in the intake manifold, it is distributed homogeneously inside the cylinder, so each cell has a similar methane fraction just before diesel injection. A lower methane fraction indicates combustion has occurred in that cell and methane has been consumed.

Results are shown for nine different engine crank angle stamps. The first and second crank angle are those crank angles where high-temperature combustion is first observed. The seventh crank angle corresponds to the crank angle where 50% of cumulative heat release (CA50) occurs for that diesel injection timing. Four different crank angles are selected between the first instance where high-temperature heat release occurs and CA50. Eighth crank angle corresponds to crank angle where 90% of cumulative heat release (CA90) occurs for that diesel injection timing. And ninth engine crank angle corresponds to 375 CAD where most of the combustion is complete for all three cases. In Figure 4.42 for 310 CAD diesel SOI, the react ratio starts out being lean indicating that the injected diesel has had sufficient time to disperse and mix resulting in very little stratification. Therefore, the first instance of high-temperature heat release occurs around 348 CAD. At 349 CAD temperature stratification is observed, i.e., temperature is between 1200 K to 1500 K. This indicates that methane is being converted to intermediate hydrocarbons and carbon monoxide, and in the process releasing energy; however, the fraction of cells where complete combustion is occurring is restricted to temperatures above 1800 K. Such cells are characterized by low react ratio magnitudes and are populated by the high concentration of CO₂ and H₂O with very little to no methane or intermediate hydrocarbons. This trend continues at 353 CAD where there is further heat release as seen in Figure 16, which is further corroborated by an increasing

fraction of cells in the temperature range between 1200 K and 1500 K, and a much greater fraction of cells that are at lower react ratio and above 1800 K. Finally, around 375 CAD when most of the combustion is complete there are cells that show a high amount of unburned methane (red color), a high amount of intermediate hydrocarbons and carbon monoxide (green color), and a relatively smaller fraction of cells that have CO₂ and H₂O (blue color). Additionally, throughout the heat release process, the fraction of cells that exceed 2000K are very small, which explains the reason for the very low NO_x concentration.

For the 320 SOI case, the first instance of high temperature heat release is observed at 345 CAD. At 347 CAD the temperature stratification appears indicating significant heat release (also seen in Figure 4.40) and clearly regions beyond 1800 K at low react ratio correspond to high concentration of CO₂ and H₂O. Whereas, regions between 1200 K to 1500 K correspond to regions where intermediate hydrocarbons and CO is likely present. Around 351 CAD where the heat release magnitude peaks there is a higher concentration of zones that have 1800K or higher where the react ratio is near zero clearly confirming high CO₂ and H₂O concentrations. The slight hook back where the react ratio increases around 2500 K indicates dissociation reactions likely occur with little fuel bound oxygen so the denominator in Eq 4.87 is small, which will increase the react ratio artificially. Finally, at 375 CAD when combustion practically ceases there is still methane remaining (red color) with some amount of CO and intermediate hydrocarbons (green) indicating that there is still some amount of unburned hydrocarbon and CO emissions.. The fraction of zones above 2000 K is significantly higher than at 310 CAD

and the residence time for these high temperature zones is also higher indicating that NO_x emissions will be high (confirmed earlier).

At 330 CAD the first instance of high temperature heat release is observed at react ratios of 1.2 at 345 CAD and within 1 CAD, at 346 CAD, temperature stratification occurs. This indicates that since the injected diesel has not had time to disperse into the surrounding methane-air mixture there is sufficient charge stratification and a high fraction of the computational cells show high heat release magnitudes (confirmed in Figure 4.41 where peak heat release magnitude occurs around 346 CAD) and reaction completion to CO₂ and H₂O. In addition, the hook back is prominent and occurs beyond a temperature of 2500 K. This indicates dissociation type reactions are likely occurring with very little free oxygen in the cells, which drives the react ratios to values greater than 2. There are cells in the 1200 K to 1500 K range that have intermediate hydrocarbons and carbon monoxide distributed between react ratio 0.5 to 1. This distribution continues until 364 CAD where most of the cells have react ratio closer to zero between 1500 K to 2700 K indicating complete reaction to CO₂ and H₂O. The residence time for which high temperatures beyond 2500 K persist are much higher in magnitude, which explains the high NO_x emissions observed at this condition.

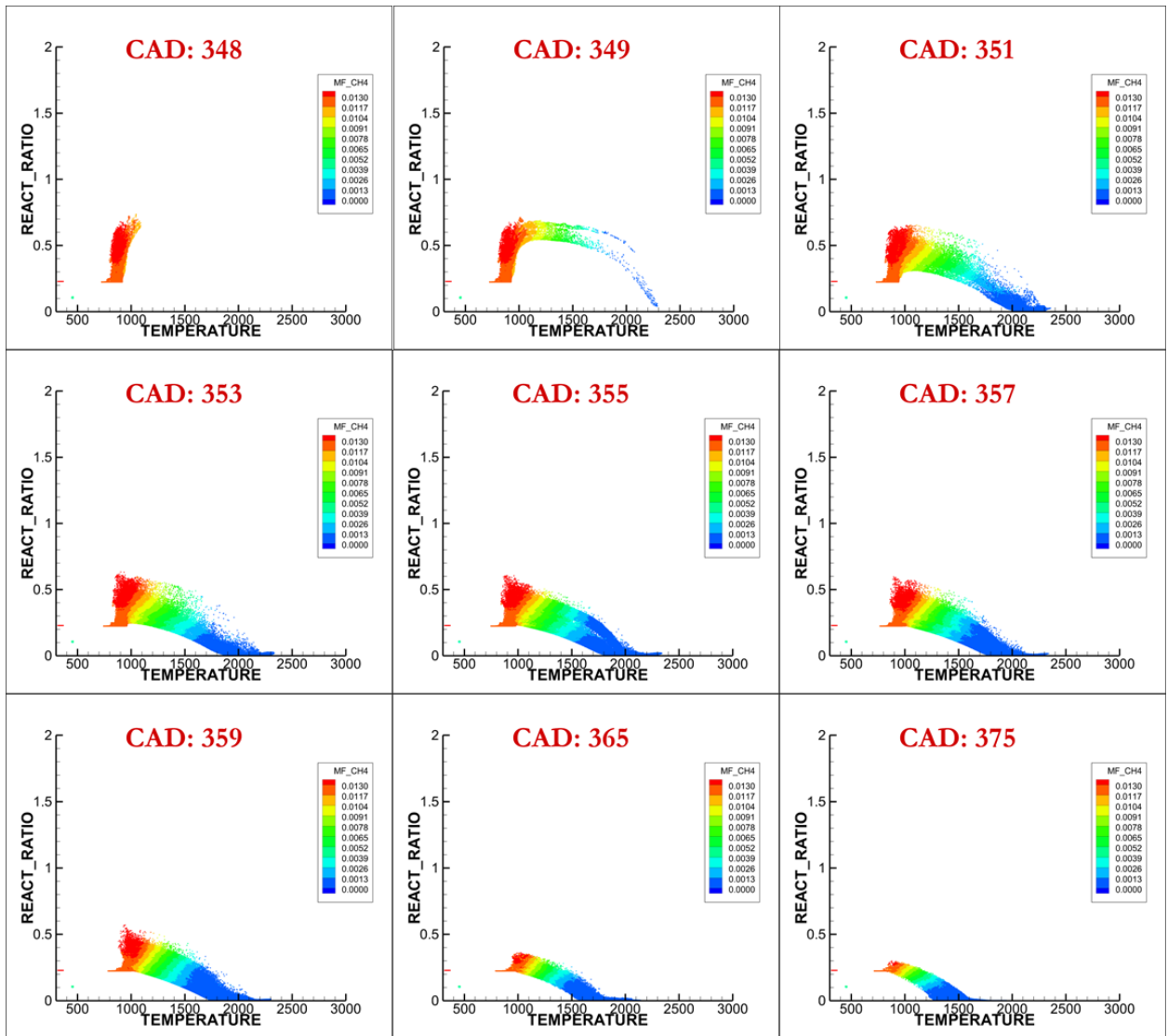


Figure 4.42 React ratio v/s temperature colored with methane mass fraction for each computational cell for 1.5 bar boost pressure, 500 bar diesel injection pressure 80 PES of methane, and 5.1 bar IMEP of engine load at diesel injection timing of 310 CAD.

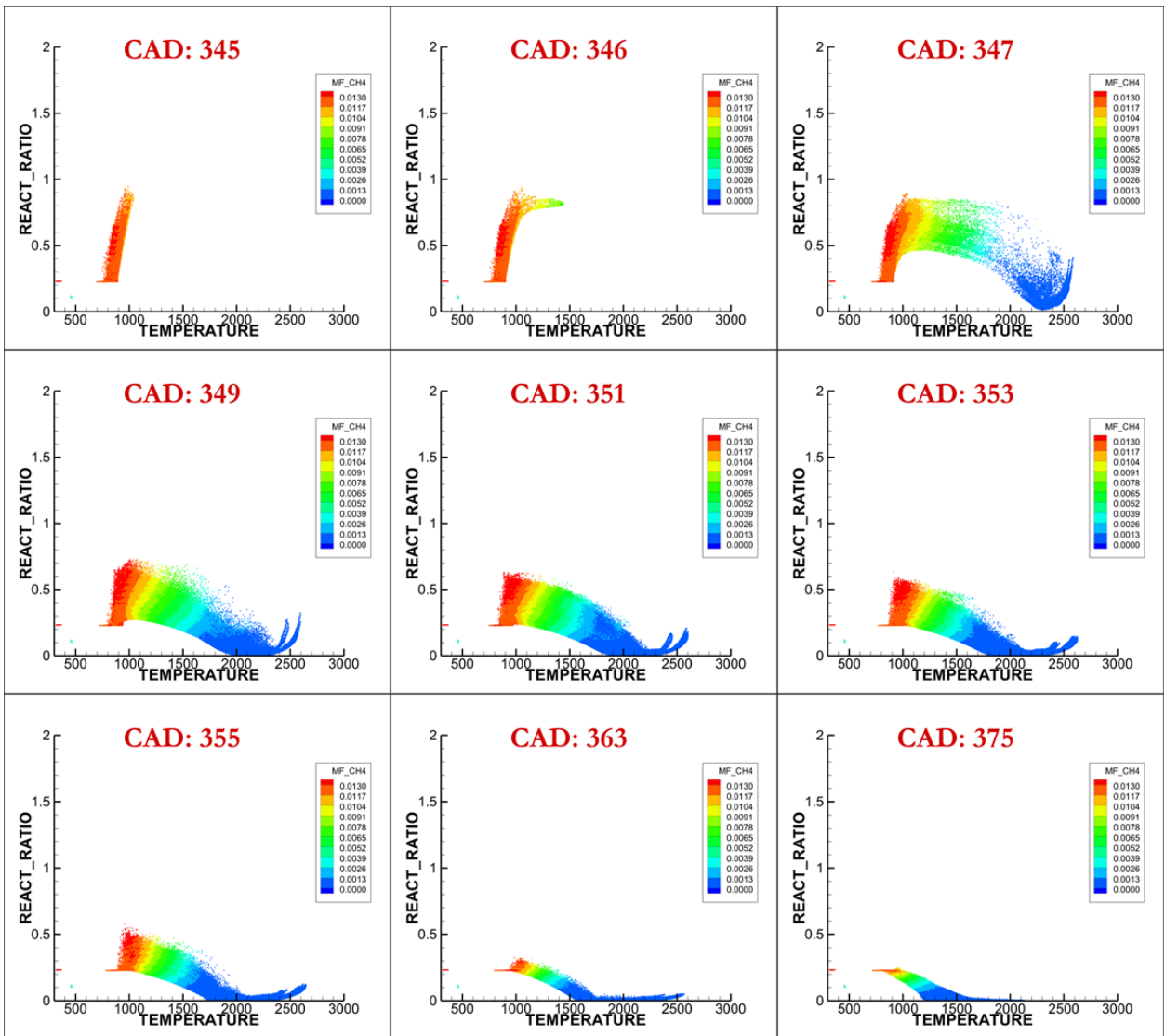


Figure 4.43 React ratio v/s temperature colored with methane mass fraction for each computational cell for 1.5 bar boost pressure, 500 bar diesel injection pressure 80 PES of methane, and 5.1 bar IMEP of engine load at diesel injection timing of 320 CAD.

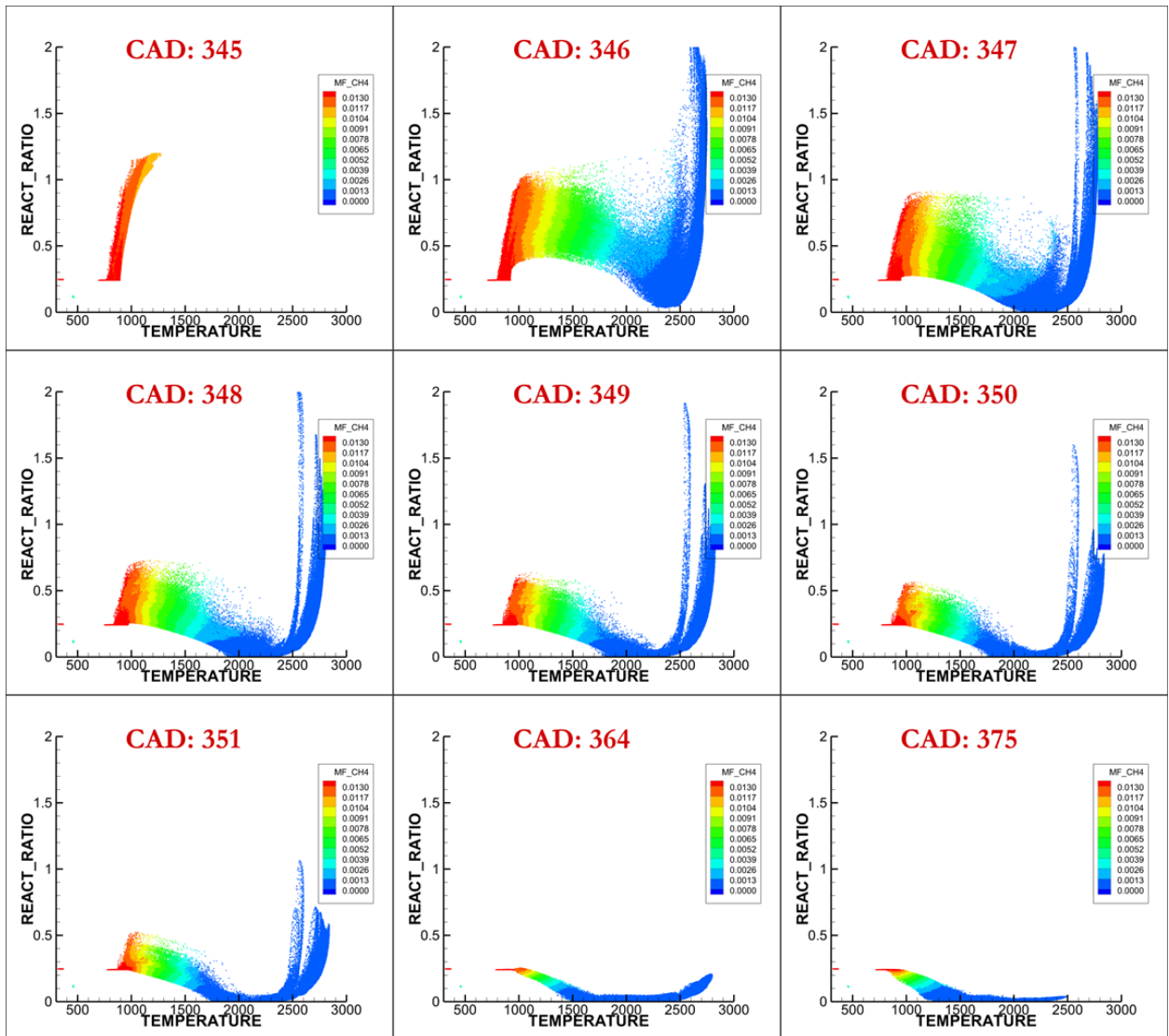


Figure 4.44 React ratio v/s temperature colored with methane mass fraction for each computational cell for 1.5 bar boost pressure, 500 bar diesel injection pressure 80 PES of methane, and 5.1 bar IMEP of engine load at diesel injection timing of 330 CAD.

To further understand the distribution of diesel inside the cylinder and explain the above-observed phenomena, fuel-air equivalence ratio v/s temperature is plotted for each computational cell. Figures 4.45, 4.46, and 4.47 show equivalence ratio v/s temperature colored by methane mass fraction for diesel injection timings of 310, 320, and 330 CAD, respectively. Since methane is fumigated in the intake manifold, it is assumed to be

distributed homogeneously inside the cylinder, so each cell has a similar methane fraction just before diesel injection. Results are shown for nine different engine crank angle stamps. The first and second crank angle are those crank angles where high-temperature combustion is first observed. The seventh crank angle corresponds to the crank angle where 50% of cumulative heat release (CA50) occurs for that diesel injection timing. Four different crank angles are selected between the first instance where high-temperature heat release occurs and CA50. Eighth crank angle corresponds to crank angle where 90% of cumulative heat release (CA90) occurs for that diesel injection timing. And ninth engine crank angle corresponds to 375 CAD where most of the combustion is complete for all three SOIs. In Figure 4.45 for 310 CAD diesel SOI, the equivalence ratio starts out being lean indicating that the injected diesel has had enough time to disperse and mix, resulting in very little stratification. Therefore, the first instance of high-temperature heat release occurs around 348 CAD. At 349 CAD temperature stratification is observed. Methane is being converted to intermediate hydrocarbons and carbon monoxide for cells with intermediate temperature (state range) and complete combustion (i.e. conversion to CO₂) is occurring only in cells above 1800 K. This trend continues at 353 CAD where there is further heat release as seen in Figure 4.39, which is further corroborated by an increasing fraction of cells in the temperature range between 1200 K and 1500 K, and a much greater fraction of cells that are at lower react ratio and above 1800 K. Finally, around 375 CAD when most of the combustion is complete there are cells that show a high amount of unburned methane (red color), a high amount of intermediate hydrocarbons and carbon monoxide (green color). Similar observation is seen for react ratio vs. temperature plot in Figure 4.42.

For the 320 SOI case, the first instance of high temperature heat release is observed at 345 CAD. At 347 CAD temperature stratification appears indicating significant heat release (also seen in Figure 4.40) and clearly regions beyond 1800 K at high equivalence ratio correspond to low concentration of hydrocarbon and carbon monoxide. Whereas, regions between 1200 K to 1500 K correspond to regions where intermediate hydrocarbons and CO is likely present. Around 351 CAD where the heat release magnitude peaks there is a higher concentration of zones that have 1800K or higher where the equivalence ratio is high indicating complete combustion. Finally, at 375 CAD when combustion practically ceases there is still methane remaining (red color) with some amount of CO and intermediate hydrocarbons (green) indicating that there is still some amount of unburned hydrocarbon and CO emissions. Similar observation is obtained for react ratio vs. temperature plot in Figure 4.43 for diesel SOI of 320CAD. At 330 CAD the first instance of high temperature heat release is observed at equivalence ratios of 1.2 at 345 CAD and within 1 CAD, at 346 CAD, temperature stratification occurs. This indicates that since the injected diesel has not had time to disperse into the surrounding methane-air mixture there is sufficient charge stratification and a high fraction of the computational cells show high heat release magnitudes and reaction completion to CO₂ and H₂O. In addition, high equivalence ratio occurs beyond a temperature of 2500 K indicating complete combustion of methane and diesel occurring in those cells. There are cells in the 1200 K to 1500 K range that have intermediate hydrocarbons and carbon monoxide distributed between react ratio 0.5 to 1. This distribution continues until 364 CAD where most of the cells have an equivalence ratio at

a higher value indicating a complete combustion. A similar observation is obtained for react ratio vs. temperature plot in Figure 4.44 for diesel SOI of 330 CAD.

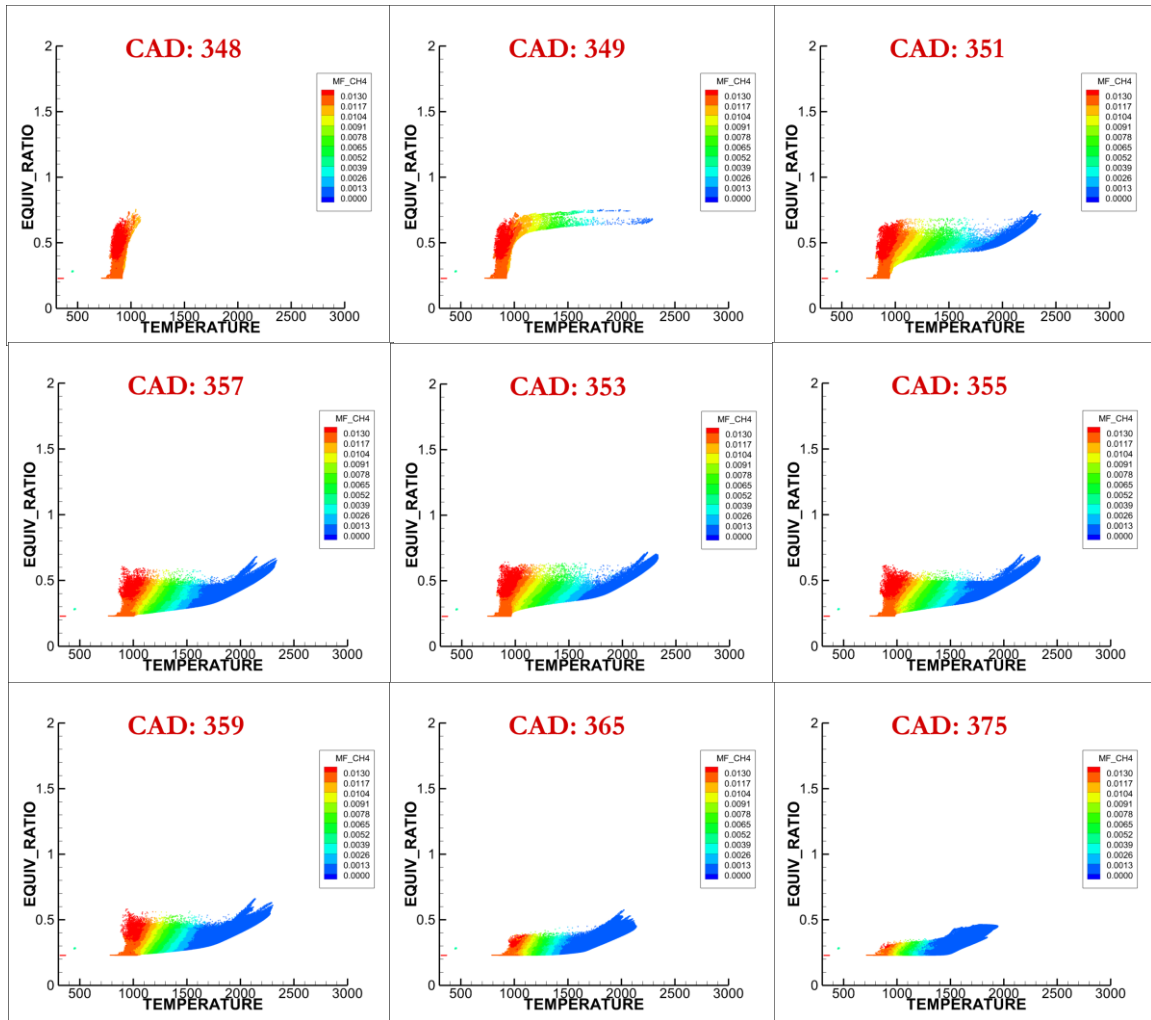


Figure 4.45 Equivalence ratio v/s temperature colored with methane mass fraction for each computational cell for 1.5 bar boost pressure, 500 bar diesel injection pressure 80 PES of methane, and 5.1 bar IMEP of engine load at diesel injection timing of 310 CAD.

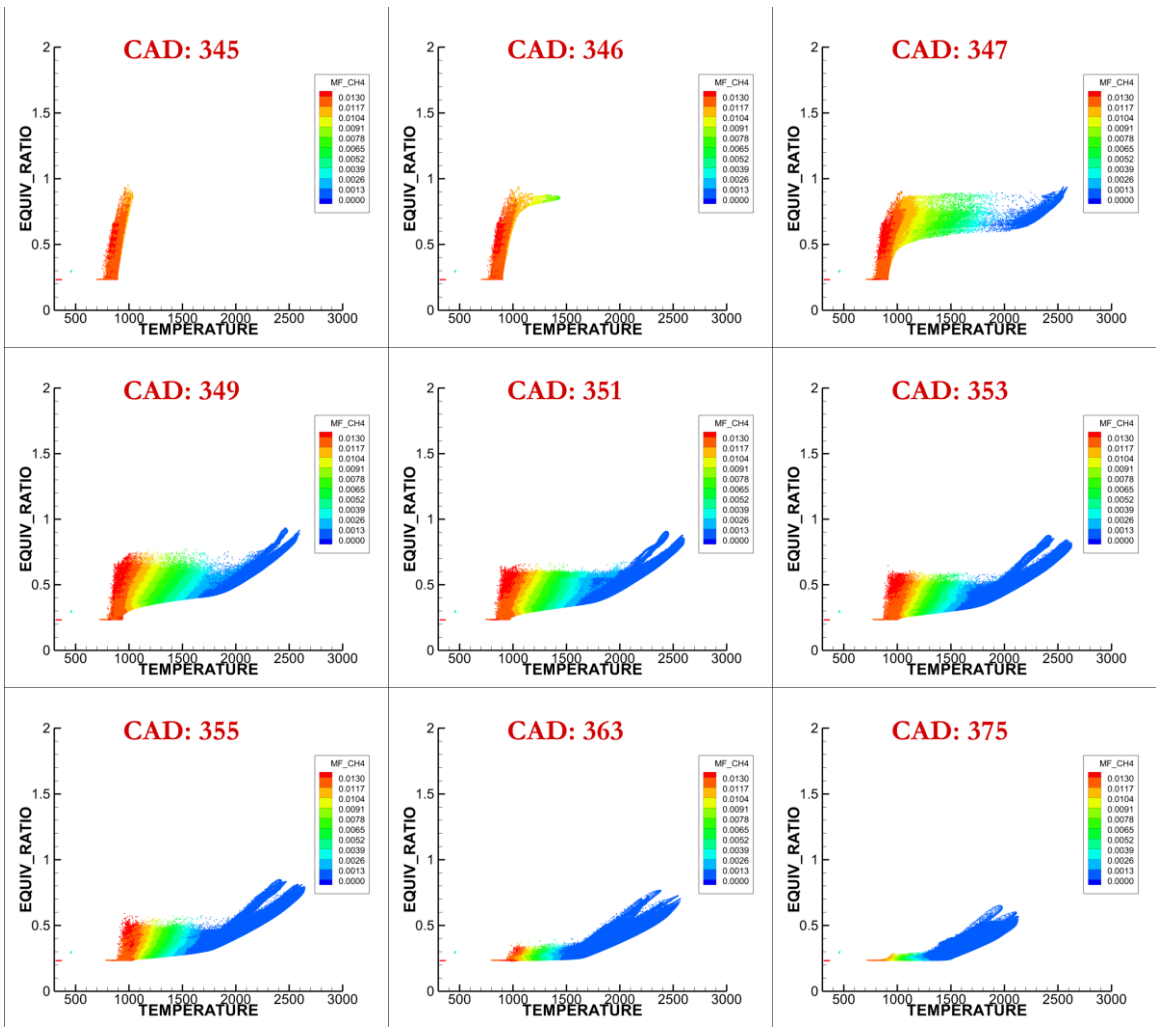


Figure 4.46 Equivalence ratio v/s temperature colored with methane mass fraction for each computational cell for 1.5 bar boost pressure, 500 bar diesel injection pressure 80 PES of methane, and 5.1 bar IMEP of engine load at diesel injection timing of 320 CAD.

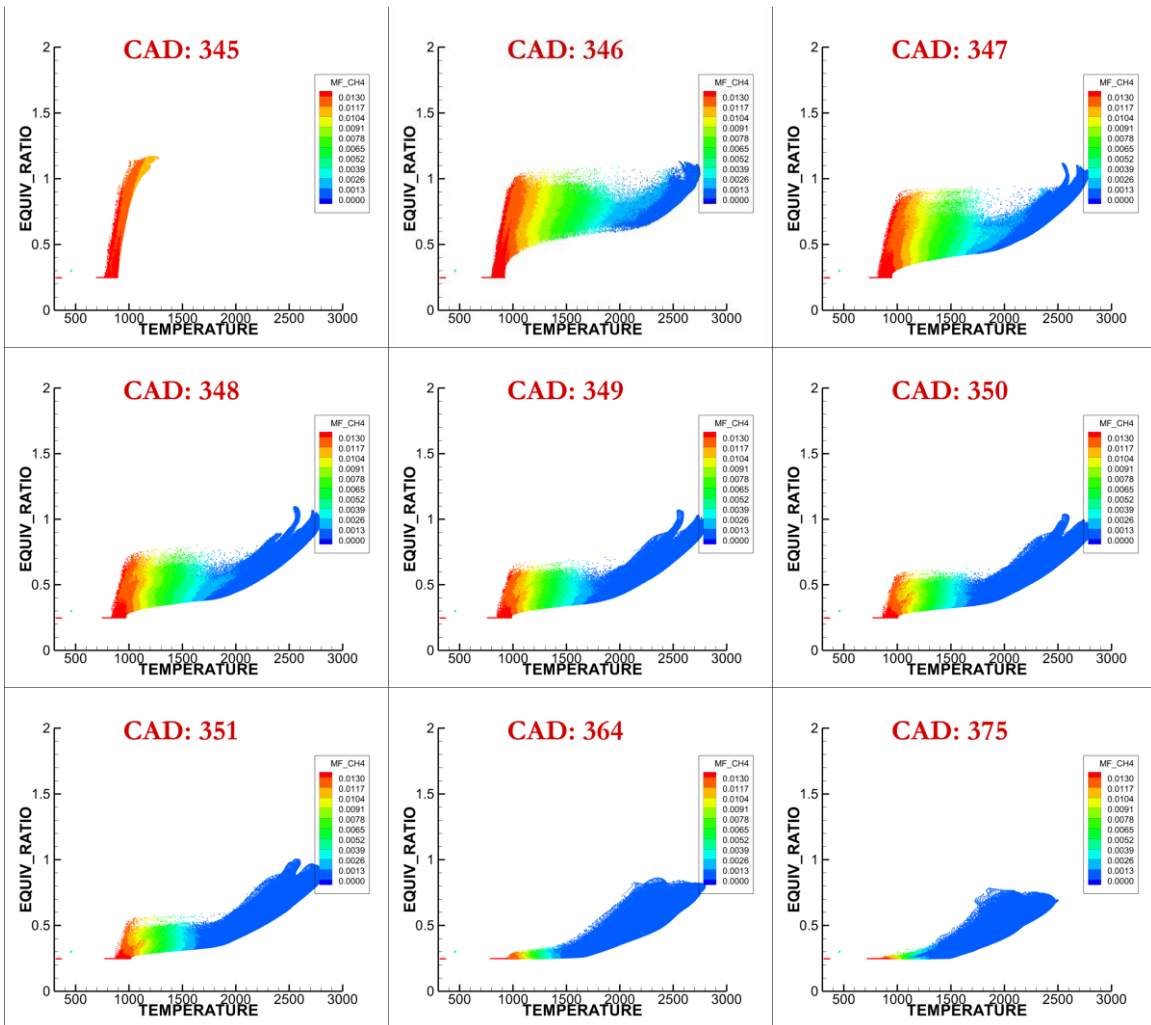


Figure 4.47 Equivalence ratio v/s temperature colored with methane mass fraction for each computational cell for 1.5 bar boost pressure, 500 bar diesel injection pressure 80 PES of methane, and 5.1 bar IMEP of engine load at diesel injection timing of 330 CAD.

Figures 4.48, 4.49, and 4.50 shows temperature contours for diesel injection timing of 310, 320, and 330 CAD, respectively. Seven engine crank angle stamp is selected to illustrate in-cylinder temperature contour. The first crank angle corresponds to the crank angle where visually high-temperature spots are observed. The fourth crank angle corresponds to the crank angle where 50% of cumulative heat release (CA50)

occurs for that diesel injection timing. Two crank angles are selected in between them. The fifth crank angle corresponds to the crank angle where 90% of cumulative heat release (CA90) occurs for that diesel injection timing. The sixth engine crank angle corresponds to 375 where most of the combustion is completed for all three cases. And the seventh corresponds to crank angle 390 which gives us an idea about what is happening later in the expansion phase. Combustion progresses slowly and with less intensity for 310 CAD SOI. Similarly, we can see combustion taking off at a faster rate and high intensity for 330 CAD SOI. When we analyze 390 CAD for all cases, we can see the combustion region near the liner wall and piston has already cooled and the temperature is in the range of 600 K indicating fast quenching occurs during low load conditions.

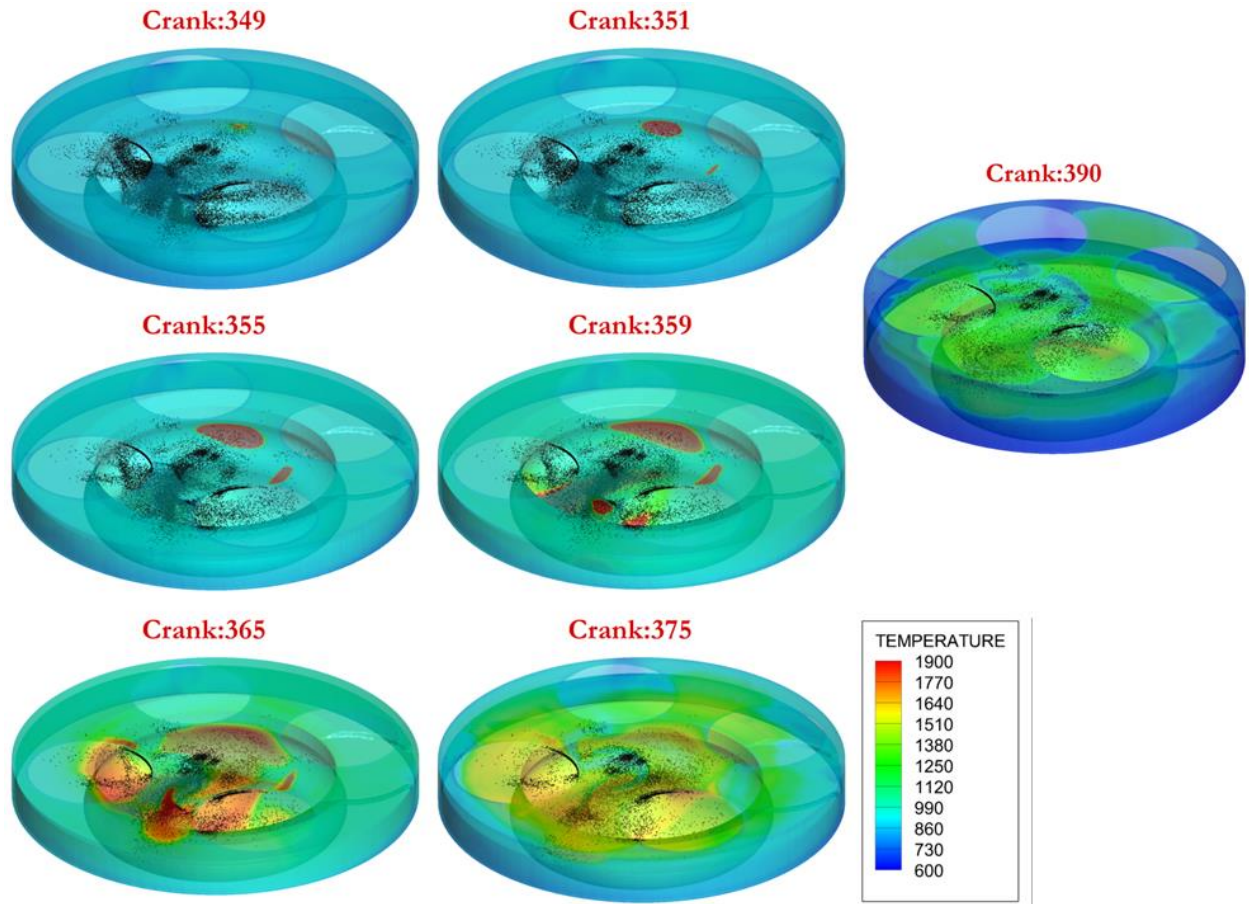


Figure 4.48 Temperature distribution observed (isometric view) for 1.5 bar boost pressure, 500 bar diesel injection pressure, and 80 PES of methane at 5.1 bar IMEP at diesel injection timing of 310 CAD.

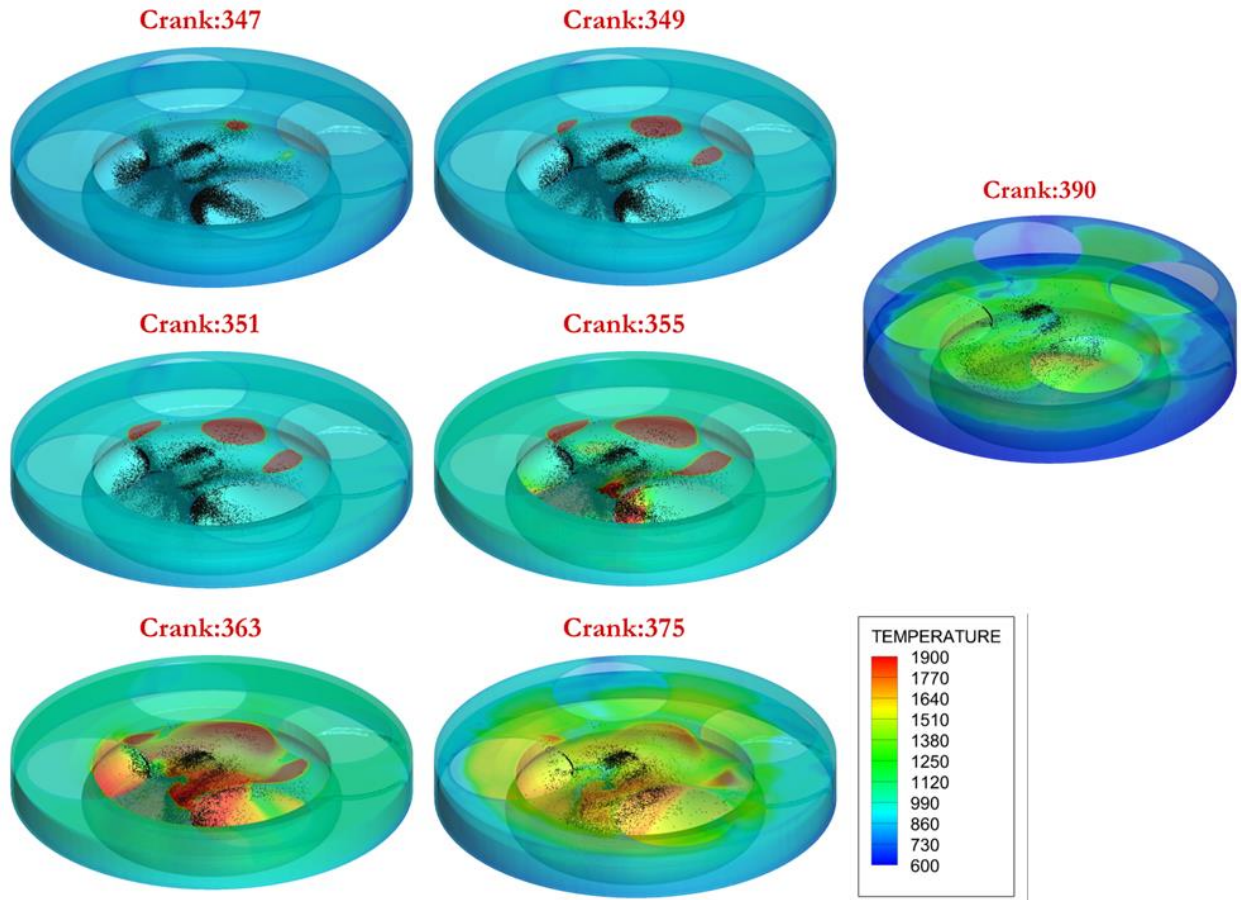


Figure 4.49 Temperature distribution observed (isometric view) for 1.5 bar boost pressure, 500 bar diesel injection pressure, and 80 PES of methane at 5.1 bar IMEP at diesel injection timing of 320 CAD.

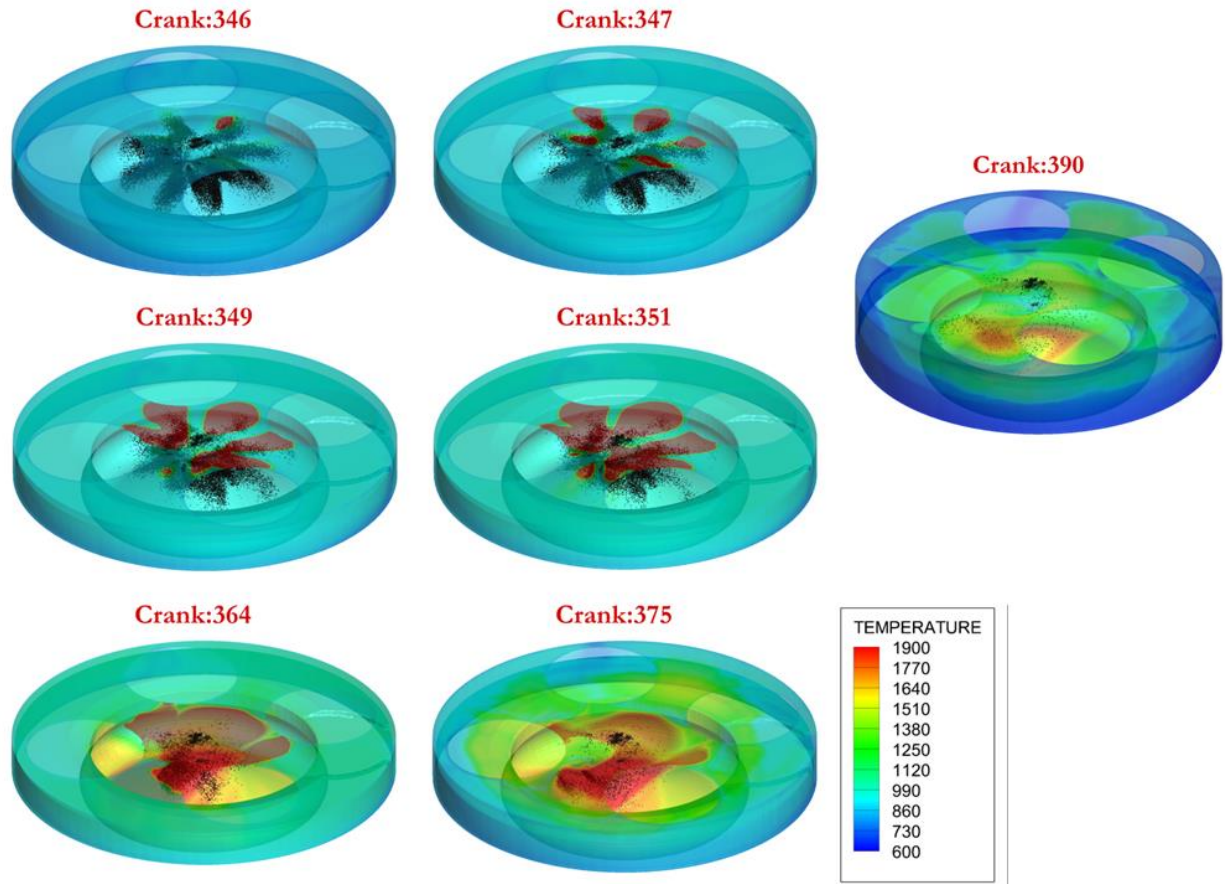


Figure 4.50 Temperature distribution observed (isometric view) for 1.5 bar boost pressure, 500 bar diesel injection pressure, and 80 PES of methane at 5.1 bar IMEP at diesel injection timing of 330 CAD.

4.5.3.2 Emission characterization

Figure 4.51 shows the total NO formed inside the cylinder at various engine crank angle for diesel injection timing of 310, 320, and 330 CAD. NO calculation was made using the NO mechanism from Chalmers mechanism and added to POLIMI_Red mechanism used in this study. NO formation mainly in the engine depends on the local equivalence ratio local combustion temperatures, and residence times of high

temperatures. Nitrogen oxide formed inside the cylinder increases exponentially as diesel injection timing is retarded from 310 CAD to 330 CAD. This has been explained in the react ratio v/s temperature plots in Figures 4.42, 4.43, and 4.44. All three criteria that favor NO formation are fulfilled for diesel injection timing of 330 CAD. Combustion occurs at a react ratio close to one leading to many computational cells exhibiting temperatures above 2000K for a longer duration. For diesel injection timing of 310 CAD, combustion occurs at a react ratio much below one leading to relatively fewer computational cells at which temperature exceeds 2000K which are not sustained for a longer duration leading to lower NO formation.

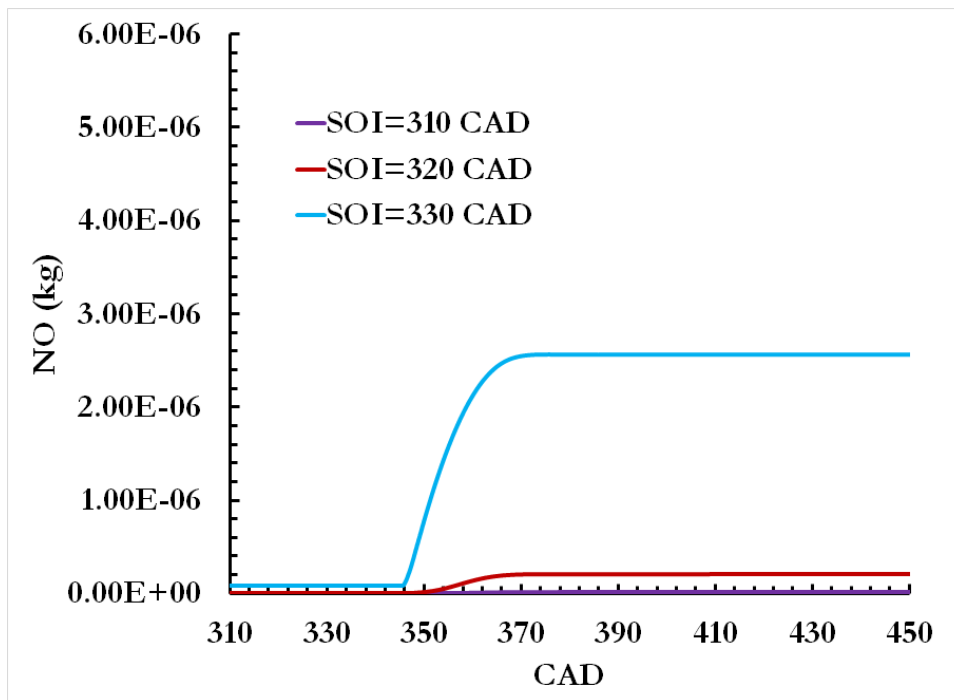


Figure 4.51 NO crank angle evolution for 1.5 bar boost pressure, 500 bar diesel injection pressure 80 PES of methane, and 5.1 bar IMEP of engine load at diesel injection timing of 310, 320, and 330 CAD.

To further visualize the in-cylinder combustion process, methane contours are plotted. Figures 4.52, 4.53, and 4.54 shows methane contours for diesel SOIs of 310, 320,

and 330 CAD, respectively. Seven engine crank angle stamp is selected to illustrate in-cylinder temperature contour. The first crank angle corresponds to the crank angle where visually high-temperature spots are observed. The fourth crank angle corresponds to the crank angle where 50% of cumulative heat release (CA50) occurs for that diesel injection timing. Two crank angles are selected in between them. The fifth crank angle corresponds to the crank angle where 90% of cumulative heat release (CA90) occurs for that diesel injection timing. The sixth engine crank angle corresponds to 375 CAD where most of the combustion is completed for all three cases. And the seventh corresponds to crank angle around 510 CAD where the exhaust valve opens so that spatial locations with high methane concentration are visualized. From these contour plots all three cases show a high amount of unburned methane in crevices and areas near the cylinder wall. This indirectly indicates that combustion never reached these areas and that there is a small amount of methane that is not consumed near the cylinder liner. Most of the methane that does not get consumed resided in crevices and areas near the piston top and liner. This observation indicates at low engine loads strategies to consume unburned methane from the near the cylinder walls needs to be investigated.

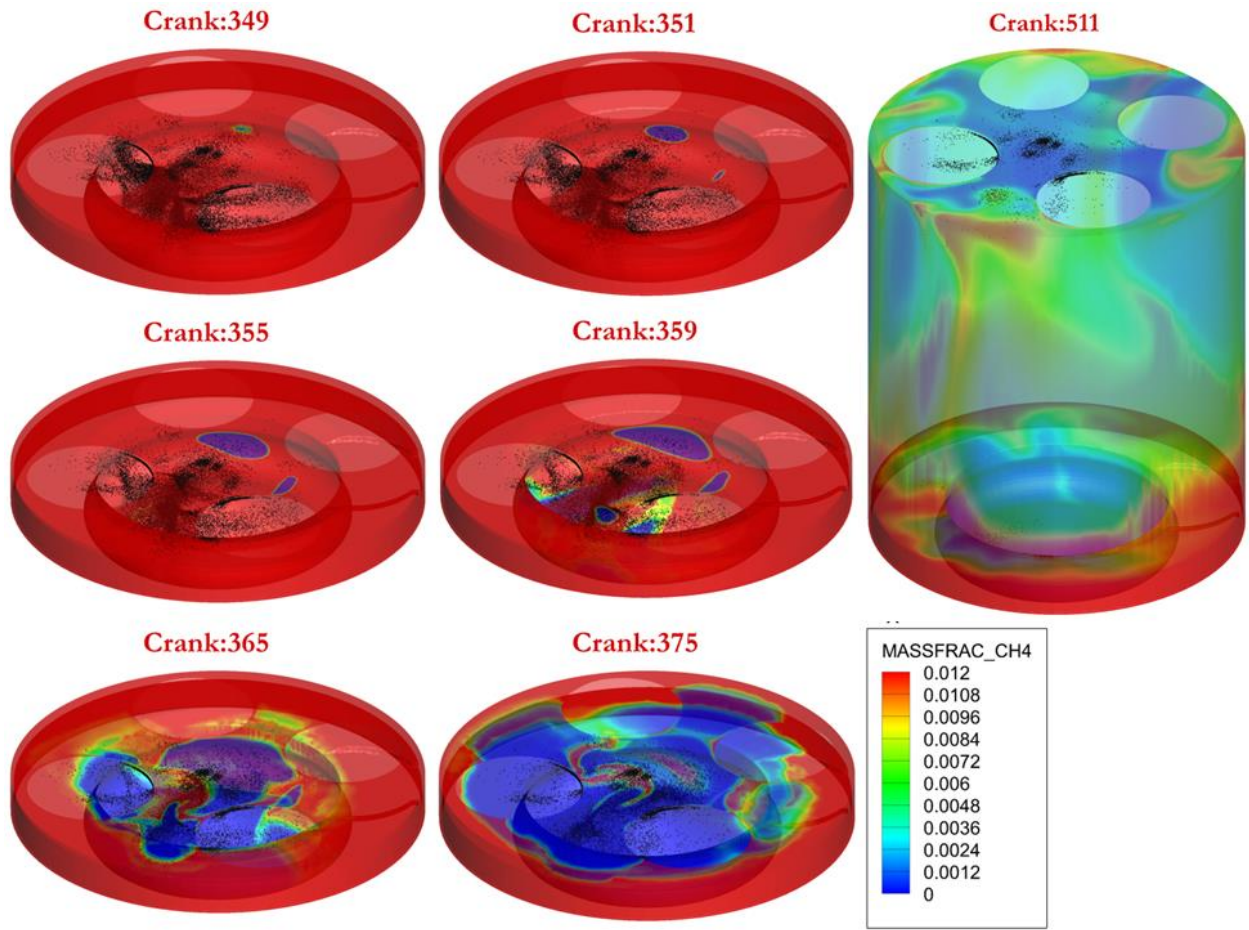


Figure 4.52 Methane distribution observed (isometric view) for 1.5 bar boost pressure, 500 bar diesel injection pressure, and 80 PES of methane at 5.1 bar IMEP at diesel injection timing of 310 CAD.

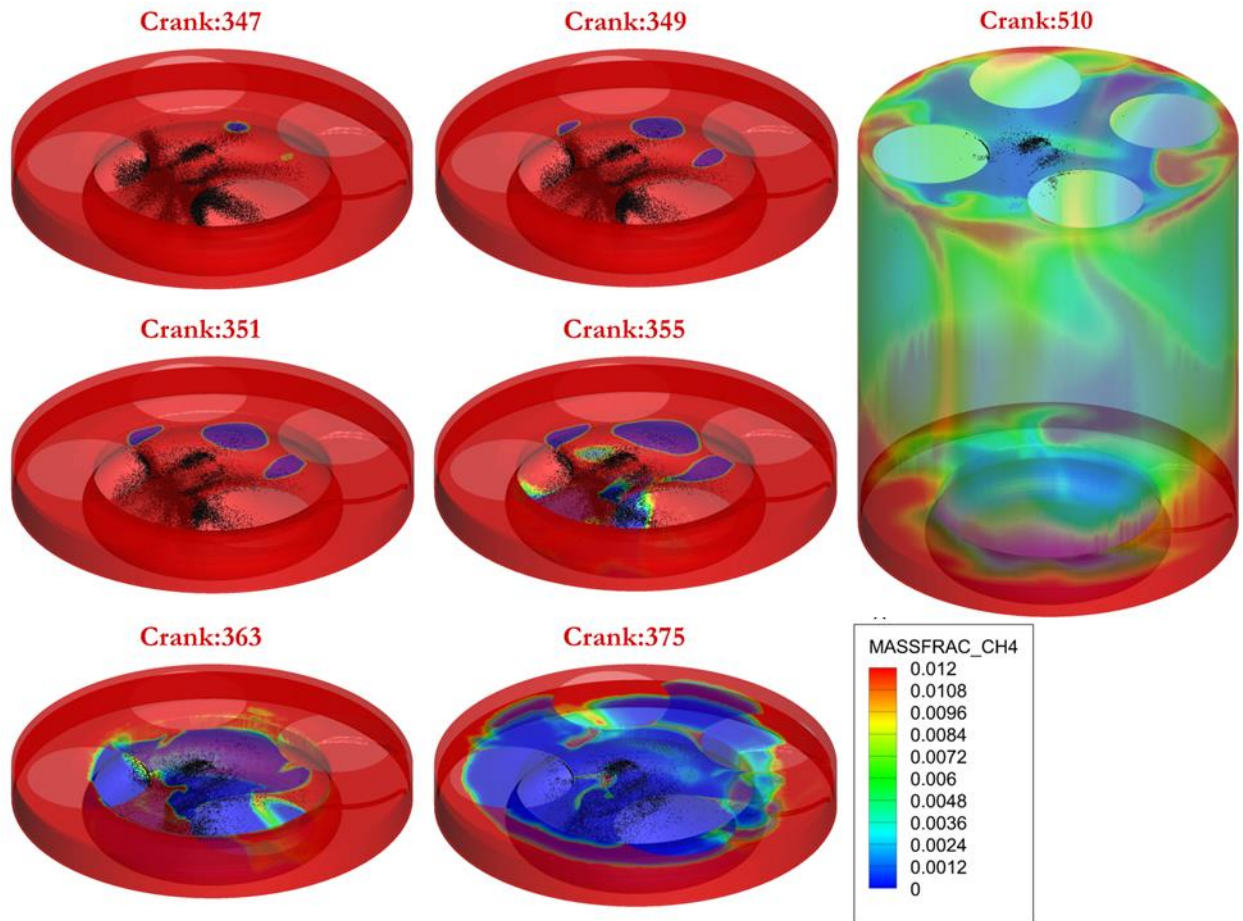


Figure 4.53 Methane distribution observed (isometric view) for 1.5 bar boost pressure, 500 bar diesel injection pressure, and 80 PES of methane at 5.1 bar IMEP at diesel injection timing of 320 CAD.

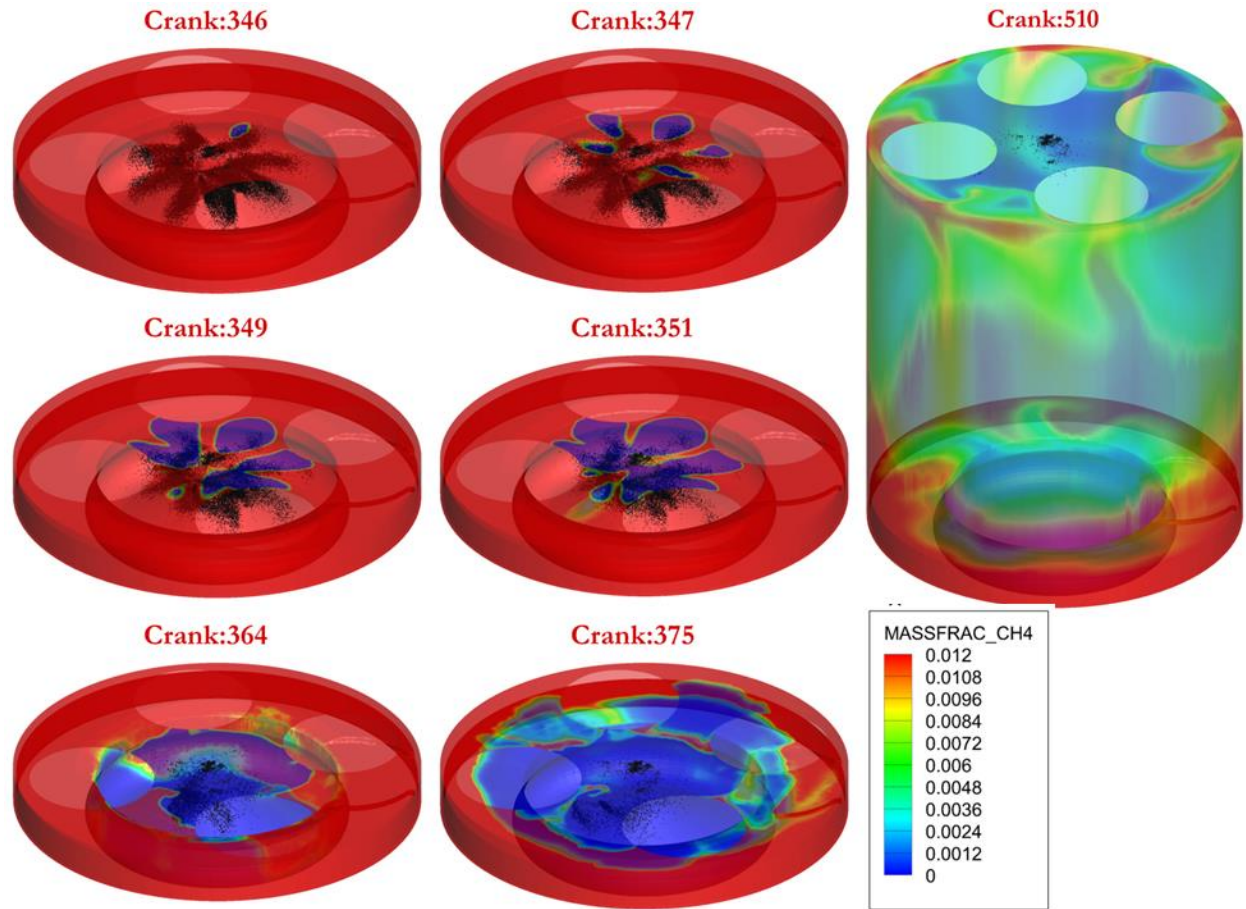


Figure 4.54 Methane distribution observed (isometric view) for 1.5 bar boost pressure, 500 bar diesel injection pressure, and 80 PES of methane at 5.1 bar IMEP at diesel injection timing of 330 CAD.

Figure 4.55 shows the total CO formed inside the cylinder at various engine crank angle for diesel SOIs of 310, 320, and 330 CAD. It is well known that CO formation and oxidation is an important intermediate step in hydrocarbon combustion, and its oxidation is governed by chemical kinetics. Oxidation of CO has two pathways, the fast one, which requires OH radicals and high bulk gas temperatures, and the other slow, which is driven by high bulk gas temperatures. With this in mind, we will discuss CO results obtained

for the cases studied in this work. We observe for diesel injection timing of 310 CAD that the initial rate of CO formation is high, this is due to combustion taking place at a lower temperature as evident from Figure 4.42. Since combustion is occurring at a lower temperature CO oxidation to CO₂ is slower. And eventually formed CO is not able to oxidize later in the expansion stroke when the bulk in-cylinder gas temperature drops rapidly. For diesel injection timing of 330 CAD, even though the temperature at which combustion is occurring is high as evident from Figure 4.44, oxidation of HC is delayed into the expansion phase which forms CO as observed in Figure 4.55 and as this formed CO is already in the expansion phase where the temperature is already dropping CO oxidation to CO₂ is further inhibited. The CO emissions are minimum for diesel injection timing of 320 CAD. Since combustion is occurring at higher temperatures than diesel injection timing of 310 and also combustion is occurring faster compared to diesel injection timing of 330 CAD providing more time for CO to oxidize to CO₂ before the temperature starts dropping and CO chemistry freezes. To further visualize the in-cylinder CO formation process, CO contours are plotted. Figures 4.56, 4.57, and 4.58 show CO contour for diesel injection timing of 310, 320, and 330 CAD respectively. The selected engine crank angle stamp is based on criteria explained for methane emissions contours. We can observe no CO formation in crevices and cylinder walls for all cases analyzed in this study. This is further corroborated by the fact that combustion does not reach this area at low loads.

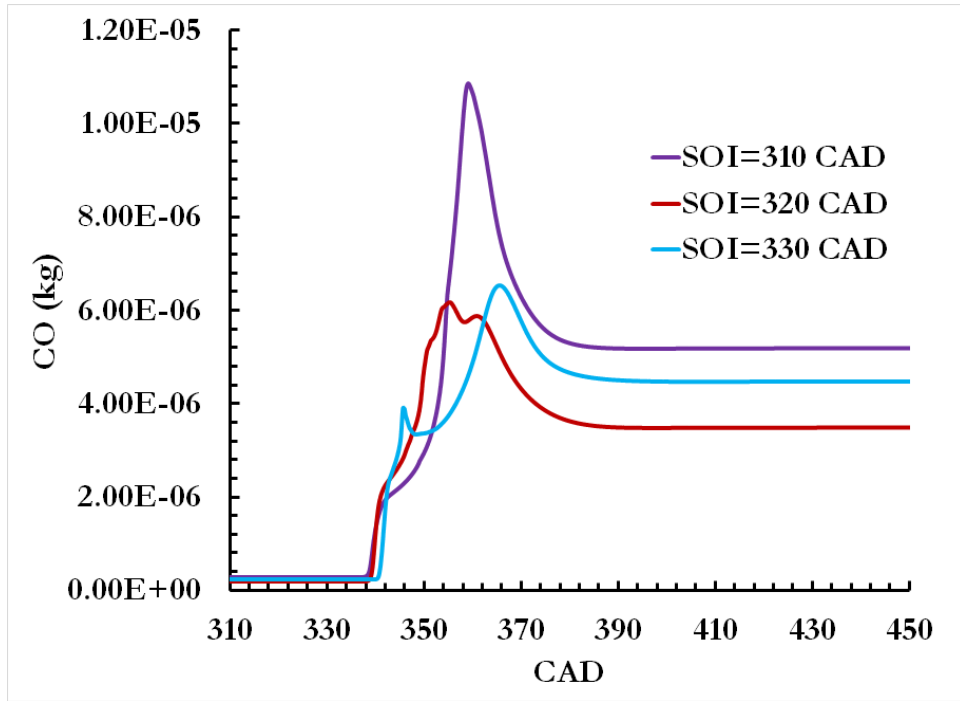


Figure 4.55 CO crank angle evolution for 1.5 bar boost pressure, 500 bar diesel injection pressure 80 PES of methane, and 5.1 bar IMEP of engine load at diesel injection timing of 310, 320, and 330 CAD.

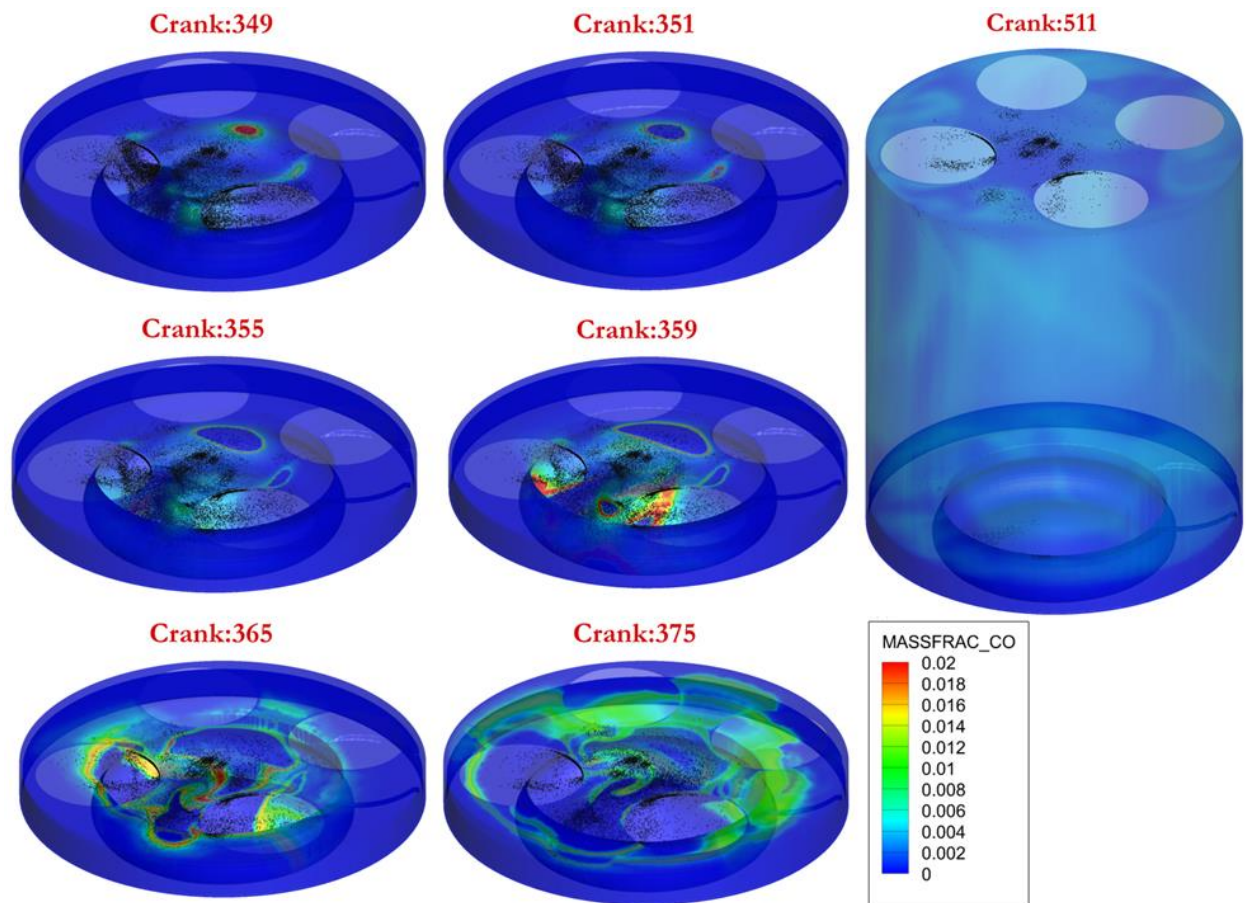


Figure 4.56 CO distribution observed (isometric view) for 1.5 bar boost pressure, 500 bar diesel injection pressure, and 80 PES of methane at 5.1 bar IMEP at diesel injection timing of 310 CAD.

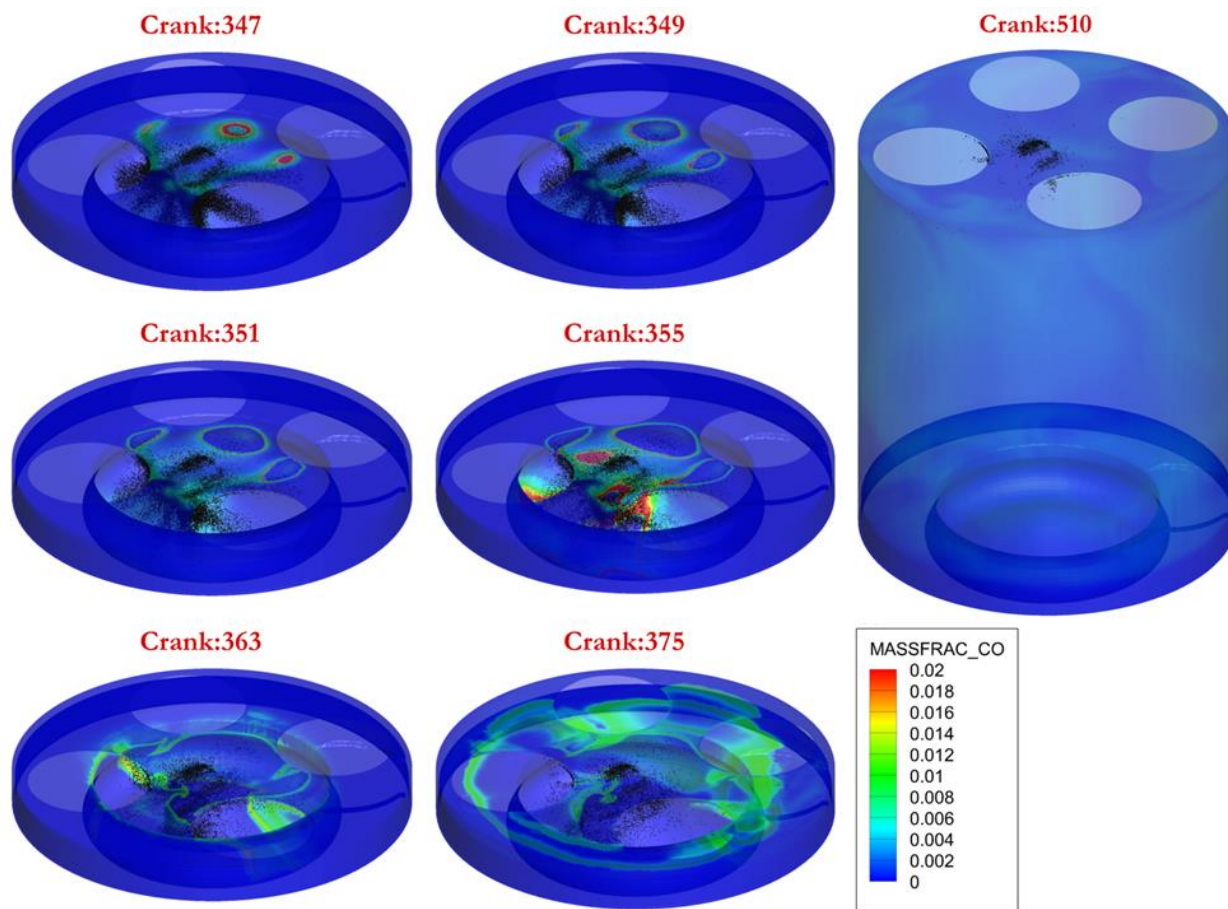


Figure 4.57 CO distribution observed (isometric view) for 1.5 bar boost pressure, 500 bar diesel injection pressure, and 80 PES of methane at 5.1 bar IMEP at diesel injection timing of 320 CAD.

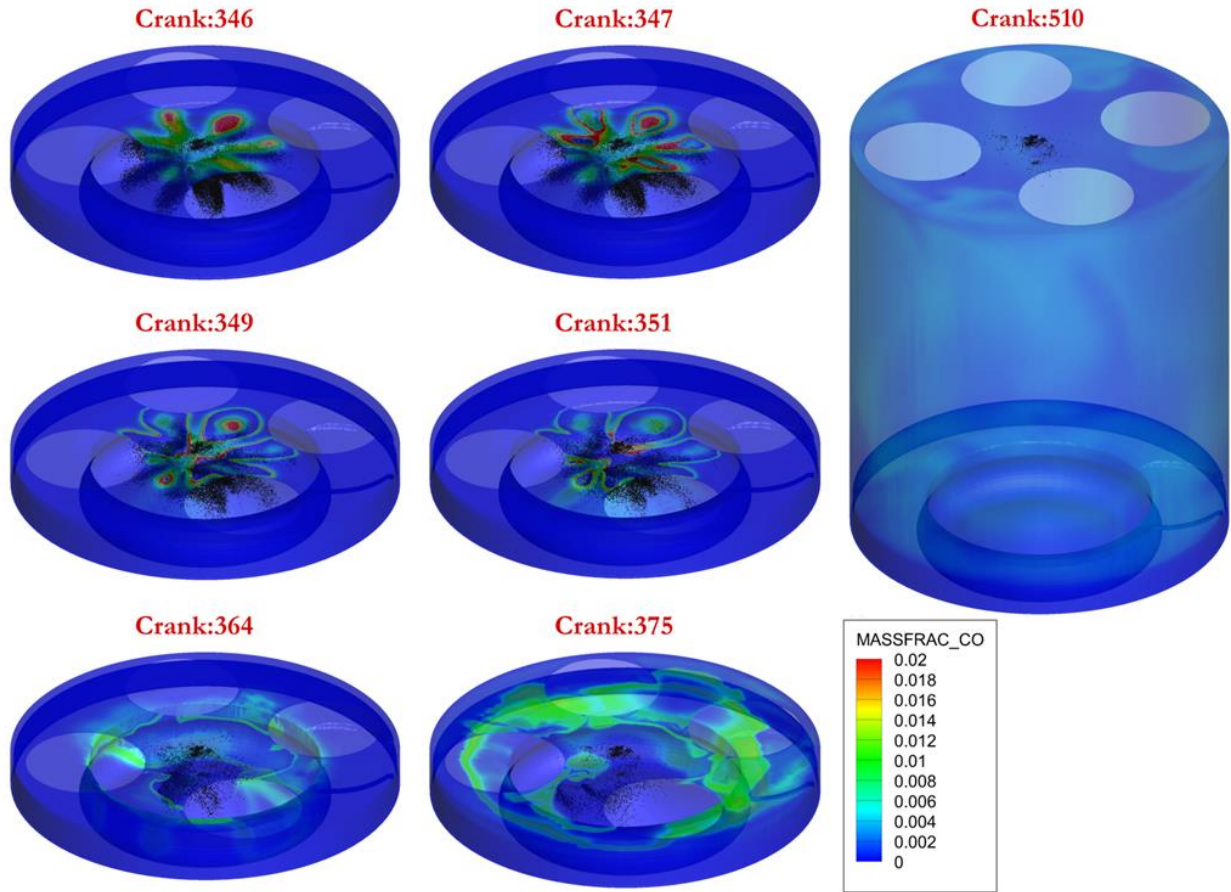


Figure 4.58 CO distribution observed (isometric view) for 1.5 bar boost pressure, 500 bar diesel injection pressure, and 80 PES of methane at 5.1 bar IMEP at diesel injection timing of 330 CAD.

4.6 Spray targeting study

4.6.1 Spray included angle sweep

Diesel fuel atomization and distribution inside the cylinder directly impact engine combustion, performance, and emissions formation. Diesel is typically injected at a high injection pressures into the cylinder in a single or multiple shot. Diesel spray included angle (Figure 4.59) affects mixture distribution, combustion phasing,

combustion duration, emissions, and heat transfer (from the piston, dome, and cylinder wall) [70]. The validated CFD model at diesel injection timing of 310 and 330 CAD, 1.5 bar manifold pressure, 500 bar diesel injection pressure at 5.1 bar IMEP is utilized to perform parametric investigation at nine half spray included angles, 27.5, 37.5, 47.5, 57.5, 67.5, 72.5, 75, 77.5, and 82.5 CAD. We will refer the half spray included angle as included angle hereafter for simplicity. The effect of included angle on emission characteristics and engine performance were compared with baseline included angle of 75 CAD and analyzed. Figure 4.60 shows pressure, AHRR, and CHR plotted over experimental cyclic data for various included angles. We can observe that as the included angle is decreased from 82.5 to 57.5 CAD ignition delay increases. On further decreasing the included angle from 57.5 to 27.5 CAD, ignition delay decreases, and minimum ignition delay is seen for the included angle of 37.5 and 27.5 CAD. AHRR shape also changes as the included angle is changed from 57.5 to 27.5 cad, AHRR shape changes from one stage heat release to two-stage heat release. Figure 4.61 compares closed cycle indicated fuel conversion efficiency (CC_IFCE) calculated for the closed cycle from IVC to EVO. The very narrow included angle of 27.5 and 37.5 have poor CC_IFCE. All other included angles have CC_IFCE greater than 40 and maximum CC_IFCE occurs at 57.5. Figures 4.62, 4.63, and 4.64 show NO, HC, and CO emissions for different included angles. For the narrow-included angle of 27.5, 37.5, and 47.5 CAD and very wide half spray included angle of 77.5 and 82.5 CAD, NO emissions are on the higher side. One major difference between a very narrow included angle and a very wide spray included angle is that combustion for a very wide included angle is better, indicated by lower HC, CO emissions compared to baseline results at 75 CAD included angle. The very narrow

included angle of 27.5 and 37.5 CAD have the highest HC and CO emissions indicating poor combustion. This clearly illustrates that the included angles have a major impact on engine combustion, performance, and emissions. Spray targeting can be utilized as a strategy to improve fuel conversion efficiency and reduce HC and CO emissions.

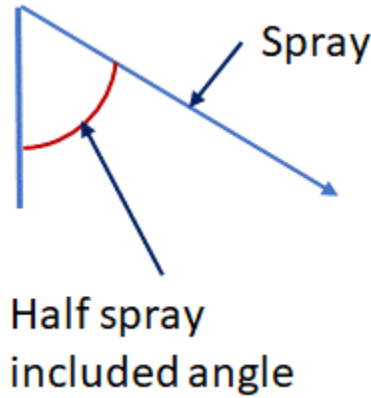
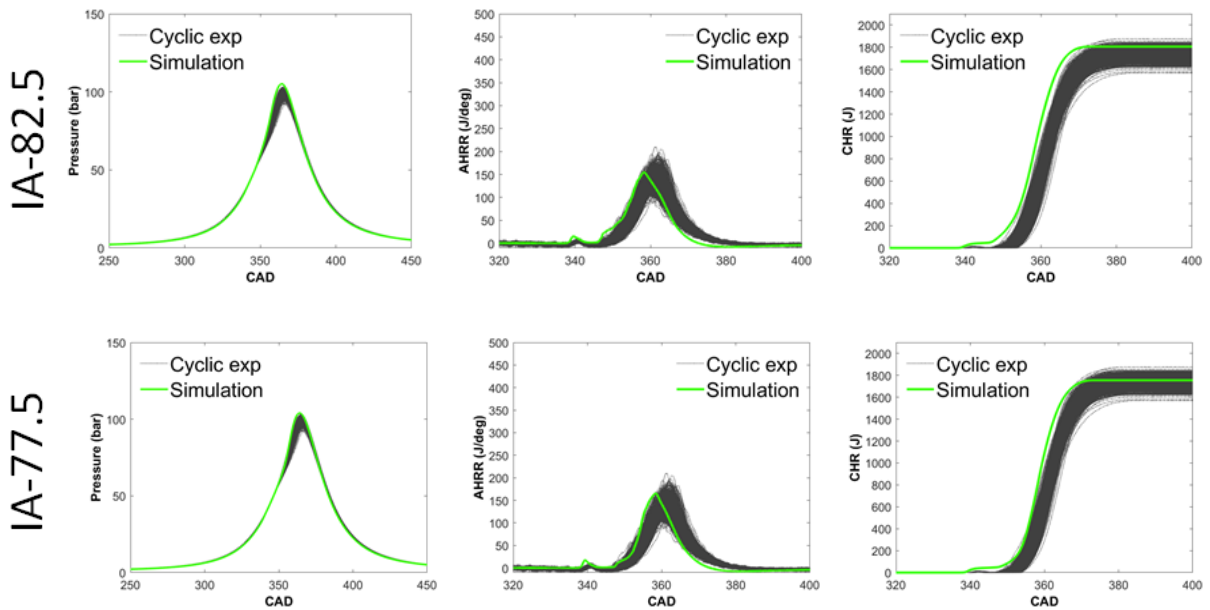
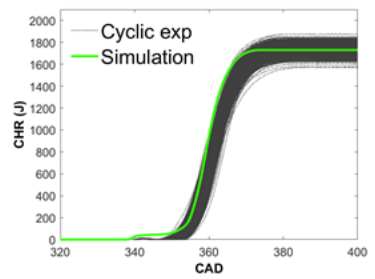
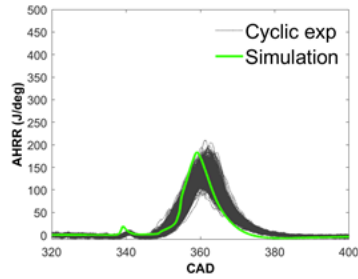
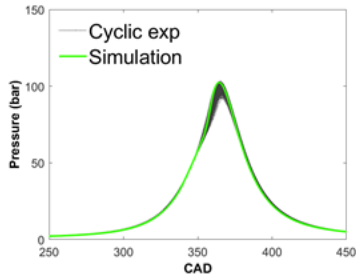


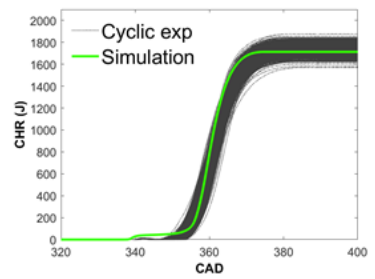
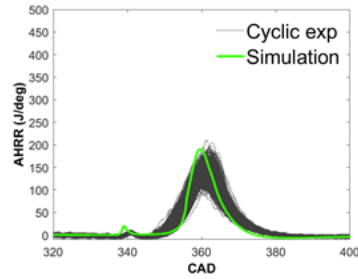
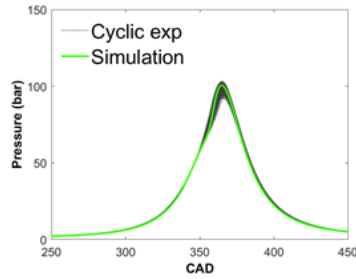
Figure 4.59 Representation of half spray included angle.



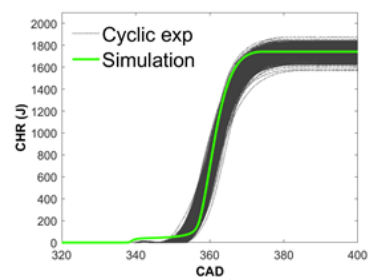
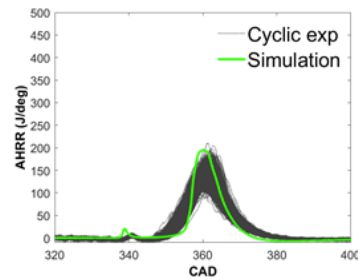
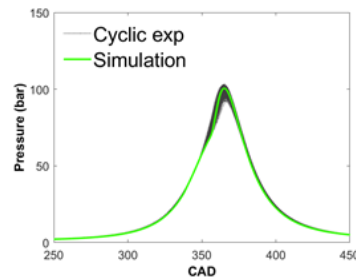
IA-75



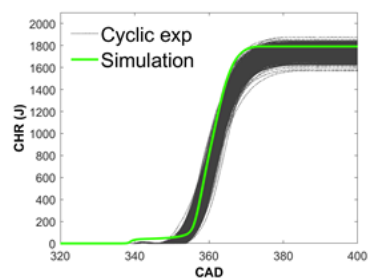
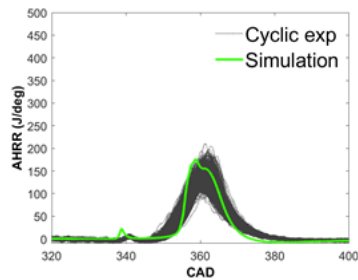
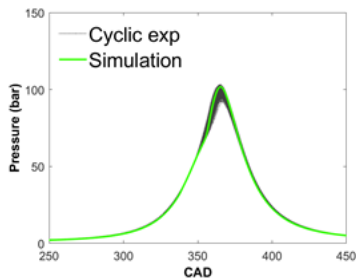
IA-72.5



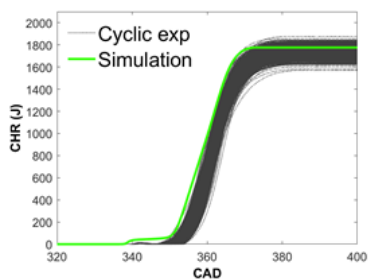
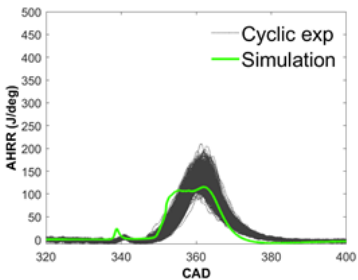
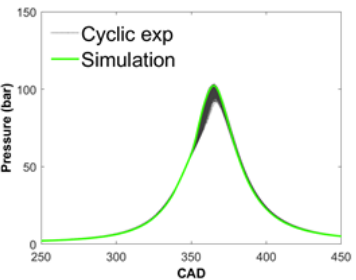
IA-67.5



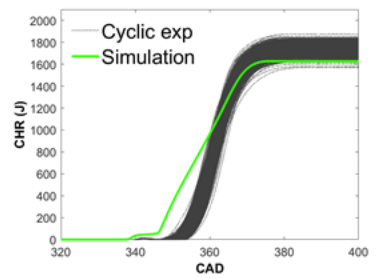
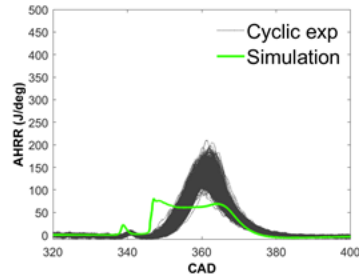
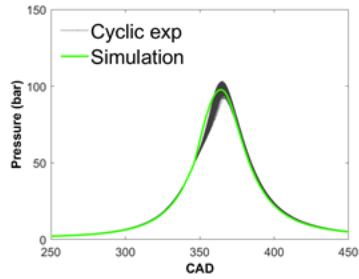
IA-57.5



IA-47.5



IA-37.5



IA-27.5

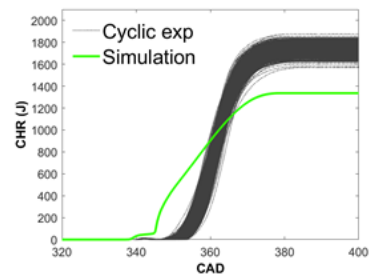
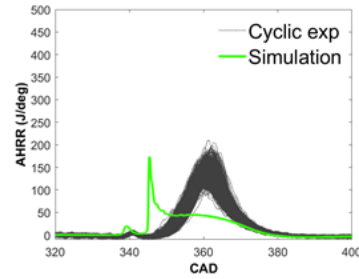
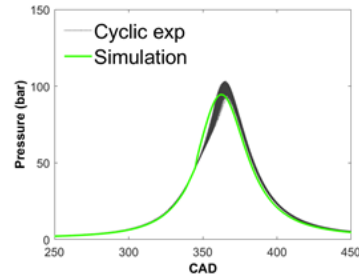


Figure 4.60 Computational pressure, AHRR and CHR histories plotted over experimental 1000 consecutive cycles for diesel injection timing of 310 CAD, 500bar injection pressure, 80 PES of methane, 1.5 bar manifold pressure, and 5.1 bar IMEP of engine load at various diesel half spray included angle

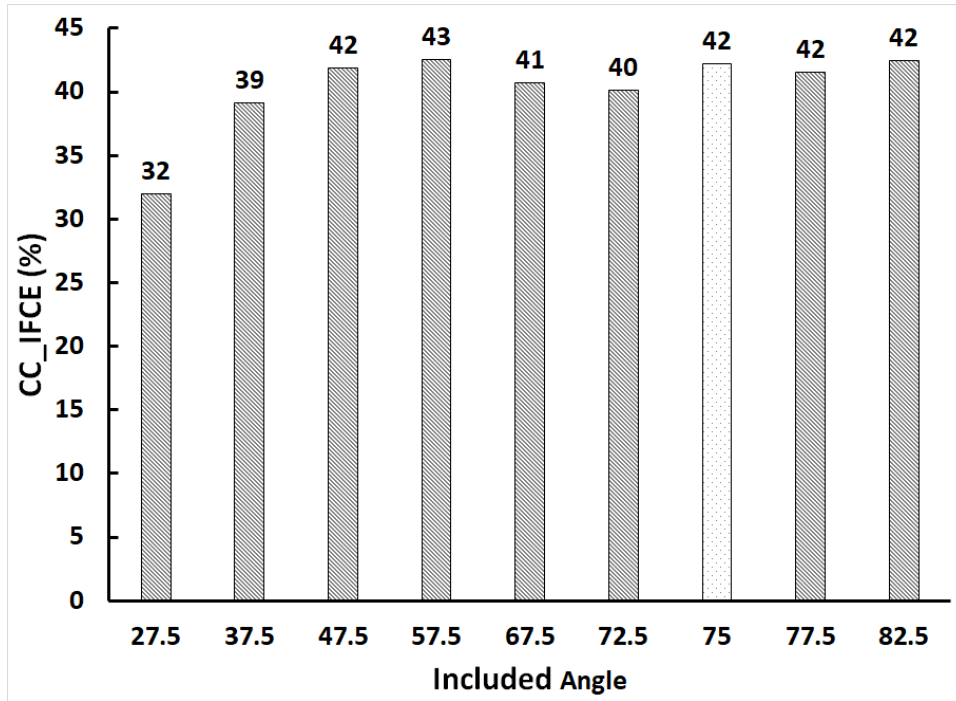


Figure 4.61 Comparison of closed cycle indicated fuel conversion efficiency (CC_IFCE) for diesel injection timing of 310 CAD, 1.5 bar manifold pressure, 500bar injection pressure, 80 PES of methane, and 5.1 bar IMEP of engine load at various half spray included angle.

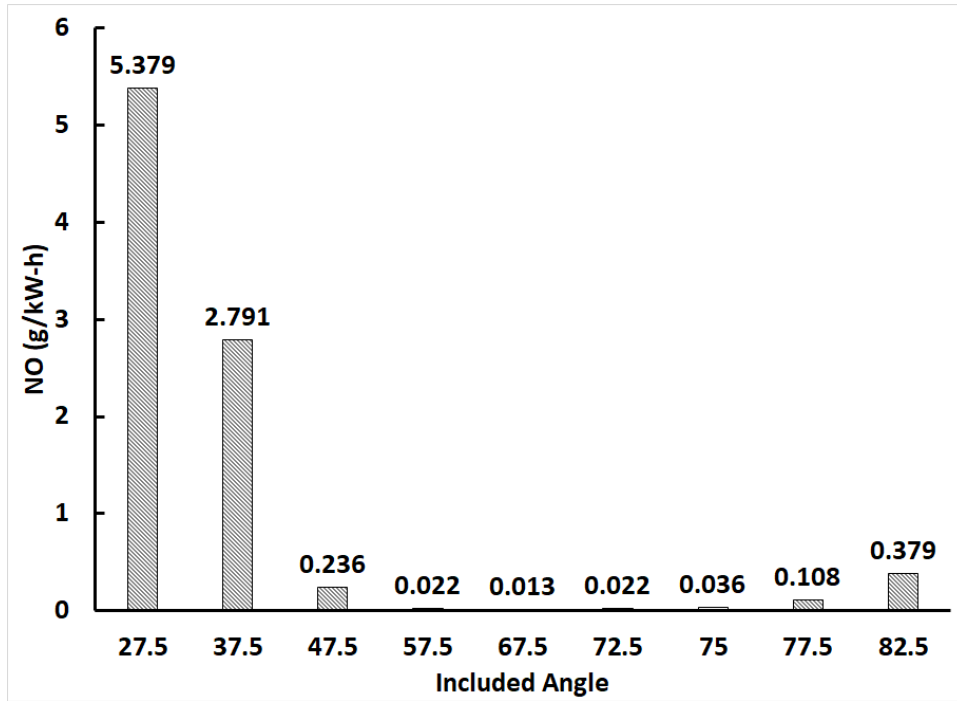


Figure 4.62 Comparison of NO emissions for diesel injection timing of 310 CAD, 1.5 bar manifold pressure, 500bar injection pressure, 80 PES of methane, and 5.1 bar IMEP of engine load at various half spray included angle.

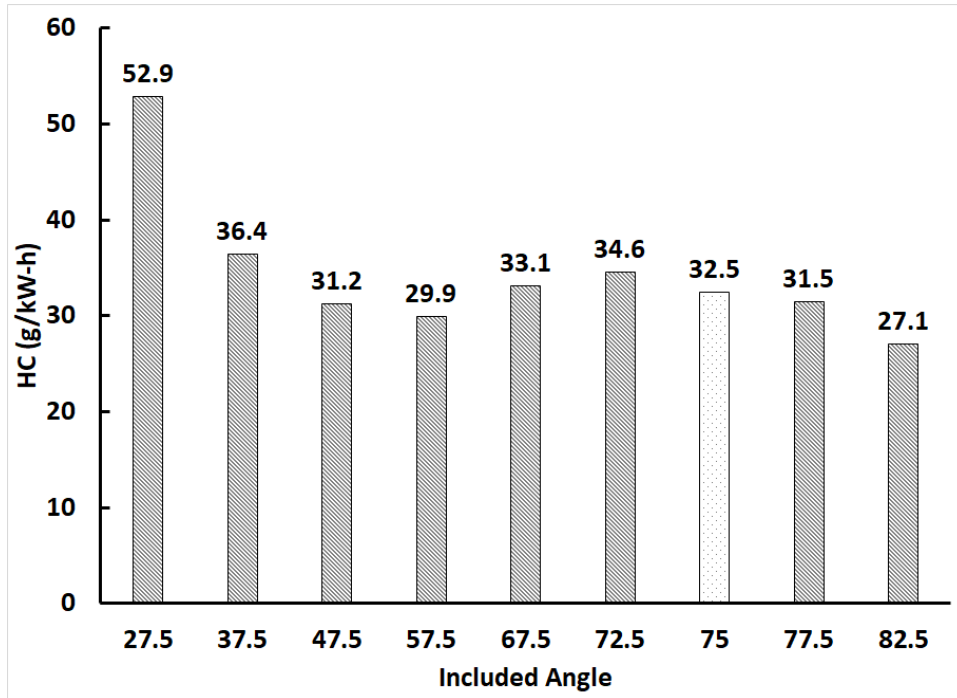


Figure 4.63 Comparison of HC emissions for diesel injection timing of 310 CAD, 1.5 bar manifold pressure, 500bar injection pressure, 80 PES of methane, and 5.1 bar IMEP of engine load at various half spray included angle.

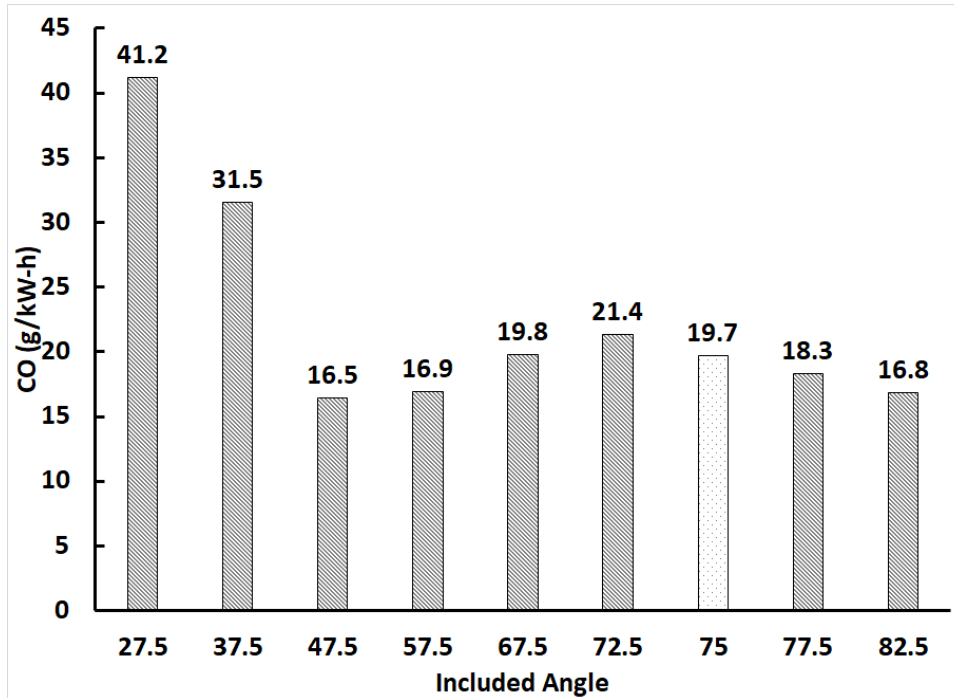


Figure 4.64 Comparison of CO emissions for diesel injection timing of 310 CAD, 1.5 bar manifold pressure, 500bar injection pressure, 80 PES of methane, and 5.1 bar IMEP of engine load at various half spray included angle.

We have selected three cases, the first one with a very narrow included angle of 27.5 CAD and the second one with best emission results at an included angle of 57.5 CAD, and the third one with a very wide included angle of 82.5 CAD to obtain further insight. These cases were further analyzed using the react ratio v/s temperature plot. The procedure of selecting a crank angle stamp for a react ratio v/s temperature and methane contour is like the one discussed in the result and discussion section 4.5.4.1.

Figure 4.65 shows react ratio v/s temperature plots for an included angle of 27.5 CAD. The first instance of high-temperature heat release is observed at 344 CAD and the react ratio starts out being rich indicating injected diesel inside the cylinder didn't get a

chance to disperse and mix. We can observe temperature stratification within one crank angle at 345 CAD temperature. Many computational cells show high heat release leading to an increase in initial AHRR (confirmed in Figure 4.60) We can observe a higher react ratio at a temperature beyond 2500K, which is likely brought upon by dissociation reactions that produces carbon, hydrogen and a small amount of free oxygen. By virtue of the definition of a react ratio even a small amount of oxygen, which appears in the denominator, would increase its magnitude. High temperature above 2000K from 345 CAD continues beyond 368 CAD. This is the culprit behind the higher NO values observed for this case. There are many computational cells within the temperature range of 1000 to 1500 K and between a react ratio of 0.25 and 1. Most computational cell with react ratio greater than 0.5 gets consumed by 354 CAD.

In Figure 4.66 for 57.5 CAD included angle, the react ratio starts out being rich and the first instance of high-temperature heat release is observed around 354 CAD. This indicates that injected diesel got a chance to disperse and mix. A slow progression of combustion can be seen compared to the 27.5 CAD included angle case and therefore, the temperature stratification is also smaller. Since combustion starts at a low react ratio maximum temperature barely crosses the 2000 K mark for the entire combustion duration. This is the reason for the lower NO observed for this case. Since diesel is well distributed inside the cylinder, we can observe that the react ratio in the range of 0.4 from 354 to 361 which is helping combustion to sustain better and provide good combustion efficiency.

Figure 4.67 shows react ratio v/s temperature plots for an included angle of 82.5 CAD. It is to be noted that the full included angle is 165 CAD, which renders the spray

almost parallel to the head. The first instance of high-temperature heat release is observed at 346 CAD and the react ratio starts out being rich indicating injected diesel inside the cylinder didn't get a chance to disperse and mix owing primarily to the inability of air entrainment into the spray, which is nearly parallel to the head. We can observe temperature stratification within one crank angle at 347 CAD temperature and react ratio increases around 2500 K. The increase in react ratio stems from the way it is defined and likely dissociation reactions at high temperatures. We don't observe many computational cells combusting at once as in 27.5 CAD case leading to a slower rate of AHRR. Temperature above 2000K is observed from 347 CAD and continued beyond 364 CAD leading to higher NO emissions for this case.

To understand the unburned HC and CO emissions trends methane contours are plotted in Figures 4.68, 4.69, and 4.70 for an included angle of 27.5, 57.5, and 82.5 CAD, respectively. From Figure 4.68, for the included angle of 27.5, we can see spray being confined inside the piston bowl and combustion being initiated inside the piston bowl. It can be also noted that initial combustion is stronger also indicated by rapid AHRR as shown in Figure 4.60. Combustion is initiated much early than the baseline case (75 CAD included angle) reducing the total time for diesel to mix inside the cylinder. The spray is being targeted inside the piston bowl thus confining diesel distribution inside the piston bowl. Due to all reasons discussed above, it is difficult for combustion to spread all over the combustion chamber leading to poor combustion efficiencies and high HC and CO emissions. For an included angle of 57.5 CAD, we can observe spray is well distributed inside the cylinder, which is also confirmed from the react ratio v/s temperature plot in Figure 4.66. Due to better distribution of diesel, which is a highly reactive fuel the

combustion of methane, which is a low reactive fuel is enhanced thus decreasing total combustion duration yielding better performance and lower emissions. Since combustion occurs at leaner ϕ and lower temperatures NO emissions are correspondingly lower. This case illustrates that it may be possible to obtain low HC, CO, and NO emissions simultaneously. Figure 4.70 shows the HC contour for an included angle of 82.5 CAD, we can observe diesel is distributed over the squish region, and combustion is initiated from the squish region. As mentioned before, it appears that there may be spray interaction with cylinder head leading to lower diesel mixing with air. It is clear from a react ratio v/s temperature plot in Figure 4.67 that combustion is initiated at a react ratio of one, which likely provided a stronger ignition source indicated by higher temperatures. This helps combustion to spread in squish region and also into cervices, which indicates the possibility of using spray targeting to consume methane charge that remains untouched in the baseline case discussed in result and discussion section 4.5.4.1.

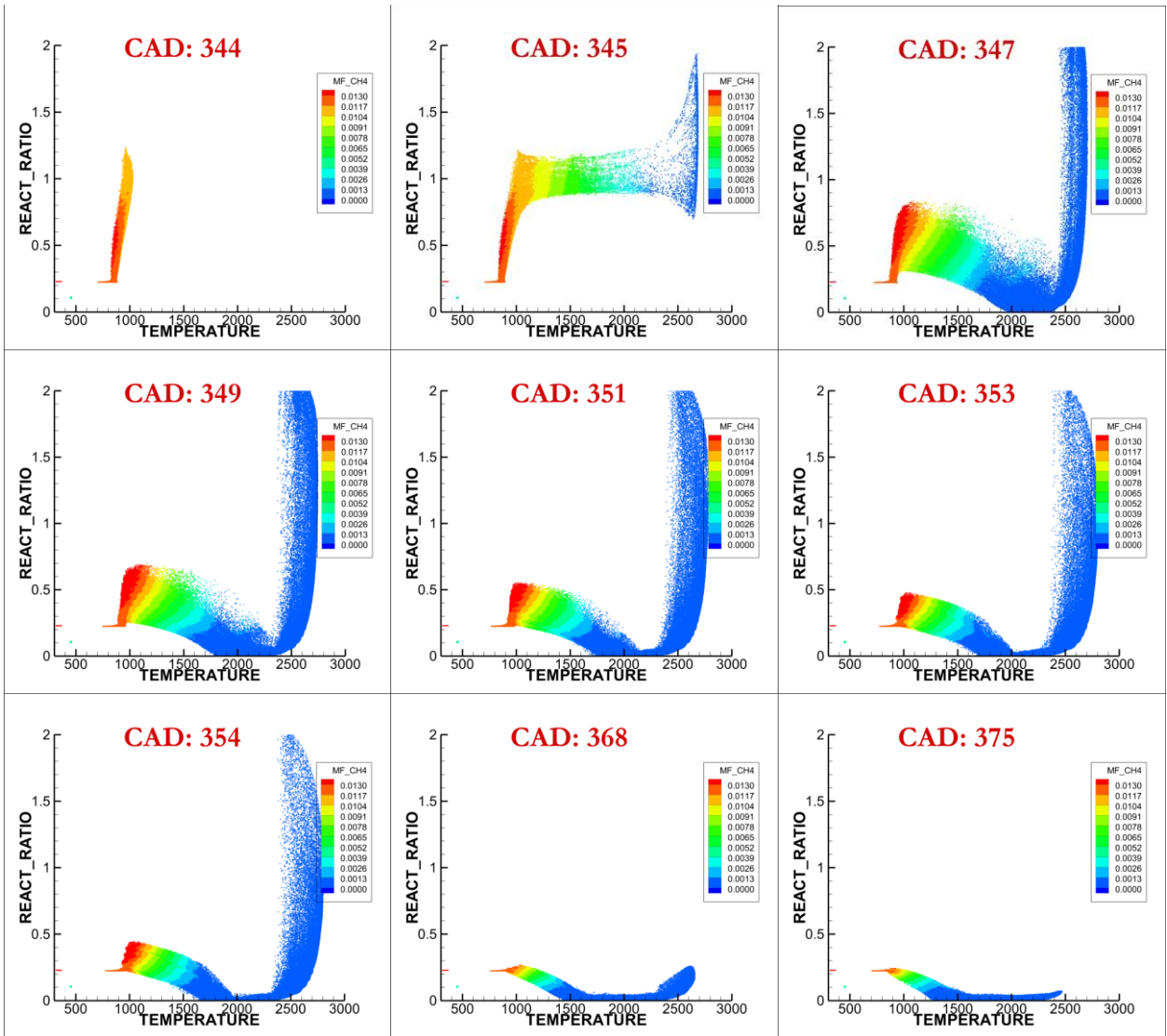


Figure 4.65 React ratio v/s temperature colored with methane mass fraction for each computational cell for diesel injection timing of 1.5 bar boost pressure, 500 bar diesel injection pressure 80 PES of methane, and 5.1 bar IMEP of engine load at half spray included angle of 27.5.

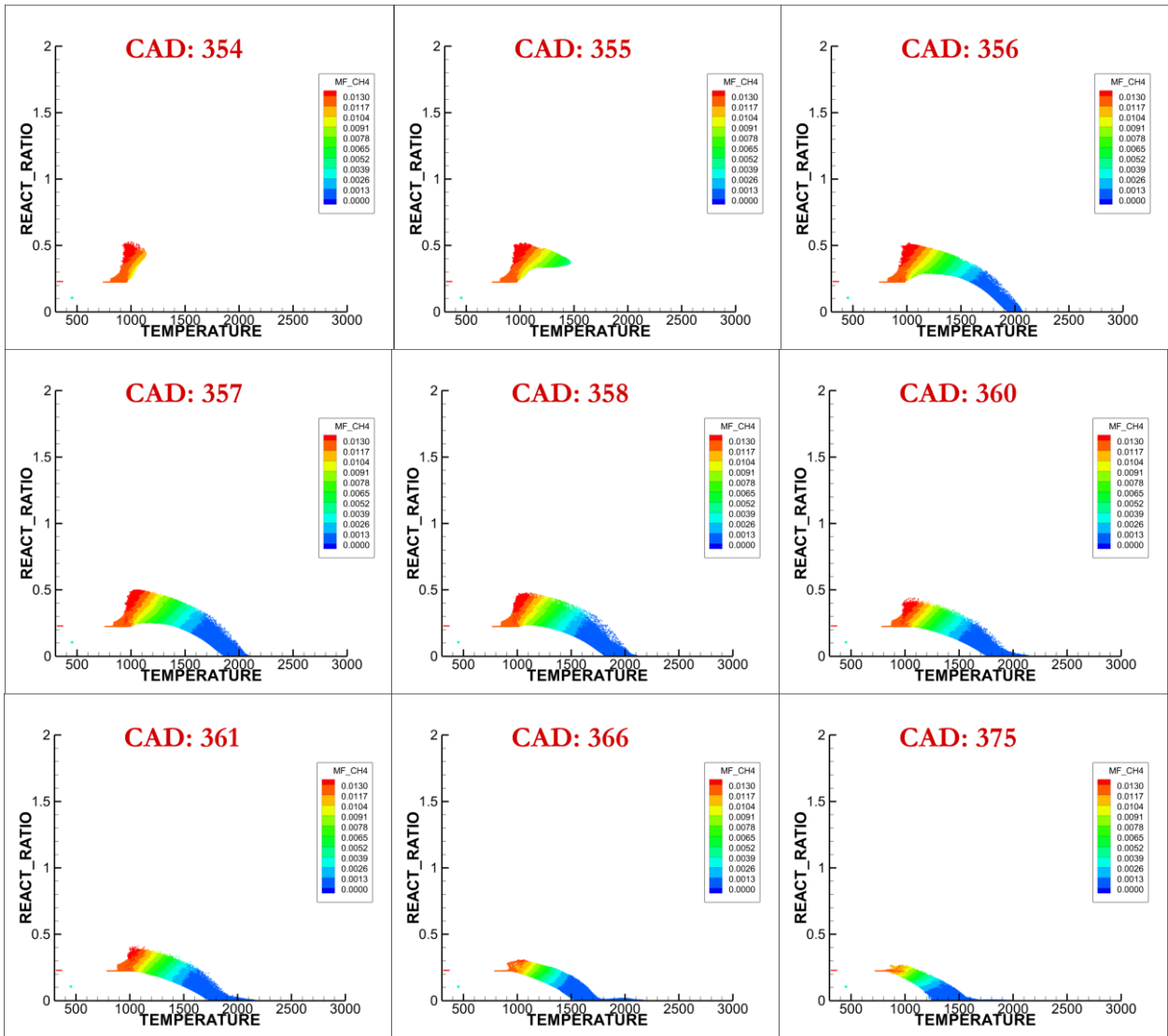


Figure 4.66 React ratio v/s temperature colored with methane mass fraction for each computational cell for diesel injection timing of 1.5 bar boost pressure, 500 bar diesel injection pressure 80 PES of methane, and 5.1 bar IMEP of engine load at half spray included angle of 57.5

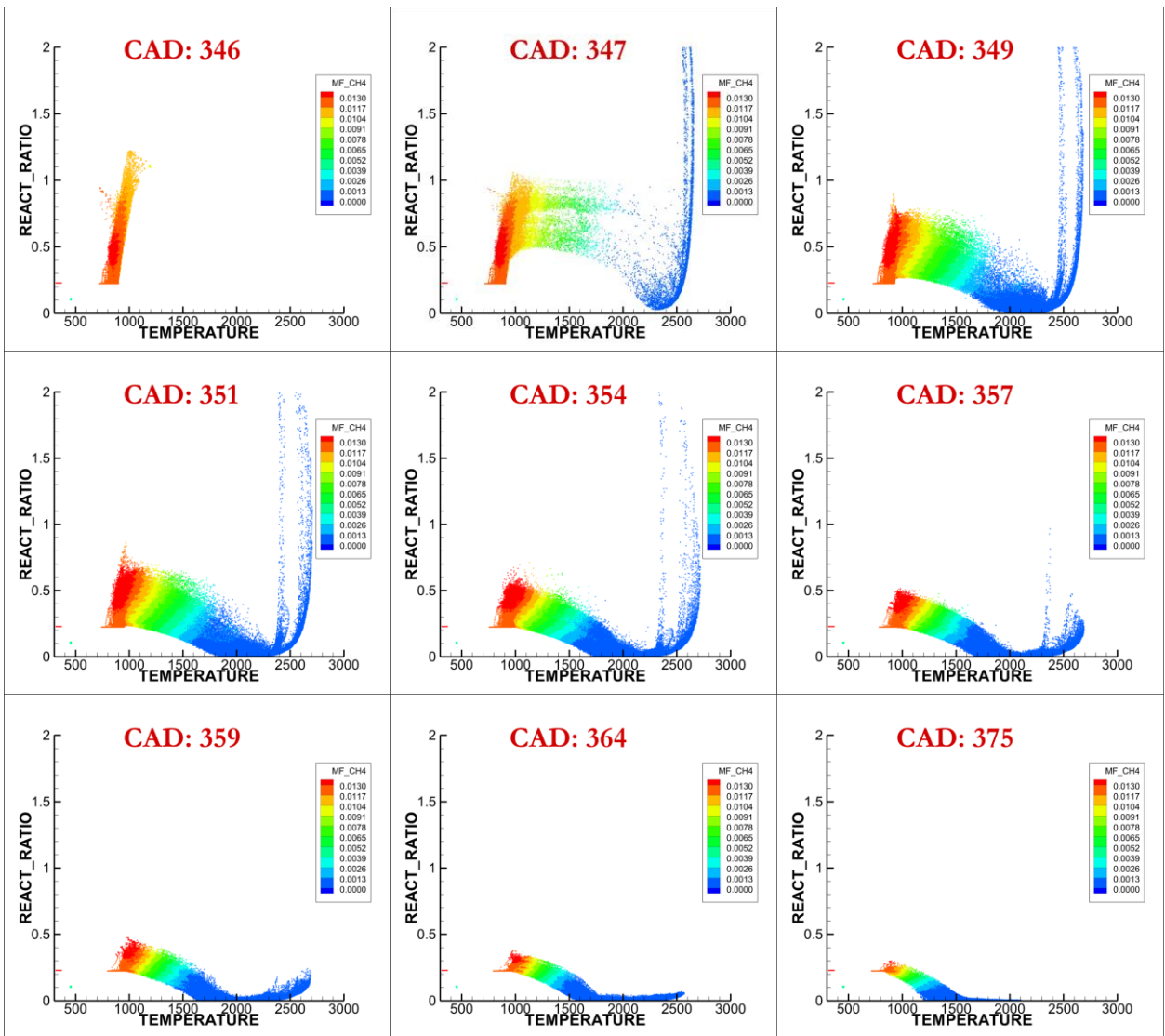


Figure 4.67 React ratio v/s temperature colored with methane mass fraction for each computational cell for diesel injection timing of 1.5 bar boost pressure, 500 bar diesel injection pressure 80 PES of methane, and 5.1 bar IMEP of engine load at half spray included angle of 82.5.

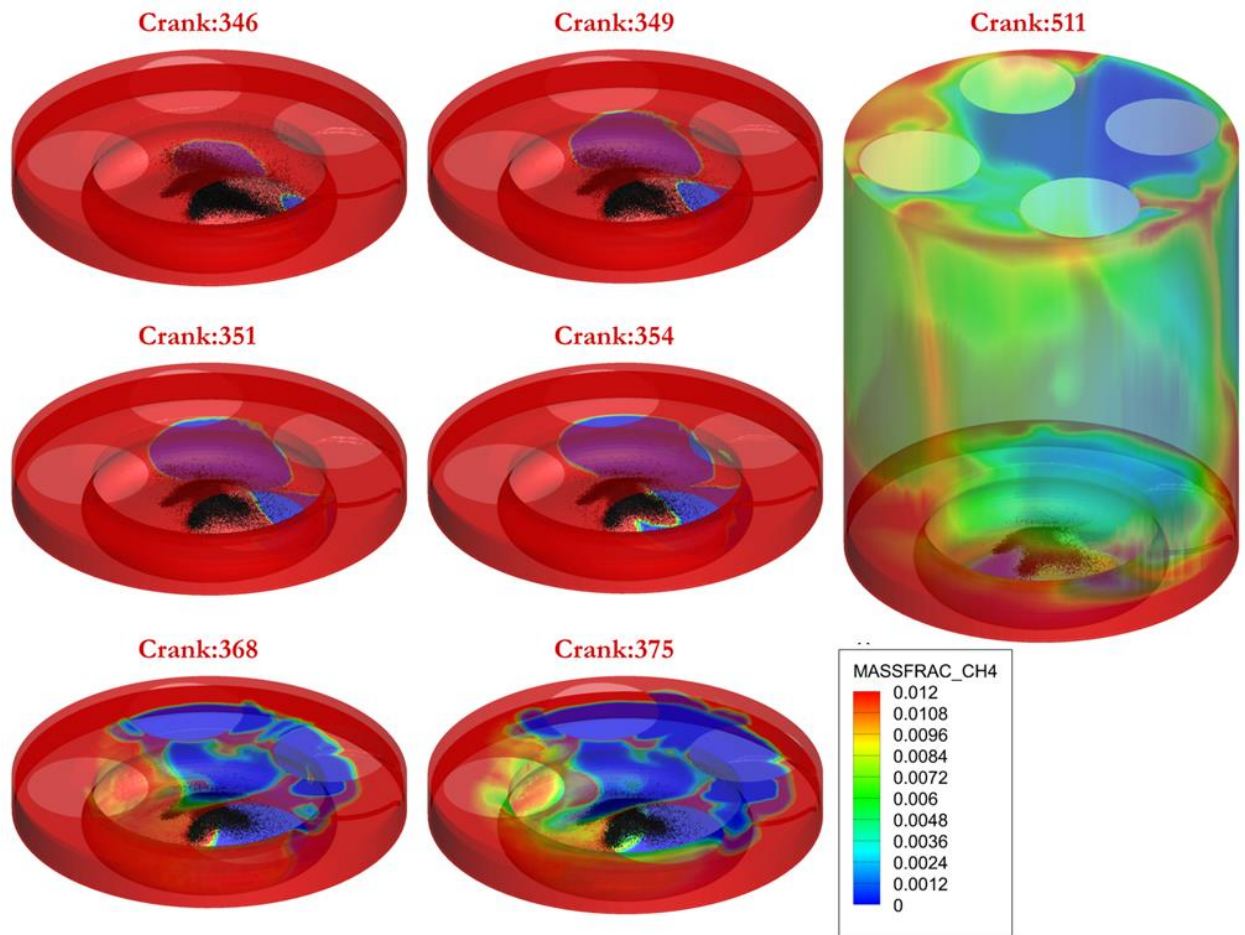


Figure 4.68 Methane distribution observed (isometric view) for diesel injection timing of 310 CAD, 1.5 bar boost pressure, 500 bar diesel injection pressure, and 80 PES of methane at 5.1 bar IMEP at half spray included angle of 27.5.

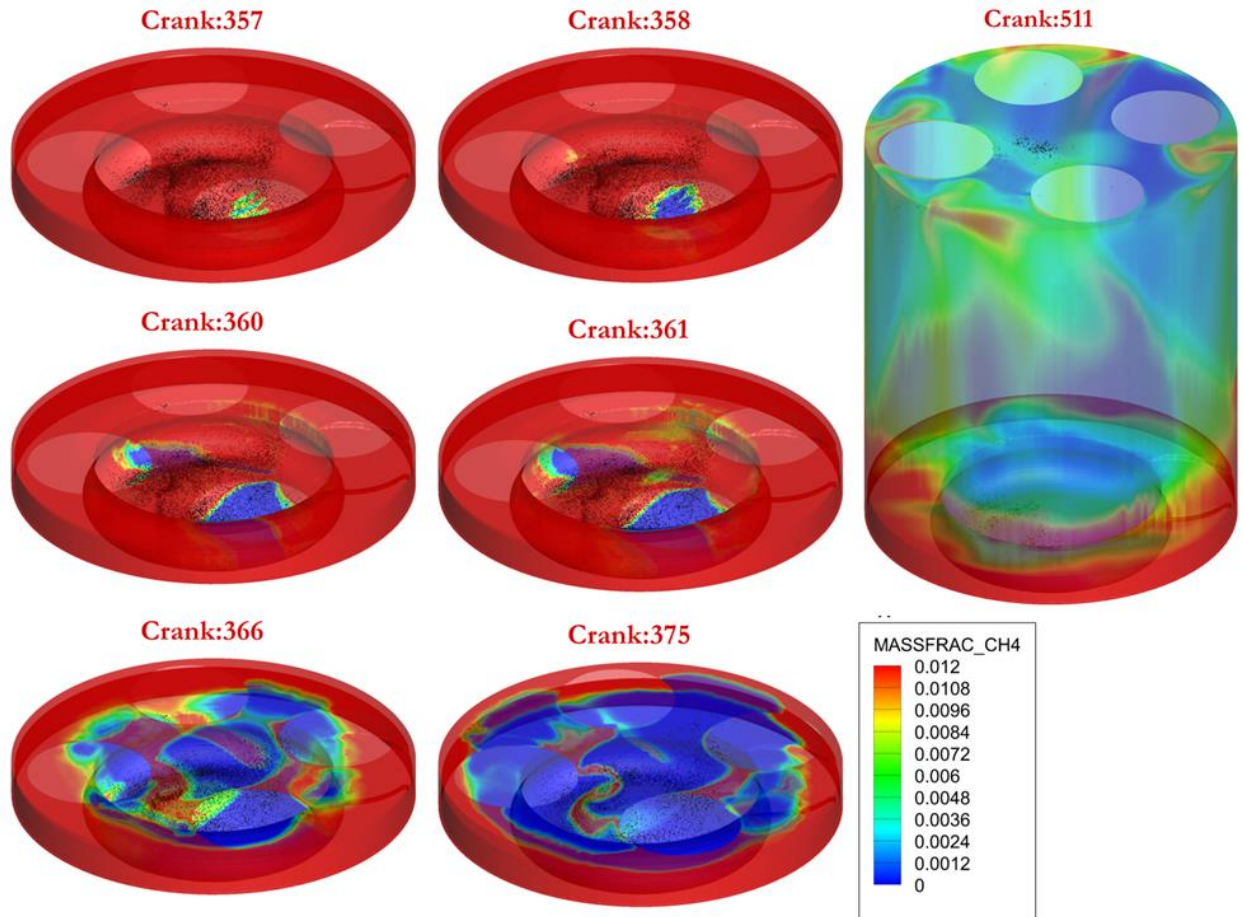


Figure 4.69 Methane distribution observed (isometric view) for diesel injection timing of 310 CAD, 1.5 bar boost pressure, 500 bar diesel injection pressure, and 80 PES of methane at 5.1 bar IMEP at half spray included angle of 57.5.

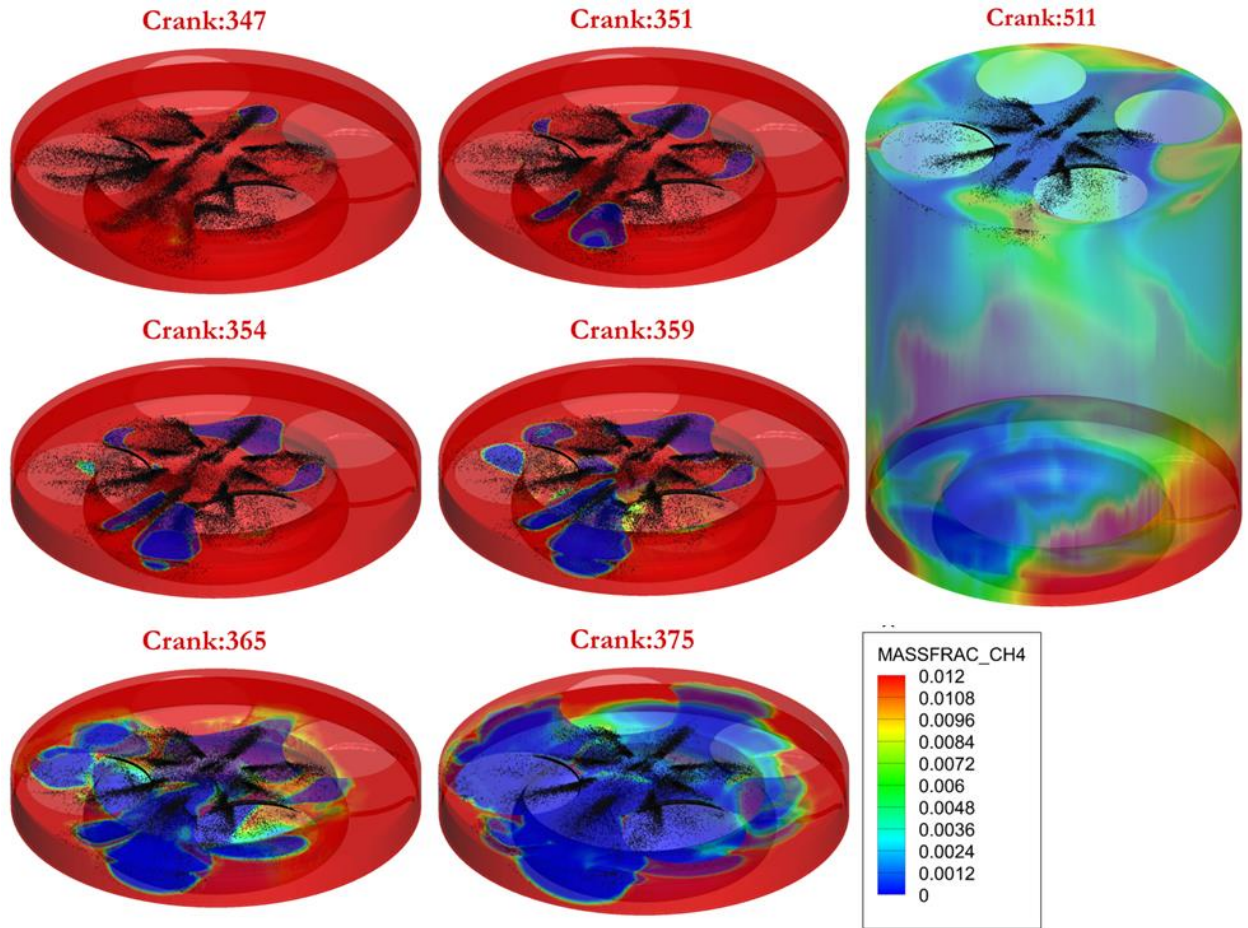


Figure 4.70 Methane distribution observed (isometric view) for diesel injection timing of 310 CAD, 1.5 bar boost pressure, 500 bar diesel injection pressure, and 80 PES of methane at 5.1 bar IMEP at half spray included angle of 82.5.

4.6.2 Spray targeting study with different number of nozzles

To further analyze spray targeting effects, the number of nozzles was changed from the stock 8 holes to 6 and 12 holes without altering the nozzle diameter and injected fuel mass. Injection duration was increased along with the discharge coefficient for 6 nozzles and injection duration and discharge coefficient was decreased for 12 nozzles. The injection pressure was kept the same in all cases as the baseline case. The analysis was performed at two different included angles of 57.5 and 75 CAD. These included angles were selected as they provided the best emissions and performance results. Figure

4.71 shows pressure, AHRR, and CHR plotted over experimental cyclic data for 12 and 6 nozzles at an included angle of 57.5 and 75 CAD.

We can observe that as the number of nozzles is increased to 12 for both included angles of 57.5 and 75 CAD, AHRR has a steep slope initially and then has slower descent, indicating faster initial combustion followed by slower combustion. While for 6 nozzle cases peak AHRR is higher than that with 12 nozzle and overall combustion is faster. Total CHR is on the higher side with 6 nozzles compared to 12 nozzles for both included angles. Figure 4.72 compares CC_IFCE for 6 nozzle and 12 nozzles at a different included angle of 57.5 and 75 CAD. Baseline case at half spray included angle of 75 CAD with 8 nozzles is also shown in Figure 4.72 for references and comparison. Cases with 6 nozzles at both 57.5 and 75 CAD included angle has better CC_IFCE than baseline; similarly, cases with 12 nozzles at both included angle has lower CC_IFCE. Figures 4.73, 4.74, and 4.75 show NO, HC, and CO emissions for 6 nozzle and 12 nozzles at an included angle of 57.5 and 75 CAD along with baseline value at half included angle of 75 with 8 nozzles. The NO emissions are observed to increase when the number of nozzles is increased to 12 and decreased to 6. It is counter-intuitive to have a higher NO value with an increased number of nozzles. Both HC and CO emissions decrease with a decreasing number of nozzles to 6 from 8 and increase with an increasing number of nozzles to 12 from 8. This suggests that the number of nozzles has changed the fuel distribution inside the cylinder thus impacting engine performance and emissions. The HC and CO emissions from baseline with 6 nozzles further motivated that spray targeting can be used to decrease HC and CO emissions in dual fuel combustion at low loads. With 6 nozzles even though HC and CO decrease NO emissions increases.

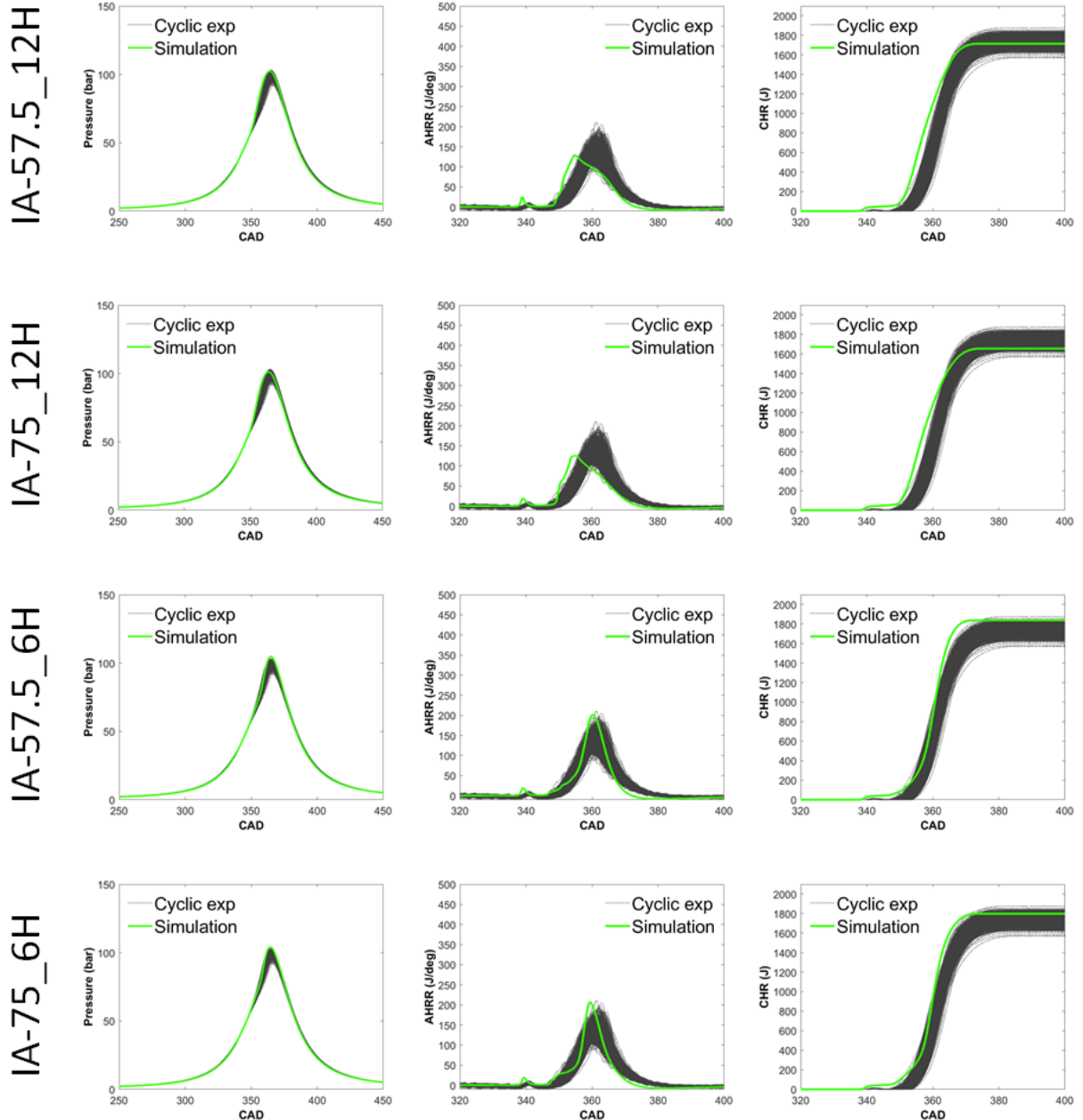


Figure 4.71 Computational pressure, AHRR and CHR histories plotted over experimental 1000 consecutive cycles for diesel injection timing of 310 CAD, 500bar injection pressure, 80 PES of methane, 1.5 bar manifold pressure, and 5.1 bar IMEP of engine load at half spray included angle of 57.5 with 12 nozzles, 75 with 12 nozzles, 57.5 with 6 nozzles, 75 with 6 nozzles and 75 with 8 nozzles.

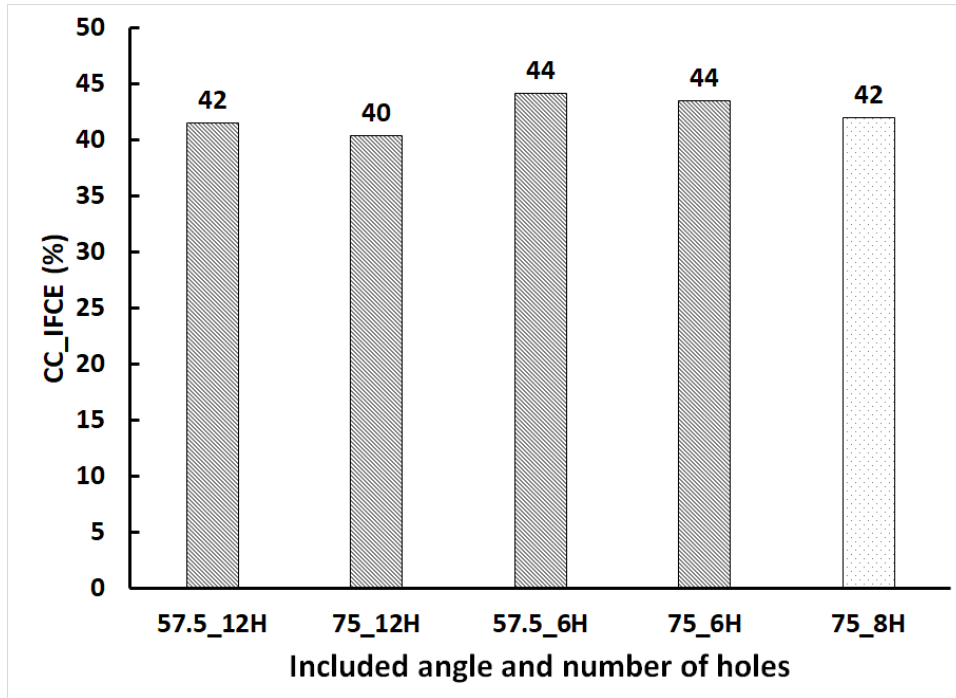


Figure 4.72 Comparison of closed-cycle indicated fuel conversion efficiency (CC_IFCE) for diesel injection timing of 310 CAD, 1.5 bar manifold pressure, 500bar injection pressure, 80 PES of methane, and 5.1 bar IMEP of engine load at half spray included angle of 57.5 with 12 nozzles, 75 with 12 nozzles, 57.5 with 6 nozzles, 75 with 6 nozzles and 75 with 8 nozzles.

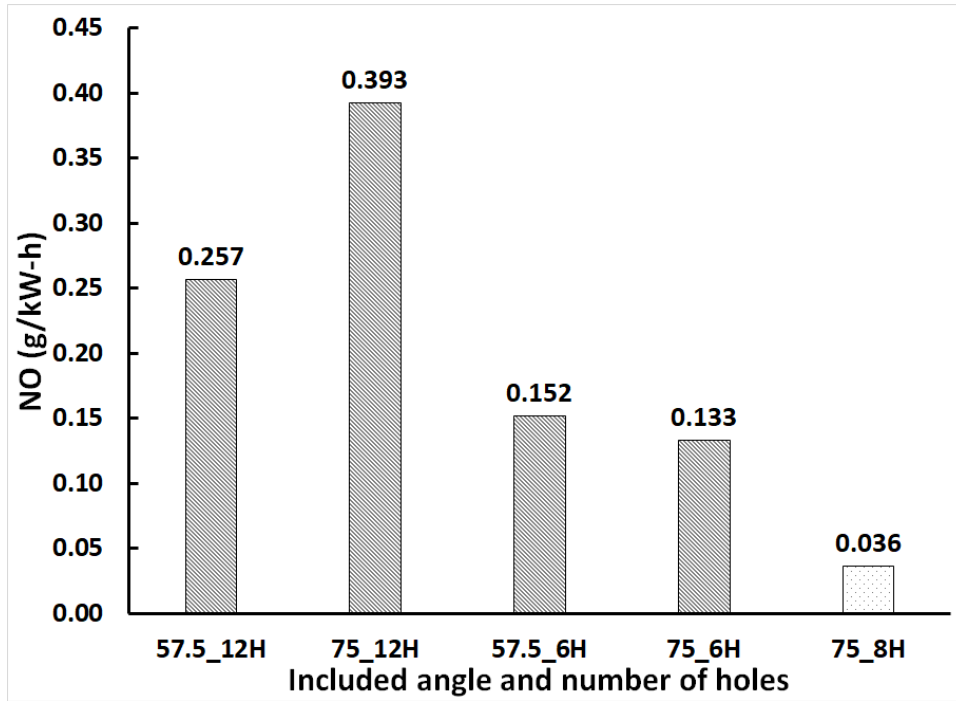


Figure 4.73 Comparison of NO emissions for diesel injection timing of 310 CAD, 1.5 bar manifold pressure, 500bar injection pressure, 80 PES of methane, and 5.1 bar IMEP of engine load at half spray included angle of 57.5 with 12 nozzles, 75 with 12 nozzles, 57.5 with 6 nozzles, 75 with 6 nozzles and 75 with 8 nozzles.

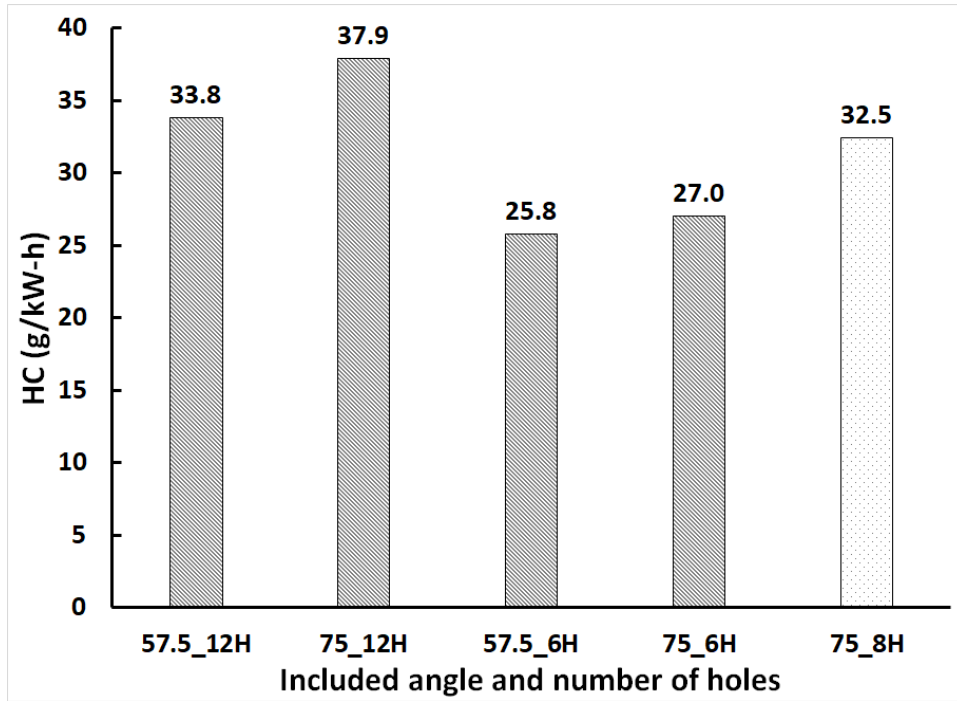


Figure 4.74 Comparison of HC emissions for diesel injection timing of 310 CAD, 1.5 bar manifold pressure, 500bar injection pressure, 80 PES of methane, and 5.1 bar IMEP of engine load at half spray included angle of 57.5 with 12 nozzle, 75 with 12 nozzle, 57.5 with 6 nozzle, 75 with 6 nozzle and 75 with 8 nozzles.

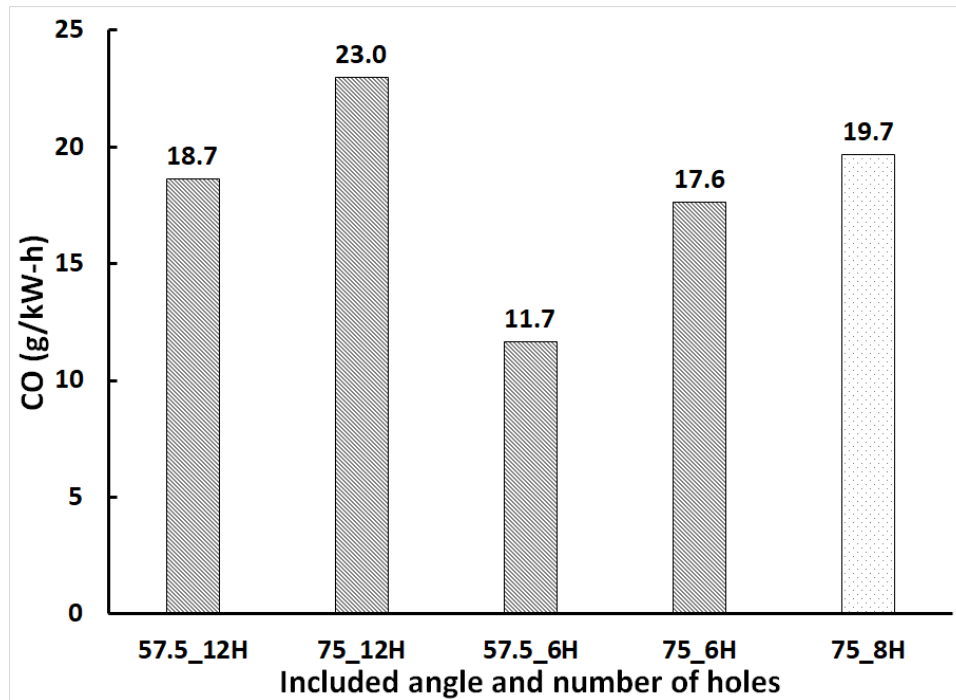


Figure 4.75 Comparison of CO emissions for diesel injection timing of 310 CAD, 1.5 bar manifold pressure, 500bar injection pressure, 80 PES of methane, and 5.1 bar IMEP of engine load at half spray included angle of 57.5 with 12 nozzles, 75 with 12 nozzles, 57.5 with 6 nozzles, 75 with 6 nozzles and 75 with 8 nozzles.

To further analyze the effect of the number of nozzles, best case and worst case are selected. An included angle of 57.5 with 6 nozzles is selected as the best-case while an included angle of 75 with 12 nozzles is selected as the worst case to further explore what is occurring inside the cylinder. They are further analyzed by plotting a react ratio v/s temperature and methane contour plots. The procedure of selecting crank angle stamp is for react ratio v/s temperature and methane contour are like the one discussed in the result and discussion section 4.5.4.1

Figure 4.76 shows the react ratio v/s temperature plot for an included angle of 57.5 with 6 nozzles. The first instance of high-temperature heat release is observed

around 346 CAD. The combustion starts at a react ratio slightly lower than one. This is expected as with 6 nozzles more amount of fuel is injected from each nozzle for a longer duration causing few computational cells with a higher react ratio at a time when combustion starts compared to the baseline case with 8 nozzles. It is evident from 347 CAD that there are few cells with react ratio closer to one and most of them combust by 349 CAD. This suggests most diesel gets a chance to disperse and mix inside the cylinder. This leads to a stronger ignition source followed by combustion, which spreads inside the cylinder where diesel is well mixed. We can observe some computational cells at a temperature higher than 2000 K leading to higher NO than the baseline case.

Figure 4.77 shows react ratio v/s temperature plots for an included angle of 75 CAD with 12 nozzles. The first instance of high-temperature heat release is observed at 349 CAD and the maximum react ratio starts out being around 0.75. This indicates diesel disperse and mix inside the cylinder. This is expected as the total number of nozzle increases leading to a lower amount of diesel being injected from each nozzle. One can expect even better diesel being dispersed and mix for this case. The combustion is initiated at a react ratio close to 0.75, which does not explain the high NO observed for this case compared to the baseline case with 8 nozzles at 75 CAD included angles.

Upon closer look we can observe case with 12 nozzle has higher temperature than baseline case with 8 nozzles at 75 CAD. For example, when we compare react ratio v/s temperature plot for baseline case in Figure 4.42 at 365 CAD in result and discussion section with 366 CAD for 12 nozzle case, we can observe that there are lots of cell which is above 2000K and approaching 2500K for 12 nozzles case but for baseline case it is confined to 2000K.

In Figure 4.78 methane contours is presented for an included angle of 57.5 CAD with 6 nozzles and in Figure 4.79 methane contours of an included angle of 75 CAD with 12 nozzles is presented. We can observe that combustion in Figure 4.78 for an included angle of 57.5 CAD with 6 nozzles is initiated from piston lip region and stronger in strength indicated by a react ratio v/s temperature plot in Figure 4.76, which helps combustion to move in both directions towards piston squish and bowl region. This is a reason for better combustion and lower emissions. Figure 4.79 for an included angle of 75 CAD with 12 nozzles shows that combustion is initiated from the piston bowl region and most combustion is confined there and slowly moves outward thus having incomplete combustion leading to high emissions results compared to 6- and 8-hole case.

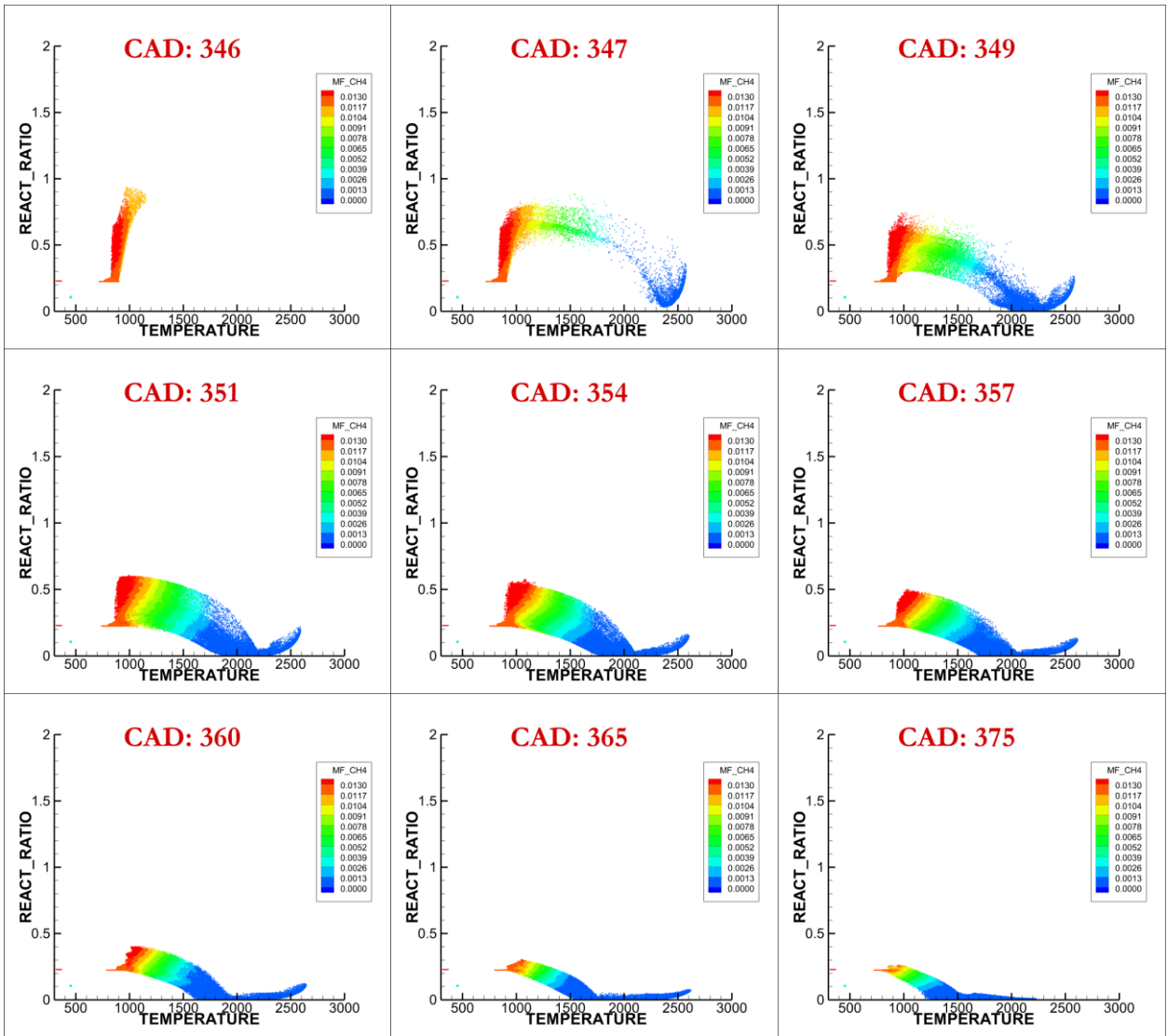


Figure 4.76 React ratio v/s temperature colored with methane mass fraction for each computational cell for diesel injection timing of 1.5 bar boost pressure, 500 bar diesel injection pressure 80 PES of methane, and 5.1 bar IMEP of engine load at half spray included angle of 57.5 with 6 nozzles.

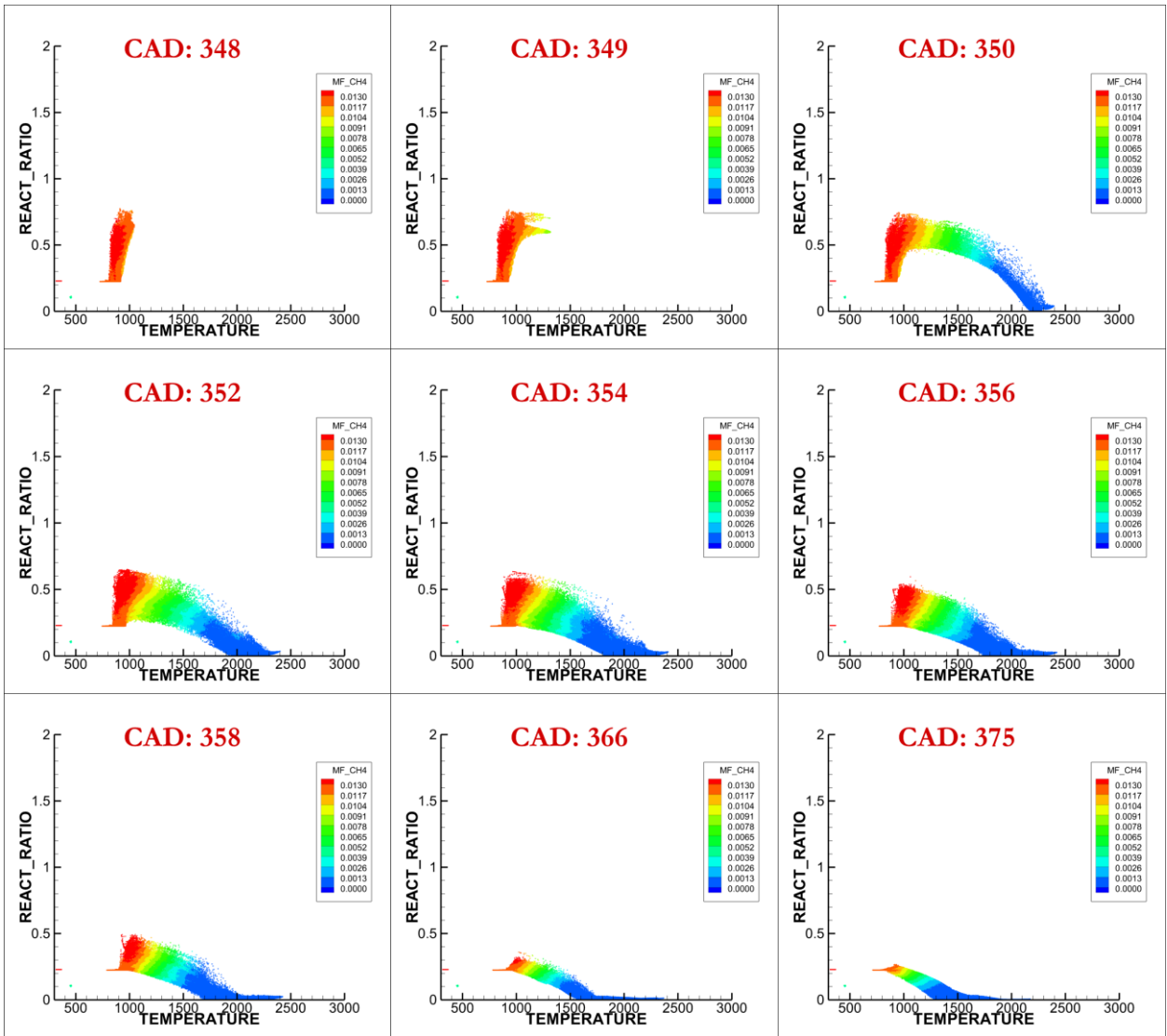


Figure 4.77 React ratio v/s temperature colored with methane mass fraction for each computational cell for diesel injection timing of 1.5 bar boost pressure, 500 bar diesel injection pressure 80 PES of methane, and 5.1 bar IMEP of engine load at half spray included angle of 75 with 12 nozzles

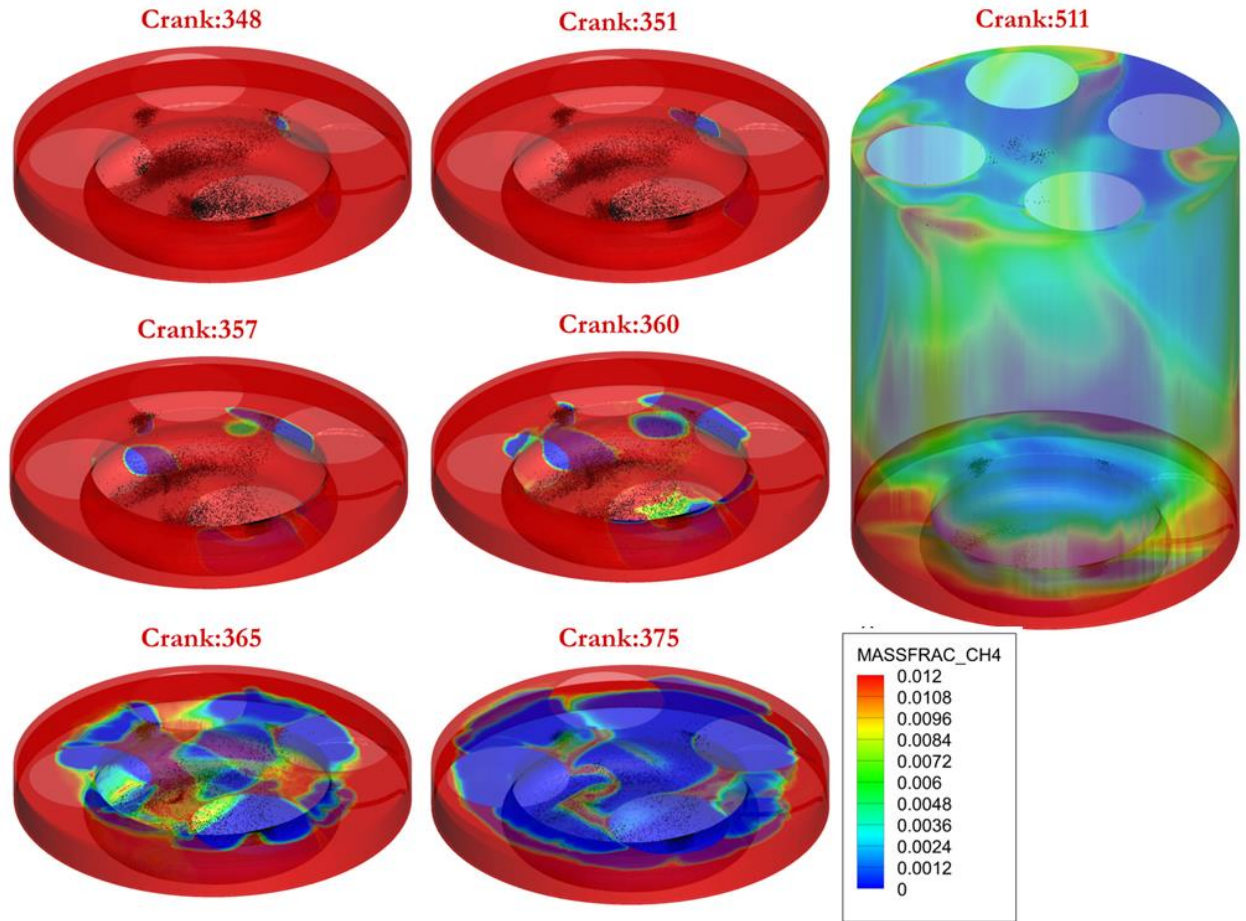


Figure 4.78 Methane distribution observed (isometric view) for diesel injection timing of 310 CAD, 1.5 bar boost pressure, 500 bar diesel injection pressure, and 80 PES of methane at 5.1 bar IMEP at half spray included angle of 57.5 with 6 nozzles.

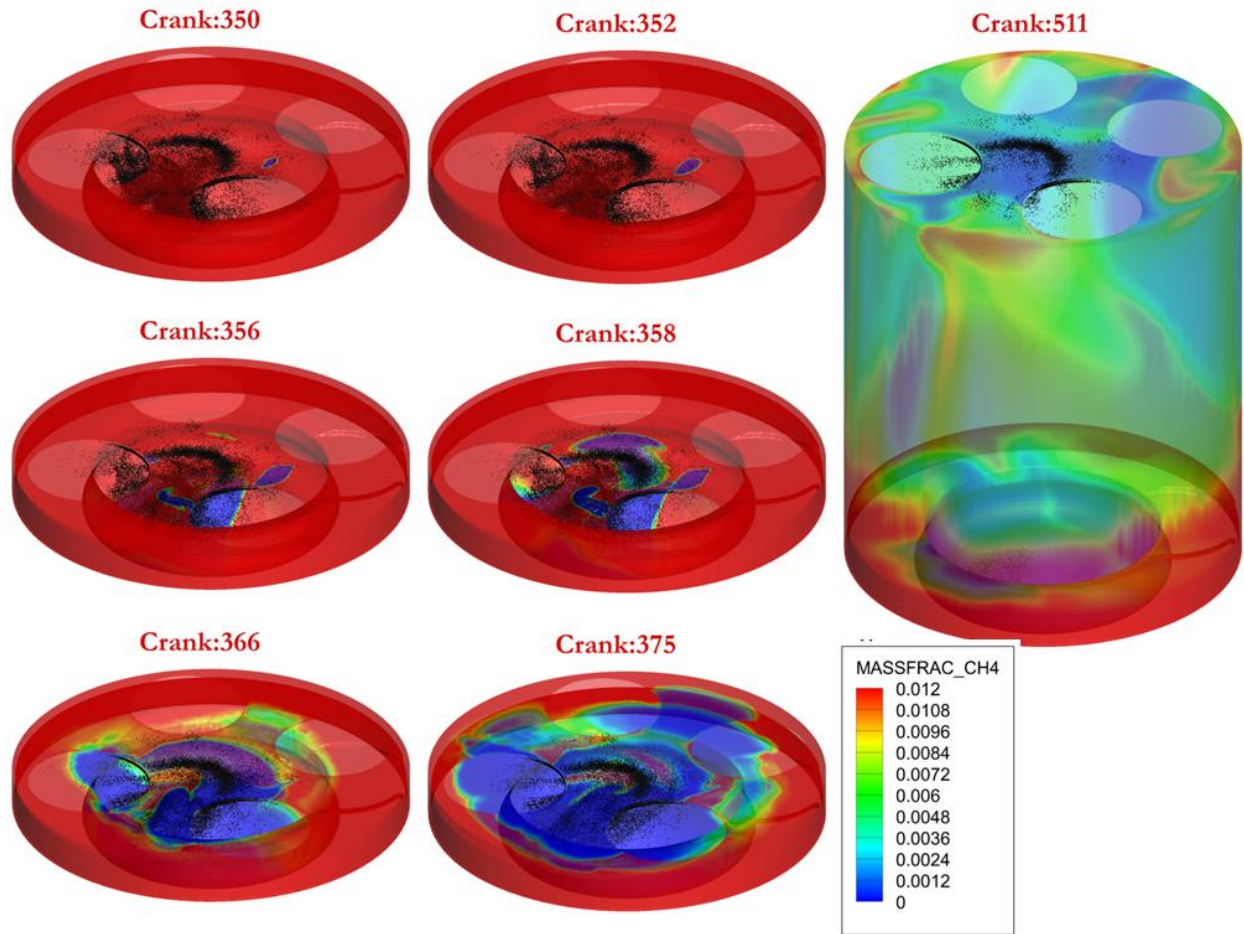


Figure 4.79 Methane distribution observed (isometric view) for diesel injection timing of 310 CAD, 1.5 bar boost pressure, 500 bar diesel injection pressure, and 80 PES of methane at 5.1 bar IMEP at half spray included angle of 75 with 12 nozzles.

4.6.3 Spray targeting study with two sets of half spray include angle in the same injector at 310 SOI

Another spray targeting study was performed in which half the number of nozzles was kept at the baseline included angle of 75 CAD and another half was kept at a different included angle, 57.5 CAD. This study was performed at diesel injection timing of 310 CAD, 1.5 bar manifold pressure, 500 diesel injection pressure, and 5.1 bar IMEP.

Arrangement of half spray included angle is shown in Figure 4.80 with 8 nozzles and two different half included angle of 75 and 57.5 CAD. This study was performed with 6, 8, and 12 nozzles.

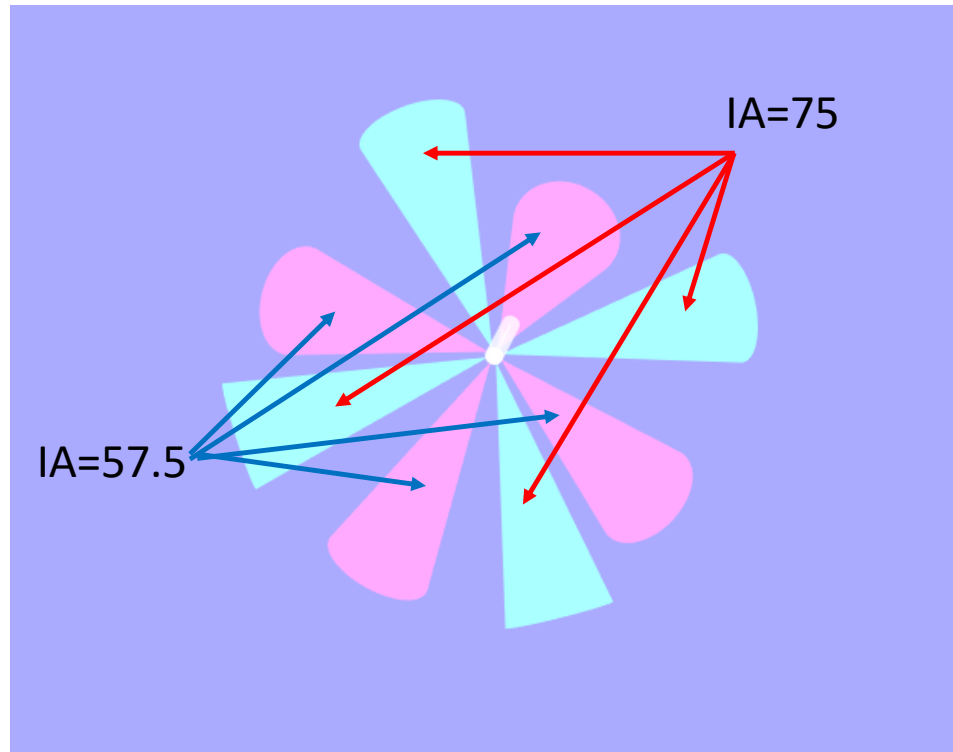


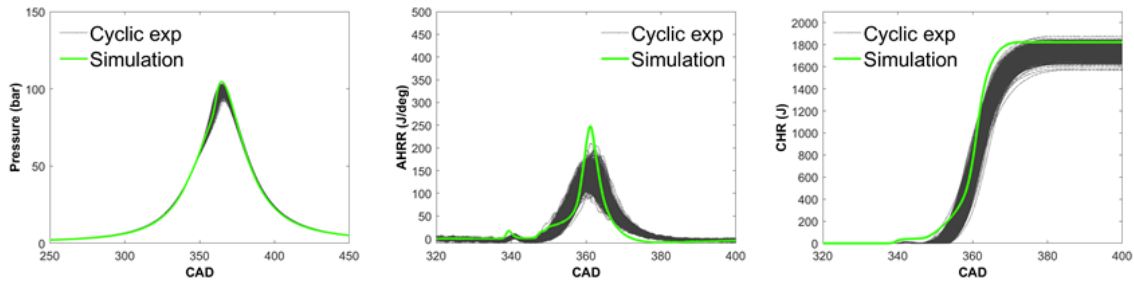
Figure 4.80 Two sets of half spray included angle schematics.

Figure 4.81 shows pressure, AHRR, and CHR plotted over experimental cyclic data for 6, 8, and 12 holes with nozzles with two sets of included angles of 57.5 and 75. We can observe that as the number of nozzles is increased from 6 to 12, the peak value of pressure, AHRR, and CHR decreases. This indicates the best combustion is obtained with 6 holes with two sets of included angles.

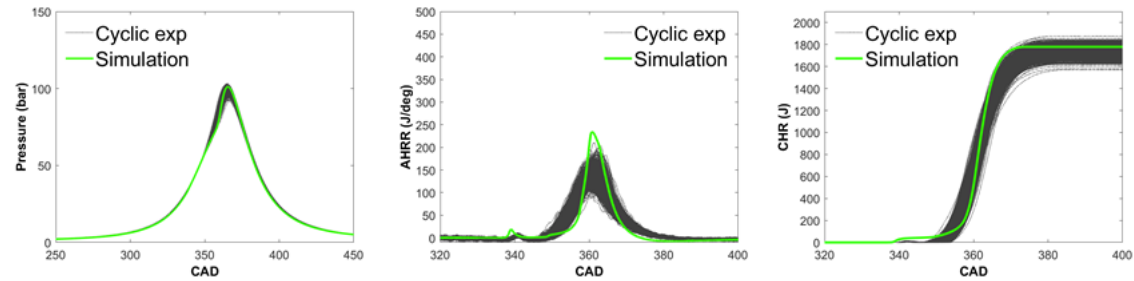
Figure 4.82 compares CC_IFCE for 6, 8, and 12 nozzle cases with two sets of included angles. Baseline case value at half spray included angle of 75 with 8 nozzles is

also shown for reference and comparison. Cases with 6 nozzles have better CC_IFCE than baseline and all other cases analyzed. One interesting case to note is CC_IFCE with two sets of included angles is better than a single included angle case with the same number of nozzles. Figures 4.83, 4.84, and 4.85 show NO, HC, and CO emissions for 6, 8, and 12 nozzles at two sets of included angles, respectively. NO emissions are lower for 8 hole nozzles than baseline case but higher for the case with 6 and 12 nozzles. Both HC and CO emissions decrease for the nozzle with 6 and 8 nozzles with two sets of the included angle compared to baseline. For 12 nozzles cases, HC is higher than the baseline case but CO is almost similar value with the baseline case. Two sets of included angles with 8 nozzles seem to bring down NO, CO and HC simultaneously and also increase CC_IFCE. Similarly, for 6 nozzle HC and CO emission values are lower than the baseline case but with higher NO values. This again suggests that the spray targeting has the potential to bring HC and CO emissions and enhance CC_IFCE.

IA-57.5_75_6H



IA-57.5_75_8H



IA-57.5_75_12H

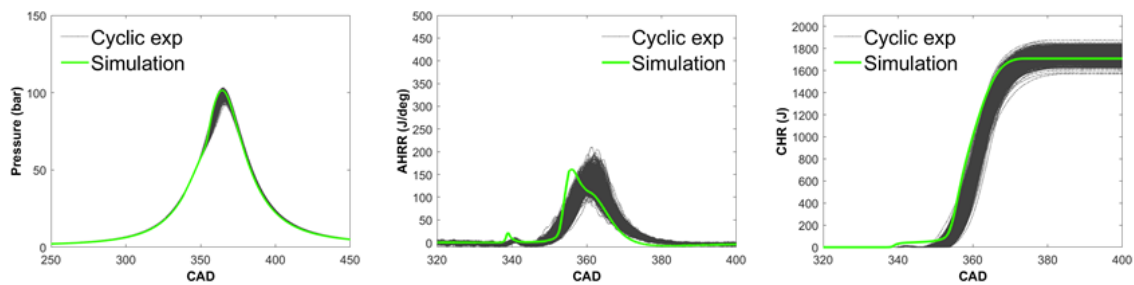


Figure 4.81 Computational pressure, AHRR and CHR histories plotted over experimental 1000 consecutive cycles for diesel injection timing of 310 CAD, 500bar injection pressure, 80 PES of methane, 1.5 bar manifold pressure, and 5.1 bar IMEP of engine load at half number of the nozzle with half spray included angle of 57.5 and another half of nozzles with half spray included angle of 75 for 6,8 and 12 number of nozzles.

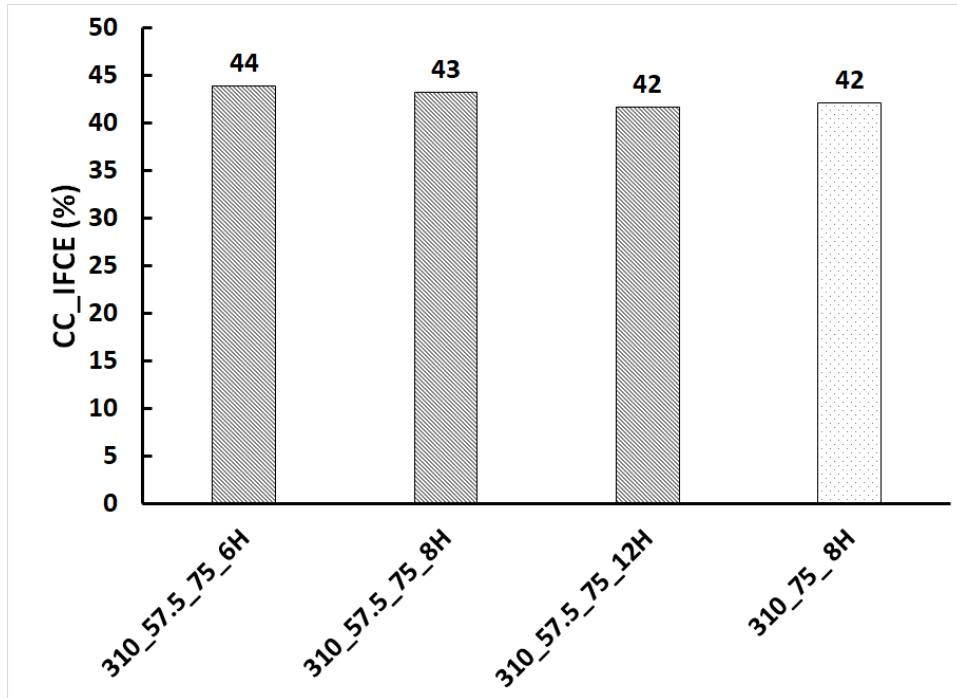


Figure 4.82 Comparison of closed-cycle indicated fuel conversion efficiency (CC_IFCE) for diesel injection timing of 310 CAD, 1.5 bar manifold pressure, 500bar injection pressure, 80 PES of methane, and 5.1 bar IMEP of engine load at half number of the nozzle with half spray included angle of 57.5 and another half of nozzles with half spray included angle of 75 for 6,8 and 12 number of nozzles.

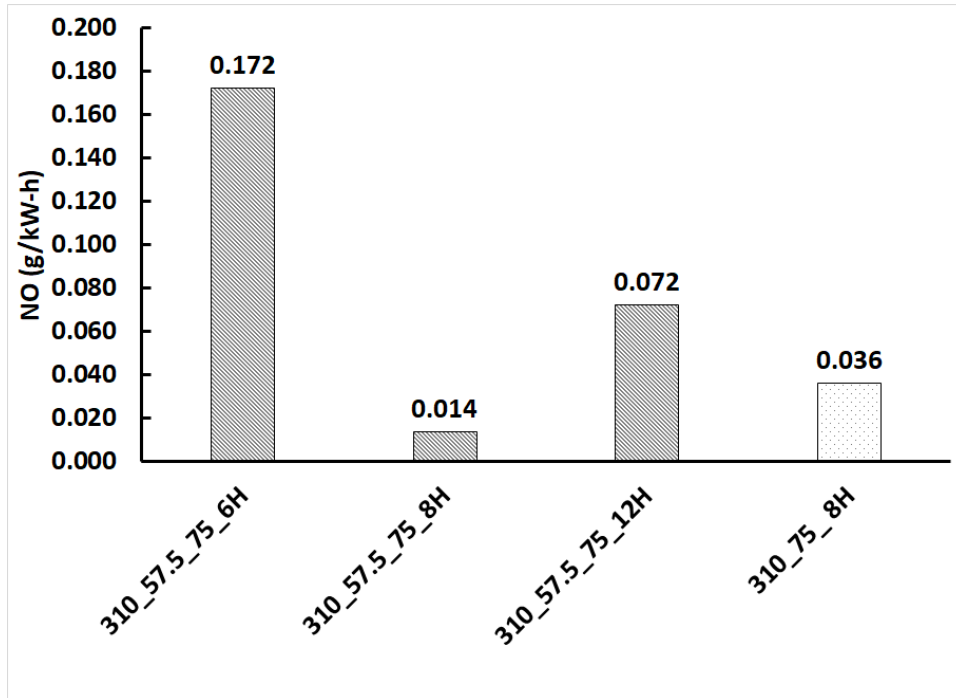


Figure 4.83 Comparison of NO emissions for diesel injection timing of 310 CAD, 1.5 bar manifold pressure, 500bar injection pressure, 80 PES of methane, and 5.1 bar IMEP of engine load at half number of the nozzle with half spray included angle of 57.5 and another half of nozzles with half spray included angle of 75 for 6,8 and 12 number of nozzles.

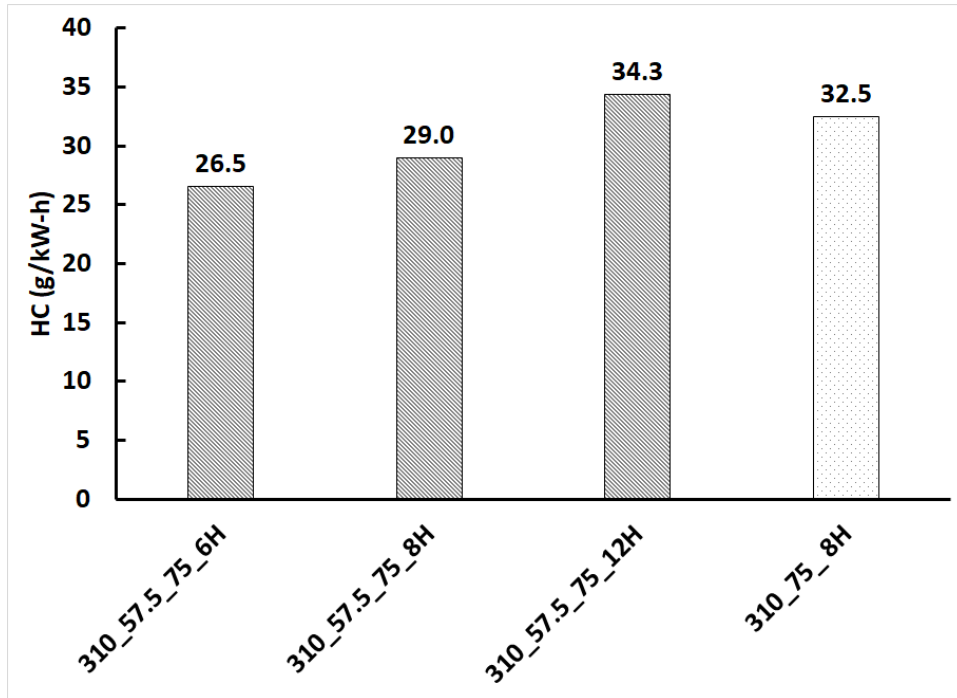


Figure 4.84 Comparison of HC emissions for diesel injection timing of 310 CAD, 1.5 bar manifold pressure, 500bar injection pressure, 80 PES of methane, and 5.1 bar IMEP of engine load at half number of the nozzle with half spray included angle of 57.5 and another half of nozzles with half spray included angle of 75 for 6,8 and 12 number of nozzles.

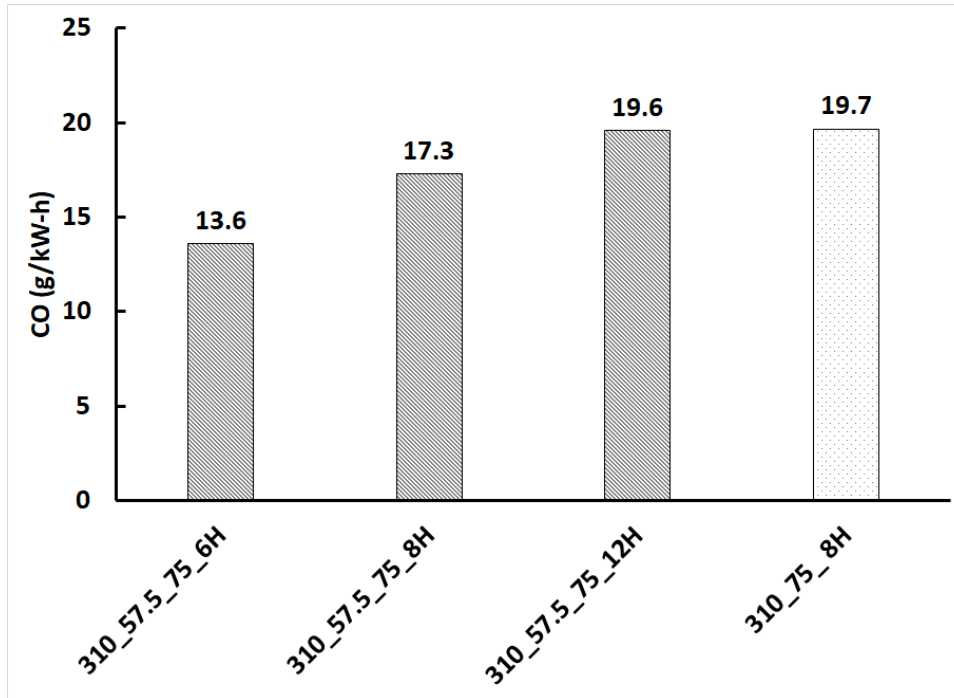


Figure 4.85 Comparison of CO emissions for diesel injection timing of 310 CAD, 1.5 bar manifold pressure, 500bar injection pressure, 80 PES of methane, and 5.1 bar IMEP of engine load at half number of the nozzle with half spray included angle of 57.5 and another half of nozzles with half spray included angle of 75 for 6,8 and 12 number of nozzles.

To further analyze this effect of using two sets of included angles, a case with 6 nozzles which has minimum HC and CO emissions was selected and react ratio v/s temperature for each computational cell and methane contour are plotted.

Figures 4.86 shows a react ratio v/s temperature plot for two sets of the included angle of 57.5 and 75 CAD with 6 nozzles. The first instance of high-temperature heat release is observed around 346 CAD. The combustion starts at a react ratio slightly lower than one (around 0.85) leading to a high temperature but not as high as in the case with a react ratio of one. It is evident from 347 CAD that there are few cells with react ratio closer to one and most of them combust by 349 CAD. The maximum react ratio observed

at 349 is around 0.7. This suggests most diesel get a chance to disperse and mix inside the cylinder. Few computational cells with react ratio closer to one lead to stronger ignition followed by combustion which spread inside the cylinder where diesel is well mixed. There are few computational cells with a temperature of 2500K where a weak dissociation reaction is observed for some computational cells causing the react ratio to increase slightly. These computational cells with high temperatures lead to higher NO compared to the baseline case. A slightly strong ignition source with sufficiently mixed diesel improves combustion thus decreasing HC and CO emissions. Figure 4.87 shows methane contours with two sets of the included angle of 57.5 and 75 CAD with 6 nozzles. Even though HC and CO emissions are lowered than the baseline case, we can still see the bulk of HC in the crevice's region remains unreacted. This suggests there is still room for improvement.

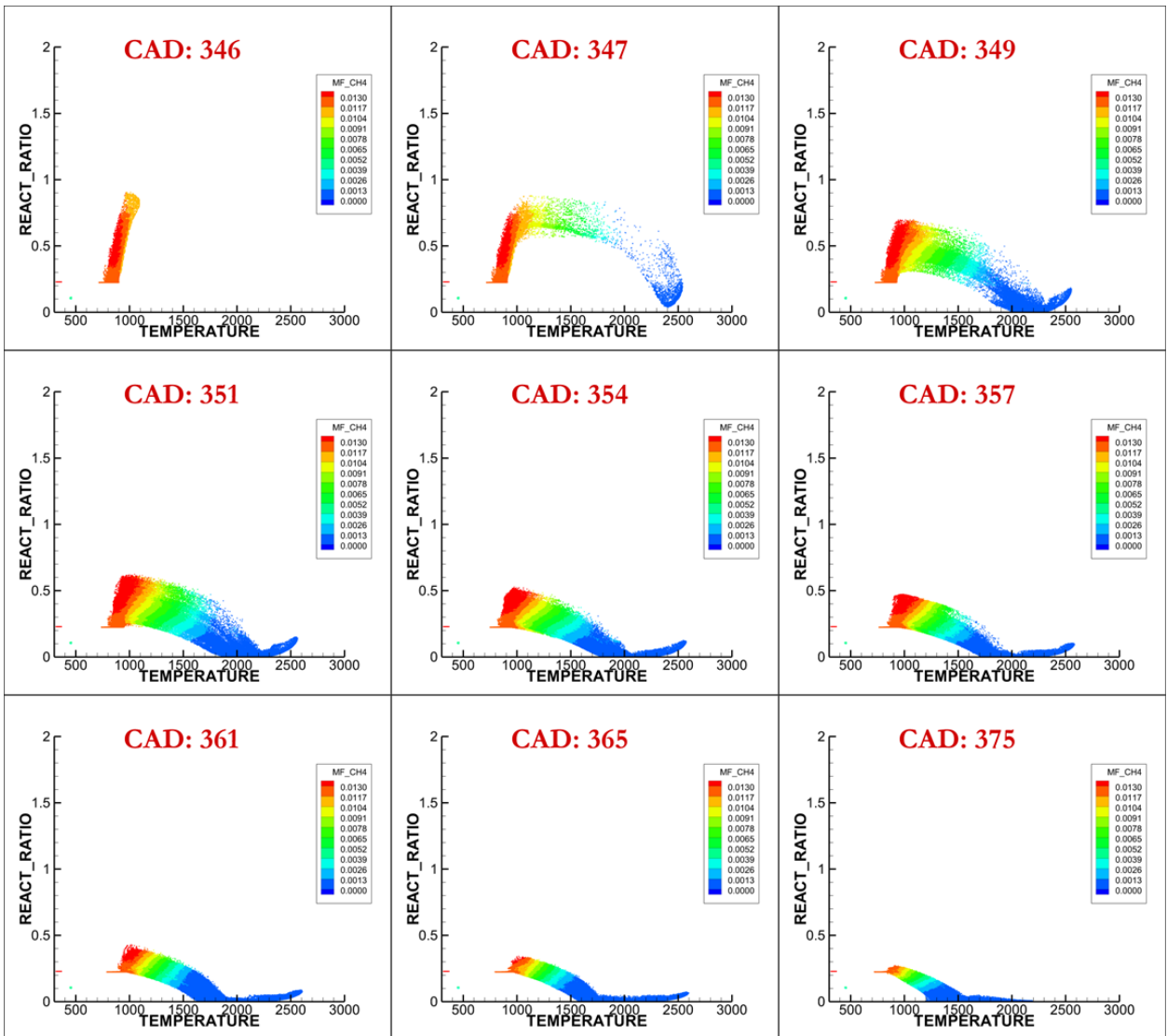


Figure 4.86 React ratio v/s temperature colored with methane mass fraction for each computational cell for diesel injection timing of 1.5 bar boost pressure, 500 bar diesel injection pressure 80 PES of methane, and 5.1 bar IMEP of engine load at half number of the nozzle with half spray included angle of 57.5 and another half of nozzles with half spray included angle of 75 for 6 nozzles.

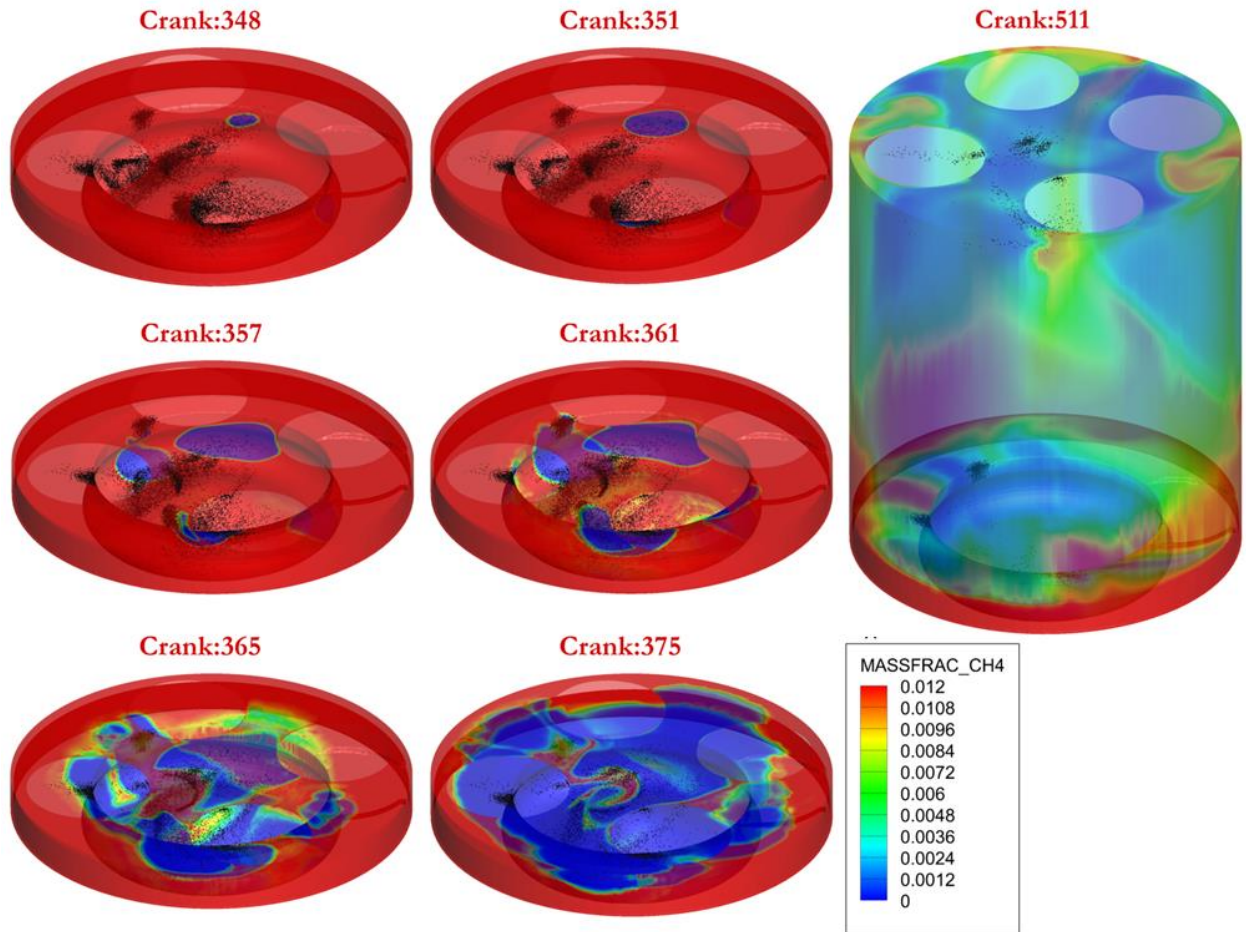


Figure 4.87 Methane distribution observed (isometric view) for diesel injection timing of 310 CAD, 1.5 bar boost pressure, 500 bar diesel injection pressure, and 80 PES of methane at half number of the nozzle with half spray included angle of 57.5 and another half of nozzles with half spray included angle of 75 for 6 nozzles.

4.7 Conclusions

In this work, CFD simulations of diesel methane dual fuel combustion in a single-cylinder research engine using CONVERGE CFD software at a low load is performed. The simulations were first validated with experimental data at three diesel injection timing of 310, 320, and 330 CAD, at an engine load of 5.1 bar indicated mean effective

pressure (IMEP), constant engine speed of 1500 rpm, 1.5 bar manifold pressure, and 500 bar diesel injection pressure. The validated model was used to perform a parametric investigation to characterize the impact of spray targeting on engine-out NO, HC, and CO emissions and CC_IFCE. The following important conclusions are drawn from the study:

- Both onsets of low-temperature heat release and the onset of high-temperature heat release of dodecane are delayed by methane. Dodecane decomposition is delayed in presence of methane which may be attributed to consumption of initially formed H, OH, and other radicals by methane forming methyl radicals.
- For early injection dual fuel engine at low loads, most of the initial high-temperature combustion comes from dodecane followed by combustion of methane.
- As diesel is injected closer to TDC, e.g. 330 CAD, ignition delays decreases as diesel has relatively less time to disperse and mix resulting in a stratified charge that auto ignites leading to several high temperature areas within the cylinder that prolong; this leads to high NO_x emissions.
- As the diesel injection is advanced, e.g. to 310 CAD, diesel has more time to mix inside the cylinder leading to most cells combusting at a lower temperatures (LTC) leading to low NO production.
- From contour plots analysis, it was observed that most of the unburned methane resided in crevices and areas near the piston top and liner.
- At low engine load, methane combustion is slow and occurs even in the expansion phase. The CO formed from the partial oxidation of methane in the expansion

- stroke does not have sufficient time to oxidize to CO₂ due to rapid bulk gas temperature drop during the expansion process, which freezes CO chemistry.
- Spray included angle sweep reveals that half spray included angles of 57.5 and 75 CAD provided best results in terms of emissions and performance. Similarly, a wide spray included angle of 82.5 has the potential to consume methane trapped inside the cervices.
 - Combustion performance deteriorates with the increase of the number of the nozzles from a baseline of 8 to 12 with an included angle of 75. Closed cycle indicated fuel conversion efficiencies (CC_IFCE) decrease by 3.7 % and both HC and CO emissions increase by 17 %. Combustion performance enhances with the decrease of the number of the nozzle from a baseline of 8 to 6 with spray included angle of 75. CC_IFCE increase by 3.7 % and both HC and CO emissions decrease by 17 and 10 % respectively.
 - Two sets of the included angle of 57.5 and 75 CAD with 8 nozzles simultaneously reduce NO, CO, and HC by 60%, 12%, and 11% respectively while increasing CC_IFCE by 2.6% relative to the baseline for this study, which is the 8 hole nozzle with 150 degrees included angle.

4.8 References

1. Thring, Robert H. Homogeneous-charge compression-ignition (HCCI) engines. No. 892068. SAE Technical paper, 1989.
2. Hardy, William L., and Rolf D. Reitz. "An experimental investigation of partially premixed combustion strategies using multiple injections in a heavy-duty diesel engine." SAE Transactions (2006): 514-531.
3. Kalghatgi, Gautam T., Per Risberg, and Hans-Erik Ångström. Partially pre-mixed auto-ignition of gasoline to attain low smoke and low NO_x at high load in a compression ignition engine and comparison with a diesel fuel. No. 2007-01-0006. SAE Technical paper, 2007.
4. Weaver, Christopher S., and Sean H. Turner. Dual fuel natural gas/diesel engines: technology, performance, and emissions. No. 940548. SAE Technical Paper, 1994.
5. Saravanan, N., and G. Nagarajan. "An experimental investigation of hydrogen-enriched air induction in a diesel engine system." International journal of hydrogen energy 33.6 (2008): 1769-1775.
6. Raihan, Mostafa S., et al. "Experimental analysis of diesel-ignited methane dual-fuel low-temperature combustion in a single-cylinder diesel engine." Journal of Energy Engineering 141.2 (2015): C4014007. Krishnan, Sundar Rajan, Kalyan Kumar Srinivasan, and Mostafa Shameem Raihan. "The effect of injection parameters and boost pressure on diesel-propane dual fuel low temperature combustion in a single-cylinder research engine." Fuel 184 (2016): 490-502.
7. Dwivedi, U., et al. "Performance and Emissions Characteristics of Diesel-Ignited Gasoline Dual Fuel Combustion in a Single-Cylinder Research Engine." Journal of Engineering for Gas Turbines and Power 136.10 (2014).
8. Wei, Hongyuan, et al. "Experimental investigations of the effects of pilot injection on combustion and gaseous emission characteristics of diesel/methanol dual fuel engine." Fuel 188 (2017): 427-441.

9. Namasivayam, A. M., et al. "Assessment of combustion in natural gas dual-fuelled compression ignition engines with dimethyl ether and rapeseed methyl ester pilot ignition." *International Journal of Engine Research* 10.3 (2009): 165-174.
10. Karim, Ghazi A. "Combustion in Gas-fueled Compression Ignition Engines of the Dual Fuel Type." *Handbook of Combustion: Online* (2010): 213-235.
11. U.S. Energy Information Administration, "Annual Energy Outlook 2020 with Projections to 2050," 0383(2020), (AEO2020).
<https://www.eia.gov/outlooks/aeo/pdf/aeo2020.pdf>
12. McTaggart-Cowan, G. P., et al. "The effects of high-pressure injection on a compression-ignition, direct injection of natural gas engine." *Internal Combustion Engine Division Fall Technical Conference*. Vol. 47365. 2005.
13. Srinivasan, Kalyan K., et al. "The advanced injection low pilot ignited natural gas engine: A combustion analysis." (2006): 213-218.
14. M.M. Abdelaal, A.H. Hegab, Combustion and emission characteristics of a natural gas-fueled diesel engine with EGR, *Energy Convers. Manag.* 64 (0) (2012) 301–312.
15. Krishnan, Sundar R., et al. "Strategies for reduced NO_x emissions in pilot-ignited natural gas engines." *J. Eng. Gas Turbines Power* 126.3 (2004): 665-671.
16. Schlatter, Stephanie, et al. Comparative study of ignition systems for lean burn gas engines in an optically accessible rapid compression expansion machine. No. 2013-24-0112. SAE Technical Paper, 2013.
17. Jha, Prabhat R., Sundar R. Krishnan, and Kalyan K. Srinivasan. "Impact of methane energy fraction on emissions, performance and cyclic variability in low-load dual fuel combustion at early injection timings." *International Journal of Engine Research* (2019): 1468087419892380.
18. Masouleh, M. Ghaderi, et al. "Comparative study on chemical kinetic schemes for dual-fuel combustion of n-dodecane/methane blends." *Fuel* 191 (2017): 62-76.
19. Kahila, Heikki, et al. "Large-eddy simulation of dual-fuel ignition: Diesel spray injection into a lean methane-air mixture." *Combustion and Flame* 199 (2019): 131-151.
20. Srna, Aleš, et al. "Effect of methane on pilot-fuel auto-ignition in dual-fuel engines." *Proceedings of the Combustion Institute* 37.4 (2019): 4741-4749.

21. Park, Hyunchun, et al. "Phenomenological micro-pilot ignition model for medium-speed dual-fuel engines." *Fuel* 285 (2020): 118955.
22. Zhang, Youtong, Song-Chang Kong, and Rolf D. Reitz. "Modeling and simulation of a dual fuel (diesel/natural gas) engine with multidimensional CFD." *SAE Transactions* (2003): 336-347.
23. Boretti, Albert. "Numerical study of the substitutional diesel fuel energy in a dual fuel diesel-LPG engine with two direct injectors per cylinder." *Fuel Processing Technology* 161 (2017): 41-51.
24. Ezoji, Hosein, Rouzbeh Shafaghat, and Omid Jahanian. "Numerical simulation of dimethyl ether/natural gas blend fuel HCCI combustion to investigate the effects of operational parameters on combustion and emissions." *Journal of Thermal Analysis and Calorimetry* 135.3 (2019): 1775-1785.
25. Pirouzpanah, V., and B. O. Kashani. "Prediction of major pollutants emission in direct-injection dual-fuel diesel and natural-gas engines." (2000): 55-67.
26. Cameretti, Maria Cristina, Roberta De Robbio, and Raffaele Tuccillo. *Performance Improvement and Emission Control of a Dual Fuel Operated Diesel Engine*. No. 2017-24-0066. SAE Technical Paper, 2017.
27. Singh, Satbir, et al. "Modeling and experiments of dual-fuel engine combustion and emissions." *SAE transactions* (2004): 124-133.
28. Singh, S., Liang, L., Kong, S. C., & Reitz, R. D. (2006). Development of a flame propagation model for dual-fuel partially premixed compression ignition engines. *International journal of Engine research*, 7(1), 65-75.
29. Jha, P. R., K. K. Srinivasan, and S. R. Krishnan. "Influence of swirl ratio on diesel-methane dual fuel combustion: a CFD investigation." *Internal Combustion Engine Division Fall Technical Conference*. Vol. 58318. American Society of Mechanical Engineers, 2017.
30. Eder, L., Ban, M., Pirker, G., Vujanovic, M., Priesching, P., & Wimmer, A. (2018). Development and Validation of 3D-CFD Injection and Combustion Models for Dual Fuel Combustion in Diesel Ignited Large Gas Engines. *Energies*, 11(3), 643.
31. Dai, Xingyi, et al. "Numerical study of combustion characteristics and emissions of a diesel–methane dual-fuel engine for a wide range of injection timings." *International Journal of Engine Research* 21.5 (2020): 781-793.

32. Aniello, Andrea, et al. "CFD Analysis of Diesel-Methane Dual Fuel Low Temperature Combustion at Low Load and High Methane Substitution." Internal Combustion Engine Division Fall Technical Conference. Vol. 51982. American Society of Mechanical Engineers, 2018.
33. Yousefi, Amin, Madjid Birouk, and Hongsheng Guo. "An experimental and numerical study of the effect of diesel injection timing on natural gas/diesel dual-fuel combustion at low load." *Fuel* 203 (2017): 642-657.
34. Gharehghani, Ayatallah, Seyed Mirsalim, and Seyed Jazayeri. Numerical Investigation of Flow Field and Combustion in a Dual Fuel Diesel Engine. No. 2010-01-0480. SAE Technical Paper, 2010.
35. Fakhari, Amir Hossein, et al. "Numerical simulation of natural gas/diesel dual-fuel engine for investigation of performance and emission." *Journal of Thermal Analysis and Calorimetry* 139.4 (2020): 2455-2464.
36. Bartolucci, Lorenzo, et al. "A Computational Investigation of the Impact of Multiple Injection Strategies on Combustion Efficiency in Diesel-Natural Gas Dual Fuel Low Temperature Combustion Engine." Internal Combustion Engine Division Fall Technical Conference. Vol. 59346. American Society of Mechanical Engineers, 2019.
37. Cameretti, Maria Cristina, Roberta De Robbio, and Raffaele Tuccillo. Performance Improvement and Emission Control of a Dual Fuel Operated Diesel Engine. No. 2017-24-0066. SAE Technical Paper, 2017.
38. Donateo, Teresa, et al. Experimental validation of a cfd model and an optimization procedure for dual fuel engines. No. 2014-01-1314. SAE Technical Paper, 2014.
39. Shojae, Kianoosh, and Majid Mahdavian. "Influences of spray angle and bowl center depth on power and exhaust emissions in a dual fuel direct injection engine." *International journal of engine research* 19.6 (2018): 643-652.
40. Kakaee, Amir-Hasan, Parvaneh Jafari, and Amin Paykani. "Numerical Study of Natural Gas/Diesel Reactivity Controlled Compression Ignition Combustion with Large Eddy Simulation and Reynolds-Averaged Navier–Stokes Model." *Fluids* 3.2 (2018): 24.
41. Liu, Xinlei, et al. "A comparative numerical investigation of reactivity controlled compression ignition combustion using Large Eddy Simulation and Reynolds-Averaged Navier-Stokes approaches." *Fuel* 257 (2019): 116023.

42. Hockett, Andrew, Greg Hampson, and Anthony J. Marchese. "Development and validation of a reduced chemical kinetic mechanism for computational fluid dynamics simulations of natural gas/diesel dual-fuel engines." *Energy & Fuels* 30.3 (2016): 2414-2427.
43. Rahimi, A., E. Fatehifar, and R. Khoshbakhti Saray. "Development of an optimized chemical kinetic mechanism for homogeneous charge compression ignition combustion of a fuel blend of n-heptane and natural gas using a genetic algorithm." *Proceedings of the Institution of Mechanical Engineers, Part D: Journal of Automobile Engineering* 224.9 (2010): 1141-1159.
44. Wijeyakulasuriya, Sameera, et al. "Multidimensional modeling and validation of dual-fuel combustion in a large bore medium speed diesel engine." *ASME 2015 Internal Combustion Engine Division Fall Technical Conference*. American Society of Mechanical Engineers Digital Collection, 2015.
45. Frassoldati A, D'Errico G, Lucchini T, Stagni A, CuociA, Faravelli T, et al. Reduced kinetic mechanisms of diesel fuel surrogate for engine CFD simulations. *Combust Flame* 2015; 162(10): 3991–4007.
46. Kannan, Jeevananthan, et al. "Large eddy simulation of diesel spray–assisted dual-fuel ignition: A comparative study on two n-dodecane mechanisms at different ambient temperatures." *International Journal of Engine Research* (2020): 1468087420946551.
47. Tekgül, Bulut, et al. "Large-eddy simulation of dual-fuel spray ignition at different ambient temperatures." *Combustion and Flame* 215 (2020): 51-65.
48. Richards, K. J., Senecal, P. K., and Pomraning, E., CONVERGE 3.0, Convergent Science, Madison, WI (2020).
49. Issa, R.I., Solution of the implicitly discretised fluid flow equations by operator-splitting. *Journal of computational physics*, 1986. 62(1): p. 40-65.
50. Pope, S.B., *Turbulent flows*. 2001, IOP Publishing.
51. Bravo, Luis, and Chol-Bum Kweon. A review on liquid spray models for diesel engine computational analysis. ARMY RESEARCH LAB ABERDEEN PROVING GROUND MD, 2014.
52. O'Rourke, P. J., and Amsden, A. A., "The TAB Method for Numerical Calculation of Spray Droplet Breakup," SAE Paper No. 872089, 1987
53. Reitz, R.D. and Bracco, F.V., "Mechanisms of Breakup of Round Liquid Jets," *Encyclopedia*

- of Fluid Mechanics, Gulf Publishing Company, 1986.
54. Reitz, R.D., "Modeling Atomization Processes in High-Pressure Vaporizing Sprays," *Atomisation and Spray Technology*, 3(4), 309-337, 1987.
 55. Schmidt, D. P., and Rutland, C. J., "A New Droplet Collision Algorithm," *Journal of Computational Physics*, Volume 164, p. 62, 2000.
 56. Naber, J., and Reitz, R. D., "Modeling Engine Spray/Wall Impingement," SAE Paper No.880107, 1988
 57. Senecal, P. K., Pomraning, E., and Richards, K. J., "Multi-Dimensional Modeling of Direct-Injection Diesel Spray Liquid Length and Flame Lift-off Length using CFD and Parallel Detailed Chemistry," SAE Paper No. 2003-01-1043, 2003.
 58. Turns, S.R., *An Introduction to Combustion*, McGraw-Hill, Inc., 1996.
 59. Heywood JB. *Internal combustion engine fundamentals*. 2nd ed. New York: McGraw-Hill, 2018.
 60. Dernote, Jérémie et al. "Influence of fuel properties on the diesel injection process in nonvaporizing conditions." *Atomization and Sprays* 22 (2012): 461-492.
 61. Guo, Hongsheng, and Liko, Brian. "Injector Tip Temperature and Combustion Performance of a Natural Gas-Diesel Dual Fuel Engine at Medium and High Load Conditions." V001T03A021. ASME. <https://doi.org/10.1115/ICEF2018-9664>
 62. Gualtieri, Carlo, et al. "On the values for the turbulent Schmidt number in environmental flows." *Fluids* 2.2 (2017): 17.
 63. Hockett, Andrew G., Greg Hampson, and Anthony J. Marchese. "Natural gas/diesel RCCI CFD simulations using multi-component fuel surrogates." *International Journal of Powertrains* 6.1 (2017): 76-108.
 64. Torelli, Roberto, et al. "Evaluation of Shot-to-Shot In-Nozzle Flow Variations in a Heavy-Duty Diesel Injector Using Real Nozzle Geometry." *SAE International Journal of Fuels and Lubricants*, vol. 11, no. 4, 2018, pp. 379–396.
 65. Swantek, Andrew, et al. "Quantification of shot-to-shot variation in single hole diesel injectors." *SAE International Journal of Fuels and Lubricants* 8.1 (2015): 160-166.

66. Narayanaswamy, K. et al. "A chemical mechanism for low to high temperature oxidation of n-dodecane as a component of transportation fuel surrogates." *Combustion and Flame* 161 (2014): 866-884.
67. Gatowski J, Balles EN, Chun K, Nelson F, Ekchian J and Heywood JB. Heat release analysis of engine pressure data. SAE technical paper 841359, 1984.
68. Sjöberg, Magnus, and John E. Dec. "An investigation into lowest acceptable combustion temperatures for hydrocarbon fuels in HCCI engines." *Proceedings of the Combustion Institute* 30.2 (2005): 2719-2726.
69. P. R. Jha, Krishnan, S. R., Srinivasan, K. K., "A CFD Investigation of the Effect of Spray Included Angle on Heavy-duty Engine Emissions and Performance" ASME 2016, ICEF2016-9486.

CHAPTER V

RECOMMENDATIONS FOR FUTURE WORK

5.1 Recommendation for Future Work

- Perform experiments with different pilot fuel (like DME, PODME and others) and observe its effects on dual fuel combustion at low loads.
- Effects of different additives (like propane, butane and others) on natural gas.
- Perform optical diagnostic on dual fuel low temperature and get better insight.
- Perform experiment with hot EGR, different intake temperature, manifold pressure to optimize combustion phasing at different energy fraction of low and high reactivity fuel.
- Perform experiment with different nozzle diameter.
- Use waste heat recovery study on exhaust gas.
- Use feedback control loop to optimize combustion phasing to improve combustion from one cycle to another to by changing different input parameter like EGR, boost pressure, injection strategy and others
- Perform cyclic study for more than 10K cycles on which Shannon entropy study can be performed. Any structure that is between one cycle to another cycle can be extracted can be used to improve engine combustion and performance.
- Emission analysis of each engine cycle needs to be performed to see its impact on HC and CO emissions in exhaust

- Perform full cycle simulation including methane injection which can help to get methane stratification.
- Use geometry of intake and exhaust runner from experimental engine to get proper fluid motion inside the cylinder
- Perform CFD results comparison with results obtained from optically accessed engine to get better model.
- Perform diesel injection rate profile to provide input to computational model.
- Incorporate rate of production and consumption of each species to better understand chemical kinetics occurring during dual fuel combustion at low loads.
- Perform many cycle studies taking into account fluctuation in initial and boundary condition.
- Incorporate conjugative heat transfer model to get better idea of heat transfer occurring from engine.
- Perform full cycle LES study of dual fuel combustion at low load.
- Perform optimization study to find the best operating parameters at low load dual fuel combustion with diesel and methane.